



**UNIVERSIDADE FEDERAL DO CEARÁ**  
**CENTRO DE CIÊNCIAS**  
**DEPARTAMENTO DE GEOLOGIA**  
**PROGRAMA DE PÓS-GRADUAÇÃO EM GEOLOGIA**

**HELANO REGIS DA NÓBREGA FONTELES**

**GEOMATHEMATICAL EVALUATION OF THE BANDED IRON FORMATIONS OF  
THE BONITO MINE (NORTHEASTERN BRAZIL): SEVERAL APPROACHES  
THROUGH MULTIVARIATE ANALYSIS, GEOSTATISTICAL  
ASSESSMENT AND 3-D GEOLOGICAL MODELING**

**FORTALEZA**

**2019**

HELANO REGIS DA NÓBREGA FONTELES

GEOMATHEMATICAL EVALUATION OF THE BANDED IRON FORMATIONS OF  
THE BONITO MINE (NORTHEASTERN BRAZIL): SEVERAL APPROACHES  
THROUGH MULTIVARIATE ANALYSIS, GEOSTATISTICAL  
ASSESSMENT AND 3-D GEOLOGICAL MODELING

A thesis submitted to the Geology Post Graduate Program of the Federal University of Ceará in partial fulfillment of the requirements for the degree of Doctor of Philosophy. Research field: Geodynamics and Mineral Resources.

Advisor: Prof. Dr. César Ulisses Vieira Veríssimo.

Co-advisor: Prof. Dr. Henrique José de Figueiredo Garcia Pereira

FORTALEZA

2019

Dados Internacionais de Catalogação na Publicação  
Universidade Federal do Ceará  
Biblioteca Universitária  
Gerada automaticamente pelo módulo Catalog, mediante os dados fornecidos pelo(a) autor(a)

---

F762g Fonteles, Helano Regis da Nóbrega.  
Geomathematical evaluation of the banded iron formations of the Bonito Mine (Northeastern Brazil) :  
Several approaches through multivariate analysis, geostatistical assessment and 3-D geological modeling /  
Helano Regis da Nóbrega Fonteles. – 2019.  
176 f. : il. color.

Tese (doutorado) – Universidade Federal do Ceará, Centro de Ciências, Programa de Pós-Graduação em  
Geologia, Fortaleza, 2019.

Orientação: Prof. Dr. César Ulisses Vieira Veríssimo.

Coorientação: Prof. Dr. Henrique José de Figueiredo Garcia Pereira.

1. Formação Serra dos Quintos. 2. Itabiritos. 3. Modelamento geológico. 4. Análise multivariada. I.  
Título.

---

CDD 551

HELANO REGIS DA NÓBREGA FONTELES

GEOMATHEMATICAL EVALUATION OF THE BANDED IRON FORMATIONS OF  
THE BONITO MINE (NORTHEASTERN BRAZIL): SEVERAL APPROACHES  
THROUGH MULTIVARIATE ANALYSIS, GEOSTATISTICAL  
ASSESSMENT AND 3-D GEOLOGICAL MODELING

Tese apresentada ao Programa de Pós-graduação em Geologia da Universidade Federal do Ceará, como requisito parcial à obtenção do título de Doutor em Geologia. Área de concentração: Geodinâmica e Recursos Minerais.

Aprovada em 16/09/2019

BANCA EXAMINADORA

---

Prof. Dr. César Ulisses Vieira Veríssimo (Orientador)  
Universidade Federal do Ceará (UFC)

---

Prof. Dr. António Jorge Gonçalves de Sousa  
Universidade de Lisboa (ULisboa)

---

Prof. Dr. Clóvis Vaz Parente  
Universidade Federal do Ceará (UFC)

---

Prof. Dr. Joel Buenano Macambira  
Universidade Federal do Pará (UFPA)

---

Prof. Dr. Mauricio Giambastiani  
Universidad Nacional de La Rioja (UNLaR)

*To the fond memory of my dear father, Antônio  
Aduino Fonteles Filho, Ph.D. Professor  
Emeritus - UFC*

## ACKNOWLEDGMENTS

Despite the fact this page comes as one of the first pages in any academic work, I think it is one of the last written. Writing the following words brought me a lot of thoughts about the fantastic opportunities that came along with this huge challenge. The journey still goes on, but it is time to present my profound gratitude for people and institutions who made possible my way to this moment.

I really thank God for all this wonderful creation that is our world and for giving me some wisdom to manage difficulties and problems that came along the trip.

My dear dad, Antônio Adauto Fonteles Filho (in memoriam), for leaving to me his example as scientist, professor and human being. I miss him so much! To him, this thesis is dedicated. To my beloved mom, Zélia da Nóbrega Fonteles, the person who always has been supportive of loving care. Without her, I'd never go anywhere! To my sister, Eveline Fonteles, I thank her for the good moments we have.

My beloved wife Carol Fonteles and my son “king” Arthur Fonteles – reason of my life. Your love and never-ending support were crucial for me to reach this point in my life. Wife! Thank you so much for helping me to organize the References section!

My lovely aunt Maria Auxiliadora Fonteles (“Tia Doia”), for her unconditional love and care.

Universidade Federal do Ceará and their professors, for the transmitted knowledge and the opportunity to improve me professionally.

My advisor and good friend, Prof. César U.V. Veríssimo. I must admit that there are very few people in the world who has such kindness and scientific proficiency. Thank you very much for this unique opportunity! This thesis is ours!

MHAG Mineração & Serviços Ltd. for allowing us access to the Bonito Mine facilities and giving us the kind permission for using their database on this work. Especially, I thank Mr. Moacir Dantas, a mining engineer, for making all much easier.

Irla G. Barbosa, for your kind help and providing petrographic samples and research material which helped me out a lot!

Prof. Dr. José de Araújo Nogueira Neto (Zeca) for granting me to join his research group embracing my own project. Thank you!

*Ciências Sem Fronteiras* scientific program (Grant number: 8887.116689/2016-00) for granting me the scholarship and making possible my Ph.D. mobility period at the

Instituto Superior Técnico/ULisboa. This study was financed in part by the Coordenação de Aperfeiçoamento de Pessoal de Nível Superior - Brasil (CAPES) - Finance Code 001.

My co-advisor Prof. Dr. Henrique Garcia Pereira (IST/ULisboa). I've learned more than I could imagine about multivariate statistics. Your guidance and dedication were truly appreciated.

Instituto Superior Técnico (IST) at the Universidade de Lisboa/Portugal, where I was very welcome during my Ph.D. mobility period at the Centro de Petrologia e Geoquímica at the Museu de Geociências. I'm indebted to Prof. Manuel Francisco who stood the hands to me and made the whole environment comfortable. I also thank Profs. Amélia Dionísio and Orquidia Neves whom I've made the first contacts at IST. I wish them the best.

Professor Jorge Sousa, who I consider as another co-advisor; he was always been available in a good mood for discussing any subject. His contributions to my apprenticeship and to this thesis are undeniable.

The managing staff of the Centro de Recursos Naturais e Ambiente (CERENA) at IST, Mrs. Elisa Costa and Mr. Paulo who helped me with the paperwork and administrative issues.

My good friend (and future Dr.) Carla Sofia A. Rocha for her support, for keeping interested in my work and for her friendship.

Chrissandro Marques, for helping me with the drilling the BIF samples and the extraction of powder for XRD analyses. Cheers mate!

My post-graduate course colleague and UFC technician Joel Pedrosa, for the elaboration of the petrographic thin sections and polished sections. I thank my other post-graduate colleagues for the good moments we had. Good coffee and good chats with Pâmella Moura and Lana Sales were pretty enjoyable.

Prof. Dr. Ana Rita Salgueiro, for her time, welcome comments, criticism, and suggestions on the preliminary versions of some chapters of this thesis.

X-Ray Laboratory at the Department of Physics of UFC, for providing me all the X-Ray diffraction analyses data I've requested to. This was possible due to CNPq #402561/2007-4 - Edital MCT/CNPq #10/2007.

Agência Nacional de Mineração (ANM) (formerly Departamento Nacional de Produção Mineral – DNPM) for the granted professional license which permitted me to dedicate myself to the scientific research during the doctorate period.

My dear colleagues at ANM, geologists Ricardo Bezerra de Sena, Fernando Antônio da Costa Roberto, Saulo de Almeida Gomes, Djalma Mourão Albano, and Jairo

Eberson Azevedo de Andrade, for their enthusiastic support during all phases of my academic work.

To the examiners of this thesis' academic jury, Dr. António Jorge Sousa (IST/ULisboa), Dr. Clóvis V. Parente (UFC), Dr. Joel B. Macambira (UFPA) and, my respectful friend, Dr. Mauricio Giambastiani (UnLaR), for their time, effort (due to the tight deadline), patience, constructive criticism and immense contributions presented to this work. Their observations on my work have improved substantially the original text.



## RESUMO

No presente trabalho buscou-se desenvolver uma abordagem pouco convencional para construção de um modelo tipológico para os minérios de ferro tipo *BIF* constituídos basicamente por minérios silicáticos e oxidados do depósito da Mina do Bonito, situada no município de Jucurutu (RN). Do ponto de vista litoestratigráfico, a mina do Bonito está posicionada na Formação Serra dos Quintos (Grupo Seridó,  $634 \pm 10$  Ma) a qual é formada por quartzitos ferruginosos, itabiritos, granada-tremolita xistos, muscovita quartzitos, gnaisses e, localmente, actinolita-xistos com magnetita, metaultramáficas, metamáficas e leuco-ortognaisses. O banco de dados geológicos abrange um conjunto multivariado de dados geoquímicos, mineralógicos, geotécnicos e operacionais relativos a 127 sondagens rotativas que foram executadas com fins exploratórios por parte da empresa detentora dos direitos minerários da mina do Bonito. Técnicas analíticas de microscopia óptica e de difração de raios X foram empregadas à caracterização petrográfica dos tipos de itabiritos. Preliminarmente, dentre as amostras de itabirito foram identificados quatro tipos: itabiritos hematíticos, itabiritos magnetíticos, itabiritos anfíbolíticos e itabiritos martíticos. Métodos multivariados foram aplicados com o intuito de construir um modelo tipológico para os itabiritos estudados com base em análises de correspondências e agrupamentos. Ao estender a análise para comportar os dados geotécnicos qualitativos disponíveis, uma avaliação das condições de intemperismo foi realizada. No presente trabalho, buscou-se, também, a construção de diagramas geoquímicos que pudesse viabilizar a classificação de formações ferríferas bandada amplamente estudadas visando um modelo de classificação inédito com enquadramento geoquímico dos itabiritos da mina do Bonito. Tendo em vista o extenso banco de dados disponível, uma avaliação da espessura mineralizada por métodos geoestatísticos de estimação (krigagem simples e ordinária) e simulação (gaussiana, sequencial direta e *simulated annealing*). O modelamento geoestatístico permitiu definir a zona de mais espessa de minério itabirítico que foi interpretada como a zona de charneira da antiforma do Bonito. Em decorrência, o modelamento geológico ocorreu de forma a criar um sólido geológico via *voxel modeling* com ênfase nas técnicas de *lithoblending* com as quais as litologias pertencentes à área de estudo foram modeladas. As principais feições obtidas que destacam-se: a estrutura dobrada da sequência litológica e o delineamento dos litotipos vulcânicos e metassedimentares não-aflorantes. A mesma abordagem foi aplicada ao modelamento do corpo itabirítico, o qual revelou complexo padrão de associação tipológica. Por fim, é apresentado um modelo de evolução geológica da área da mina do Bonito ao considerar a

associação litológica estudada como resultado de um ambiente bacinal de mar raso com expressivo aporte fluvial após a implantação de uma plataforma paleoproterozóica (representada pelos ortognaisses da Suíte Poço da Cruz). O ambiente extensional progrediu favorecendo o espessamento da pilha sedimentar originalmente pelítica com progradação representada por sedimentos psamíticos imaturos (arenitos arcossianos). O vulcanismo surgiu com o estabelecimento de zonas de fraqueza crustais com a extrusão de vulcanitos em ambiente subaquático. Tal manifestação ígnea, é considerada como a fonte das plumas contendo óxidos de ferro solubilizados que precipitaram na forma de hematita e/ou magnetita (?) em alternância com os finos estratos de sílica cuja fonte pode ter sido igualmente vulcânica como continental terrígena. Os sedimentos carbonáticos viriam a ser depositados em resposta a uma mudança climática drástica em uma bacia de circulação restrita. O modelo proposto é constituído por seis estágios, sendo o último deles, representativo dos eventos de deformação (dobramento) e metamorfismo da sequência vulcano-sedimentar. Outras considerações sobre a possibilidade de os eventos descritos serem sin ou tardi-orogênicos (Brasiliano/Pan-Africano) são apresentadas.

**Palavras-chave:** Formação Serra dos Quintos. Análise multivariada. Itabiritos. Grupo Seridó. Modelamento geológico.

## ABSTRACT

This research was focused on the Banded Iron Formations (BIF) of the Bonito Mine. The database is stemmed from an exhaustive drilling program at the mining site. Therefore, hundreds of iron ore samples were assayed for  $\text{Fe}_2\text{O}_3$ ,  $\text{SiO}_2$ ,  $\text{Al}_2\text{O}_3$ , P and Mn grades, and qualitative geotechnical data such as weathering grades, physical ore type, voids, and coring depth levels were collected from drilling core samples. The Seridó Group ( $634 \pm 10$  Ma) was divided from base to top: (a) Serra do Quintos Formation (NPsq), composed of ferruginous quartzites, hematite and/or magnetite itabirites, garnet-tremolite schist, muscovite-quartzite, gneiss, actinolite-schist with magnetite and, in some places, metaultramafics, metamafics and leucogneiss; (b) Jucurutu Formation (NPj), composed mainly by paragneisses, with intercalations of a basal conglomerate, marbles, calc-silicate rocks, mica-schist, quartzite, iron formations, metavolcanics and metacherts; (c) Equador Formation, predominantly composed of muscovite-quartzite with arkosic facies containing interbedded polimitic metaconglomerates, and (d) the Seridó Formation, which is formed of feldspathic mica schists or aluminous medium to high grade metamorphic facies on the most part of the unit. Locally, marbles, calc-silicate rocks, quartzite, and metavolcanics are interbedded in the main lithotype. A previous petrographic study has shown that there are four BIF types: amphibolitic itabirites, martitic itabirites, hematitic itabirites, and magnetitic itabirites. In order to enhance this study, a multivariate model using geochemical and geotechnical data under a systemic approach was employed. This approach was conceived to account for the whole available information, both quantitative and qualitative, through the Correspondence Analysis and Cluster Analysis grounded appropriate methodology. Another goal of this study was the classification scheme of BIFs based on major oxides grades (wt.%) and REE data ratio used for the construction of bivariate and ternary diagrams regarding the tectonic environments of the BIF deposits. The major goal of the analysis was the identification of the tectonic setting of some well-representative BIF deposits and search for a geological correlation based on metallogenic origin. A study aiming to the delineation of the mineralized thickness was performed using geostatistical estimation (simples and ordinary kriging) and simulation (Gaussian, direct sequential and simulated annealing) methods to map this geological attribute. We have demonstrated that the banded iron formations thicker areas may correspond to the antiform fold as the dominant tectonic feature at the mining site. Geological modeling was executed to compose the lithological package encompassed by the Bonito Mine study area. The relevant information obtained from the rounds of geomodeling is comprised of

interbedded magmatic rocks (basic and acid intrusive and volcanic rocks) and the less voluminous rocks such as phyllite, ferruginous quartzite, and mylonite. The geologic solids were generated by voxels modeling through the lithoblending algorithm. The same methodology was applied to the typological classification obtained from the previous multivariate analysis. The typological solids revealed complex association patterns regarding the BIF types. Finally, we propose a geological evolution concept model of the study area. This model is comprised of 6 stages describing an evolving sequence since the implantation of the sedimentary depositional environments; the start of the volcanic activity which has contributed with the input dissolved iron oxides; the deposition of banded iron formations (itabirites); formation of a narrow sea with the later deposition of the carbonates which has evolved as a rift basin. The final stage describes the deformational and metamorphic events in the Brasiliano-Pan African orogeny framework. Some aspects regarding the timing of orogeny events are discussed.

**Keywords:** Serra dos Quintos Formation. Multivariate analysis. Itabirites. Seridó Group. Geological modeling.

## TABLE OF CONTENTS

<b>1</b>	<b>INTRODUCTION</b> .....	15
<b>1.1</b>	<b>Multivariate analysis approach</b> .....	18
<b>1.2</b>	<b>Applied geostatistics</b> .....	19
<b>1.3</b>	<b>Geological modeling</b> .....	19
<b>1.4</b>	<b>The goals of this thesis</b> .....	20
<b>1.5</b>	<b>How this thesis was structured</b> .....	20
<b>2</b>	<b>THEORETICAL BACKGROUND</b> .....	24
<b>2.1</b>	<b>Principal components analysis (PCA)</b> .....	24
<b>2.2</b>	<b>Correspondence analysis (CA)</b> .....	26
<i>2.2.1</i>	<i>Summarized theory</i> .....	29
<i>2.2.2</i>	<i>Projection of active and supplementary elements</i> .....	31
<i>2.2.3</i>	<i>Absolute and relative contributions</i> .....	31
<b>2.3</b>	<b>Cluster analysis</b> .....	32
<i>2.3.1</i>	<i>Non-hierarchical classification: K-means clustering</i> .....	33
<i>2.3.2</i>	<i>Ascending hierarchical classification methods</i> .....	34
<b>2.4</b>	<b>Geostatistical methods</b> .....	37
<i>2.4.1</i>	<i>Spatial variance analysis and estimation techniques</i> .....	37
<i>2.4.2</i>	<i>Geostatistical simulation</i> .....	39
<i>2.4.2.1</i>	<i>Sequential Gaussian simulation (SGS)</i> .....	39
<i>2.4.2.2</i>	<i>Direct sequential simulation (DSS)</i> .....	40
<i>2.4.2.3</i>	<i>Simulated annealing (SA)</i> .....	40
<b>3</b>	<b>MATERIALS AND METHODS</b> .....	42
<b>3.1</b>	<b>The database</b> .....	42
<b>3.2</b>	<b>Laboratory work</b> .....	46
<b>3.3</b>	<b>Multivariate and geostatistical analysis tools</b> .....	47
<b>3.4</b>	<b>Geological modeling</b> .....	48
<b>4</b>	<b>GEOLOGICAL FRAMEWORK OF THE STUDY AREA</b> .....	49
<b>4.1</b>	<b>Tectonic setting</b> .....	50
<b>4.2</b>	<b>Petrography and X-ray analysis of the Bonito Mine BIF rocks</b> .....	52
<b>4.3</b>	<b>Mineral assemblages: X-ray diffraction data assesement</b> .....	54
<b>5</b>	<b>MULTIVARIATE MODELING OF GEOLOGICAL DATA OF THE</b>	

	<b>BONITO MINE</b> .....	67
<b>5.1</b>	<b>Identifying geochemical anomalies through principal components analysis (PCA)</b> .....	67
5.1.1	<i>PCA results</i> .....	67
5.1.2	<i>Discussion</i> .....	72
<b>5.2</b>	<b>The Bonito Mine BIF typology model based on a geomathematical approach</b> .....	73
5.2.1	<i>Geochemical evaluation with correspondence analysis</i> .....	74
5.2.2	<i>Application of K-means clustering technique: Building a bridge between the factorial space and the BIF typological model</i> .....	76
5.2.3	<i>Discussion</i> .....	80
<b>5.3</b>	<b>Weathering conditions evaluation aided by a coupled cluster-correspondence analysis approach</b> .....	82
5.3.1	<i>Geochemical and geotechnical data encoding for Multivariate Analysis</i> .....	82
5.3.2	<i>A qualitative approach using a coupled cluster-correspondence analysis strategy</i> .....	85
5.3.3	<i>Discussion</i> .....	89
<b>6</b>	<b>PROPOSITION OF SIMPLE CHEMICAL CRITERIA FOR GEOCHEMICAL CLASSIFICATION OF BIF DEPOSITS</b> .....	91
6.1	<b>Chemical database</b> .....	93
6.2	<b>Geochemical data evaluation</b> .....	93
6.3	<b>Discussion</b> .....	101
<b>7</b>	<b>MINERALIZED THICKNESS MODELING BASED ON GEOSTATISTICAL ANALYSIS</b> .....	104
7.1	<b>Geological database and analytical tools</b> .....	104
7.2	<b>Exploratory analysis</b> .....	105
7.3	<b>Estimating mineralized BIF ore thickness</b> .....	108
7.4	<b>Geostatistical conditional simulations</b> .....	112
7.5	<b>Discussion</b> .....	117
<b>8</b>	<b>TRIDIMENSIONAL GEOLOGICAL MODELING OF THE BONITO MINE</b> .....	119
8.1	<b>3-D geologic model of the Bonito mine site</b> .....	120
8.1.1	<i>Solid modeling</i> .....	120

8.1.2	<i>3-D isopach modeling</i> .....	111
8.2	<b>3-D typogical model of the Bonito mine site</b> .....	131
8.2.1	<i>Solid modeling</i> .....	131
8.2.2	<i>3-D isopach modeling</i> .....	137
9	<b>GEOLOGICAL EVOLUTION MODEL OF THE STUDY AREA</b> .....	141
9.1	<b>Preliminary geological evolution stage-model</b> .....	143
9.2	<b>Stage 6: Metamorphism and deformation</b> .....	148
9.3	<b>Discussion</b> .....	150
10	<b>CONCLUSIONS, FINAL REMARKS AND SUGGESTIONS FOR FUTURE WORKS</b> .....	152
10.1	<b>Petrographic and mineralogical characterization of the BIF</b> .....	152
10.2	<b>Identification geochemical outliers with PCA</b> .....	152
10.3	<b>The Bonito Mine BIF multivariate typology model</b> .....	153
10.4	<b>Weathering conditions evaluation through multivariate analysis</b> .....	153
10.5	<b>Simple chemical criteria for geochemical classification of the analyzed BIF</b> ..	154
10.6	<b>Geostatistical modeling of the mineralized thickness</b> .....	155
10.7	<b>Tridimensional geological modeling of the Bonito Mine</b> .....	156
10.8	<b>Evolution model of the Bonito Mine study area</b> .....	157
10.9	<b>Suggestions for future work</b> .....	158
	<b>REFERENCES</b> .....	159
	<b>ANNEX A – LITHOLOGIC MAP OF THE STUDY AREA</b> .....	177

## 1 INTRODUCTION

Since the final of World War II, iron ore reserves and recovering issues have been discussed. The main concern was related to its depletion and/or scarcity in the U.S. in the aftermath of this great war. The logical solution was to find new iron ore deposits even they were in other countries, as the companies of that time did it (KAKELA, 1981).

Iron is not considered a *noble metal*, however, it is unquestionable that is the one of the most important production input ever exploited, not to mention that iron is the fourth most abundant element in Earth's crust.

In the past fifteen years, the global industry has increased - mainly China and India with high economic growth rates in terms of average global growth - due to large efforts on urban areas expansions, continental (railways) and transcontinental logistics (naval shipments) and metallurgical engineering (MOHR *et al.* 2014).

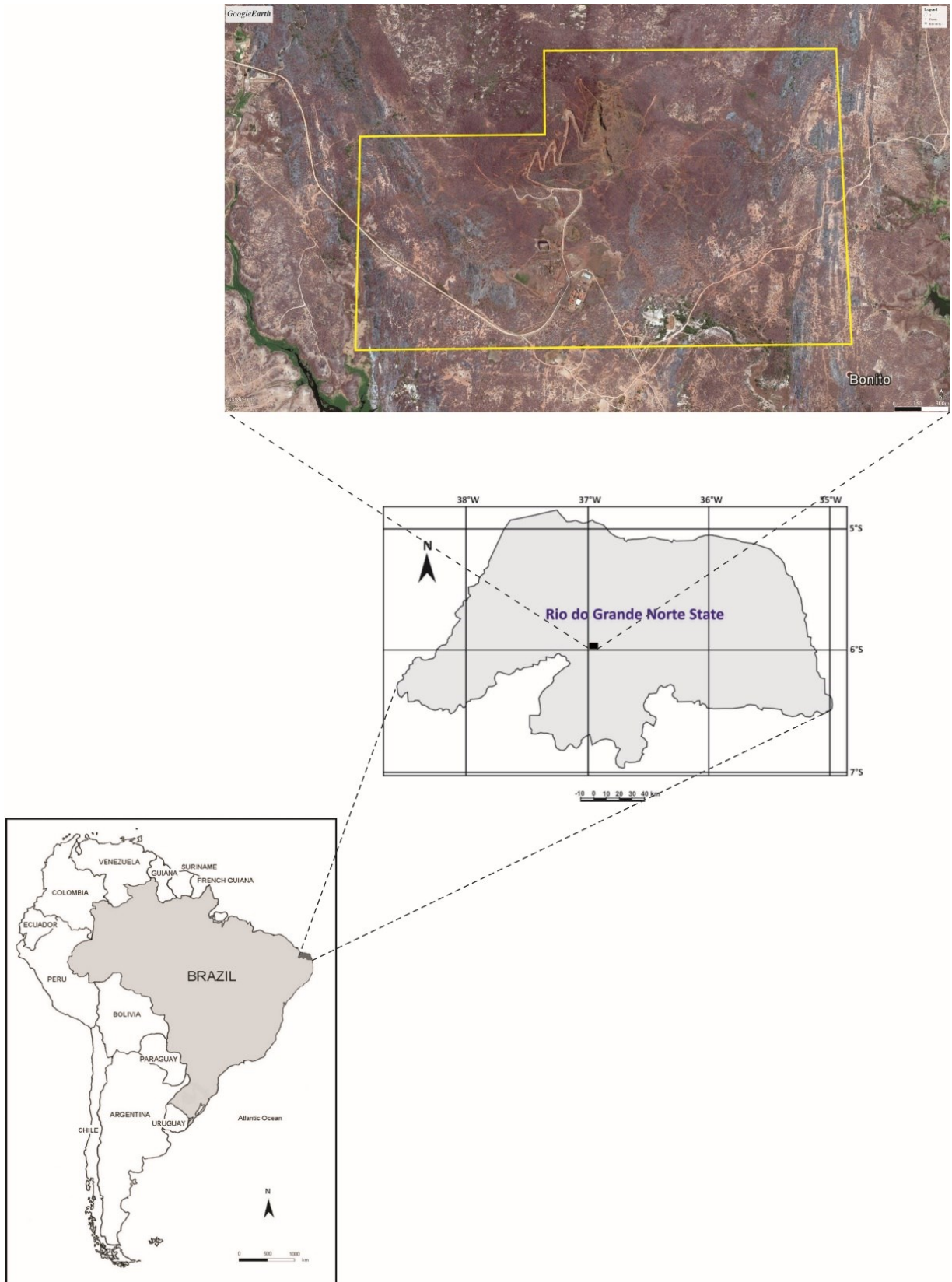
In that economic scenario, even low-grade iron ore deposits were considered in the global steel market. The iron demand turnout observed on earlies 2000 brought to light small but feasible (in technical-economic terms) iron ore deposits. However, when the ore resource is not abundant mining planning plays a definitive role in avoiding technical mistakes, geological uncertainties and, most of all, the correct identification of the ore type to be exploited. This issue was addressed by considering some methods to classify and assess the ore resources.

The Bonito iron mine is located in Jucurutu, Rio Grande do Norte State (Northeastern Brazil). MHAG Serviços e Mineração S/A company has the legal rights (Process ANM #848.211/2003) to exploit the iron ore resources since 2006 within an area of 425.44 ha (Figures 1 and 2). The access way to the study area can be done by taking the CE-040 road from Fortaleza city (Ceará State) until reaching Aracati city (146.7 km away), and then riding through BR-304 road reaching Assu town (in Rio Grande do Norte State).

Taking the road towards South through RN-233 road, we arrive at the crossroad with RN-226 and from this point on, we ride until entering the Bonito district which is closer to the entrance of the Bonito Mine facilities (Figure 3). The entire route from Fortaleza to Bonito Mine reaches 388 km.



Figure 1 – Location map of the study area.



Source: Elaborated by the author. Satellite image provided by Google Earth®

The study area is related to the Serra dos Quintos Formation, Seridó Group which is formed mainly by schist, gneiss, marble and ferruginous quartzites and banded iron formations (BIFs), from which the geochemical database is mainly derived. Most studies point a Neoproterozoic age to the sedimentation and metamorphic processes (VAN SCHMUS *et al.* 2003; NASCIMENTO *et al.* 2004).

Although the geological expression banded iron formations (BIFs) is already worldwide known describing rocks with alternating bands of iron ore minerals and silicate minerals, in this thesis, we also refer to itabirites as metamorphosed BIFs which have been studied since the 19<sup>th</sup> century (ESCHWEGE, 1824 *in* RENGER, 2005; LEITH; HARDER, 1911; HARDER, 1914; DORR II; BARBOSA, 1963; MAXWELL, 1972; CASTRO, 1994; VERÍSSIMO, 1999; ROSSI *et al.* 2019).

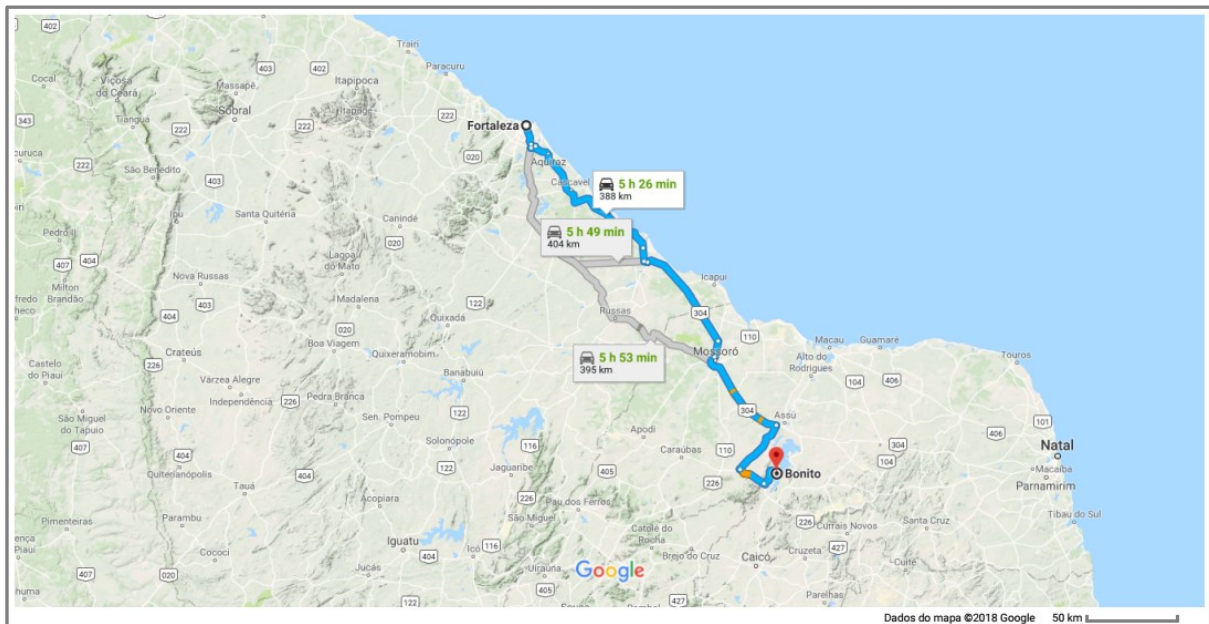
According to Barbosa (2013), the Bonito Mine resources were originally divided into two iron ore groups, mainly in consequence of their different range of Fe<sub>2</sub>O<sub>3</sub> grades, but also due to their geochemical and petrological compositions. The high-grade ores (and most feasible) are represented by magnetitic ore (91.60 - 94.20 %Fe<sub>2</sub>O<sub>3</sub>) and the magnesian skarn (60.30 - 72.33 %Fe<sub>2</sub>O<sub>3</sub>). The other iron ore group, which is the target of the proposed research, is formed of banded iron formations (itabirites) and, in contrast with the first group, contains low-grade iron ore (30.97 - 60.30 %Fe<sub>2</sub>O<sub>3</sub>).

Figure 2 – Front view of the Bonito Mine (higher ground) in the second plane. The first plane shows the soil developed upon the schist and marble rocks.



Source: Taken by the author.

Figure 3 – Schematic road map depicting the access to the study area.



Source: GoogleMaps®

## 1.1 Multivariate analysis approach

Principal Component Analysis (PCA), like one of the most popular multivariate methods, was and still is applied to several geological issues. These range from exploratory geochemical studies to geostatistical-combined approaches to mining, metallurgical and ore resources evaluation (Sousa, 1988).

The first consistent usage of automatic classification methodologies in geological sciences was performed by Parks (1966), tailed – among others – by Rhodes (1969), in a specific application to granites.

Factorial techniques had, in general terms, a more descriptive mark, which put them away from the core of automatic classification instruments. Moreover, their application in statistical terms is far from being truthful, given that they usually rely on unrealistic hypotheses like multivariate gaussianity.

The only distribution-free factorial method is Correspondence Analysis (CA), put forward by Benzécri (1973, 1977) and applied by Pereira (1981) in ore typology. This purely geometric method has the advantage of searching for a unique artificial space where individuals and properties are jointly projected, as shown by Pereira *et al.* (2015).

When sample projections onto significant CA axes are clustered using a non-hierarchical supervised method, meaningful ore types are obtained, which are plausibly explained in scientific terms, taking advantage of the previous CA/geochemical interpretation.

## **1.2 Applied geostatistics**

Ore resources evaluation is often performed by estimating grades and tonnages. It is fundamental to the economic feasibility of mines. Hence, it is vital that exploratory drilling programs yield the appropriate data for geological modeling. This must include operational drilling data, lithological/stratigraphic intervals, structural descriptive features, and geotechnical parameters. Another source of data can be associated, e.g. geophysical profiling, hydrological and structural measurements.

Geological modeling includes many approaches to geological problems. The most typical would be the geometry of ore bodies. Volumetric methods are applied to create tridimensional shapes with an emphasis on distinguishing each lithological type individually. The ore bodies can be referred to as an individual lithological type or as a separated lithology. Structural features such as fractures, fault planes, and shear zones, if they exist, can be integrated into the model (MALLET, 2002).

Geostatistical evaluation, an ore resources assessment tool, may be classified as a special case of geological modeling. The theory presented by Matheron (1963,1965), which is based on the pioneering study by Krige (1951) on South African mines, exhibits a complete applied statistical innovation for addressing mining geology problems.

The concepts of spatially-dependent variance and ore grade estimation procedures have contributed to the progress in mining science and technology. Estimation methods were developed to determine metal grade values and evaluating the uncertainty attached to estimates (JOURNEL; HUIJBREGTS, 1978).

## **1.3 Geological modeling**

Geological modeling has evolved from several situations and specific demands. As properly pointed out by Jessell (2001), geological mapping, over a pair of centuries, has been conducted improving Earth's crust knowledge. From the underground, we can account for indirect and/or direct geological record. Indirect record is depicted by geophysical data such as magnetic, electric and gravimetric surveyed data, for instance.

Direct record or data are generated by surface mapping, cross-sections and, boreholes logs (KAUFMAN; MARTIN, 2008). Both sources of data are not mutually conflicting. On the contrary, the collection of all possible data can be integrated.

Diverse as the geological data sources, different modeling methods are available for database processing. Considering the available computation resources most recently, one category of modeling methods is known as implicit geological modeling (VOLLGGER *et al.* 2015; SILVEIRA BRAGA *et al.* 2019) that uses Radial Basis Functions (RBF) to interpolate lithological data. The outcomes are represented by geological solids with smooth geological contacts between the lithological units.

#### **1.4 The goals of this thesis**

The scientific project that embraced the works developed during the Ph.D. research period was established as the “Geomathematical Evaluation of Earth Sciences Data” (Tratamento Geomatemático de Dados nas Ciências da Terra) which was sponsored by the Coordenação de Aperfeiçoamento de Pessoal de Nível Superior (CAPES).

The exhaustive geological database provided by MHAG Serviços e Mineração S/A company has presented a broad field for investigation: multiple approaches based on the multivariate data analysis, geostatistical evaluation, and tridimensional modeling techniques. Thus, the goals proposed here are:

- 1. Proposal of a typological model based on geochemical and petrographic data;*
- 2. Geotechnical and geochemical data analysis for weathering conditions evaluation;*
- 3. Spatial modeling of geological attributes of BIF rocks;*
- 4. Proposal for new chemical criteria for geochemical classification of BIF deposits;*
- 5. Geological modeling of the study area regarding the lithological available data;*
- 6. Presentation of a preliminary geologic evolution concept model for the study area.*

#### **1.5 How this thesis was structured**

This thesis was organized to assemble a number of manuscripts that present the results obtained from the multivariate and geostatistical analyses and, the geological modeling as well. Furthermore, additional chapters complement the whole work dealing and discussing the

geological framework and providing the basic concepts and models applied in the entire research work.

Chapters 5, 6, 7 and 8 were structured as isolated manuscripts to be submitted to specialized journals. During the development of the entire research, some of these manuscripts were submitted. The reader already used to follow up scientific publications will promptly recognize these article-structures.

The author has chosen to present this thesis in a traditional fashion in order to follow the suggestions previously received during his Qualify Exam. The previous chapters related to the present one, the theoretical background and materials and methods were originally written in Portuguese, and now are presented on their final versions in English.

Overall, this thesis was structured as it follows:

- ✓ **Chapter 2 – Theoretical Background.** This chapter is dedicated to present to readers the basic models and concepts of Principal Components Analysis (PCA), Correspondence Analysis (CA), Grouping Methods (Cluster Analysis) and, the geostatistical applied methods. The idea behind this chapter is to present, to the non-specialist reader, the ground knowledge of the applied methods in this study. No intention to profound into theoretical developments or questioning procedures was considered. Suggestions for complementary reading are made throughout the text;
- ✓ **Chapter 3 – Materials and Methods.** This chapter presents how the analytical and experimental data were obtained and organized forming a comprehensive geological databank. In a simple fashion way, the steps followed to overcome the work tasks are presented;
- ✓ **Chapter 4 – Geological Framework of the Study Area.** Regional geological information is presented considering the tectonic setting and the lithostratigraphy of the study area. Additionally, a petrographic study on the basis of optical microscopy and X-Ray diffraction data of the itabirites of the Bonito Mine is also discussed. In this chapter, the petrographic typology is described. This chapter mixes literature information with geological data assessment from petrographic and XRD analyses.
- ✓ **Chapter 5 – Multivariate Modeling of Geological Data of the Bonito Mine:** it contains a proposal of a BIF typological model and the weathering conditions evaluation regarding

the itabiritic rocks. A previous study based on PCA to identify geochemical outliers within the BIF chemical data is presented; followed by the typological model for the itabirites that resulted from an unusual multivariate approach. Adding qualitative geotechnical data to the previous model, the correlations between the proposed typology model and the weathering conditions of the itabirites is discussed. This chapter was subdivided into three sections; each of them was submitted to scientific events and to peer-review scientific journals;

- ✓ ***Chapter 6 – Proposition of Simple Chemical Criteria for Geochemical Classification of BIF Deposits.*** As the title says, due to the compilation of several geochemical data depicted from widely spread and well-known BIF deposits, new chemical diagrams are posed in order to address a preliminary geochemical classification scheme with respect to the main metallogenic environments;
- ✓ ***Chapter 7 – Mineralized Thickness Modeling Based on Geostatistical Analysis.*** A simple approach for the geostatistical mapping of ore resources pertaining to mineralized thickness is presented. The Serra dos Quintos Formation hosts iron formations resources that are represented by amphibolitic itabirites, magnetitic itabirites, martitic itabirites, and hematitic itabirites. Several estimation and simulation methods were applied to map the BIF thicker zones. This chapter was extracted from an original manuscript submitted to a peer-review scientific journal;
- ✓ ***Chapter 8 – Tridimensional Geological Modeling of the Bonito Mine.*** This chapter is dedicated to the presentation of the tridimensional models for the lithologic and typological (separately) assemblies which revealed several and intriguing geological features of the Bonito Mine. The Bonito Fold was defined, beforehand, in the geostatistical evaluation, but the geological modeling of this structure is presented on its final geometry. The 3D typological model enhances the full understanding of BIF types and their complex spatial distribution over the mining site;
- ✓ ***Chapter 9 – Geological Evolution Model for the Bonito Mine area.*** This closing chapter stands as the summarizing text for the great part of the information unveiled in the previous chapters. Additionally, interpretation of the major events discussed in the well-documented geology of the Seridó mobile belt had a ‘closer looking’ regarding the

lithostratigraphic architecture of the study area. An evolution concept model was then developed on a staged basis. The genetic model is strongly supported by the information comprehended during the geomodeling studies.

- ✓ ***Chapter 10 – Conclusions, Final Remarks, and Suggestions for Future Works.*** This chapter gathers the concluding remarks extracted from the previous chapters and sections. Some remaining issues are addressed as suggestions for future research.



## 2 THEORETICAL BACKGROUND

This chapter presents the basic concepts and summarized theories regarding the multivariate methods which were applied to the typological model of the itabirites of the Bonito Mine, and their weathering conditions as well. Additionally, the general exposition of the geostatistical methods is intended to support the spatial modeling of the mineralized thickness in the study area.

### 2.1 Principal components analysis (PCA)

Pearson (1901) introduced the concept of graphical representation of the correlation among variables by searching the “best fit” of points to a line or plane. Hotteling (1933a,b) conceived the theoretical basis of the principal components, as it is currently known, on the grounds of the multiGaussian distribution assumption and the independency of all components.

According to Lebart *et al.* (1984) and Wold *et al.* (1987), factorial analysis techniques above-mentioned aiming to reduce the multidimensionality of the data and then - obtain a simplified representation of the patterns of correlations and to maintain the mathematical rigor of the interpretation. The results are represented in a Cartesian plan where variables and samples will be displayed in a bi-dimensional graph fashion. Due to mathematical reasons, variables and samples are usually plotted onto separated plane graphs.

The factorial plan for the display of variables is based on the diagonalization of the correlations matrix. Meanwhile, as presented by Sousa (1988), the samples’ factorial display is drawn due to the distance similarity provided by the variance-normalized Euclidean metric.

The reduction of the multidimensional data matrix is due to a less linear data combination with a minimum of loss of primary information and preventing the distortion in the original variables’ relations (LEBART *et al.*, 1984).

Let us consider the covariance between two random variables (dimensions)  $X$  and  $Y$  expressed by:

$$Cov(X,Y) = E[E(X) - X] \cdot E[E(Y) - Y] \quad (1)$$

The variance-covariance matrix  $\mathbf{A}$  is calculated given by

$$Cov(X, Y) = \sum_{i=1}^N \frac{(x_i - \bar{x})(y_i - \bar{y})}{N} \quad (2)$$

The next step is related to the calculation of the eigenvalues referring to the matrix  $\mathbf{A}$ . This matrix can be assumed as a symmetric matrix with  $J \times J$  dimensions represented by  $a_{i,j} = cov(i,j)$ . The eigenvalue is given by the resolution of the following equation:

$$(\mathbf{A} - \lambda_i \mathbf{I})\mathbf{V}_i = 0 \quad (3)$$

given

$\lambda_i$  is the  $i^{\text{th}}$  eigenvalue;

$\mathbf{V}_i$  is the  $i^{\text{th}}$  eigenvector and,

$\mathbf{I}$  is the identity matrix.

Finding eigenvalues and eigenvectors can be done by computation by variance-covariance matrix or correlation matrix (with Pearson's  $r$  values). The  $r$  correlation coefficient can be determined by

$$r = \frac{cov(X, Y)}{[\text{var}(X) - \text{var}(Y)]^{1/2}} \quad (4)$$

Nonetheless, Pearson (1901), Hotelling (1933a), Lebart *et al.* (1984) and Mellinger (1987a) recommended that PC calculations should be performed on the correlation matrix, instead of the variance-covariance matrix. Excessive perturbation on factorial space can be noticed when variance values are quite different.

The stability of the equations system will be assured by the diagonal trace of the matrix  $\mathbf{A}$  that is equal to the sum of the eigenvalues. The PCA outcomes are, firstly, expressed by a table with the eigenvalues (ordinated in decreasing order). The eigenvalue that represents the first principal component (PC1) will be assigned by the highest value and it will retain the most part of the explained variance.

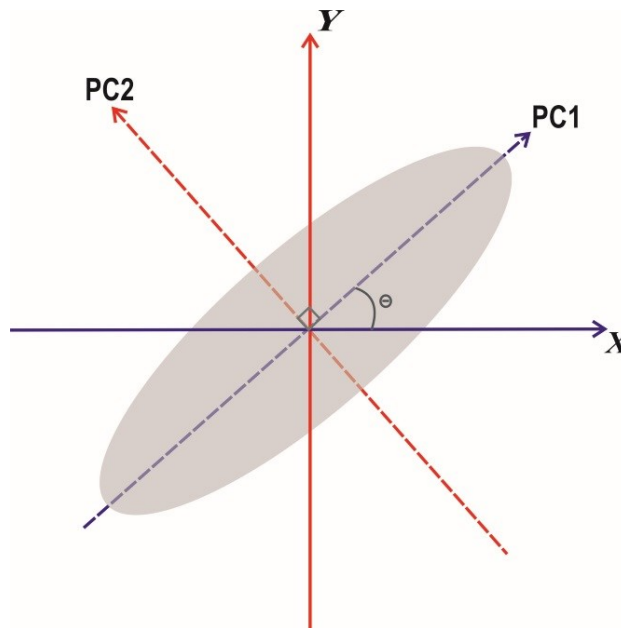
In terms of geometrical projection, PC1 will exhibit the best fit for the multivariate data cloud. The following PCs will be assigned by minor eigenvalues, thus, lower percentages of variance (Figure 4). For practical reasons, Kaiser's criterion is usually applied

to determine if PC1 and PC2, or even PC3, can be used to draw factorial plans. This rule implies to select the PCs with eigenvalues  $\geq 1$ .

Regarding the computer tools, some software packages use the R-mode and Q-mode terminologies to identify the type of analysis to be performed. The R-mode is related to the calculation of factorial loads of the columns (variables) and the Q-mode refers to the estimation of the factorial loads of the lines (samples).

According to Wold *et al.* (1987), PCA has been applied in very diverse fields of knowledge, since psychology to geosciences, especially geochemistry (MELLINGER, 1987a; PEREIRA *et al.* 2003). One of the most important features of PCA is the identification of geochemical anomalies (PEREIRA *et al.* 2003; FONTELES *et al.* 2019a).

Figure 4 – Factorial plan exhibiting the ellipsoidal data cloud and adjusted principal components 1 and 2.



Source: Adapted from Benzécri (1977).

## 2.2 Correspondence analysis (CA)

Correspondence Analysis (CA) is a geometric data treatment methodology focused on qualitative variables aiming at representing tabular data graphically, in order to assist their interpretation. The basic idea behind such a methodology – developed in the 1960s by the French mathematician Jean-Paul Benzécri (BENZÉCRI, 1973; 1977) – is that any matrix (input table) of non-negative numbers put as some form of contingency tables

concatenation can be converted into a series of two-dimensional plots representing rows and columns items in the same graph.

The primary aim of factorial analysis methods is to reduce the multidimensionality of large datasets (GRENACRE; BLASIUS, 2006; PEREIRA *et al.* 2015). For this case, let us consider a large data matrix composed of  $n$  observations (rows) tabulated according to  $p$  variables (columns) that exhibits geological, geochemical or geotechnical data, altogether. Quantitative data (hard data) may be represented by geochemical content (%wt), mineral percentages, density values, and uniaxial compressive strength test values. Qualitative data (soft data), on the other hand, is depicted by categorical, ordinal or binary codes that convey geological information.

Avoiding unnecessary *a priori* assumptions as much as possible, the interpretation of the CA results provides a means of revealing and evaluating patterns of relationships between input data (previously unintelligible, when given under a tabular form).

The mathematical rules for interpretation arise directly from the CA algorithm, as Benzécri and his followers put it forward. The first requirement, before applying the algorithm, is to ensure that the input matrix is a valid concatenation of contingency tables cross-tabulating two qualitative variables, with the modalities of the variables in each contingency table encoded in such a way as to ensure comparability and unambiguity.

For instance, for the case of the Bonito Mine, the above-mentioned requirement is met, since the initial matrix crossing samples x grades can be viewed as the cross-tabulation of two ‘qualitative variables’: rows are modalities of the variable *sample* and, columns are modalities of the variable *grade*.

Hence, it is allowed to sum upgrades for a given sample, adding up 100 if the grade is given in % (grand total = 100n) and along rows, for one column, representing the *quantity of metal* (divided by 100, since grade is given in %) for all samples (in the case of Fe and Mn), and the division by 100 of the total weight of SiO<sub>2</sub>, Al<sub>2</sub>O<sub>3</sub> and P contained in all samples (grand total = 100n). A similar rationale applies when contingency tables are concatenated in several ways, in the premise that the closure propriety is always met.

A useful advantage of CA over other – applied more frequently – multivariate statistical methods like PCA is that (in the most usual case of  $n > p$ ) such method produces always  $\underline{p}$  axis (in the most usual case where there is no proportionality between columns), whereas CA always produces  $p-1$  axes for each concatenated contingency table (the dimensional reduction starts from a smaller basis).

The meaning of interpretation in the scope of CA as put forward by Pereira *et al.* (2015) is that relationships between all projections are disclosed in terms of their linkage to each axis.

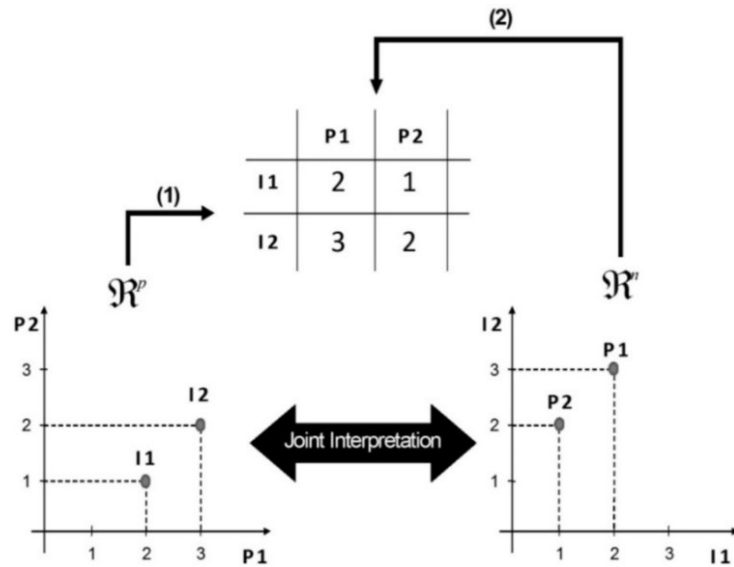
Once outlined a first interpretation scheme, there is usually a need to modify the encoding of the variables (and sometimes, of the individuals), in order to improve results. Any improvement by interactive encoding is considered as ‘satisfactory’ when the model emerging from CA outputs meet the relevant geological/geochemical information. Furthermore, in line with the CA paradigm, the model obtained as the final result of the methodology is not ‘validated’ by any statistical test of hypothesis, but by its ability to yield valuable and helpful insights into the problem posed, enhancing, in addition, the geological/geochemical *a priori* knowledge.

The input table, under the form of an  $n \times p$  matrix, can be geometrically represented by displaying the elements contained in its rows and/or columns as coordinates of points in an abstract space. As illustrated in Figure 5, depending on how the matrix is inspected (along columns or along rows), it may be converted into a cloud of  $n$  rows in the  $R^p$  space (Case 1), or into a cloud of  $p$  columns in the  $R^n$  space (Case 2). The fundamental thesis of CA is that the two geometric representations in  $R^p$  and  $R^n$  are equivalent, as demonstrated mathematically by Pereira *et al.* (2015).

This entails looking for similarities and differences from column to column, from row to row, and between columns and rows, through proximity, opposition or orthogonality analysis of the graphical outputs in terms of the topology of projections onto such graphs of the relevant input codes (representing items given in rows and columns).

This allows for the joint interpretation of rows and columns in the same plot, which means that the separate graphs displayed in Figure 5 can be combined into a single plot, even though they are produced by two different ways of viewing the basic matrix (for Case 1, rows are projected onto the columns space and the reverse for Case 2).

Figure 5 – Example of the geometric representation of the elements of a simple fictitious matrix for visualization purposes.

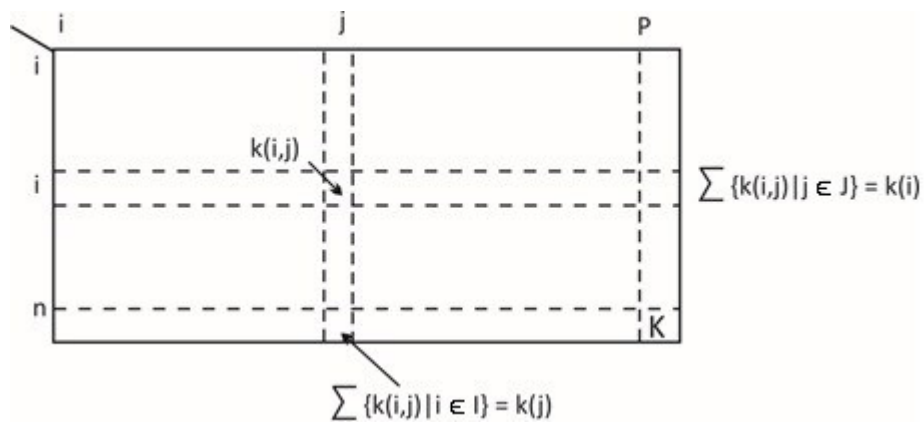


Source: Pereira *et al.* 2015

**2.2.1 Summarized Theory**

Let  $K = [k(i,j)]$ ,  $i \in I, j \in J$ , be a matrix with  $J$  columns (variables) and  $I$  lines (samples), represented by quantitative or coded qualitative data (Figure 6).

Figure 6 – Schematic illustration of  $I \times J$  data matrix.



Source: TEIL (1975).

For each line and column of this matrix, a distribution function can be drawn simultaneously and estimated given

$$f_{ij} = \frac{k(i,j)}{K}, K = \sum_i \sum_j k(i,j) \tag{5}$$

According to TEIL (1975),  $f_{ij}$  is probability estimate given

$$f_{ij} = \{f_{ij} | j \in J\}; f_{ij} \in k_j \text{ thus,}$$

$$f_j^i = \frac{f_{ij}}{f_i} = \{(f_{ij}/f_i | j \in J), f_i \text{ is the total mass in line } i.$$

$f_j^i$  represents the “profile” or conditional probability of  $j$  for a given  $i$ . The  $\chi^2$  metric is then used to calculate the distance between samples (distributional distance between  $i$  and  $i'$ ) expressed by

$$d^2(f_j^i, f_j^{i'}) = \sum_{j=1}^p \frac{1}{f_j} (f_j^i - f_j^{i'})^2 \quad (6)$$

The algorithm of CA will allow the simultaneous factorial extraction on R-Q mode, which is the representation of variables and samples onto the same factorial plane (ZHOU *et al.* 1983). The graphical display of CA differs from PCA due to the same distance metric used to estimate the distance between the profiles of variables and samples. The geometric model considered on the analysis of the matrix K is drawn by a data cloud that the aim is to obtain the moments of inertia (eigenvalues).

The most significant outputs from CA are standard Cartesian graphs showing the simultaneous projection of the points representing rows and columns onto the axes that convey the maximum fraction of the total inertia of the input matrix. The total inertia of the same clouds denotes the analog of variance in classic statistics, *i.e.* – in geometric language – the product of the point mass by the squared distance to the entire cloud gravity center). Moreover, given the symmetric encoding of the contingency tables, the axes produced by CA define a single coordinate system.

The gravity center is expressed by the following equation:

$$g_j = \sum_{i=1}^n f_i \frac{f_{ij}}{f_i \sqrt{f_j}} = \sqrt{f_j} \quad (7)$$

The inertia matrices of the data cloud are obtained estimating the distance between each point of the cloud and the gravity center ( $g$ ). The elements of the inertia matrices related to samples ( $i$ ) and variables ( $j$ ) can be calculated using:

$$I_{ig} = \sum_i \{f_i \cdot d^2(i, i_g), i \in I\} \quad (8)$$

$$I_{jg} = \sum_j \{f_j \cdot d^2(j, j_g), j \in J\} \quad (9)$$

### 2.2.2 Projection of active and supplementary elements

The CA method provides an extra approach when dealing with an exhaustive database that encompasses quantitative and qualitative data. The advantage is to project variables with diverse measurement units onto the same factorial plan. Although the CA works as a qualitative analytical tool in the general sense, the proper active variables encoding is crucial to successful analysis, in terms of logical juxtaposing the input data matrix.

The supplementary projection of some variables and/or samples can be performed by assuming that their addition or subtraction from the factorial plan will not consistently disturb the overall projection. In this case, active variables will be displayed drawing the main structure and the supplementary variables or samples will be plotted as ancillary information improving the interpretation of the active variables (LEBART *et al.* 1984; PEREIRA *et al.* 2015).

### 2.2.3 Absolute and relative contributions

The joint graphical representation of variables and samples allows obtaining additional means to aid the interpretation of the factorial plan. This is particularly useful to interpret the axes regarding variables and samples.

According to Lebart *et al.* (1984), absolute contributions refer to the significance of each class of the variables for a given factorial axis. Furthermore, they give a percentage of the variance explained by each variable in relation to each axis.

Relative contributions (or *squared correlations*, as referred by Lebart *et al.* 1984) is related to the part of the variance of the variable is explained by a principal axis. In other words, relative contributions help to interpret how the analyzed axis influences the variables.

Comprehensive theory explanations and applications to several geological issues are well described by Balladour (1970), Benzécri (1973, 1977), Hill (1974), Teil (1975), Teil and Cheminee (1975), Teillard and Volle (1976), Vallenchon (1982), Lebard *et al.* (1984),



Mellinger (1983, 1987b), Birks (1987), Reis *et al.* (2004), Grenacre and Blasius, (2006), Patinha *et al.* (2008) and Pereira *et al.* (2015).

### 2.3 Cluster analysis

There is a myriad of clustering techniques fully governed by blind mathematical algorithms alone. Performing such algorithms does not require any statistical or probabilistic assumptions, neither the prior data transformation is necessary. The numerical calculations support thousands of input data and numerical processing rely only on the hardware configurations (PARKS, 1966; RHODES, 1969; COLLYER; MERRIAM, 1973, DENESS *et al.* 1978; ROY, 1981; SAHA *et al.* 1986; BIRKS, 1987; GUTERRES, 1993; JI *et al.* 1995; MAERZ; ZHOU, 1999; PODANI, 2000; MATA, 2009; SHIMIZU, 2012; KLEN, 2015).

Such methods have been successfully applied to paleontological and taxonomical studies, social patterns recognition and, forestry diagnosis, just to name a few (PODANI, 2000). However, they are not suited for studies involving a large number of samples, without proper encoding avoiding an information overload on the graphical structure.

By contrast, *K-means* clustering algorithms require a simple and straightforward agglomeration mechanism, which is well adapted to large data sets the moving centers non-hierarchical clustering techniques. (JAIN, 2010; CELEBI *et al.* 2013).

According to Jain (2010), data clustering methods have been performed to:

- ✓ *Unveil the subjacent data structure:* identify outliers and build hypotheses;
- ✓ *Propose natural classification:* search the degree of similarity among objects;
- ✓ *Compress data:* clusters represent compressed data into similar categories.

Furthermore, the concatenation of different multivariate methods can be performed enhancing the phenomena interpretation. For instance, CA outcomes may provide a clear and comprehensive topological space, where samples and variables can be interpreted. The articulation of factorial methods with cluster techniques can improve the understanding of the relation between the groups formed in that space (SOUSA, 1988; GUTERRES, 1993; JI *et al.* 1995; REIS *et al.* 2004; CARVALHO, 2017; FONTELES *et al.* 2019b).

### 2.3.1 Non-hierarchical classification: K-means clustering

This class of clustering methods (partitioning methods) is based on the idea by gathering objects into mathematical similar groups around a point or centroid, which is considered as a representative center to the group. The groups are generated as a major initial partition without an imposed hierarchical structure. The mathematical criterion for creating the groups is based on the maximum similarity within the objects inside a group and the maximum variance between groups.

K-means clustering method, among others, is frequently used due to its simplicity, easy-going implementation, efficiency and, acceptable results under low computational costs (JAIN, 2010; AMORIM, 2016). The common trace among the non-hierarchical grouping methods is that the final scheme is built as a non-supervised classification model.

In this study, as it will be presented and discussed, K-means clustering was performed as a post-processor of the CA outcomes, in order to propose a BIF typology model of the Bonito Mine.

According to Jain (2010), the algorithm is described by the following formulae: let  $X = \{x_i\}$ ,  $i = 1, \dots, n$ , a set of  $n$  points  $d$ -dimensional to be grouped into a set of  $K$  clusters,  $C = \{c_k, k = 1, \dots, K\}$  in the Euclidean space. The K-means routine must find a partition in such way that the squared mean error between the empirical mean ( $\mu_k$ ) of a cluster ( $c_k$ ) and the point of the cluster will be minimized given by

$$J(c_k) = \sum_{x_i \in c_k} \|x_i - \mu_k\|^2 \quad (10)$$

Equation 10 defines the minimum variance within the objects in a cluster, that is, the maximum similarity among them. The empirical mean ( $\mu_k$ ) is interpreted as the centroid of the cluster ( $c_k$ ). The general solution of K-means clustering is obtained by minimizing the sum of the squared mean errors given by

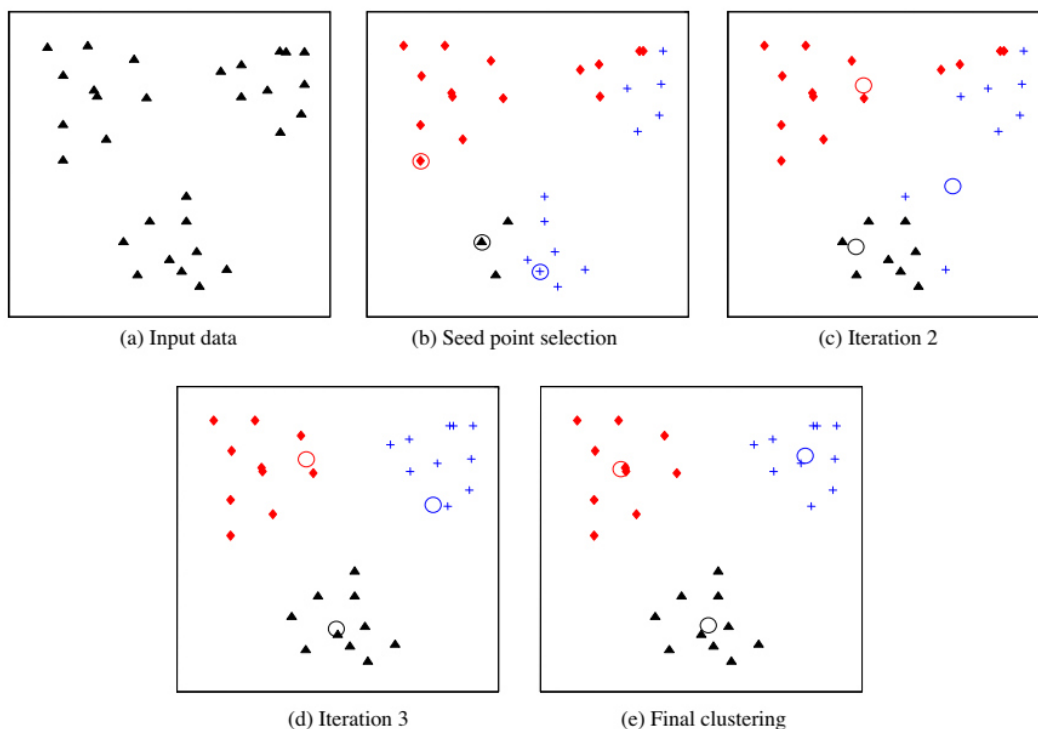
$$J(C) = \sum_{k=1}^K \sum_{x_i \in c_k} \|x_i - \mu_k\|^2 \quad (11)$$

The fundamental point of K-means is that the clustering operations are executed recursively until reaching convergence and/or reach the final number of pre-defined  $K$  clusters under the constraint of equations 10 and 11. Maximizing variance among clusters, as

expressed in Equation 11, means that the dissimilarity between K groups is mathematically the highest.

In most cases, arbitrary seeds or centroids are introduced as starting points to the iterative process (Figure 7). These seeds are iteratively moved until their positions meet the requirements constrained by Equations 10 and 11. The outcomes are represented by clusters centered by the centroids. Each centroid will gather a finite number of objects.

Figure 7 – Schematic illustration of K-means algorithm (a) 2D input data with three clusters; (b) three seed points selected as clusters centers and initial assignment of the data points to clusters; (c) and (d) intermediate updating cluster labels and their centers; (e) final clustering obtained by K-means algorithm at convergence.



Source: JAIN (2010)

### 2.3.2 Ascending hierarchical classification

Among the grouping techniques, clustering methods are the most popular multivariate analytic tools. Ascending Hierarchical Classification (AHC) algorithms are often used in the geological investigation (HONGJIN *et al.* 1995; MAERZ; ZHOU, 1999). Several grouping algorithms or linkage rules are available for AHC clustering: single linkage (nearest neighbor), complete linkage (furthest neighbor), Ward's method (minimum variance method), weighted pair-group average, unweighted pair-group average (median linkage) and weighted pair-group centroid (PODANI, 2000; HAIR *et al.* 2005). The common graphic representation is the *dendogram*.

Let be a data matrix  $K = [k(i,j)]$ ,  $i \in I$ ,  $j \in J$  (Figure 6), where  $I$  represents the samples and  $J$ , the variables. Firstly, a similarity matrix based on a distance metric is built. For the case of variables (R-mode), Pearson's coefficient  $r$  can be used as the distance metric; for the case of samples (Q-mode), several distance metrics are available for the distances calculations (Table 1). For each mode, a distance between two points is estimated. Therefore, the distance matrices for variables  $[n \times n]$  and samples  $[p \times p]$  will be obtained.

Many options of dissimilarities or distance measures are available to perform the amalgamation process such as Euclidean, squared Euclidean, City-Block (Manhattan), Chebyshev metric and Minkovski Power metric. Some of those are commonly used taking into account the previous knowledge of the nature of the database and their geological features (Table 1).

Table 1 – Some usual metrics used in distance matrix calculations.

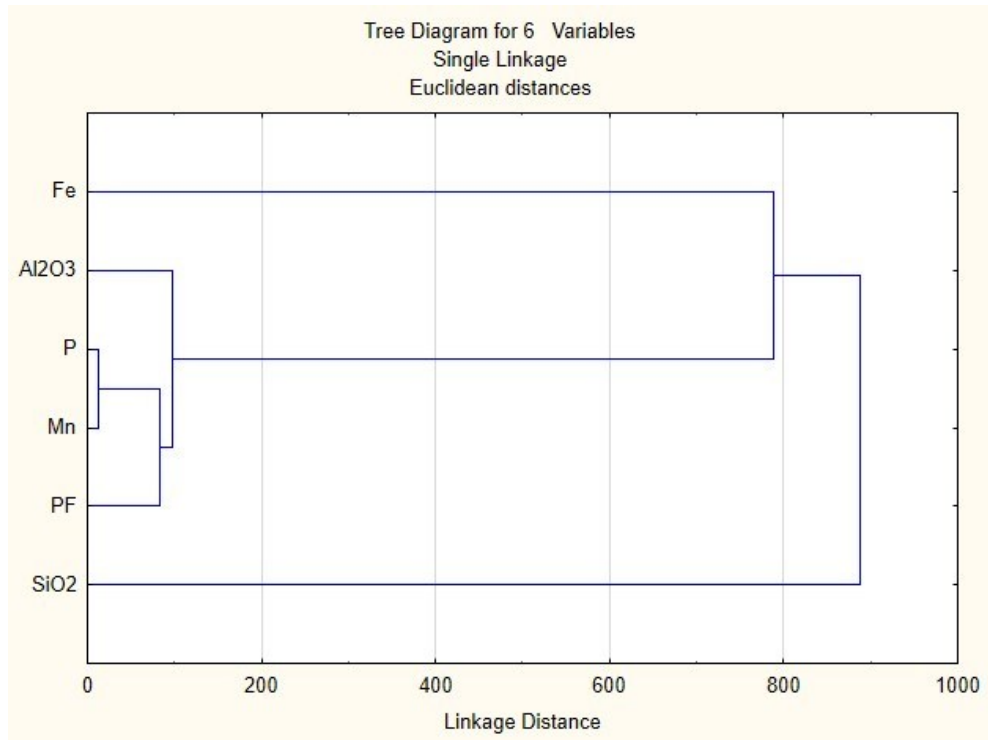
<b>Metric</b>	<b>Mathematical Formulae</b>	<b>Brief description</b>
Euclidean	$\{\sum_i (x_i - y_i)^2\}^{1/2}$	Most usual and recommended inferring distances between samples measured on the same scale.
Squared Euclidean	$\sum_i (x_i - y_i)^2$	Similar to Euclidean, but it allows to infer a crescent weight to further samples.
<i>City-block (Manhattan)</i>	$\sum_i  x_i - y_i $	Similar to Euclidean, but become more affected by outliers.
<i>Chebyshev</i>	$Max. x_i - y_i $	This metric measures distance between less similar samples. It is indicated to build up a dendrogram searching for a clear distinction between objects.

Source: STATSOFT. INC. (2010)

The nested structure of the dendrogram is based on the assumption that samples (Q-mode) or variables (R-mode) have a multidimensional similarity. Thus, the dendrogram will create similar groups in hierarchical levels, starting with a specific level until the most general level.

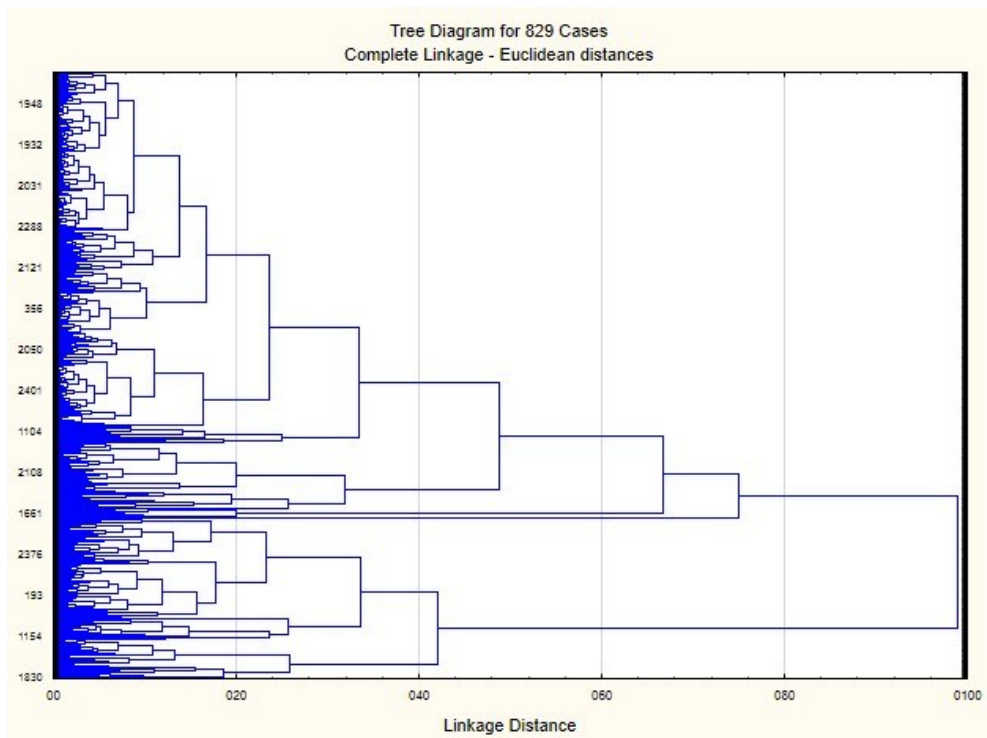
Although dendograms are, in most cases, easy to interpret, some cases may exhibit an intricate and confusing graphic display that implicates some issues due to a large number of elements in the structure (Figures 8 and 9).

Figure 8 – Dendrogram depicting the relations between geochemical variables (R-mode).



Source: Elaborated by the author.

Figure 9 – Dendrogram depicting the relations between samples. Note the intricate graphic structure which does not allow recognizing the elements (Q-mode).



Source: Elaborated by the author.

## 2.4 Geostatistical applied methods

In this section, a comprehensive exposition of the theory of geostatistical modeling owing to its wide-spread knowledge will be not presented. Instead, a brief summary of some methods used in this study will be presented.

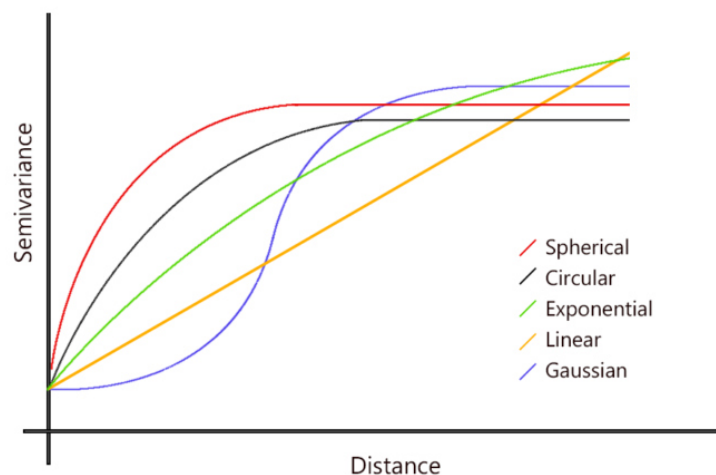
### 2.4.1 Spatial variance analysis and estimation techniques

According to the classic theory and practice presented by Matheron (1963, 1965), Journel and Huijbregts (1978), and Goovaerts (1997), variographic analysis is a simple and powerful tool for spatial dispersion assessment based on the minimum quadratic difference between two points in  $R$  space. Experimental semivariograms alone are insufficient to describe spatial phenomena, thus, adjusted theoretical models will yield structural parameters for estimation methods, widely known as kriging. The experimental semivariogram is, thus, expressed by

$$\gamma(h) = \frac{1}{2n} \sum_{i=1}^n [(z(x_i) - z(x_{i+h}))]^2 \quad (12)$$

for estimation of the spatial variance between two points ( $x_i$  and  $x_{i+h}$ ) separated from each other by the experimental Euclidean distance  $h$ . The structural parameters for variogram modeling are obtained by fitting the experimental semivariogram to a theoretical model (Figure 10).

Figure 10 – Some usual theoretical semivariogram models.



Kriging estimators form an extensive ensemble of linear and nonlinear interpolators to address stationary and nonstationary phenomena (KRIGE, 1951; DEUTSCH; JOURNAL, 1992). Some of them were developed to address Gaussian, multi-Gaussian and non-Gaussian distribution functions. In addition to the interpolated values, an estimation variance measure is available despite some criticism that emerged concerning the usefulness of such a measure (YAMAMOTO, 2000; 2008).

Among the linear interpolators, ordinary kriging and simple kriging may be considered the most used techniques hitherto. The difference between them relies upon the acknowledgment of the stationary mean. Based on the ordinary kriging theory, the phenomenon to be investigated is second-order stationary but its local mean is assumed unknown. Thus, neighboring kriging weights are set to total to 1.

When estimating with simple kriging, the premise of second-order stationarity remains; nonetheless, the global mean is supposedly known (BOUFASSA; ARMSTRONG, 1989; GOOVAERTS, 1997).

Estimation of an unknown value  $z^*(x_i)$  by simple kriging is given by

$$z^*(x_0) = m + \sum_{i=1}^n \lambda_i [z(x_i) - m] \quad (13)$$

$m$  is the assumed known global mean and  $\lambda_i$  is the  $i^{\text{th}}$  weight obtained by equation system resolution related to experimental semivariogram modeling. The simple kriging variance is, thus, expressed by

$$\sigma_{SK}^2 = C(0) - \sum_i \lambda_i C(x_0 - x_i) \quad (14)$$

$C$  is the spatial covariance.

Estimation of an unknown value  $z^*(x_i)$  by ordinary kriging is given by

$$z^*(x_0) = \sum_{i=1}^n \lambda_i z(x_i) \quad (15)$$

The ordinary kriging system is based on the unknown global mean, hence, the estimates are constrained by kriging weights summation

$$\sum_{i=1}^n \lambda_i = 1 \quad (16)$$

The primary criticism of kriging estimation is smoothing issues that are obvious when the original extreme values of the data range are underestimated and/or overestimated. Many authors have addressed these problems over the years (JOURNEL, 1974; JOURNEL; HUIJBREGTS, 1978; BOUFASSA; ARMSTRONG, 1989; DEUTSCH; JOURNEL, 1992; YAMAMOTO, 2008). Nonetheless, this interpolation method continues to be applied in several geological situations.

#### **2.4.2 Geostatistical simulation**

Stochastic simulation has been applied to Earth Sciences problems since the 1970s, however, its effectiveness has always relied on the computational capacity of the machines of that time. Geostatistical simulation methods have evolved along with the kriging methods exhibit the same appeal, but with different purposes (JOURNEL, 1974).

Similar to the kriging methods, currently, assorted options of simulations algorithms have been developed and become available to users through private-use and freeware computational programs since the 1990s. In the following section, the basic ideas behind the sequential Gaussian simulation, direct sequential simulation, and simulated annealing will be shortly described.

##### **2.4.2.1 Sequential Gaussian simulation (SGS)**

SGS is a popular geostatistical simulation algorithm that has been broadly used in natural resources modeling and environmental uncertainty (JOURNEL, 1974; GOOVAERTS, 1997; HOHN; MCDOWELL, 2001; LIN *et al.* 2001a,b; EMERY; PELÁEZ, 2011; ZHAO *et al.* 2014; PARVARZAR *et al.* 2015).

SGS realizations result from a normal score transformation of raw data into a new dataset referring to the normal conditional distribution function. The entire process involves the calculation of new conditional data through a systematic algorithm in which simple



kriging is performed in a loop-based mode. Further details of this method were presented by Deutsch and Journel (1992), Goovaerts (1997) and Yamamoto (2008).

#### 2.4.2.2 *Direct sequential simulation (DSS)*

DSS is a conditional simulation method developed to improve natural resources modeling with no dependency on the Gaussian anamorphosis of the original data values. Journel (1994) demonstrated that simulated values can be obtained from a local conditional distribution based on simple kriging. Although it was perceived that the spatial covariance of the original variable could be replicated, the problem discovered was the inability to reproduce the experimental histogram.

Caers (2000) and Soares (2001) presented their own solutions to overcome this drawback. Caers (2000) proposed adding local accuracy to the global accurate realization by constraining the simulated nodes to the variable histogram.

Soares (2001) demonstrated improvement by applying simple kriging mean and variance to sample from a global conditional distribution function and subsequently using Gaussian transformation to create local distribution subsets of the target histogram intervals.

#### 2.4.2.3 *Simulated annealing (SA)*

The SA stochastic simulation method differs from the others described thus far owing to the particular solution given to a problem related to thermal interaction between particles through a numerical implementation of an optimization technique (METROPOLIS *et al.* 1953). The “annealing” model was developed by comparing the melting process of a single crystal and subsequently reducing the temperature to control its annealing that can be monitored by stages until the system reaches its “freezing point” (KIRKPATRICK *et al.* 1983). GEMAN; GEMAN (1984) extended the concept of SA to restore degraded images by applying Bayesian and Markovian statistics.

The SA algorithm instructs the creation of a 3-D model by thermal perturbation that imputes random values obtained from a histogram at each data location. The next step is related to the objective function that may be described as the squared difference between the experimental and the modeled semivariograms. The image (3D model) is eventually perturbed by swapping a pair or sets of values, randomly.

Similar to other stochastic algorithms, SA requires a convergence criterion explicitly by the gradual decrease in temperature (parameter of the Boltzmann's distribution). When swapping stops, the final "annealed" image, e.g. stochastic realization, is generated (DEUTSCH, 1992; DEUTSCH; COCKERHAM, 1994; GOOVAERTS, 1998).

### 3 MATERIALS & METHODS

The research work was developed through a phase sequential path allowing the execution of important tasks that were completed whilst the outcomes were analyzed and validated in terms of scientific meaning. These phases are described as it follows:

- *Relational data management: The databases provided as drill core logs, chemical assays, geomechanical qualitative data, and lithological data were systematically organized under Microsoft Access<sup>®</sup> 2010 relational data manager in order to optimize the data queries and enhance the geological and geochemical data exploitation;*
- *Fieldwork: BIF and other rocks samples were collected from previously selected drill cores for preparation of polished and thin sections for optical mineralogy studies (Figure 10);*
- *Laboratory work: Petrographic study of thin sections and polished sections for mineralogical determination were carried at the SEM Laboratory at the Department of Geology at the UFC and the Petrology and Geochemistry Laboratory of the Geosciences Museums at the Department of Civil Engineering and Georesources of the Superior Technical Institute at the ULisboa. Powder materials extracted from BIF samples were submitted to X-Ray diffraction analysis in X-Ray Laboratory at the Department of Physics at the UFC.*
- *Data analysis: this phase embraced all the studies concerning the multivariate analysis, geostatistical evaluation and geological modeling. Several input data matrices were structured for data processing and its interpretation.*

#### 3.1 The database

The geological database is composed of 127 drill core logs comprising quantitative and qualitative data: lithological descriptions, boreholes intervals, geotechnical features, drilling orientation paths, and chemical assay data (Figure 11). The drilling operations gathered 16,335 meters of geological record. Among the total of 127 drill cores, 87 were classified as “positive”, that is, within these cores, itabirites were described and sampled

within 9,579 meters of drilling record. The lithological descriptions are available for each 3 meters-interval in the drill core (Figure 12).

The chemical data were obtained from samples prepared at MHAG's geomechanics laboratory and sent to SGS-GEOSOL Labs. Ltd (Minas Gerais State, Brazil) for treatment with lithium tetraborate fusion for XRF spectrometry of Fe, SiO<sub>2</sub>, Al<sub>2</sub>O<sub>3</sub>, Cr<sub>2</sub>O<sub>3</sub>, V<sub>2</sub>O<sub>5</sub>, TiO<sub>2</sub>, CaO, MgO, K<sub>2</sub>O, Na<sub>2</sub>O, P, and Mn (%wt) (Figure 13).

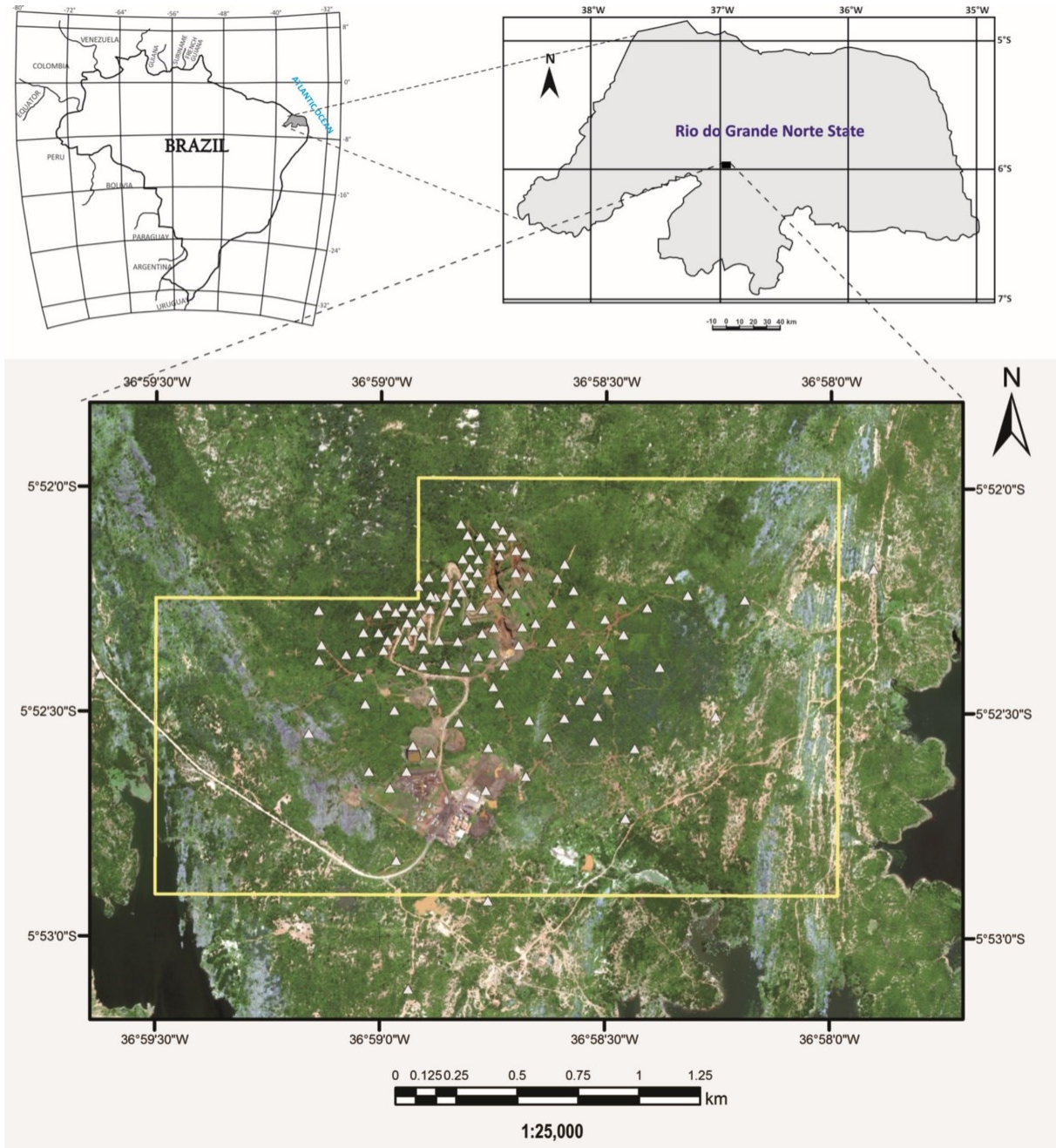
The loss on ignition (LOI) assay on samples was performed by the calcination process (at 1000 °C) until reaching constant masses. The iron content (Fe) assayed for the mine feasibility evaluation was converted to Fe<sub>2</sub>O<sub>3</sub> values using the division factor of 0.6994.

Figure 10 – Description of geological features on drill cores stored in boxes.



Source: Taken by the author.

Figure 11 – Location map of the drill cores in the study area.



Source: Elaborated by the author.

Figure 12 – BIF drill core box exhibiting lithological features commonly seen.



Source: Taken by the author.

Figure 13 – Graphic interface of the relational databank manager used for geological data handling.

MHAG\_Database\_DR\_version: Banco de dados (formato de arquivo do Access 2000) - Microsoft Access

Arquivo | Página Inicial | Criar | Dados Externos | Ferramentas de Banco de Dados

Modo de Exibição | Colar | Recortar | Copiar | Pincel de Formatação | Área de Transferência | Classificar e Filtrar

Filtrar | Crescente | Decrescente | Remover Classificação | Avançado | Alternar Filtro

Atualizar Tudo | Salvar | Excluir | Mais | Novo | Totais | Ortografia | Localizar | Substituir | Ir para | Selecionar

Formatação de Texto

Formulários

SISTEMA GERENCIADOR

DADOS GEOLÓGICO-GEOQUÍMICOS

Dados Operacionais Sondagem

Geologia Geoquímica Global

Lista Empresa subformulário

SISTEMA GERENCIADOR

Tabela Furo

**Sistema Gerenciador do Banco de Dados**

DEPARTAMENTO DE GEOLOGIA

**DADOS BÁSICOS**

SR\_ID: 1

MHAG\_ID: BTO-FSR-022

UTM Leste: 723419.41

UTM Norte: 9350616.73

Z (m): 198.07

Recuperação (m): 62.05

Recuperação (%): 83.40

**Dados Operacionais**

Azimute: 331°31'20"

Inclinação: 60°

Registro: 1 de 1

**Geologia e Geoquímica Global**

Am-FSR\_ID: [ ]

FROM: 0.00 TO: 3.00

Espessura: 3.00 LITOLOGIA: ITB

SAMPLEID: GLBTO01019 SAMPLELAB: 2173,00

Fe	28.00	K2O	0.19
FeO	1.36	Na2O	<0,1
SiO2	49.60	V2O5	NC
Al2O3	2.58	Cr2O3	NC
P	0.04	TiO2	0.06
Mn	0.70	PF	1.99
CaO	2.28	MgO	1.01

Registro: 1 de 23

Modo formulário

Num Lock

Source: Elaborated by the author.

### 3.2 Laboratory work

The petrographic analysis was performed with optical microscopy work in order to describe minerals, petrographic fabric, intergrain contact relations, grain size and to obtain percentage estimates. For this purpose, 39 samples were used for the preparation of 32 polished sections and 17 thin sections were described. The whole material was prepared at the Petrographic Preparation Laboratory at the Department of Geology/UFC. Geologist M.Sc. Irla G. Barbosa kindly contributed 16 samples (among the total of 39) used in this study.

X-ray diffraction analysis was also performed in order to address some mineralogical issues recognized after petrographic studies. The analyses were carried on by the X-Ray Laboratory at the Department of Physics/UFC. The goal was the identification of some silicate and oxide mineral phases that were not properly described during the petrographic analysis.

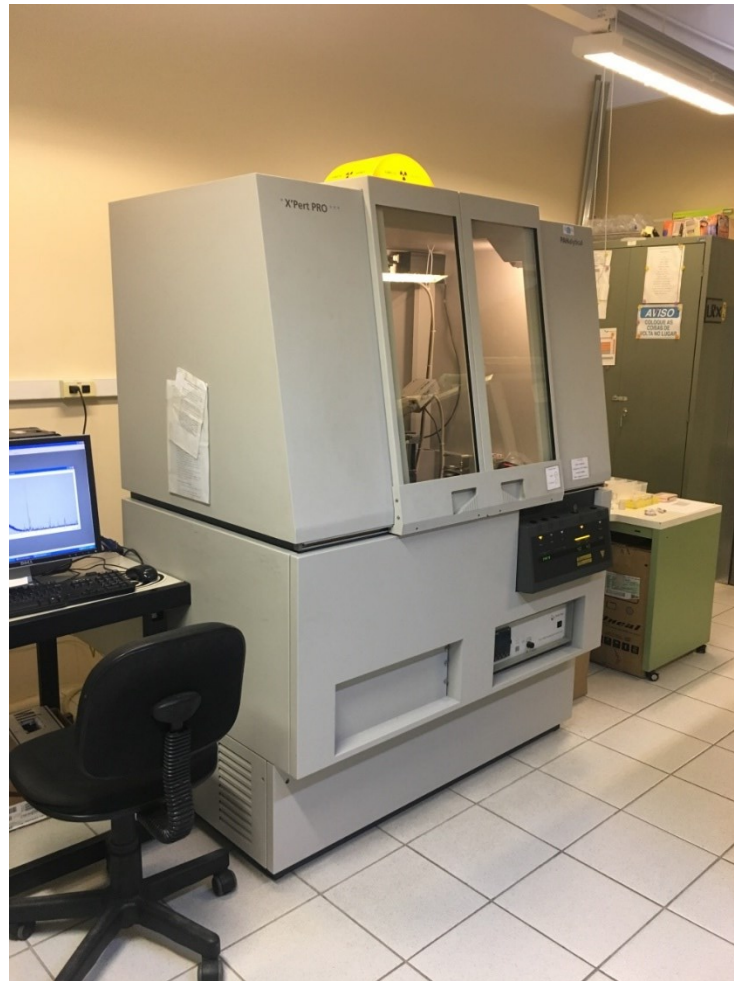
The preparation of the samples implied on drilling the BIF samples to extract approximately 1g of powder. PANalytical X'pert Pro MPD (Figure 14) was used in order to obtain the results performing with cobalt tube and full range scanning (initial  $2\Theta = 10^\circ$ , final  $2\Theta = 100^\circ$  with  $\Delta\Theta = 0.013^\circ$ ). This analytical technique is based on X-ray incidence on samples which provokes reflections inside the crystalline structure. Each mineral has its own collection of  $2\Theta$  spacing angles that describes the crystallographic structure.

To process the X-ray analytical results in *HighScore Plus*<sup>®</sup> 3.0.4 software, two different crystallographic databases were handled: International Centre for Diffraction Data (ICDD-PDF2003) and Crystallography Open Database (COD2016).

The data treatment was executed running basic routines for mineral identification and matching the experimental data to the available patterns recorded in the databases. Not all suggestions that appeared in the software's list were plausible owing to the previous geological knowledge of each BIF rock. Thus, the petrographic study has aided the identification of the mineral phases.

The results are illustrated by Cartesian graphs (diffractograms) displaying the X-axis as the  $2\Theta$  angle values and the Y-axis as the intensities of the X-ray incidence responses. Thus, the identification of some silicate and oxide mineral phases, that were not properly described during the petrographic analysis, was relevant for additional mineralogical information.

Figure 14 – The PANalytical X'pert Pro MPD diffractometer used for XRD analysis (X-Ray Laboratory at the Department of Physics/UFC)



Source: Taken by the author.

### 3.3 Multivariate and geostatistical analysis tools

Looking at the entire database, the emphasis was given to low-grade BIF considering the ratio  $\text{Fe}_2\text{O}_3/\text{SiO}_2 \leq 1.00$ . The other major oxides weren't included in the multivariate analyses because not all BIF samples had the input values to be considered. Thus, these missing data could introduce uncertainty and restrict the geochemical interpretation of the data matrix as a whole. Thus, the geochemical variables which formed the input data for PCA and CA were based on  $\text{Fe}_2\text{O}_3$ ,  $\text{SiO}_2$ ,  $\text{Al}_2\text{O}_3$ , P, and Mn grade values.

The geotechnical data was collected during a systematic survey of the boreholes' logs. From each borehole's 3 meter-interval core data - such as ore/rock type, structures, fracturing, core recovery, mechanical type, and weathering grade - were organized on a database system for further comparisons and analyses.



Most of these data sources can be depicted as categorical data and the properties disclosed by them can be encoded describing important geotechnical aspects. Four qualitative variables were taken to be included in the multivariate modeling: depth of the ore samples (m), weathering condition, mechanical type and porosity (voids). Further details can be consulted in Section 5.3 of this thesis.

The statistical work was carried on ANDAD 7.20 (CVRM, 2002) software and *Statsoft Statistica*<sup>®</sup> 10 Enterprise software package. Spatial data management was fully supported by *Microsoft Access*<sup>®</sup> 2010 and ESRI *ArcMap*<sup>®</sup> 10.1 systems. Rockware *RockWorks*<sup>®</sup> 16 was used for the 3D lithological drill core modeling.

For the case of the geostatistical analysis, the procedures were executed using the Geostatistical Modelling Software (GeoMS – CMRP/IST). Graphically enhanced maps were obtained by finishing work on Golden<sup>®</sup> *Surfer* v.12.

### **3.4 Geological modeling**

The geological borehole database provided by MHAG Company is formed by drill core logs that encompass lithological descriptions, “from-to” intervals measurements (m), drilling orientation, total depth values (m) and elevation values (m).

To assess the entire geological data, some procedures were necessary to be executed. *Microsoft*<sup>®</sup> *Excel* plans were elaborated combining operational and geological data. Elevation values vary from 0.00 to 415 m and depth values vary from 10 to -508 m.

Most parts of the drill holes were vertically orientated, but some of them, due to the geology of the area, were executed with heading specific directions. Geodetic coordinates are referenced to the UTM Zone 24S, SAD’69 datum.

*Rockworks*<sup>®</sup> 16 demanded the proper encoding for BIF typology and the lithology data. The models, that have been generated, are constrained by geographic information and typological/lithological data only.

#### 4. GEOLOGICAL FRAMEWORK OF THE STUDY AREA

The Caicó Complex (2,250 – 2,078 Ma U-Pb) comprises metabasalts, amphibole-gneiss, and garnet-biotite-gneiss  $\pm$  muscovite  $\pm$  sillimanite located in the central part of Rio Grande do Norte State. Angelim *et al.* (2006) recognized, as a younger unit, a suite with a diverse composition (gabbroic, tonalitic, granodioritic, granitic, dominantly tonalitic-granitic) that defines an orthogneiss unit. Besides these two great sequences, in some small areas marble, amphibolite and banded gneiss were identified and described as well (Figure 15a).

The Poço da Cruz suite's lithotypes (1,990 Ma U-Pb) were described as augen leuco-gneiss with quartz-monzonitic to granitic composition. Porphyroblasts of microcline are dispersed throughout the amphibolite-biotite-quartz-feldspathic fabric. As reported by Angelim *et al.* (2006) a consensus has not been reached concerning the geodynamics of this unit's batholiths. Some authors considered whether these batholiths as Transamazonian syn-tectonic related or, late-tectonic related. Meanwhile, other authors proposed a Paleoproterozoic anorogenic emplacement affected by Brasiliano deformational event (CABY *et al.* 1995).

The adopted stratigraphical scheme in this work was presented by Angelim *et al.* (2006). As discussed by these authors, the Seridó Group consists of four units (from bottom to top): Serra dos Quintos Formation, Jucurutu Formation, Equador Formation, and Seridó Formation.

The Serra dos Quintos Formation is composed of ferruginous quartzite, hematite and/or magnetite itabirite, garnet tremolite schists in some places, metaultramafic, metamafic rocks, and leucogneisses. The exact stratigraphical position is not well known. This unit occurs overlaid the Jucurutu Formation, although Angelim *et al.* (2006) reported that it may be possible to identify rocks presumed to be related to the Caicó complex and Jucurutu Formation.

The Jucurutu Formation consists of biotite  $\pm$  epidote  $\pm$  amphibole paragneisses, marbles, calc-silicate rocks. Skarn, mica schist, quartzite, iron formations, metavolcanic rocks, and metachert were identified as interbedded lithologies. Basal polymictic metaconglomerate was interpreted in some areas as the discordant contact between Jucurutu Formation and the underlying Paleoproterozoic basement (Caicó Complex).

Based on SHRIMP U-Pb zircon data obtained from a sample of paragneiss of this complex, Van Schmus *et al.* (2003) presented a minimum age of  $634 \pm 10$  Ma suggesting that sedimentation occurred in Ediacaran Period.

Within the Equador Formation, the most representative rocks are muscovite-quartzites with arcoesean facies containing interbedded polymictic metaconglomerates, calc-silicate rocks and mica schist. This unit contacts Jucurutu and Seridó Formations by a progressive compositional variation. The quartzite, as part of a QPC-type assemblage (quartzites, pelites and carbonates association), resulted from marine shallow-water deposition.

The metasediments of the Seridó Formation (628 Ma U-Pb) standing at the top unit of the Seridó Group are composed of feldspathic or aluminous mica-schist related to medium/high metamorphic grade facies on the most part of the unit. Locally, marbles, calc-silicate rocks, quartzites, and metavolcanic rocks in the main lithotype. The tectonic discordant contact with the Paleoproterozoic basement outstands on the west limit of orogenic belt.

Detailed descriptions of the lithological units of the Poço da Cruz Suite and the Seridó Group can be consulted in Angelim *et al.* (2006) and Barbosa (2013).

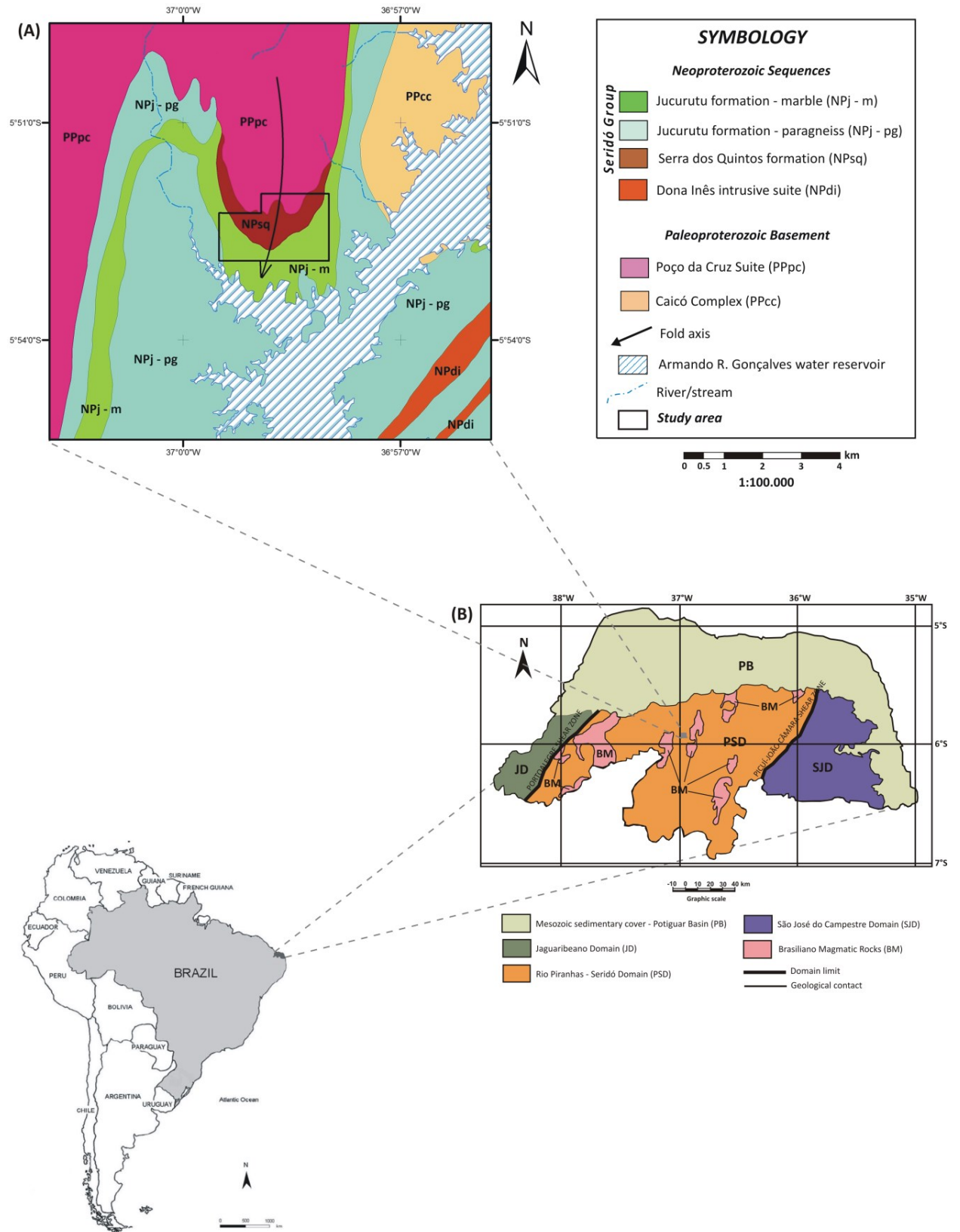
#### 4.1 Tectonic setting

The Rio Piranhas-Seridó Domain (PSD) occupies an extensive area in the central portion of the Rio Grande do Norte State, bounded to the east by the São José do Campestre Domain (SJD) and to the west by the Jaguaribeano Domain (JD). Both contacts between the domains are tectonic, through the ductile shear zones of Porto Alegre (to the east) and Picuí-João Câmara (to the west) (Figure 15a).

The Bonito Mine is located in the Rio Piranhas-Seridó Domain (PSD) which comprises a Paleoproterozoic basement represented by the Caicó Complex (CC) composed of amphibolitic and migmatized metasedimentary rocks and granitic gneiss. Associated with the lithologies of this complex, Angelim *et al.* (2006) described and interpreted the granitic *s.l.* Paleoproterozoic rocks of the Poço da Cruz Suite been related to shear zones as the contact between the basement and the Neoproterozoic supracrustals of the Seridó Group.

According to Sá *et al.* (1995), the Seridó Group resulted from an intense polyphasic compressional tectonics (folding and thrust faulting) with mass transport to the northwest. A third deformational phase was assumed to be the main cause of the vertical transposition of the strata with NNE-SSW orientated foliation and the Neoproterozoic transcurrent kinematics, according to Van Schmus *et al.* (2003).

Figure 15 – Simplified geological map. **A)** Regional geological framework of study area. **B)** Geotectonic sketch map showing the most important units and shear zones.



Source: Adapted after Angelim *et al.* (2006).

Earlier studies performed during the 1980s suggest a poly-orogenic evolution model explaining the collage and tectonic evolution of the Borborema Province, Northeastern Brazil. However, on the grounds of structural surveys (CABY *et al.* 1991, 1995; HACKSPACHER *et al.* 1997) and geochronological research (VAN SCHMUS *et al.* 2003), the deformational history of the Seridó Group has been ascribed to a monocyclic evolution model developed throughout three primary events under the same metamorphic conditions during the Brasiliano/Pan-African orogeny.

The Seridó mobile belt has been studied as a geodynamic setting characterized by intense deformation processes (especially the transpressional strain), granitic magmatic accretion and the development of NNE-SSW orientated transcurrent structures during the Brasiliano/Pan-African orogeny in the Borborema Province (BRITO NEVES, 1975; ARCHANJO; BOUCHEZ, 1991; SÁ *et al.* 1995; CABY *et al.* 1995; HACKSPACHER *et al.* 1997; NASCIMENTO, 2002; NASCIMENTO *et al.* 2004; ANGELIM *et al.* 2006; ARCHANJO *et al.* 2013; SIAL *et al.* 2015).

#### **4.2 Petrography and X-ray analysis of the Bonito Mine BIF rocks**

Regarding the study area, according to Angelim *et al.* (2006), Barbosa (2013) and, Fonteles *et al.* (2018), the BIFs (itabirites) were classified as metasediments with alternating bands of silicate minerals (amphiboles and quartz, mainly) and iron oxides (hematite, magnetite, martite and goethite) that was locally affected by low Eh fluids, as remarked by the presence of pyrite and chalcopyrite (possibly related to a post-sedimentation event).

As a complementary analytical tool, the X-ray diffraction analysis (XRD) was assayed to identify mineral phases unable to be observed on optical microscopy work. Mineralogical abbreviations are presented according to the nomenclature proposed by Kretz (1983).

For multivariate data analysis, BIF types could not derive exclusively from the information unveiled from the exhaustive assessment of database concentrations. In fact, petrographic studies – relying both on reflected and transmitted light microscopy – have shown how indispensable they were to establish a meaningful ore typology. Hence, a mathematical classification method combining all available information (like CA) was crucial to deal with this particular site-specific typological problem.

According to mineralogy, texture, intergrain contact relations, and modal percent estimations, the itabirites include the following categories: 1) silicates, which are composed mainly of quartz, amphiboles (hornblende, anthophyllite, gedrite and tremolite/Fe-actinolite)

and, in less proportion, iron oxides and sulfides; which are represented by the amphibolitic itabirites; 2) the iron oxides (hematite, magnetite, and martite) are expressively present in the samples and silicate minerals as well. Pyrite and chalcopyrite were also described in some samples. This category comprises the other BIF types which are

The ***amphibolitic itabirites (AmI)*** are composed of tremolite/Fe-actinolite (15-89%), hornblende (20-70%), quartz (25-75%), magnetite (1-10%) and pyrite (1-10%). The observed texture varies from grano-lepidoblastic (hornblende) to lepido-granoblastic (tremolite/Fe-actinolite). Under crossed polars, quartz crystals are extensively anhedral and show shadowy extinction. Magnetite and martite were observed on 1-10% proportion and pyrite is rare (Figures 16b,f; 18c,d).

The ***hematitic itabirites (HI)*** have on their composition quartz (50- 60%), Fe-actinolite (15-25%) and hematite (20%). Magnetite/martite (1-4%) and pyrite (1%) may occur under low percentages. The predominant texture is lepidoblastic with unequigranular Fe-actinolite crystals that exhibit orientated lamellar shapes within the metamorphic foliation.

Goethite appears as an alteration product of this mineral. Hematite shows a white-gray high reflective color. Magnetite was recognized in the polished section due to its rose-tint color and the cubic form. Pyrite crystals were identified as strong little yellow prismatic grains (Figures 16e; 18a,b).

The ***magnetitic itabirites (MgI)*** are the most representative petrographic BIF type among the samples. The slight banded texture varies from lepido-granoblastic to lepidoblastic. The main minerals are: quartz (1-70%), amphibole (10-30%, tremolite/Fe-actinolite), magnetite (20-70%) and martite (1-50%) (Figures 16c; 17e,f). Pyrite and chalcopyrite occur in low percentages (1-5%). (Figures 16a; 17b). Diffractogram depicted in Figure 21 confirms the presence of sulfide phases. Kaolinite and ilmenite were not identified in polished sections or on thin sections. Figures 21 to 29 show the identified mineral phases in this BIF type.

Tremolite/actinolite crystals usually show lamellae or acicular form and strong pleochroism under crossed polars. On polished sections, pyrite crystals are easily identified due to the highly reflective yellow color and its cubic hipidiomorphic form. Chalcopyrite (most reflective yellow color) was observed as mineral inclusions on pyrite crystals (Figure 17b).

The ***martitic itabirites (MI)*** have a special meaning as a petrographic feature on the genetic and evolving context of the Bonito mine BIFs. On polished sections, the martitization process was interpreted as a phase-mineral transformation enhanced by substitution of primary magnetite by martite - a pseudomorph of the primary iron ore (RAMDOHR, 1981;

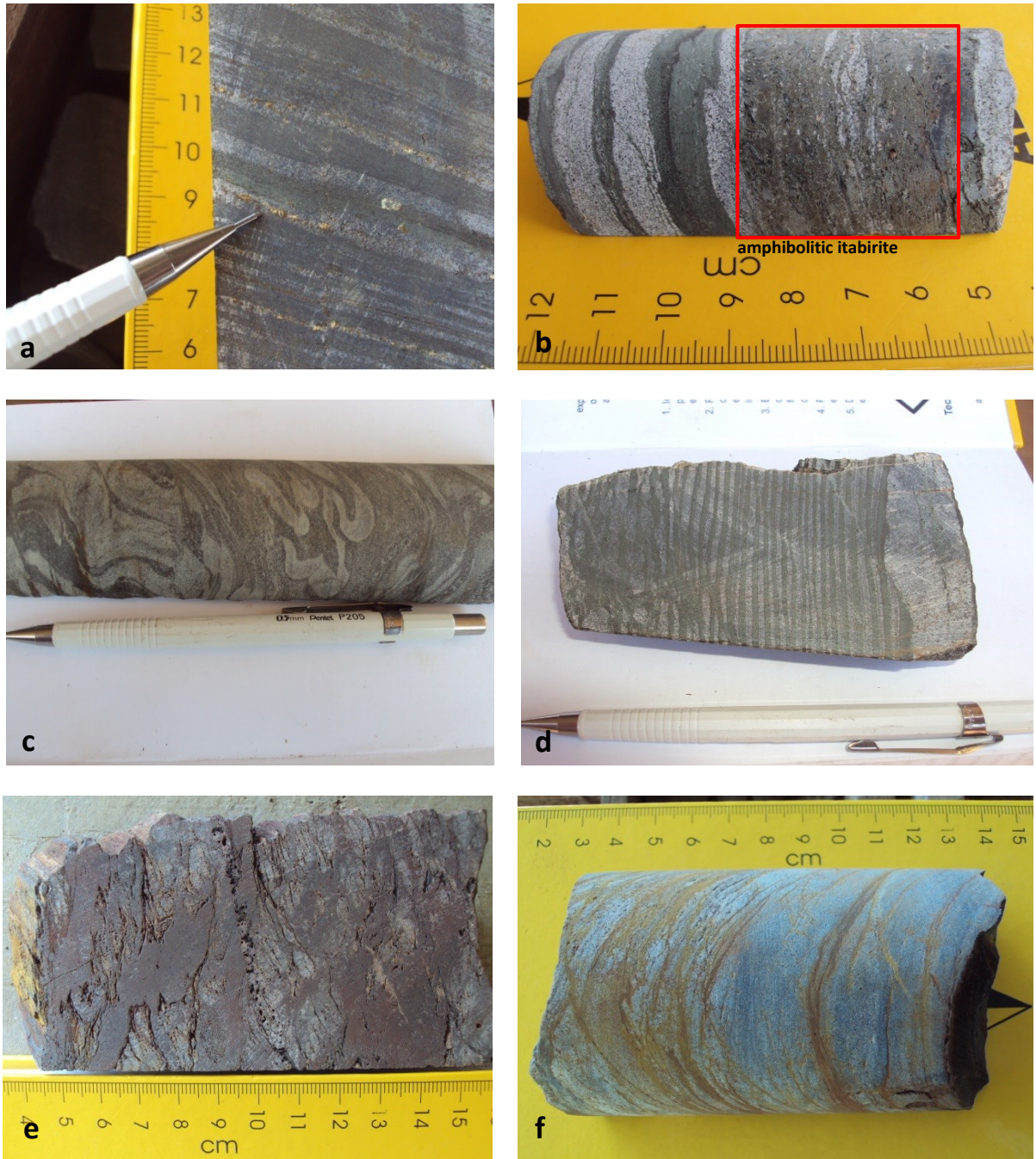
CRAIG; VAUGHAN, 1984). The lepido-granoblastic metamorphic texture was drawn by the following mineral association: quartz (30-60%), tremolite, anthophyllite/Fe-gedrite (20-25%), martite (15-35%), magnetite (2-15%) and pyrite (<2%) (Figures 16d;17c,d). The natural magnetism was preserved just as it was observed on drill core samples. Figures 30 to 32 exhibit the diffractogram that displays the identified mineral phases.

#### **4.3 Mineral assemblages: X-Ray diffraction data assesement**

Mineral phases identified under XRD analysis are presented in Table 2. The silicate facies of the studied itabirites have depicted peculiar mineralogical associations improving the knowledge of the metamorphic conditions regarding the BIF. Although no specific mineral chemistry data was presented in this study, the qualitative XRD results yielded relevant information related to approximate metamorphic conditions of the BIF. Figures 19 and 20 exhibit the basic mineralogical assemblage of hematite, quartz, and goethite related to hematitic itabirites. Although chemical weathering is not an extensive alteration process, goethite was assumed to be an alteration product of hematite.

Figure 21 illustrates the diffractogram depicting assorted mineralogical assemble extracted from a magnetitic itabirite sample (See 36-88.30A sample in Table 2 for reference). The only iron oxide phase is represented by magnetite. Sulfide phases represented by pyrite and chalcopyrite are related to millimetric veinlets among oxide/silicate bands (Figures 17a and 18b). Kaolinite is probably related to an alteration phase of ferrogedrite which is an aluminous orthorhombic amphibole.

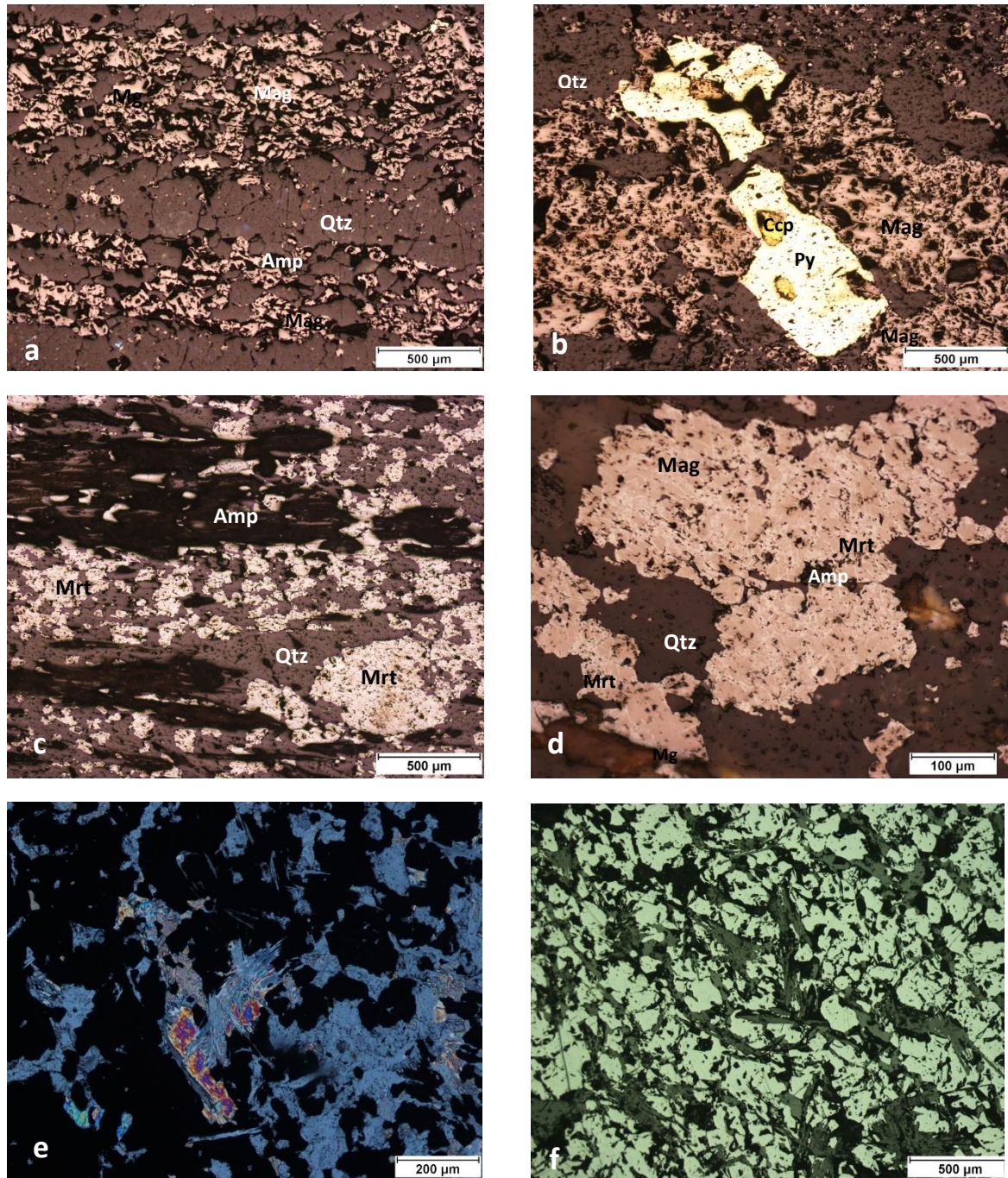
Figure 16 – Samples were taken from the boreholes cores showing some of the main mineralogical and structural features of the Bonito Mine low-grade BIF. **a)** magnetitic itabirite with millimetric sulfide veins (pyrite); **b)** magnetitic/martitic itabirite associated to amphibolitic itabirite; **c)** magnetitic itabirite showing local intrafoliation folding; **d)** Martitic itabirite with an almost rhythmic banding; **e)** irregular banding on hematitic itabirite with ore pods **f)** fractured amphibolitic itabirite filled with goethite.



Source: Photos taken by the author.

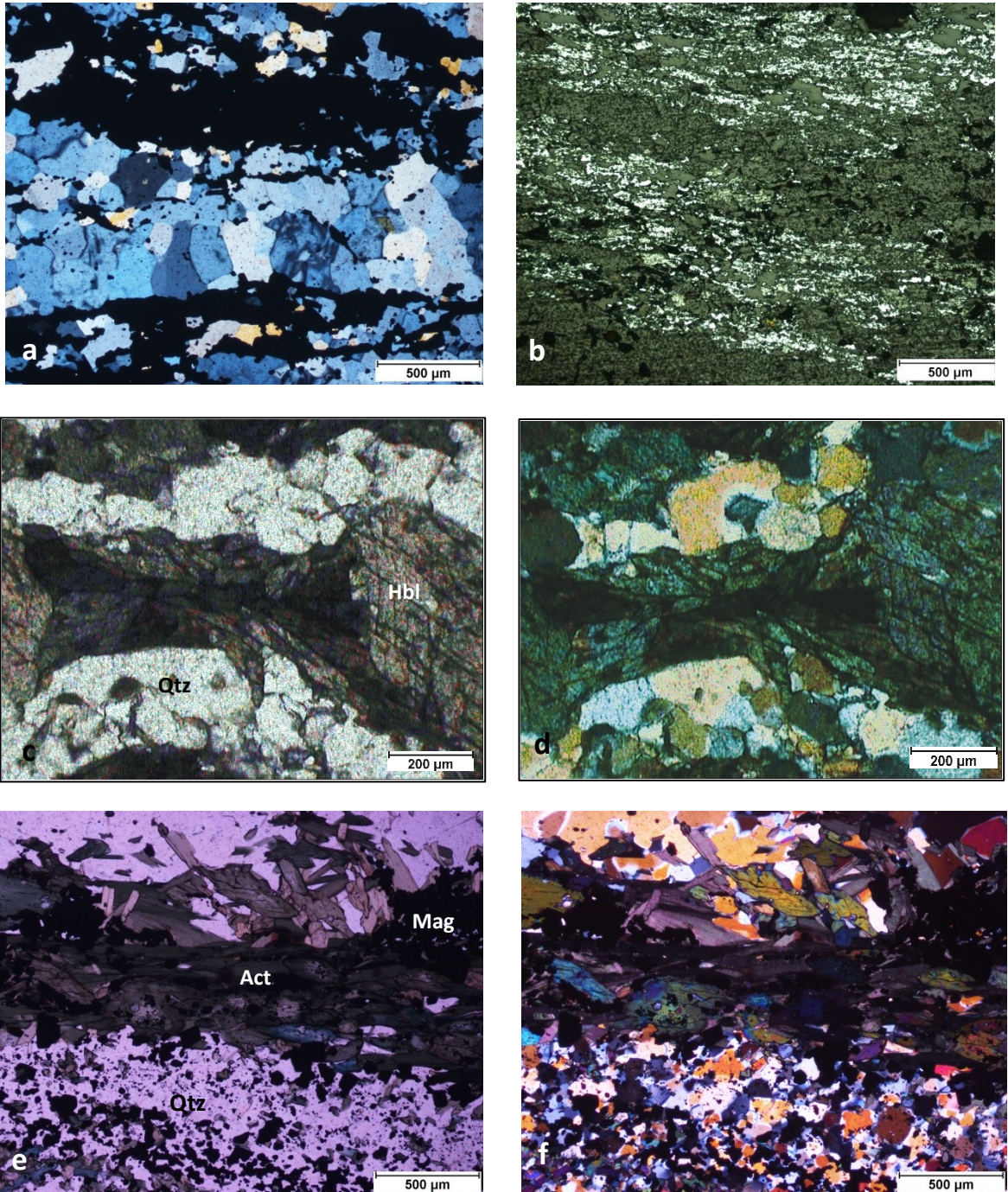


Figure 17 – Photomicrographs of the studied itabirites. **a)** Magnetitic itabirite with well-developed bands of quartz and magnetite+hornblende. Magnetite has a subhedral cubic form; **b)** Pyrite crystals exhibit cubic (yellow) with anhedral chalcopyrite as an inclusion (dark yellow). In some cases, these sulfides can include minerals from the itabiritic fabric; **c)** Martitic itabirite. Martite crystals still preserve complete pseudomorphosed magnetites' habit. **d)** Magnetitic itabirite partially martitized; **e)** Magnetitic itabirite on thin section with crossed-polars showing anhedral crystals of tremolite/Fe-actinolite with strong pleochroism and fibrous habit; **f)** Polished section of the magnetitic itabirite with high reflective subhedral magnetite crystals on plane-polarized light. Abbreviations: quartz (Qtz), amphibole (Amp), magnetite (Mag), martite (Mrt), pyrite (Py) and chalcopyrite (Ccp).



Source: Photos taken by the author.

Figure 18 – Photomicrographs of the studied itabirites. **a)** Thin section on crossed-polars. Hematitic itabirite with typical banding on a grano-lepidoblastic texture; **b)** Same sample. Polished section showing anhedral porous hematite crystals with highly reflective white color. Pyrite crystals occur in a 1% proportion; **c)** Amphibolitic itabirite. Thin section on plane-polarized light where a hornblende crystal can be seen with typical cleavage planes, positive relief and strong greenish-brown color in the grano-lepidoblastic texture; **d)** Same sample on crossed polars. The anhedral quartz crystals can be identified due to its shadowy extinction. **e)** Silicate band from a sample of magnetitic itabirite (plane-polarized light); **f)** same sample under crossed-polars. Abbreviations: Actinolite (Act), magnetite (Mag), quartz (Qtz) and hornblende (Hbl).



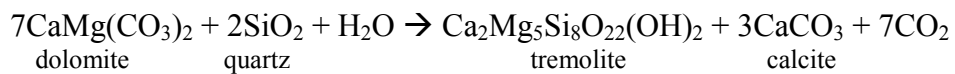
Source: Photos taken by the author.

Table 2 – XRD results summary. The last column refers to the figure exhibiting the related diffractogram.

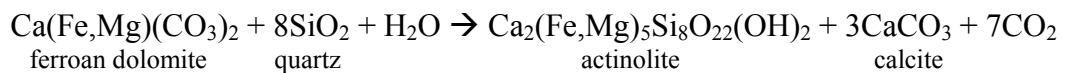
Sample	Typology	XRD Identification	Figure
30 – 267	HI	goethite, quartz, hematite	19
146 - 1830	HI	quartz, hematite, goethite	20
36 - 88.30A	MgI	pyrite, chalcopyrite, quartz, magnetite, kaolinite, Fe-gedrite, actinolite	21
30 - 282A1	MgI	anthophyllite, gedrite	22
30 - 282A2	MgI	anthophyllite, tremolite, actinolite, magnetite	23
22 - 31.60	MgI	magnetite, quartz, pyrite, tremolite	24
129 - 23.95A	MgI	magnetite, maghemite, hematite	25
129 - 23.95B	MgI	goethite, magnetite, hematite, kaolinite	26
121 - 36.10A	MgI	magnetite, quartz, biotite, kaolinite, chalcopyrite	27
121 - 36.10B	MgI	magnetite, quartz, tremolite, chalcopyrite, biotite	28
146 - 1847	MgI	magnetite, quartz, actinolite	29
77 - 5.10	MI	tremolite, magnetite, dolomite, greenalite	30
26 - 8.00A	MI	anthophyllite, magnetite, tremolite, actinolite	31
26 - 8.00B	MI	magnetite, anthophyllite, Fe-gedrite	32

Figures 25 to 28 show diagrams obtained from the same samples, but different mineral bands (Table 2). The presence of anthophyllite and gedrite shows clear evidence of a metasomatic phase that occurred during the major metamorphic event.

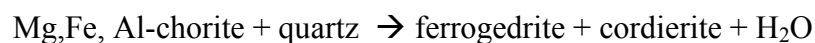
Regarding the sample 77-5.10 (Figure 30, Table 2) owing to the presence of dolomite in the mineral group identified in the diffractogram, a possible metamorphic reaction for tremolite can be recreated, as it follows (DEER *et al.* 1992):



In Precambrian metamorphosed BIF rocks, according to Klein (1973), the formation of actinolite can be described as



Formation of ferrogedrite, supposedly in the context of the Bonito Mine BIF, would be described by the following metamorphic reaction (AKELLA; WINKLER, 1966)



No chlorite, nor cordierite was properly identified on diffractograms, thus, the metasomatism of these primary minerals still remains on the hypothetical field. The possible existence of Al-chlorite and cordierite on lithotypes of Seridó group rocks can be interpreted as sedimentary input to the former basin.

Greenalite, as a forming mineral of the itabirites in the study area, remains as an uncertainty. Although it was recognized on XRD results, additional analytical work is required to confirm this preliminary finding. According to Mel'nik (1982), this mineral is expected to be ascribed to diagenetic or low-grade metamorphic conditions. Klein and Bricker (1977) described greenalite as part of the mineralogical assemblage of proterozoic sedimentary BIF deposits. The approximate composition range of greenalite is given by



Concerning the itabirites of the Bonito Mine, the reconnaissance of greenalite as a possible mineral belonging to the mineralogical assembly would be interpreted as a mineral relict from the sedimentary record of the basin. The protoform of the former could be carried on by the continental influx into the basin as an iron-bearing silica gel and to be deposited with other terrigenous components (MEL'NIK, 1982).

In general, the identification of the tremolite and anthophyllite, as silicate phases of the itabirites of the Bonito Mine, unveils that metasomatic transformation of primary sedimentary minerals can be related to action of hydrothermal fluids took place, possibly, during the deformational event, or related to a post-orogenic magmatic event.

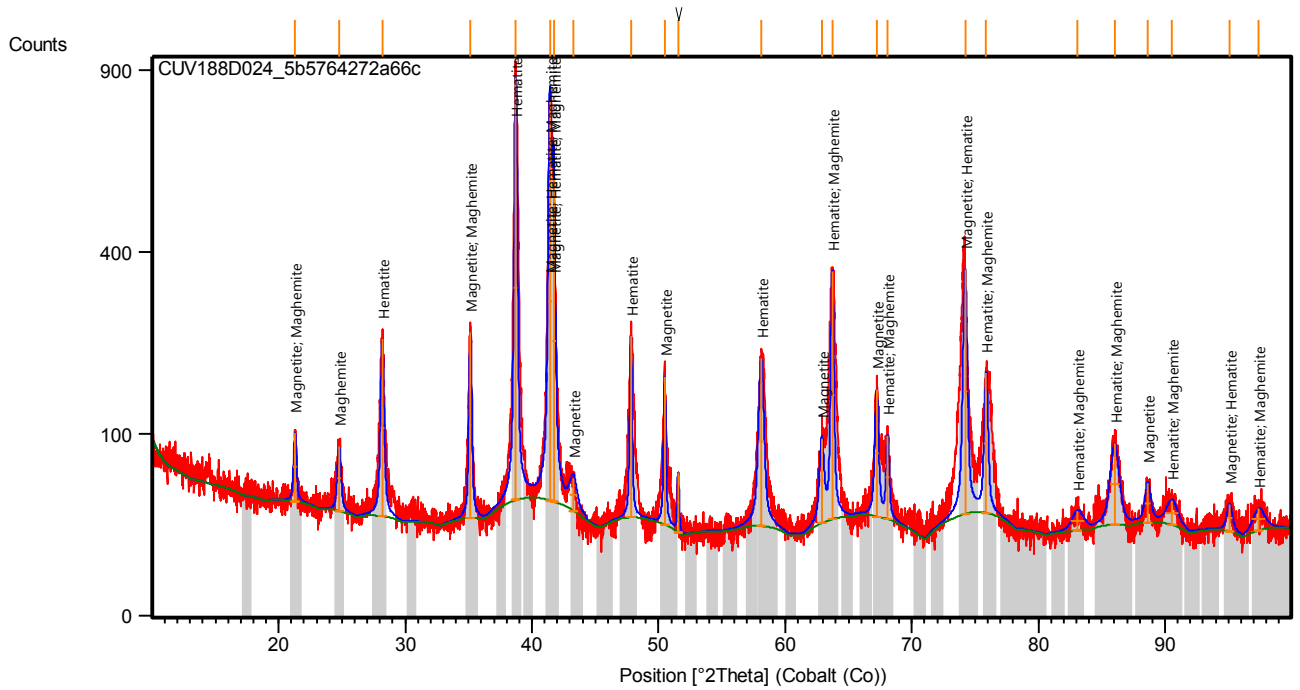
Among the assayed samples, maghemite was identified in 129 - 23.95A sample (Figure 25). This neoformed iron oxide appears to be a product from punctual weathering of magnetite (SMITH, 1979). Also, it has been characterized as a transitional metastable phase that appears during martitization. In the following sections, the weathering conditions issues were addressed on the basis of a joint analysis of geochemical data and geotechnical qualitative data.





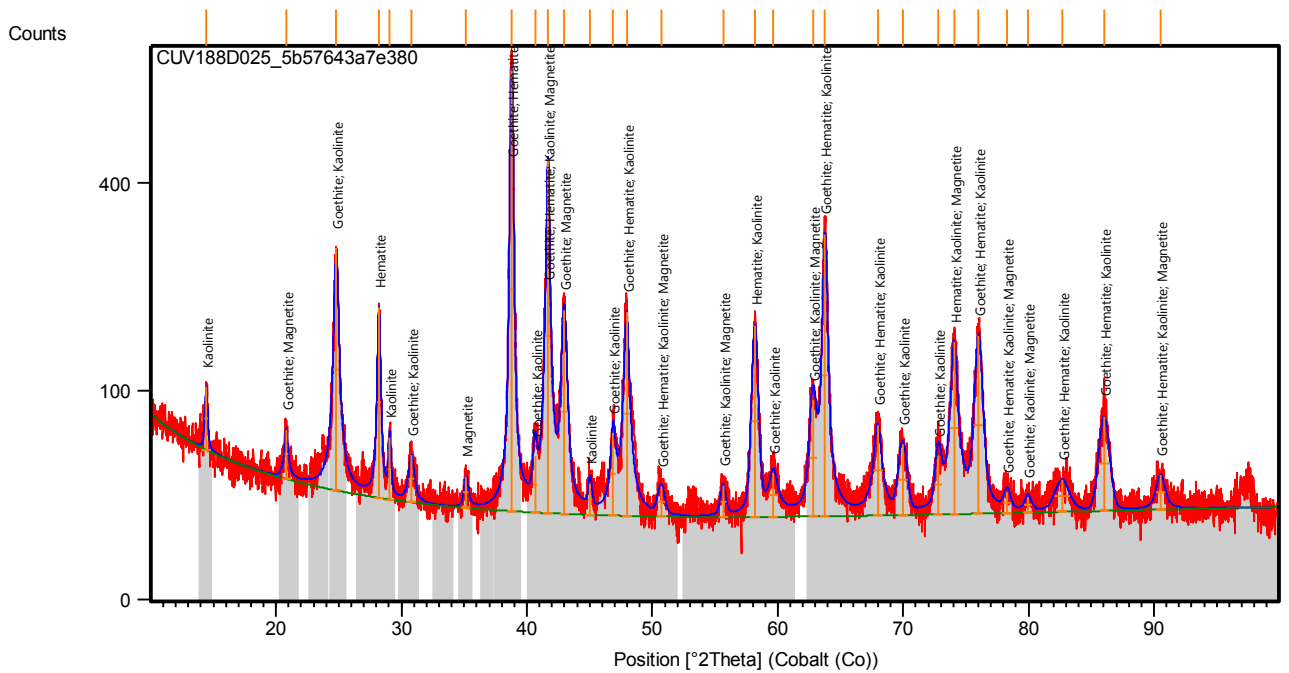


Figure 25 – Diffractogram from sample 129-23.95A (magnetitic itabirite).



Source: Elaborated by the author.

Figure 26 – Diffractogram from sample 129-23.95B (magnetitic itabirite).



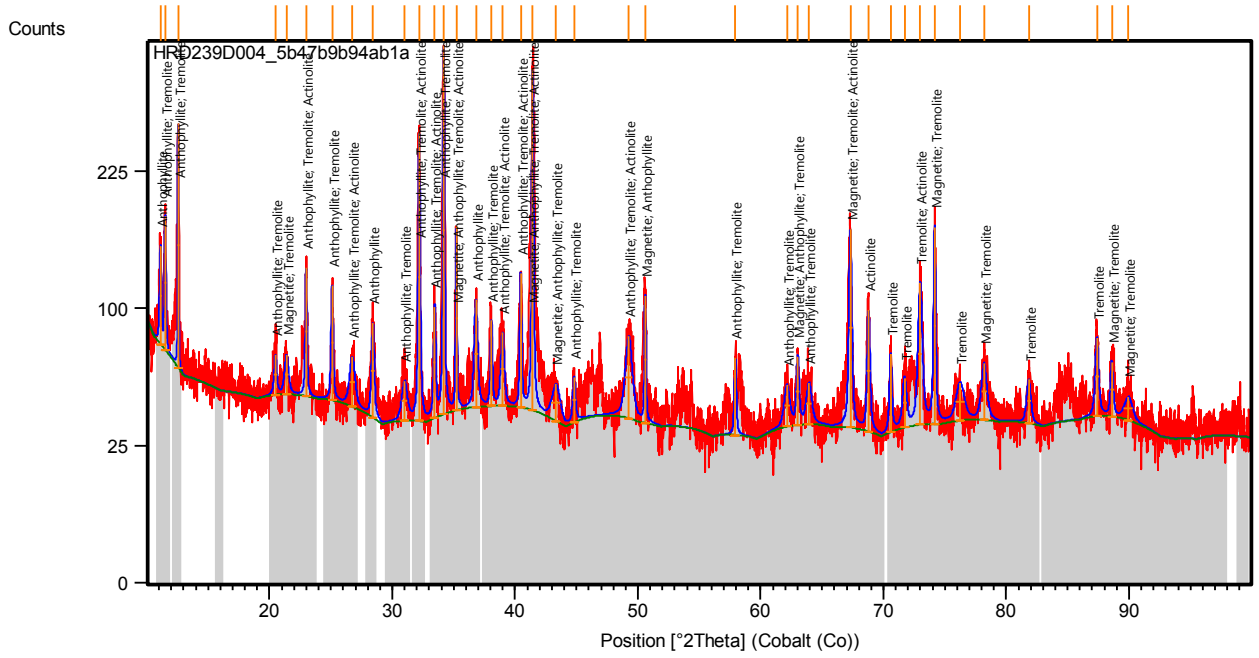
Source: Elaborated by the author.





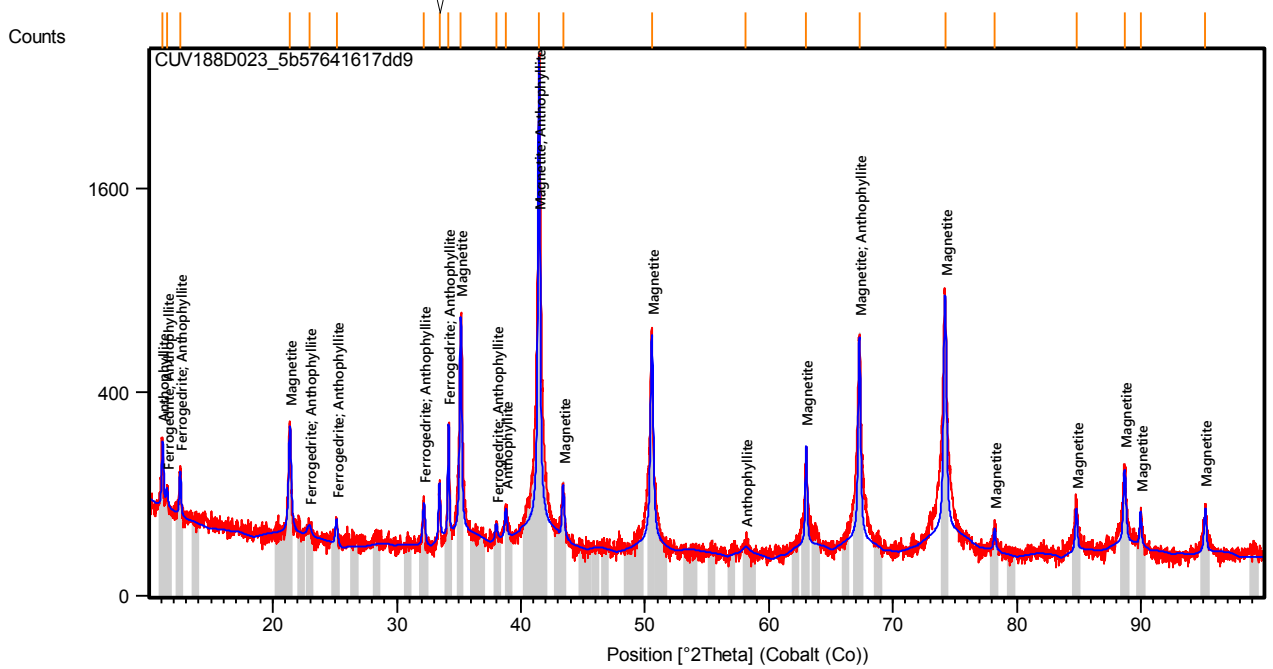


Figure 31 – Diffractogram from sample 26-8.00A (martitic itabirite – silicate facies).



Source: Elaborated by the author.

Figure 32 – Diffractogram from sample 26-8.00B (martitic itabirite – oxide facies).



Source: Elaborated by the author.

## 5 MULTIVARIATE MODELING OF THE GEOLOGICAL DATA OF THE BONITO MINE

This chapter gathers the results achieved from the multivariate analysis work. The first section brings the factorial model of the multivariate data outliers within the geochemical database. The second section is dedicated to present the outcomes obtained from the coupling correspondence tools/K-means clustering algorithm strategy in order to delineate an integrated typological model. The third section deals with the extension of the typological model regarding the weathering conditions of the BIF rocks.

### 5.1 Identifying geochemical anomalies through principal components analysis (PCA)<sup>1</sup>

PCA procedures were chosen as a reliable method to disclose some underlying geological relations among variables and samples. In the first round of interpretation work, geochemical trends can be easily assessed. Meanwhile, in the presence of anomalous values, PCA outcomes may reveal relevant information in order to identify unclear geochemical relationships

PCA is one of the most used multivariate statistical methods, as an exploratory tool for large datasets. Therefore, the main goal here is to reduce the dimensionality of databases and to provide an intelligible graphical display of the data points, given by their factorial coordinates.

Furthermore, PCA has a great advantage of promoting a quick assessment of outlier data points. The dataset comprises 1.384 samples related to five variables ( $\text{Fe}_2\text{O}_3$ ,  $\text{SiO}_2$ ,  $\text{Al}_2\text{O}_3$ , P, and Mn), available in eighty-four drill holes.

#### 5.1.1 PCA results

The whole set was treated in order to obtain the principal components and summarize all the geochemical data. With such an application it was possible to look at the geological relations between the variables through the samples. The basic descriptive statistics are listed in Table 3. High Coefficient of Variation (C.V.) values may indicate expressive data variability.

---

<sup>1</sup> This section was originally published in 2019 as the Chapter #59 of the book “Petrogenesis and Exploration of the Earth’s Interior”. Springer Nature. [https://doi.org/10.1007/978-3-030-01575-6\\_59](https://doi.org/10.1007/978-3-030-01575-6_59)

An exploratory linear regression analysis has been performed to examine correlations between variables. However, weak correlations were obtained and the exception was the  $\text{SiO}_2 \times \text{Fe}_2\text{O}_3$  linear regression fit which yielded a Pearson's coefficient  $r = -0.6669$ .

Table 3 – Exploratory statistics summary (% wt).

Variable	Mean	Median	Min.	1 <sup>st</sup> Quant.	3 <sup>rd</sup> Quant.	Max.	Std. Dev.	C.V. (%)
$\text{Fe}_2\text{O}_3$	41.68	43.18	4.81	38.01	46.90	70.01	8.54	20.48
$\text{SiO}_2$	56.83	55.68	28.11	52.28	60.17	90.23	7.77	13.67
$\text{Al}_2\text{O}_3$	1.134	0.505	0.010	0.250	0.905	18.230	2.26	199.60
P	0.041	0.040	0.007	0.030	0.050	0.252	0.02	55.82
Mn	0.309	0.210	0.010	0.130	0.360	2.030	0.29	95.20

Source: Elaborated by the author.

The analysis of Table 4 shows that two axes are sufficient, at first sight, to interpret the geochemical data set. In fact, plane PC1-PC2 (given in Figure 33) retains almost 73% of the cloud information, and all variables were 'reasonably' interpreted, just on the grounds of their projection onto this plane, as shown in Figure 33. Factorial loads on PC1 to PC4 are presented in Table 5. These values are interpreted (Figure 33) as qualitative correlations indexes.

Table 4 – Eigenvalues.

PC	Eigenvalue	% Exp	% Accum
1	2.243	44.86	44.86
2	1.400	28.00	72.86
3	0.803	16.07	88.93
4	0.553	11.07	100

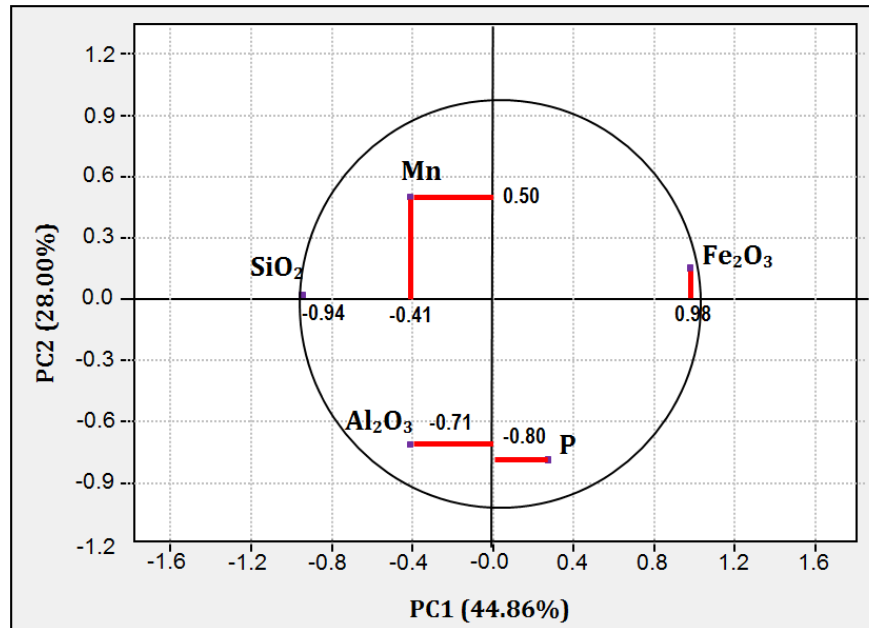
Source: Elaborated by the author.

Table 5 – Factorial loads on PC1 to PC4.

Variable	PC1	PC2	PC3	PC4
$\text{Fe}_2\text{O}_3$	0.9763	0.1530	-0.1362	-0.0705
$\text{SiO}_2$	-0.9386	0.0223	0.2774	0.2038
$\text{Al}_2\text{O}_3$	-0.4098	-0.7098	-0.3397	-0.4614
P	0.2752	-0.7919	-0.1817	0.5139
Mn	-0.4066	0.4952	-0.7480	0.1731

Source: Elaborated by the author.

Figure 33 - Projection of variables onto plane PC1-PC2, exhibiting their linear correlation coefficients with the axes they correlate.



Source: Fonteles *et al.* (2019a)

All variables can be interpreted in statistical terms in the plane PC1-PC2, assuming that a linear correlation coefficient higher than 0.5 is 'significant'. It is nevertheless worth noting that 'significance' can only be dealt with, in a multivariate Gaussian context, which is not obviously the case of Bonito Mine input data. However, once the multivariate gaussianity is not strictly feasible to assess, the 0.50 boundary is acceptable, even for Mn. The same rule implies the interpretation of other variables at the factorial plane (Figure 33).

Assuming these conditions, the interpretation of Figure 33 is clear:

- SiO<sub>2</sub> and Fe<sub>2</sub>O<sub>3</sub> are strongly negatively correlated, governing the plot general trait. PC1, onto Fe<sub>2</sub>O<sub>3</sub> and SiO<sub>2</sub> project very closely, explains almost half of the global information contained in the variables cloud.
- Independently of this relationship (because it stems from orthogonal PC2), there is another relatively important one, linking Al<sub>2</sub>O<sub>3</sub> and P, with linear correlation coefficients with PC2 in the order of magnitude of 0.71/0.80.
- Regarding Mn, it correlates weakly with PC's 1 and 2 (0.50, 0.41).

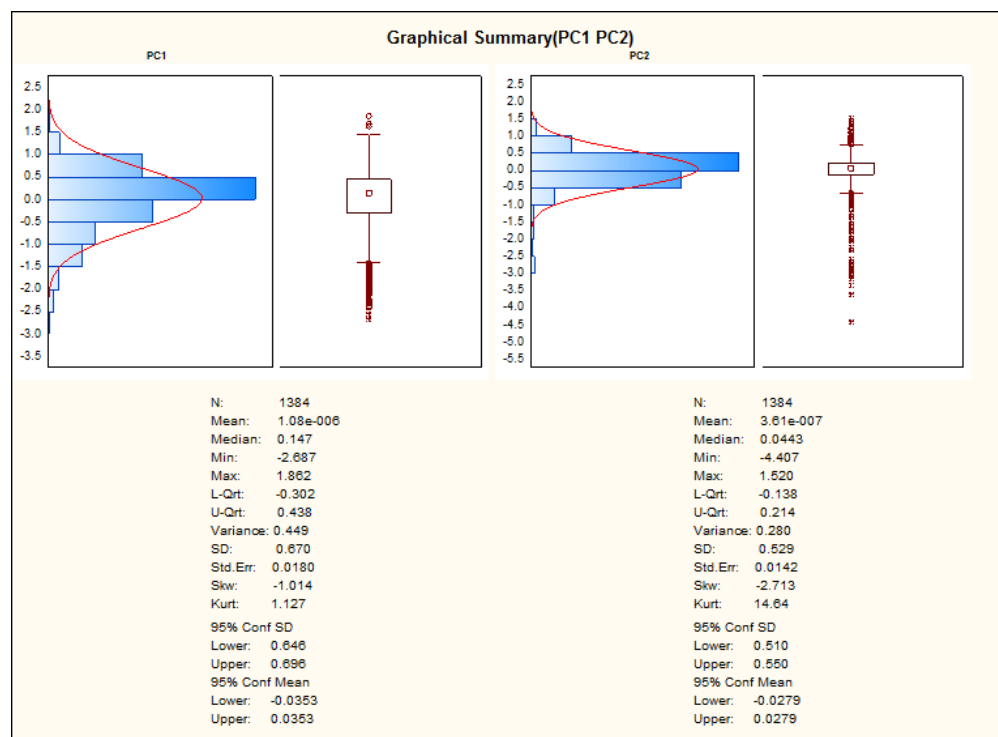
Assuming that the samples' factorial loads on PC1 and PC2 can be treated according to the Gaussian probabilistic model, box and whisker plots were obtained in order to draw the limits and identify the outliers' values. The limits established are expressed by  $\text{Mean} \pm 1.96 \cdot \text{SD}$  for each PC (Figures 34 and 35).

Figure 36 depicts the identification of the outliers in the multivariate dataset. The identification of such anomalous values is due to the patterns exhibited in Figure 33.

It can be noticed that there is a continuum of samples projecting along PC1. The smaller is the sample coordinates in PC1, the greater is its  $\text{SiO}_2$  content; conversely, the higher its coordinate value in PC1, the greater its  $\text{Fe}_2\text{O}_3$  content. This is a geochemical portrait of the very meaning of the banded iron formation or *itabirite* (namely in this study), once the rock is defined by the alternating bands of silicate minerals (mainly quartz) and iron oxide minerals.

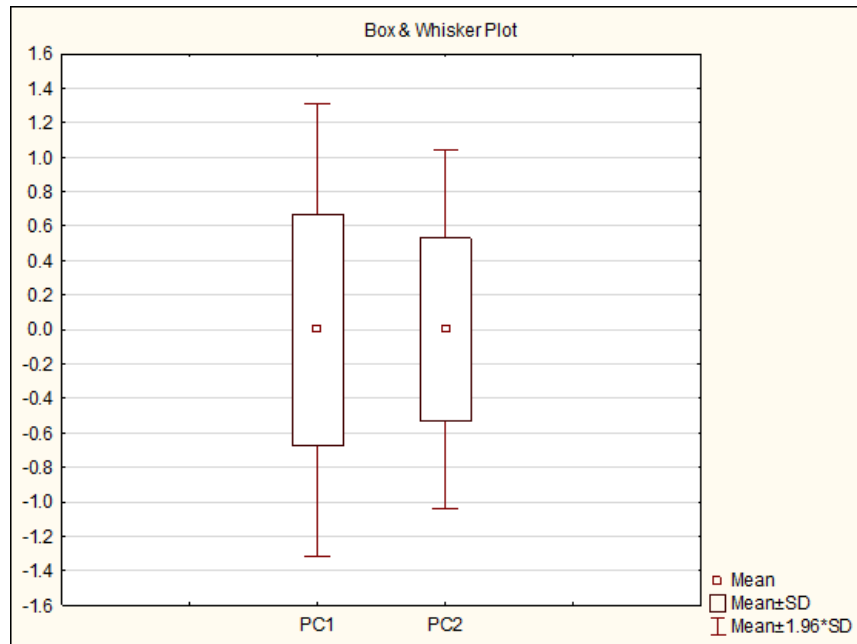
Regarding the samples linked to PC2, it may be stated that there is an arbitrary upper limit for Mn influence (the farther from the origin - along PC2, the stronger that influence: conversely, there may be an arbitrary lower limit for  $\text{Al}_2\text{O}_3 + \text{P}$  influence, the farther from the origin, along PC2, the stronger the influence). Box #2 (split into 2 sub-boxes) contains samples with P- $\text{Al}_2\text{O}_3$  anomalies. Inside box #2a, samples with high  $\text{Al}_2\text{O}_3$  grades are positioned and the same can be observed in box #2b for the P grades.

Figure 34 – Box-plots obtained for PC1-PC2 factorial loads and summary statistics.



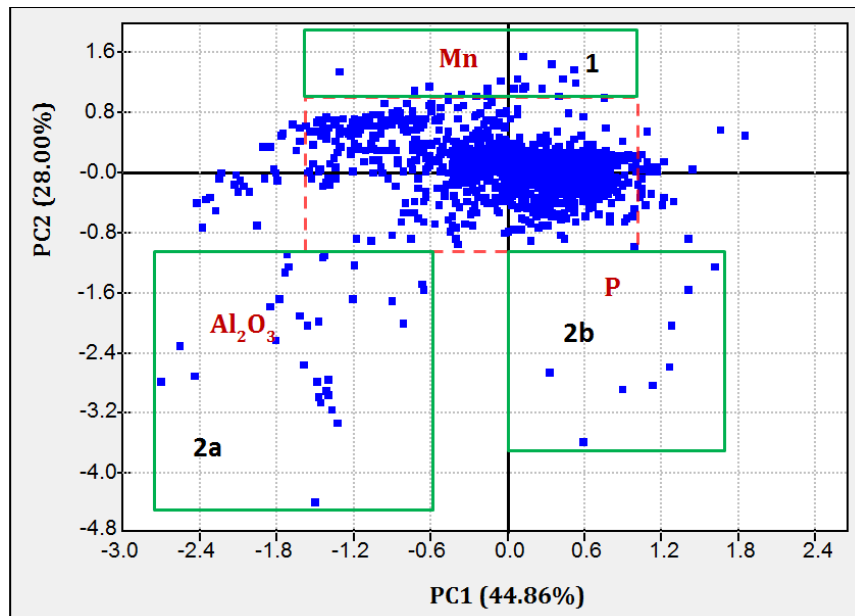
Source: Elaborated by the author.

Figure 35– Constraining statistical limits based on the intervals of confidence.



Source: Elaborated by the author.

Figure 36. Projection of samples onto plane PC1-PC2. The dashed red box outlines the statistical limits provided by the box-plots. The outliers are positioned into the delimited green boxes (see text for reference).



Source: Fonteles *et al.* (2019a)

Box #1 encompasses the richer Mn-content. The raw geochemical values are higher than the average content (see Table 3 for reference). In terms of PC-reading perception, the farther samples from PC2 (along the PC1) will be displayed as poorer Mn



values. The geochemical cycles of manganese and iron are well-known for a long time. These elements have similar geochemical behaviors due to their chemical properties (ionic radii, ionic charges, etc.). However, in the deposition environments where pH-Eh conditions play an important role, manganese tends to follow a distinct path away from iron on the sedimentary processes (KRAUSKOPF, 1957; RANKAMA; SAHAMA, 1960). Thus, Figure 36 clearly displays many samples in a proper field on factorial plane.

### **5.1.2 Discussion**

Despite the absence of chemical data of the minerals and in an overall view, it is reasonable to expect that anomalous Mn grades can be related to the Fe-rich silicate ores as a result of geochemical affinity to silicate minerals of amphibolitic and martitic itabirites, and some cases to magnetitic ones. Therefore, the anomalies inside the box#1 may represent peculiar conditions of solubilization and precipitation of manganese as a metal included in BIF mineralogy.

The  $\text{Al}_2\text{O}_3$  grades are essentially attached to terrigenous input to the basin. The anomalies were interpreted as possible punctual events due to an increase of the pelitic sedimentation into the basin as a product of the weathering of felsic rocks. Meanwhile, phosphorus grades bring some new information about the iron oxide ores.

This element has a dual geochemical character being both siderophile and lithophile and as it can be seen in Figure 36 the highest P values are related to iron richer BIFs samples, such as the hematitic itabirites (RANKAMA; SAHAMA, 1960). This could be explained by taking into account the possibility that phosphate radicals could be brought by colloidal iron hydroxides due to their linkage to the surface of this compound (ALBÈREDE, 2009).

Although the multiGaussian distribution model does not necessarily fit the research data presented in this study; PCA has proven to be a quick start to evaluate the exhaustive dataset and to map the geochemical anomalies within it. Once the main correlation ( $\text{Fe}_2\text{O}_3 \times \text{SiO}_2$ ) was determined on the factorial plane, the other variables were interpreted as an auxiliary source of relevant information. The joint  $\text{Al}_2\text{O}_3$ -Mn plot analysis exhibits an important terrigenous input to the basin. Phosphorus content has a strict relation to the origin of the Fe-rich BIF.

## 5.2 The Bonito Mine BIF typology model based on a geomathematical approach<sup>2</sup>

The Bonito iron ore mine, according to Barbosa (2013) was originally divided into two iron ore groups, mainly in consequence of their different range of Fe<sub>2</sub>O<sub>3</sub> grades, but also due to their geochemical and petrological compositions. The high-grade ores (and most feasible) are represented by magnetitic ore (91.60 - 94.20 %Fe<sub>2</sub>O<sub>3</sub>) and the magnesian skarn (60.30 - 72.33 %Fe<sub>2</sub>O<sub>3</sub>). The other iron ore group, which is the target of the proposed research, is formed of banded iron formations (BIF) and, in contrast with the first group, contains low-grade iron ores (30.97 - 60.30 %Fe<sub>2</sub>O<sub>3</sub>).

The purpose of the study presented here is the improvement of the actual knowledge of the geology of the Bonito iron mine. The geomathematical methodology presented here embraces the multi-dimensionality of the available geochemical database.

For this purpose, the methodology that was applied to this deposit merges interactively two areas of inquiry:

- (a) A complete enhanced geological/geochemical study of the orebody was accomplished, based on similarity – or, alternatively, distinction – from one formation to the other, providing a conceptual model focused on their relationships. Concerning the data model underlying this study, it may be viewed as a  $n \times p$  matrix, with  $n$  rows representing 1.384 samples and  $p$  columns representing concentrations for the following elements: Fe<sub>2</sub>O<sub>3</sub>, SiO<sub>2</sub>, Al<sub>2</sub>O<sub>3</sub>, P, and Mn.
- (b) The second area of research, aimed at producing significant ore types with geochemical meaning, relies on Correspondence Analysis as a purely geometric method to compress data in a  $p_1 < p$  artificial space onto samples and concentrations are simultaneously projected, using the chi-square distance applied to the matrix elements, appropriately recorded into grade classes.

The aim of the proposed methodology is to put forward a new approach taking advantage of CA explanatory potential when coupled with geological interpretation, stemming from the modeling of lithochemical data and petrographic ore characterization.

---

<sup>2</sup> This section takes part of an original manuscript submitted (under review status) to the Journal of Geochemical Exploration in June/2018.

Once a joined mathematical/geochemical model is delineated, the application of a non-hierarchical partitional algorithm (in this case, the K-means method) was used to delimitate homogeneous (or acceptable heterogeneous) groups of samples, which are the elements of the required typology.

### 5.2.1 Geochemical evaluation with correspondence analysis

Correspondence Analysis (CA) was applied to obtain a new geometric space where samples and variables are jointly projected. In contrast with some algorithms in the multivariate realm (*e.g.*, cluster analysis and discriminant analysis), CA demands an intrinsic geological knowledge of the underlying geochemical phenomena to allow a reasonable interpretation of the results, given under the form of projection onto the axes defining the new geometric space.

Since the CA method requires qualitative variables as input, the grade range for each variable was split into two or three classes. Limits of each class were iteratively established in a way that each class conveys a geological meaning. The results of the final class splitting process are given in Table 6. Hence, each initial quantitative variable (grade) was substituted for a code (*I*, if the grade belongs to the prescribed class, and *0* otherwise). By this procedure, the initial table was transformed into an indicator matrix.

Table 6 – Class limits defined by CA modeling.

Variable	Class	Cum. Freq.	Grade limits%	Average content
Fe <sub>2</sub> O <sub>3</sub>	Fe1	0.334	4.18 – 40.60	32.40
	Fe2	0.668	40.60 – 45.62	43.17
	Fe3	1.000	45.62 – 70.10	49.50
SiO <sub>2</sub>	Si1	0.501	28.11 – 55.68	51.26
	Si2	1.000	55.68 – 90.23	62.42
Al <sub>2</sub> O <sub>3</sub>	Al1	0.517	0.010 – 0.500	0.27
	Al2	1.000	0.500 – 18.23	2.06
P	P1	0.547	0.007 – 0.040	0.03
	P2	1.000	0.040 – 0.252	0.06
Mn	Mn1	0.368	0.010 – 0.160	0.10
	Mn2	0.679	0.160 – 0.300	0.23
	Mn3	1.000	0.300 – 2.030	0.63

Source: Elaborated by the author.

Table 7 shows the eigenvalues calculated as a result of the iteration taking into account the presented values in Table 6. At a first sight, one can observe that 79.11% of the

inertia importance is explained by the first three axes, even though 66.33% of this inertia clearly describes the main scenario where the class-coded variables build up the idea for the typological model. It is worth noting that seven axes are enough to explain the total of 12 classes, given that one degree of liberty is subtracted for each one of the five contingency tables whose concatenation gave rise to the input indicator matrix.

Table 7 – Eigenvalues.

Axis	Eigenvalue	% Explained	% Cumulated
1	0.1845	49.9782	49.9782
2	0.0604	16.3537	66.3319
3	0.0472	12.7816	79.1135
4	0.0357	9.6714	88.7849
5	0.0234	6.3393	95.1242
6	0.0167	4.5155	99.6397
7	0.0013	0.3603	100

Source: Elaborated by the author.

Table 8 unveils the main absolute contributions which are spread along the seven axes representing the amount of influence of each class on the axis. The variables Fe1 and Fe3 together sum up to 28% of contribution on Axis 1. The same can be noted with A11 and A12 which are well-positioned on Axis 2 (Figure 37).

Table 8 - Absolute contributions of the classes. The bold values refer to threshold contributions on the three main axes (AC > 8.3%).

Class	Axis1	Axis 2	Axis 3	Axis 4	Axis 5	Axis 6	Axis 7
Fe1	<b>21.4088</b>	1.8688	2.3394	2.2785	8.8313	3.1097	26.6523
Fe2	0.3250	<b>11.8261</b>	<b>32.1923</b>	0.0947	16.9611	5.2009	0.0121
Fe3	<b>16.5292</b>	4.3115	<b>17.2492</b>	1.4502	1.3207	0.2685	25.6554
Si1	<b>16.9475</b>	1.5878	1.8896	2.2057	3.4130	1.0256	22.9157
Si2	<b>16.9977</b>	1.5924	1.8955	2.2119	3.4225	1.0287	23.0010
A11	0.3292	<b>23.0347</b>	2.0952	3.1486	12.9562	6.3349	0.4558
A12	0.3518	<b>24.6196</b>	2.2391	3.3652	13.8482	6.7708	0.4899
P1	4.2834	1.6653	2.0189	23.7309	5.5932	7.9978	0.0175
P2	5.1718	2.0108	2.4377	28.6523	6.7532	9.6567	0.0206
Mn1	<b>9.1258</b>	<b>11.4760</b>	0.2771	6.8742	0.2451	34.6683	0.4369
Mn2	0.1178	<b>15.9185</b>	<b>15.5773</b>	22.5256	11.5916	3.1763	0.0218
Mn3	<b>8.4096</b>	0.0874	<b>19.7863</b>	3.4620	15.0616	20.7602	0.3196

Source: Elaborated by the author.

The use of CA as a modeling tool required, in this study, some samples were previously studied in petrographic terms. Although some geochemical patterns can be drawn from the interpretation of factorial axes, without some guiding samples in supervised classification, no meaningful geological information can be extracted and/or combined with other available data (Figure 38). Therefore, the guiding information was provided by the petrographic and geochemical data (Table 9).

Table 9 – Geochemical composition of the BIF petrographic samples.

<b>BIF type</b>	<b>Sample</b>	<b>Fe<sub>2</sub>O<sub>3</sub></b>	<b>SiO<sub>2</sub></b>	<b>Al<sub>2</sub>O<sub>3</sub></b>	<b>P</b>	<b>Mn</b>
Amphibolitic Itabirite	AmI1	18.28	68.96	12.54	0.049	0.170
	AmI2	39.56	57.90	2.25	0.056	0.220
	AmI3	30.75	68.33	0.57	0.057	0.290
Hematitic Itabirite	HI1	52.71	46.38	0.82	0.050	0.040
	HI2	51.83	47.49	0.54	0.030	0.110
	HI3	50.57	49.01	0.26	0.010	0.160
Martitic Itabirite	MI1	43.54	56.12	0.24	0.031	0.060
	MI2	36.78	58.91	3.37	0.021	0.920
	MI3	42.06	57.28	0.49	0.040	0.130
	MI4	42.98	56.72	0.01	0.031	0.260
Magnetitic Itabirite	MgI1	53.98	45.69	0.10	0.072	0.150
	MgI2	46.18	53.52	0.10	0.041	0.160
	MgI3	47.05	52.53	0.34	0.020	0.060
	MgI4	38.21	61.02	0.54	0.032	0.200
	MgI5	45.53	54.16	0.19	0.051	0.070
	MgI6	50.01	48.97	0.17	0.039	0.820
	MgI7	45.96	53.47	0.40	0.052	0.120
	MgI8	45.56	52.61	1.54	0.034	0.250

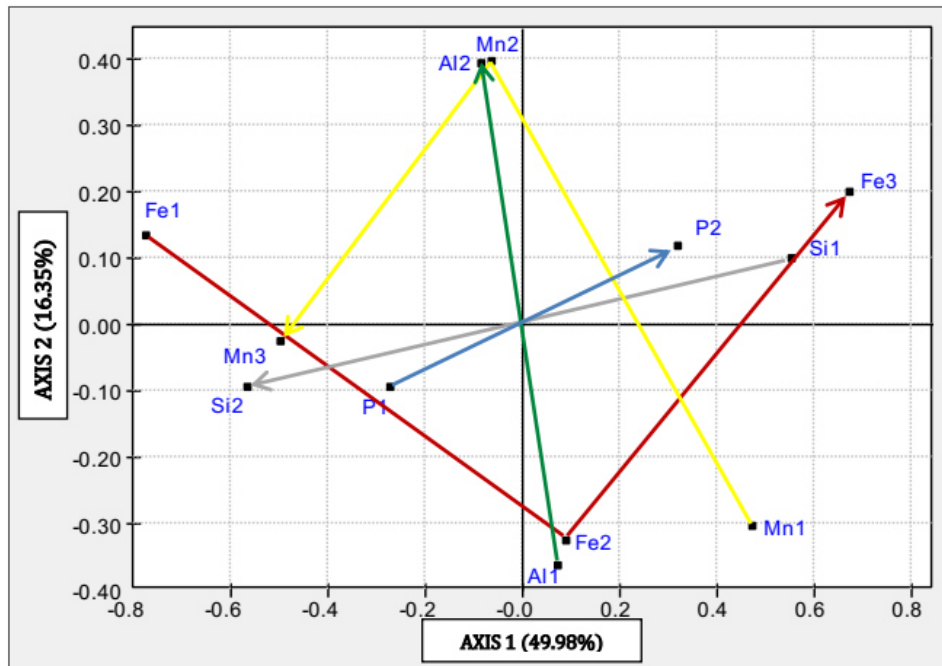
Source: Elaborated by the author.

### ***5.2.2 Application of K-means clustering technique: Building a bridge between the factorial space and the BIF typological model***

The K-means clustering method was applied in order to establish the limits among the BIF types firstly interpreted as domains on the factorial space (Figure 39). The numerical solution was provided by an algorithm implemented in Statistica<sup>®</sup> 10 software package which is based on FORTRAN original code developed by Hartigan and Wong (1979).

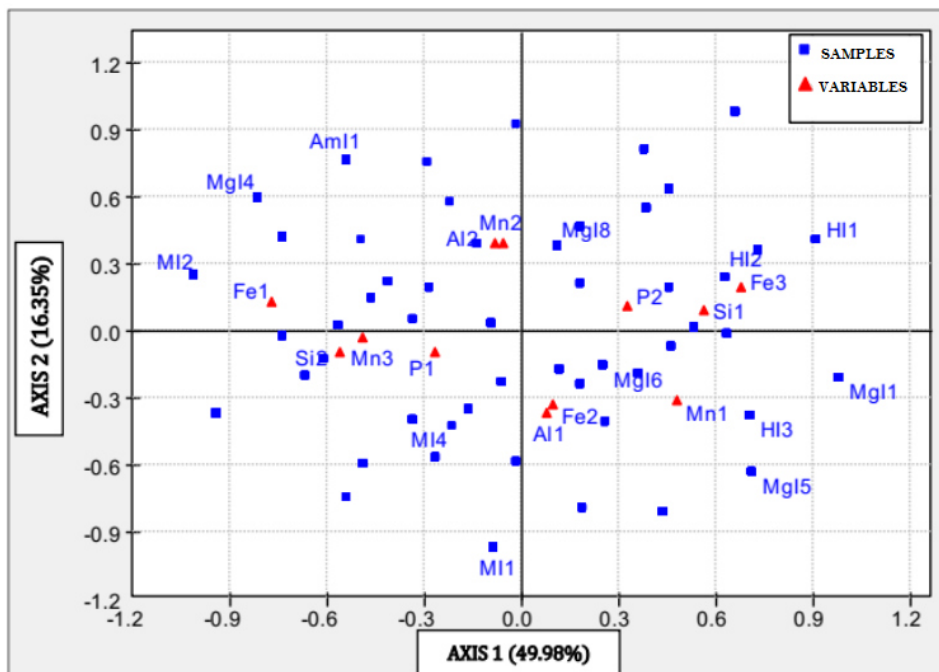
The input data was conveyed by the factorial scores from the Axes 1 and 2. No seeds were preselected as it was assumed that the K clusters' centers would be calculated when the final number of iterations was reached.

Figure 37 – Projection of variables' classes onto plane A1-A2. The arrows indicate the direction of the grade variation according to table 6.



Source: Elaborated by the author.

Figure 38 - Projection of variables' classes and samples onto plane A1-A2. Some petrographical samples occupy the same position in the plane: Am11=Am12=Am13, Mg11= Mg12= Mg17, MI1=MI3, and HI3=Mg13.



Source: Elaborated by the author.

Once the input data is displayed in an orthogonal fashion (i.e. the CA factorial scores are positioned on a Cartesian plane), no anomalies are expected on the Euclidean distances. Thus, the calculation of the clusters' centers will meet the within/between-group variance criteria.

After several tests with an assorted number of clusters (4 to 12), the definitive arrangement was completed with 8 clusters ( $K = 8$ ). Due to the low number of variables (axes 1 and 2), the algorithm was set to perform 10 iterations operation, but after 2 iterations the solution was obtained (Figure 39). The K-means clustering main results are presented in Table 10.

The K-means clustering method allowed us to redefine and upgrade the previous and uncomplete ore petrographical typology, in which initially four petrographical ore types were described and identified. The bridge built between the CA typology ore model and the K-clustering method led to 8 updated geochemical ore types. The table 11 is now presented depicting the re-interpreted ore types (Table 11). The Cluster 8 (provisionally nominated as *X-Itabirites*) defines a geochemical group with no direct association to a previous petrographic ore type.

Table 10 – Summarized K-means results. The clusters' means were positioned as factorial coordinates onto the A1-A2 plane.

Cluster	Cluster means (variable coordinates)		Number of clustered samples	BIFcluster
	Axis1	Axis2		
1	0.0739	-0.1356	174	MgI6
2	0.2267	0.3017	113	MgI8
3	-0.1570	-0.7531	176	MI1-MI3-MI4
4	0.6268	0.5753	239	HI1-HI2
5	-0.8135	0.2674	164	MI2
6	0.7983	-0.3449	239	HI3-MgI1- MgI2-MgI3-MgI5- MgI7
7	-0.6491	0.6718	105	AmI1-AmI2-AmI3-MgI4
8	-0.8614	-0.2724	174	<i>X-I (X-itabirites)</i>

Source: Elaborated by the author.

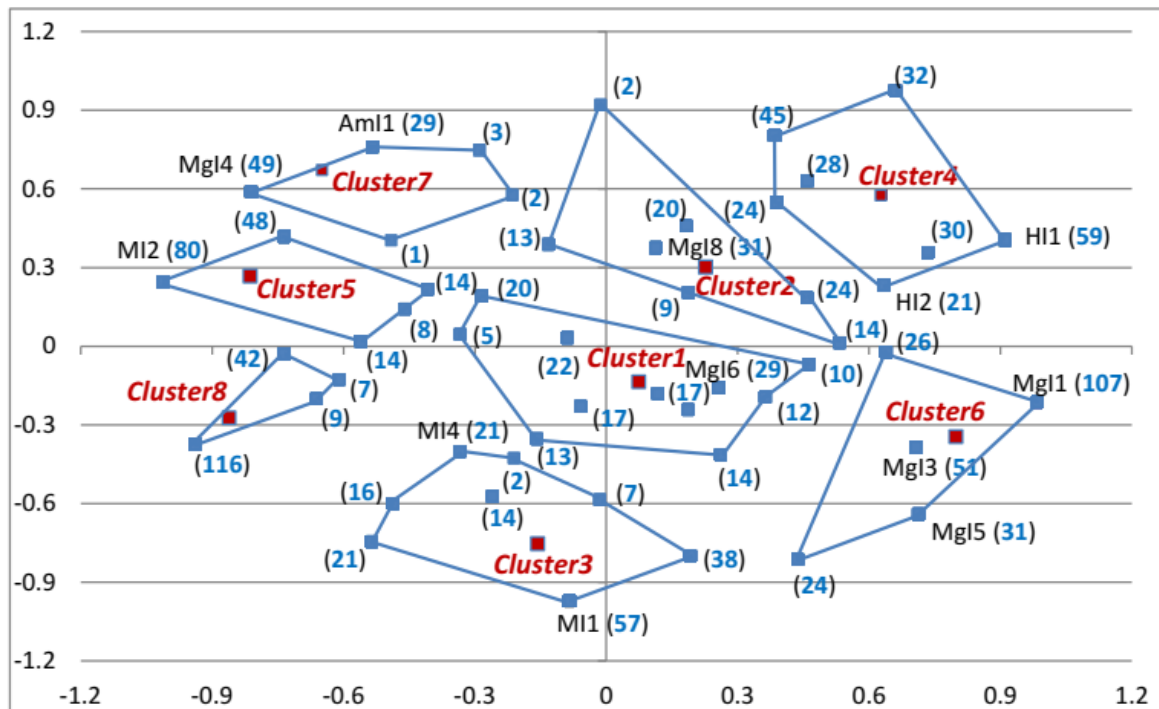
Due to its position between the martitic itabirites clusters (Clusters 5 and 3), the samples present high  $\text{SiO}_2$  and Mn contents and low  $\text{Al}_2\text{O}_3$ ,  $\text{Fe}_2\text{O}_3$  and P contents as well. Taking this into account and, from the strict geochemical point of view, Cluster 8 was interpreted as another MI cluster and classified as a silicate-martitic itabirite (Si-MI) (Figure 40).

Table 11 –Typological classification proposed to the Bonito mine BIFs.

Cluster	BIF cluster	BIF typology
1	MgI6	Magnetitic Itabirite (MgI)
2	MgI8	Aluminous-Magnetitic Itabirite (Al-MgI)
3	MI1-MI3-MI4	Martitic Itabirite (MI)
4	HI1-HI2	Hematitic Itabirite (HI)
5	MI2	Aluminous-Martitic Itabirite (Al-MI)
6	HI3-MgI1- MgI2-MgI3-MgI5- MgI7	Hematitic-Magnetitic Itabirite (H-MgI)
7	AmI1-AmI2-AmI3-MgI4	Magnetitic-Amphibolitic Itabirite (Mg-AmI)
8	<i>X-Itabirites</i>	Silicate-Martitic Itabirite (Si-MI)

Source: Elaborated by the author.

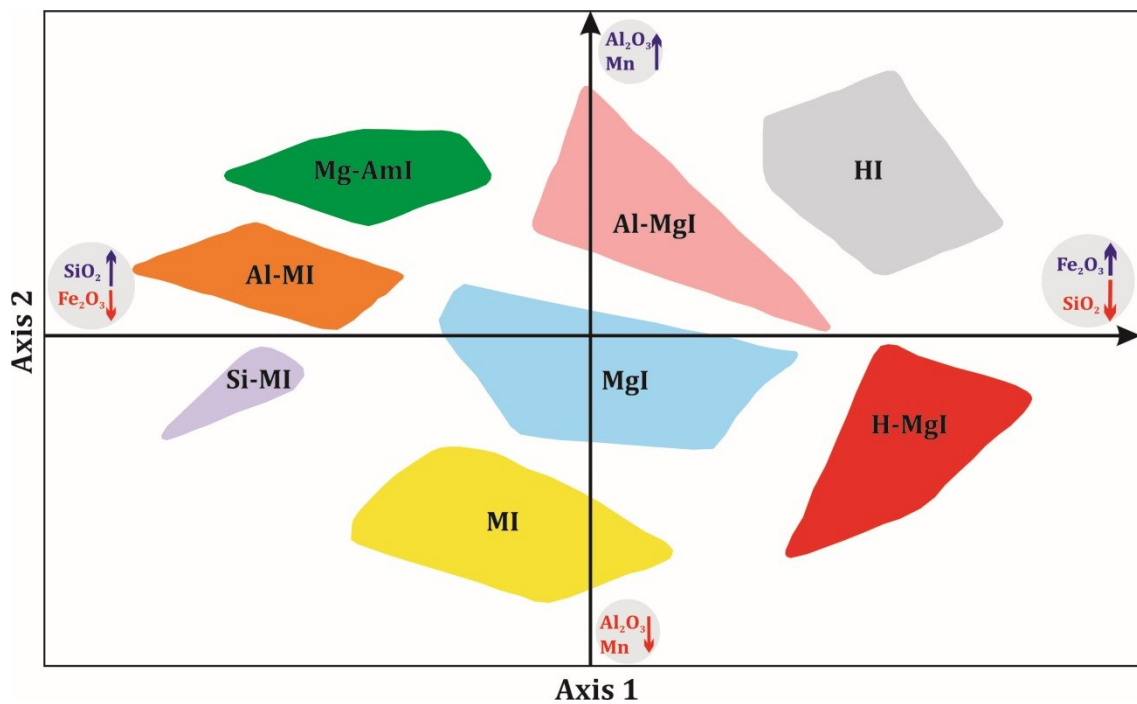
Figure 39 – Plane A1-A2 showing the K-clusters for the Bonito Mine BIF typology. The numbers between the parentheses indicate how many samples were grouped by each point in the plane.



Source: Elaborated by the author.



Figure 40 – Factorial plane displaying the BIF types after the clustering treatment based on the K-means procedure.



Source: Elaborated by the author.

### 5.2.3 Discussion

The dual variables' classes-samples projection on the CA factorial plane allows interpreting them jointly. Thus, some observations can be drawn:

- The Fe<sub>2</sub>O<sub>3</sub> richer samples were positioned on Axis 1's positive side of the plane and they are essentially represented by hematitic and magnetitic itabirites. The samples near Axis 2 are likely to be Al<sub>2</sub>O<sub>3</sub> richer. Mgl8 is a representative sample of this case.
- The negative side of Axis 1 represents the poorer Fe<sub>2</sub>O<sub>3</sub> itabirites, nevertheless, one magnetitic itabirite (Mgl4) is positioned nearby the amphibolitic itabirites (AmI1, AmI2, and AmI3) with high Al<sub>2</sub>O<sub>3</sub> content.
- Axis 2 defines how much Al<sub>2</sub>O<sub>3</sub> content is present in geochemical samples. As can be seen in table 11 this variable has an outstanding absolute contribution. The location of the samples Mgl4, AmI1, AmI2, AmI3, and MI2 is explained by the presence of hornblende, known as an aluminous amphibole.

- P grades have little geochemical meaning on the plane A1-A2 due to its low contributions values. The most significant contributions of this variable are related to Axis 4 alone. Therefore, no valid correlations can be extracted due to the low percentage of explained variance of that factor (Table 7).

The Mn content on Bonito Mine BIF iron ore is expressively low to form a manganese ore mineral. Thus, Mn grade can be related to a possible continental input to the basin within the terrigenous sediments deposited due to fluvial systems.

Additionally, Mn grades tend to be a 'companion' to SiO<sub>2</sub> content and, as it seems, there is no relation to Fe<sub>2</sub>O<sub>3</sub> enrichment. The oxidation processes during metamorphism and/or weathering events didn't concentrate Mn content on Fe<sub>2</sub>O<sub>3</sub> richer itabirites. Martitic and amphibolitic itabirites (MI and AmI) are slight Mn richer.

The geochemical behaviors of iron and manganese on sedimentary processes are almost independent. When the sedimentary processes started to form the BIFs of the Bonito Mine manganese presumably did not have precipitated with iron compounds and continued solubilized in the water due to specific pH-Eh conditions (KRAUSKOPF, 1957).

The grouping of magnetitic and hematitic itabirites shows that oxidation processes may have occurred in a diverse way and hematitic itabirites may have the same sedimentary history with their own geochemical peculiarities. Martitization took place on magnetitic itabirites as well, and this process is related to the loss of FeO molecules nevertheless the newly formed ore still preserves their magnetic properties. As depicted in Figure 40, martitization may be interpreted as a process that happened with the increase of Mn and SiO<sub>2</sub> contents.

### **5.3 Weathering conditions evaluation aided by a coupled cluster-correspondence analysis approach<sup>3</sup>**

Geological evaluation of ore deposits always has been an important task during the development of the mining project. As a fundamental step prior to mining planning, weathering conditions appraisal must be taken into account in order to expand the knowledge about the most friable zones of the iron ore and, conversely, the hardest ones. Hence, one of the great challenges nowadays relies on understanding how to treat and interpret exhaustive and large geological databases. This issue becomes even more incisive when dealing with the decision making related to increasing geological information framework or ore mining operations.

Among many tasks, mining geology work comprises core identification and description, which may disclose relevant qualitative data collected by observing some physical or geomechanical aspects of ore material, such as the weathering grade, ore type, and voids. This qualitative information, often neglected, is crucial for ore geological research, especially regarding iron ore from BIF, which are naturally heterogeneous rocks, and their mineralogical composition can input geological uncertainties during the ore assessment process.

Rodrigues and Brandão (2017) reported that distinguishing hard ore and friable ore types would affect the production costs, in terms of energy outlay and loss of efficiency in comminution and concentration processes. Compact iron ore types standing out of the specifications are able to prejudice mineral liberation and metal recovery. Thus, the raise in production costs sometimes can create a negative input on the cash flow of the mining project. Establishing the previous zoning of occurrence of compact and friable ore materials enriches the mineral processing planning steps.

#### ***5.3.1 Geochemical and geotechnical data encoding for multivariate analysis***

The active variables will draw the main factorial input, which is the geochemical data. As the CA modeling algorithm calls for discrete data encoding, the quantitative geochemical raw data was ranked into classes as shown in Table 6.

---

<sup>3</sup> This section takes part in an original manuscript published in Anuário do Instituto de Geociências, 2019 - v.42, n.2. [http://dx.doi.org/10.11137/2019\\_2\\_86\\_99](http://dx.doi.org/10.11137/2019_2_86_99)

The geotechnical data was collected during a systematic description of the boreholes' lithological sampled material. From each borehole's 3 meter-interval core data - such as ore/rock type, structures, fracturing, core recovery, mechanical type, and weathering grade were organized on a database system for further comparisons and analyses.

Most of these data sources can be depicted as categorical data and the properties disclosed by them can be encoded describing important geotechnical aspects. Three qualitative variables were added to the multivariate analysis: weathering condition, mechanical type, and voids.

The weathering condition data were tabulated according to Dearman (1974), Fookes (1997) and Basu *et al.* (2009) as described in Table 12.

Table 12 – Description and encoding of weathered ore/rock mass (Adapted after DEARMAN, 1974; FOOKES, 1997; BASU *et al.* 2009).

<b>Weathering grade</b>	<b>Description</b>	<b>Code</b>
Unweathered (UW)	Rock shows no evidence of weathering or staining.	1
Slightly (SW)	Rock shows weak or slightly discoloring with little or no change of strength from a fresh rock.	2
Moderately (MW)	Rock strength is usually reduced by weathering. The rock may be highly discolored basically by Fe staining.	3
Highly (HW)	Rock has almost similar properties as soils and has weak strength in the presence of water.	4

Source: Fonteles *et al.* (2019b).

The category 'mechanical type' was adopted in this work as an attribute describing the physical aspect of the BIFs as it was observed at the mining site and in the drilling cores. The complete description is given in Table 13.

Table 13 – Description and encoding of mechanical characteristics of the BIFs.

<b>Type</b>	<b>Description</b>	<b>Code</b>
Friable (FRB)	Weathered BIF crushed down under one field hammer blow. Eventually flattened BIF with irregular shapes and powdered BIF that usually passes through 100 mesh sieve can be found.	1
Compact (COMP)	Hard BIF rock that breaks under several field hammer blows. It's clearly correlated to unweathered rocks.	2

Source: Fonteles *et al.* (2019b).

The void classification was done by visual observation during the inspection and describing procedures of the lithologies in drill cores. It was not a purpose providing exact figures or replace strict porosity tests' results but only to point out this visual feature with a descriptive mark. Therefore, the classification scheme adopted in this research relies on the visual aspect concerning the presence of voids or cavities in the sample. Table 14 exposes the description and ranking of core samples.

Table 14 – Voids characterization and encoding for BIF ores.

Type	Description	Code
<b>Porous (HP)</b>	<b>Presence of visible voids or cavities in ore rock samples due to prior weathered minerals.</b>	1
Non-porous (NP)	Massive aspect of the ore rock's fabric without expressive pores or voids.	2

Source: Fonteles *et al.* (2019b).

Depth intervals values (m) were obtained directly from the operational drilling core data and ranked in three categories. Thus, depth interval values will be treated as another qualitative variable (Table 15).

Table 15 – Depth-intervals encoding for BIF ores.

Depth (m)	Code
Dep1: 0 - 70	1
Dep2: 70 - 145	2
Dep3: > 145	3

Source: Fonteles *et al.* (2019b).

A petrographic study has shown that the Bonito Mine BIFs are comprised of hematitic itabirites, martitic itabirites, magnetitic itabirites, and amphibolitic itabirites (Figure 41). These BIF rocks occur in different depth levels displayed as lens forms as illustrated by an NW-SE geological section (Figures 42 and 43). This section was constructed on the basis of the lithological interpretation of nine drill holes logs positioned in that direction.

### 5.3.2 A qualitative approach using a coupled cluster-correspondence analysis strategy

The joint projection of active and supplementary variables onto A1-A2 factorial plane (Figure 44) allows identifying a clear separation of Fe-poorer/unweathered/compact/non-porous BIF ores (left side of the factorial plane) and the Fe-richer/moderately to highly weathered/friable/porous BIF ores (right side). Looking closer to Axis 1, one can note that the depth of the samples tends to decrease from the negative to the positive side of that axis. As shown in Table 16 the first two axes explain more than 66% of the total inertia - accumulated explained variance.

Table 16 – Eigenvalues. The bold value expresses the amount of accumulated retained inertia that explains the most part of the variance within the multivariate database.

Axis	Eigenvalue	% Exp.	% Accum.
1	0.1838	49.9680	49.97
2	0.0608	16.5261	<b>66.49</b>
3	0.0452	12.2891	78.78
4	0.0362	9.8048	88.59
5	0.0237	6.4188	95.01
6	0.0170	4.6039	99.61
7	0.0015	0.3917	100.00

Source: Fonteles *et al.* (2019b).

Taking advantage of a singular feature available on CA, figure 45 displays the joint projection of all variables and petrographic samples onto the A1-A2 factorial plane. The negative side of the Axis 1 plot is linked to the Fe-poorer BIFs, mainly exposing martitic and amphibolitic itabirites. The Fe-richer BIFs are composed of magnetitic and hematitic itabirites.

The factorial coordinates obtained from the two axes of CA (Table 16) were employed to build up an input matrix in order to model a single dendrogram assembling active and supplementary variables and the representative samples onto the same space (Figure 45).

After several experiments aiming to reach a structure that would describe and reveal a sound multivariate arrangement, the ultimate result has produced a model based on the Complete Linkage and Minkovski Power metric (NISHISATO, 2002).

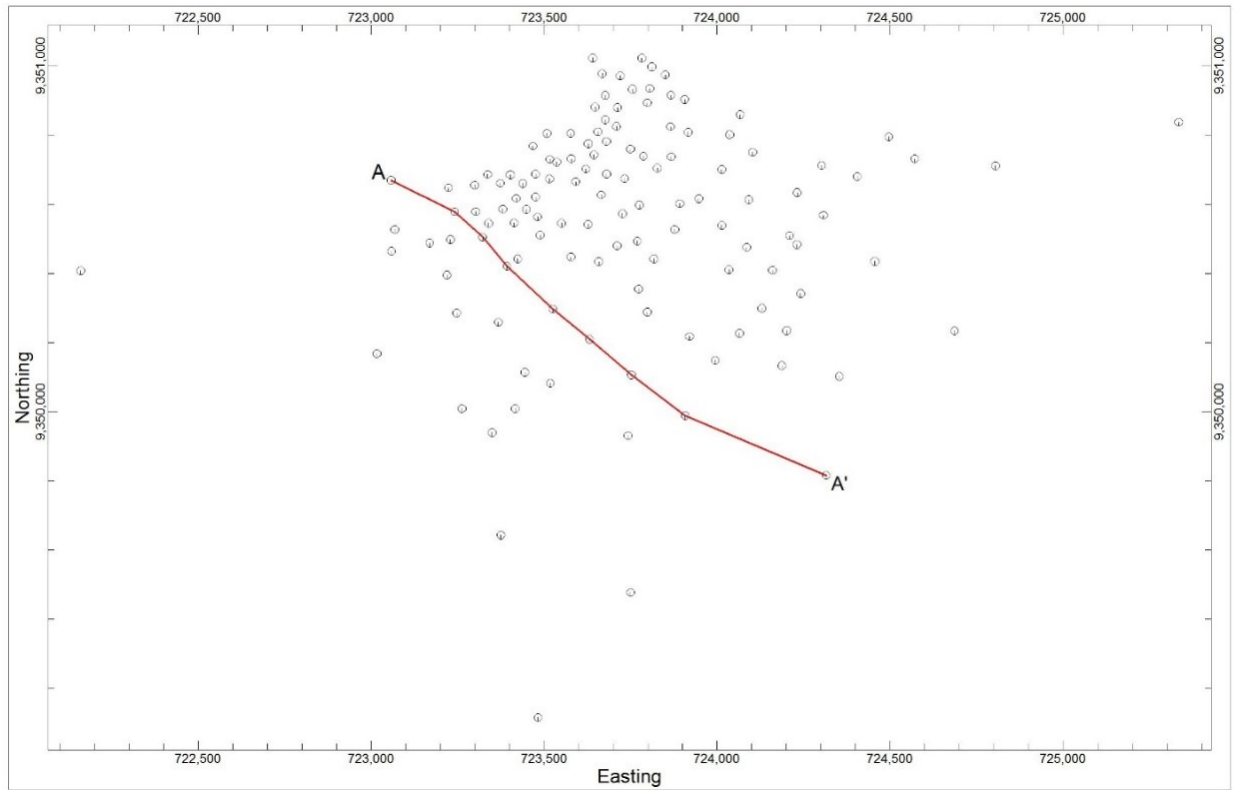
The metric's values were normalized giving a proportional distance measure among the clusters. As presented in Figure 46, two major groups were identified exhibiting substantial differences which are defined by the opposition of geotechnical variables.

Figure 41 – Banded iron formations (itabirites) drill cores exhibiting some accounted for geological features. **A)** Unweathered non-porous martitic itabirite (fresh rock); **B)** Slightly weathered amphibolitic itabirite; **C)** Moderately weathered hematitic itabirite; **D)** porous weathered hematitic itabirite; **E)** highly weathered magnetitic itabirite; **F)** friable highly weathered magnetitic itabirite.



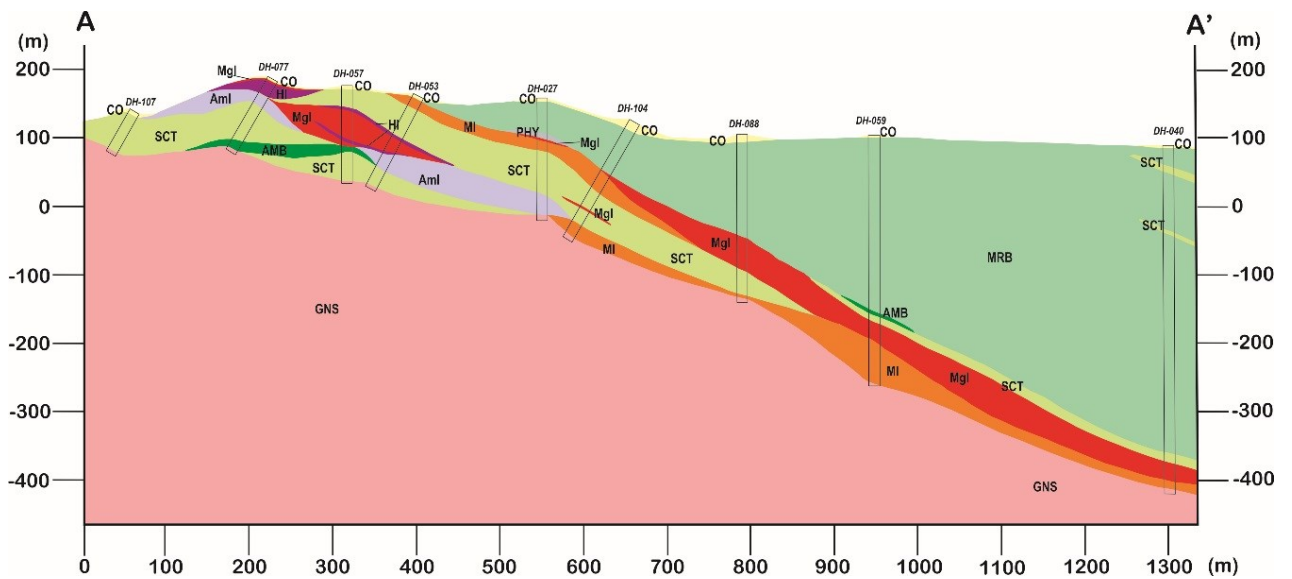
Source: Fonteles *et al.* (2019b).

Figure 42 - Locational map of the geological cross-section A-A' passing through the boreholes points.



Source: Fonteles *et al.* (2019b).

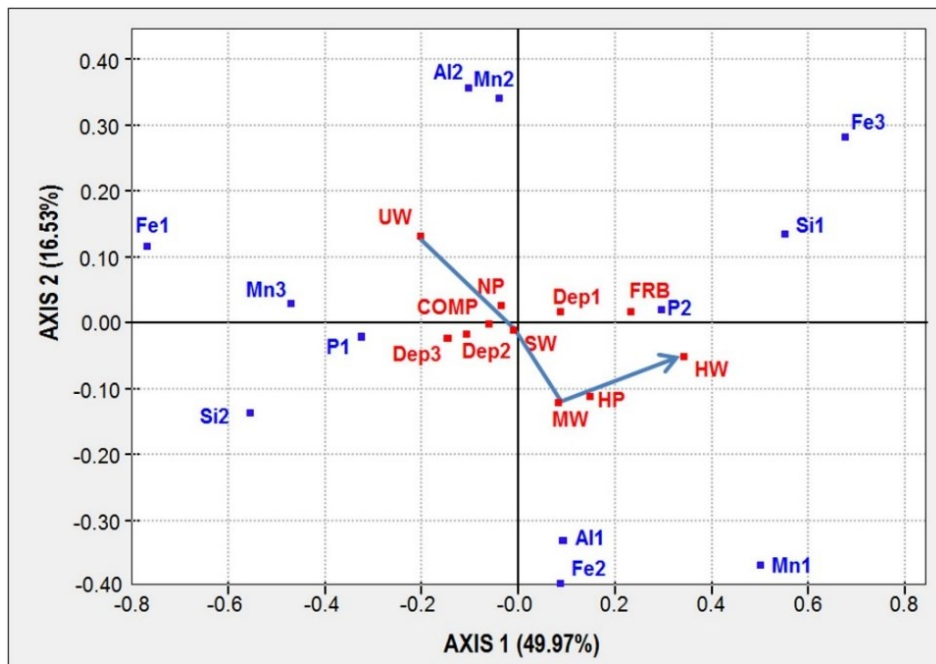
Figure 43 – Geological cross-section A-A' of the Bonito Mine. List of abbreviations: AmI – amphibolitic itabirite; HI – hematitic itabirite; Mgl – magnetitic itabirite; MI – martitic itabirite; MRB – marble; SCT – schist; AMB – amphibolite; PHY – phyllite; CO – colluvium; GNS – gneiss.



Source: Fonteles *et al.* (2019b).

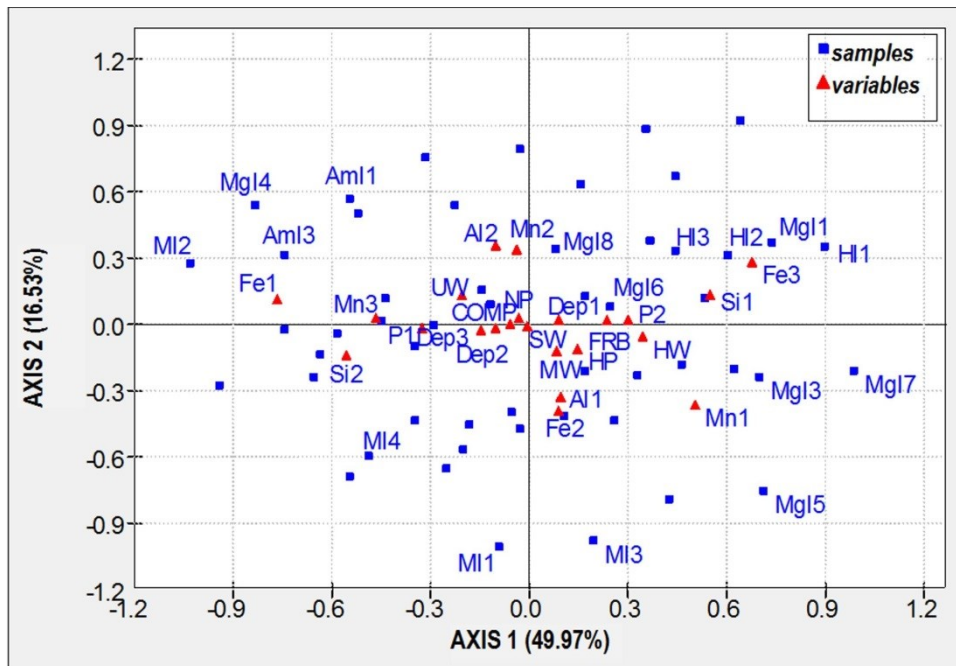


Figure 44 – Plot of active (blue) and supplementary (red) variables onto factorial plane A1-A2. The blue arrow shows the weathering path through the graphic display.



Source: Fonteles *et al.* (2019b).

Figure 45 – Projection of all variables and samples onto the A1-A2 factorial plane. Some petrographical samples occupy the same position in the plane: AmI1=AmI2; MgI1=MgI2.



Source: Fonteles *et al.* (2019b).

### 5.3.3 Discussion

CA provided a factorial scenario with the geochemical (active) and geotechnical (supplementary) variables and samples displayed onto the same space. Examining the eigenvalues (Table 16) one can notice that almost 70% of total inertia was retained by the first two axes (factors).

The petrographic study by Fonteles *et al.* (2018) did not recognize mineralogical alteration products like goethite or any aluminous mineral occurring extensive and massively throughout the drilling core samples. Silica-richer BIF ores tend to resist more than the oxide-richer ones in the study area. Aluminum oxide grades lowering along Axis 2 (Figure 45) shows a decrease of Al-Fe-Mg hydrated-silicates (amphiboles) modal content in BIF rocks (See Table 9 for reference).

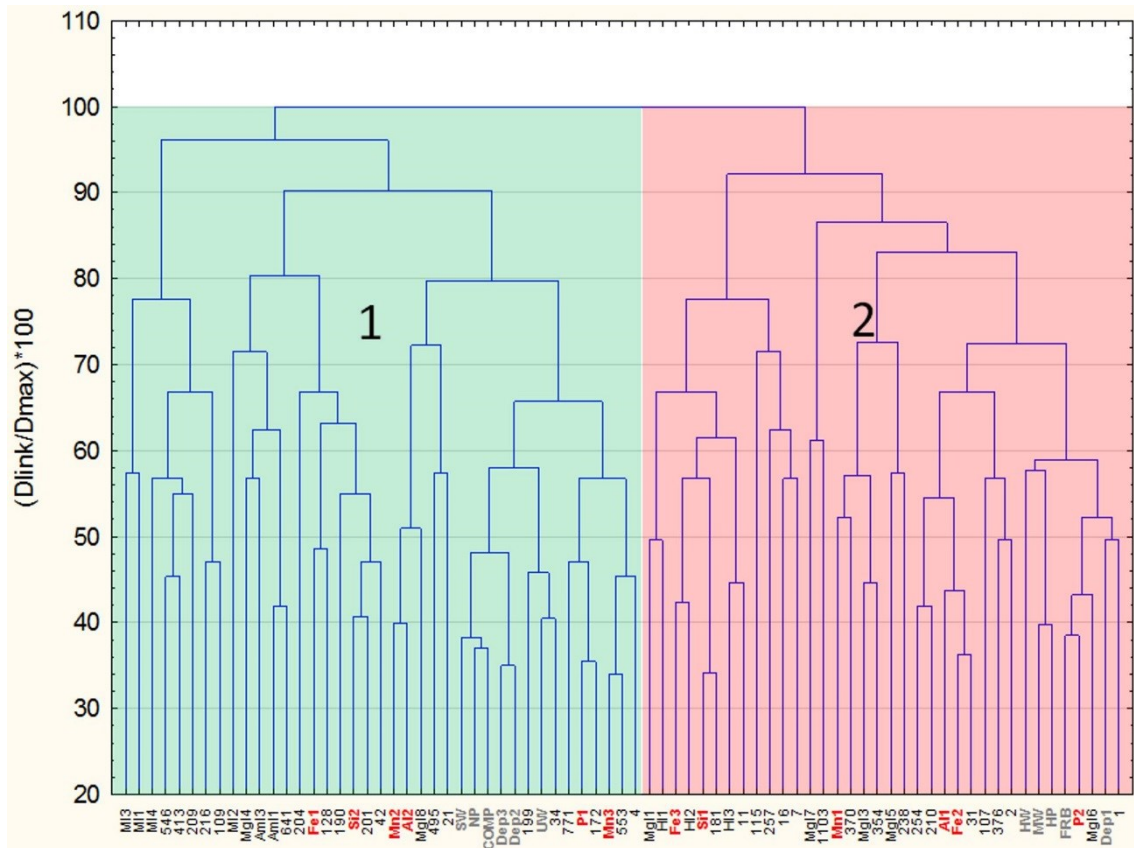
The two major clusters unfold the inter-related active and supplementary variables and petrographic samples. Cluster 1 is characterized by the Fe-poorer/High-Al BIF ores describing a peculiar association of magnetitic itabirites martitic, itabirites to amphibolitic itabirites. These BIF rocks are tended to be positioned deeper than 70 meters and they are usually slightly weathered or unweathered.

Cluster 2 groups Fe-richer/Low-Al BIF ores composed of martitic, magnetitic and hematitic itabirites which are described as moderately to highly weathered porous friable ore materials. Despite the lithological banding feature, the BIFs in Cluster 1 behave like compact and non-porous itabirites.

As already shown, Cluster 1 encompasses all amphibolitic itabirites with higher percentages of Al-amphiboles (Fe-gedrite and hornblende) and, some samples of magnetitic and martitic itabirites with Fe-poorer content (see Table 6 for reference). These BIF types are related to deeper levels (> 70m) in the mining site (Figure 47).

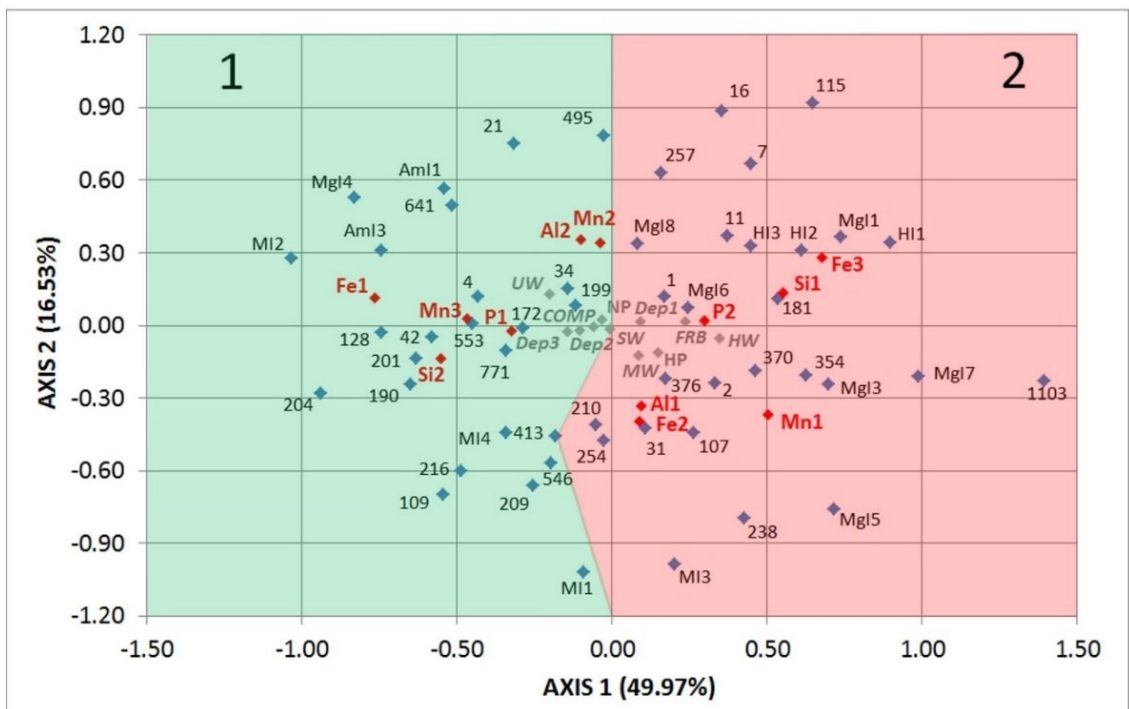
The achieved results indicate the most incisive weathering processes are due to the physical disintegration of the primary BIF rocks. The itabirites of Bonito Mine seem to be an exception to some well-studied BIF deposits in the world (AIRES-BARROS, 1963; DORR II; BARBOSA, 1963; BRONNER; CHAUVEL, 1979; CASTRO, 1994; VERÍSSIMO, 1999; MORRIS; KNEESHAW, 1999); where assorted conditioning weathering processes broadly induced the formation of extensive deposits with well-formed soil profiles often reaching more than ten meters deep.

Figure 46 – Dendrogram of active and supplementary variables (colored text) jointly represented with supervising BIF samples. The numbers represent samples' codes according to the primary geological database.



Source: Fonteles *et al.* (2019b).

Figure 47 – Factorial dual-display of variables samples regarding their positions on the dendrogram model. The numbers represent samples' codes according to the primary geological database.



Source: Fonteles *et al.* (2019b).

## 6 PROPOSITION OF SIMPLE CHEMICAL CRITERIA FOR GEOCHEMICAL CLASSIFICATION OF BIF DEPOSITS

Banded Iron Formations (BIF) have been deposited, metamorphosed and, deformed since Paleoproterozoic to Neoproterozoic and Neoproterozoic (KLEIN, 2005; ILYN, 2009; KONHAUSER *et al.* 2017). As illustrated by Figure 48 during the Mesoproterozoic Era, an expressive lack of BIF deposition is noticed. The return of the deposition of new BIF rocks came with the global tectonics events and radical climatic changes in the Neoproterozoic Era (COX *et al.* 2013). Rapitan Group, Jacadigo Group/Santa Cruz Formation (Urucum District), and Damara diamictite, as BIF deposits, were formed under the strong influence of massive glaciation events (BREITKOPF, 1987; KLEIN; BEUKES, 1993; KLEIN; LADEIRA, 2004).

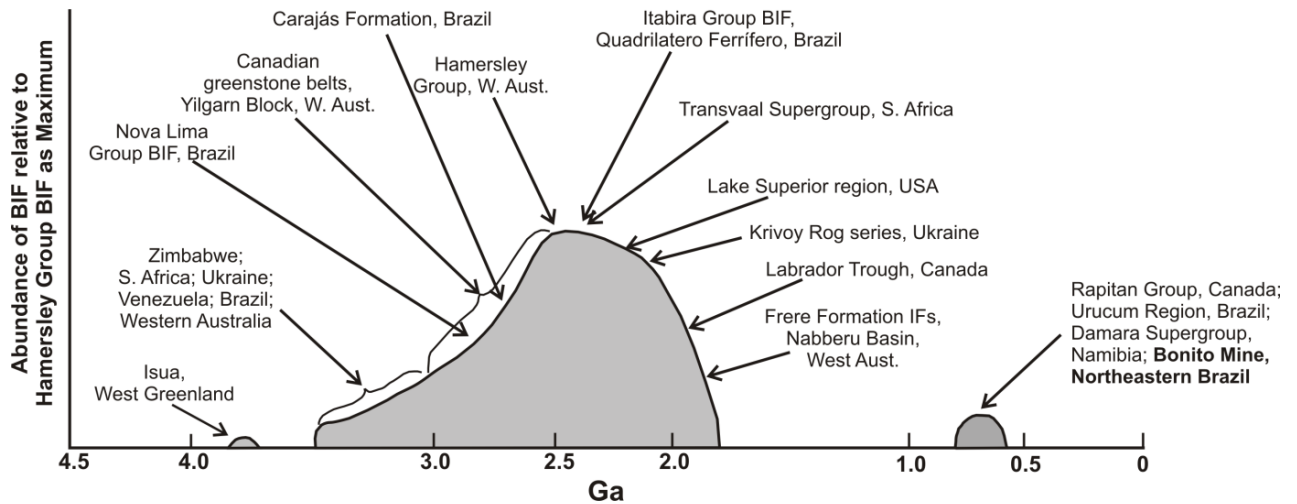
Most of the known relevant BIF deposits were formed during the Neoproterozoic to Paleoproterozoic Eras. Some of them have great economic feasibility such as Hamersley Group (NW Australia), Carajás IOCG Complex (Northern Brazil) and, the Quadrilátero Ferrífero/Itabira Group (Southeastern Brazil).

Their geological setting has been subjected to several geochemical evaluations; most of them based on major oxides, trace elements and Rare Earth Elements (REE) (BOSTRÖM, 1970; BONATTI, 1975; GRAF Jr., 1978; DERRY; JACOBSEN, 1990; MURRAY, 1994; DUPUIS; BEAUDOIN, 2011).

The proposed schemes in this section are based on major oxides grades (wt.%) and REE data ratio used on the construction of bivariate and ternary diagrams regarding the tectonic environments of the BIF deposits. The major goal of this study is the identification of the tectonic setting of some well-representative BIF deposits and the search for a geological correlation based on metallogenic origin.

Some of the worldwide BIF deposits were broadly assessed, including the itabirites from the Bonito Mine; BIF rocks that occur at Boa Viagem and Quixeramobim cities (Northeastern Brazil) and, the Bom Sucesso BIF (Southeastern Brazil) (VERÍSSIMO *et al.* 2009; NERI *et al.* 2013). Other cases from Africa and China were also included (BASTA *et al.* 2011; XU *et al.* 2014; SYLVESTRE *et al.* 2015).

Figure 48 – Schematic diagram regarding the relative abundance of some Precambrian BIFs taking Hamersley BIF Group's maximum volume as reference. Some of these deposits were included in the present study.



Source: Modified from Klein (2005).

The database was compiled from the scientific literature gathered by published papers and academic dissertations. Additionally, geochemical data of the Bonito Mine is stemmed from previous studies performed by Barbosa (2013), Fonteles *et al.* (2018), Fonteles *et al.* (2019a), Fonteles *et al.* (2019b) and from the geological databank provided by MHAG Company.

It is expected the classification diagrams cannot be unrestrainedly applied to all possible situations concerning the assorted metallogenic environments. However, it is expected to present a general guideline aiding the understanding of how BIFs of the Bonito Mine can be classified through simple chemical criteria. Based on the available published descriptions, the chemical data represents four metallogenic models: glaciogenic, sedimentary, volcano-sedimentary and, hydrothermal.

During the data compilation, we have found that some BIF deposits would be related to more than one metallogenic setting. Hence, we have considered the dominant geological processes that imposed the most significant features. For instance, some sedimentary deposits were affected by hydrothermal input and the task, in this case, was to verify if this input was relevant to the iron concentration in the BIF-hosted deposit. Therefore, the denomination 'hydrothermal model' was employed in this study to classify the BIF-hosted deposits which

were affected by high-temperature fluids. These processes were assumed to improve the iron enrichment within the BIF rocks.

## 6.1 Chemical database

The geochemical database employed in this study was mainly obtained from the available scientific literature and chemical data of the Bonito Mine (Table 17). No experimental constraint regarding the number of samples of each case of the study was designed. Thus, the number of representative samples of each BIF-related iron deposit is different. For the case of the Bonito Mine BIFs, 482 samples were used, and the average grade is listed in Table 18.

The major oxides referred to in this study are  $\text{Fe}_2\text{O}_3$ ,  $\text{SiO}_2$ ,  $\text{Al}_2\text{O}_3$ ,  $\text{MnO}$ ,  $\text{CaO}$ ,  $\text{MgO}$ ,  $\text{K}_2\text{O}$  and  $\text{TiO}_2$ .  $\text{P}_2\text{O}_5$  content was not included due to unreported values in some scientific studies. Regarding  $\text{MnO}$  grades, the data content was converted to Mn values due to experimental data of the Bonito Mine which is reported as Mn grade content (Table 18). The REE data used in this study are listed in Table 19, including Bonito Mine data (BARBOSA, 2013).

## 6.2 Geochemical data evaluation

As a first step, PCA was performed in order to explore the main qualitative correlations between major oxides values. This round of geochemical data evaluation has shown significant correlations expressed through the eigenvalues and the factorial loads on PC1 and PC2 (Tables 20 and 21, Figure 49).

According to Kaiser's criterion (MANLY, 1994), PC1 and PC2 are represented by eigenvalues superior to 1.00 (Table 20). Hence, these two PCs explain almost 60% of the retained variance of the multivariate data. PC1 encompasses  $\text{Fe}_2\text{O}_3$ ,  $\text{CaO}$ ,  $\text{MgO}$  and  $\text{K}_2\text{O}$  grades whereas PC2 is described mostly by  $\text{SiO}_2$ ,  $\text{Al}_2\text{O}_3$ , and  $\text{TiO}_2$  (Figure 49, Table 21).

Table 17 – List of scientific literature used to search the chemical data.

<b>BIF Deposit</b>	<b>Bibliographic data reference</b>
Rapitan, Canada	Klein and Beukes (1993)
Urucum, Brazil	Klein and Ladeira (2004)
Damara Diamictite, Namibia	Breitkopf (1987)
Transvaal Kuruman, South Africa	Beukes and Klein (1990); Horstmann and Hälbich (1995)
Transvaal Griquatown, South Africa	Beukes and Klein (1990); Horstmann and Hälbich (1995)
Hamersley - Dales Gorge Member, Australia	Webb (2003); Pecoits <i>et al.</i> (2009)
Hamersley - Joffre Member, Australia	Haugaard <i>et al.</i> (2016)
Bababudan, India	Arora <i>et al.</i> (1995)
Shilu, Hainan, China	Xu <i>et al.</i> (2014)
Lake Superior-type, Canada/USA	Gross & McLeod (1980)
Orissa, India	Majumder <i>et al.</i> (1982)
Umm Nar, Egypt	Aref <i>et al.</i> (1993)
Eastern Alegria, Brazil	Veríssimo (1999)
Krivoy Rog Basin 1, Ukraine	Belevtsev <i>et al.</i> (1983)
Krivoy Rog Basin 2, Ukraine	Kulik and Korzhnev (1997); Mboudou <i>et al.</i> (2012)
Kushtagi Chert, India	Khan and Naqvi (1996)
Kushtagi Shale, India	Khan and Naqvi (1996)
<b>Bonito Mine, Brazil</b>	Barbosa (2013); <b>This study</b>
Bom Sucesso, Brazil	Neri <i>et al.</i> (2013)
Ntem Greenstone Belt, Cameroon	Sylvestre <i>et al.</i> (2015)
Damara Type 1, Namibia	Breitkopf (1987)
Damara Type 2, Namibia	Breitkopf (1987)
Quixeramobim, Brazil	Veríssimo <i>et al.</i> (2009)
Boa Viagem, Brazil	Veríssimo <i>et al.</i> (2009)
Um Anab, Egypt	Basta <i>et al.</i> (2011)
Algoma-type, Canada	Gross and McLeod (1980)
Isua Greenstone Belt, Greenland	Appel (1980); Dymek and Klein (1988)
Abitibi, Québec/Canada	Taner and Chemam (2015)
Carajás, Brazil	Macambira and Schrank (2002)

Source: Compiled by the author.

Table 18 – Major oxides of the studied BIF-hosted deposits (%wt).

BIF Deposit	Acronym	Fe <sub>2</sub> O <sub>3</sub>	SiO <sub>2</sub>	Al <sub>2</sub> O <sub>3</sub>	Mn	CaO	MgO	K <sub>2</sub> O	TiO <sub>2</sub>	Model
Rapitan, Canada	RAP	33.03	62.32	0.17	0.01	1.13	0.19	0.014	0.030	Glaciogenic
Urucum, Brazil	URU	55.03	39.44	1.22	0.39	1.05	0.38	0.013	0.134	
Damara Diamictite, Namibia	DAM-d	56.05	38.07	1.24	0.09	1.72	0.08	0.420	0.040	
Transvaal Kuruman, S. Africa	T-KUR	26.49	45.16	0.31	0.16	2.09	2.99	0.430	0.010	Hydrothermal
Transvaal Griquatown, S. Africa	T-GQT	22.50	48.01	0.17	0.35	2.75	3.43	0.180	0.020	
Hamersley, Dales Gorge	H-DG	40.60	43.80	0.36	0.18	3.32	3.18	0.480	0.010	
Hamersley, Joffre Member	H-JF	44.38	50.12	0.41	0.05	1.56	1.91	0.570	0.030	
Bababudan, India	BAB	46.37	45.51	0.27	0.05	2.81	2.49	0.060	0.010	
Bom Sucesso, Brazil	BSC	51.00	44.90	0.09	0.12	4.45	4.28	0.200	0.010	Sedimentary
Shilu, Hainan - China	SHI	39.50	28.59	5.24	0.36	7.76	1.48	1.350	0.250	
Lake Superior-type, Canada/USA	LSP	35.40	47.20	1.39	0.57	1.58	1.53	0.140	0.030	
Orissa, India	ORS	47.02	44.16	0.70	0.57	1.58	0.13	0.140	0.020	
Umm Nar, Egypt	UNR	58.23	34.92	2.28	0.05	3.01	0.73	0.070	0.110	
Alegria East Sector, Brazil	AGR	61.50	36.44	0.50	0.04	0.05	0.11	0.010	0.050	
Krivoy Rog Basin 1, Ukraine	KRB1	40.75	57.20	0.36	0.02	0.40	0.18	0.020	0.010	
Krivoy Rog Basin 2, Ukraine	KRB2	30.13	43.00	0.58	0.07	1.18	2.41	0.240	0.030	
Kushtagi Chert, India	KST-c	43.58	55.63	0.37	0.00	0.02	0.04	0.020	0.030	
Kushtagi Shale, India	KST-s	59.26	22.09	11.66	0.02	0.22	1.51	0.570	0.350	
Ntem Greenstone Belt, Cameroon	NTEM	58.19	39.98	0.48	0.06	0.02	0.06	0.020	0.030	Volcano-sedimentary
Damara Type 1, Namibia	DAM-t1	65.45	26.38	1.70	0.07	2.91	0.08	0.110	0.080	
Damara Type 2, Namibia	DAM-t2	35.28	46.02	7.10	0.14	4.63	2.37	0.150	0.640	
Quixeramobim, Brazil	QXB	45.83	51.35	0.28	0.02	0.59	1.83	0.040	0.030	
Boa Viagem, Brazil	BVG	43.93	53.52	0.77	0.03	0.07	0.33	0.030	0.025	
<b>Bonito, Brazil*</b>	BTO	38.88	53.36	1.89	0.26	1.99	3.74	0.340	0.100	
Um Anab, Egypt	UAB	35.14	54.62	3.60	0.05	2.98	1.28	0.120	0.200	
Algoma-type, Canada	ALG	26.90	50.50	3.00	0.17	1.51	1.53	0.580	0.140	
Isua Greenstone Belt, Greenland	ISU	48.93	29.30	0.27	0.14	0.28	1.28	0.020	0.070	
Abitibi, Canada	ABI	26.27	45.39	8.63	0.04	1.53	2.21	1.750	0.310	
Carajás, Brazil	CAJ	53.65	44.60	0.63	0.04	0.04	0.10	0.020	0.02	

Source: Data compiled by the author and \*research data.



Table 19 – La and Ce data of BIF-hosted deposits and NASC geochemical standard.

<b>BIFdeposit</b>	<b>Acronym</b>	<b>La</b>	<b>Ce</b>	<b>La<sub>n</sub></b>	<b>Ce<sub>n</sub></b>
Rapitan	RAP	3.97	8.66	0.128	0.130
Urucum	URU	8.31	14.1	0.267	0.211
Kuruman	T-KUR	0.88	1.06	0.028	0.016
Griquatown	T-GQT	0.96	1.19	0.031	0.018
Dales Gorge Member	H-DG	0.79	1.2	0.025	0.018
Joffre Member	H-JF	4.32	9.03	0.139	0.135
Bababudan	BAB	4.69	6.74	0.151	0.10
Lake Superior-type	LSP	4.84	11.9	0.156	0.178
Orissa	ORS	0.01	2.18	0.000	0.033
Eastern Alegria	AGR	1.613	6.345	0.052	0.095
Krivoy Rog 2	KRB2	4.8	12.45	0.154	0.187
Kushtagi Chert	KST-c	3.31	5.45	0.106	0.082
Kushtagi Shale	KST-s	15.78	29.59	0.507	0.444
Ntem greenstone belt	NTEM	0.222	0.706	0.007	0.011
Quixeramobim	QXB	41.45	58.35	1.333	0.875
Boa Viagem	BVG	3.7	7.4	0.119	0.111
Isua greenstone belt	ISU	2.88	3.4	0.093	0.051
Bonito Mine	BTO	7.55	13.51	0.243	0.203
Abitibi	ABI	16.93	32.63	0.544	0.489
Carajás	CAJ	1.87	2.38	0.060	0.036
Um Anab	UAB	12.13	27.09	0.390	0.406
Shilu	SHI	17.6	41.6	0.566	0.624
Bom Sucesso	BSC	1.4	1.82	0.045	0.027
<i>North American Shale Composite</i>	<i>NASC</i>	<i>31.10</i>	<i>66.70</i>	<i>---</i>	<i>---</i>

Source: Data compiled by the author.

Table 20 – Eigenvalues.

<b>PC</b>	<b>Eigenvalue</b>	<b>% Exp</b>	<b>% Cumm</b>
<b>1</b>	2.5245	31.56	<b>31.56</b>
<b>2</b>	2.2413	28.02	<b>59.57</b>
3	0.9920	12.40	71.97
4	0.8661	10.83	82.80
5	0.8476	10.59	93.39
6	0.2750	3.44	96.83
7	0.1822	2.28	99.11
8	0.0713	0.89	100.00

Source: Elaborated by the author.

Table 21 – Factorial loads on Principal Components. Bold values are related to the most significant factorial loads.

Variable	PC1	PC2	PC3	PC4	PC5	PC6	PC7	PC8
Fe <sub>2</sub> O <sub>3</sub>	<b>0.7061</b>	-0.4766	-0.3699	-0.0928	-0.1533	0.2037	-0.2471	0.0531
SiO <sub>2</sub>	-0.2453	<b>0.6892</b>	0.5953	-0.1587	0.0111	0.2197	-0.1919	-0.0012
Al <sub>2</sub> O <sub>3</sub>	-0.2797	<b>-0.8815</b>	0.2365	0.0981	0.1815	-0.0191	-0.1231	-0.1754
Mn	-0.3972	0.3060	-0.4183	0.0851	0.7461	0.0396	-0.0882	0.0204
CaO	<b>-0.6981</b>	-0.0932	-0.3303	-0.5481	-0.1605	0.2269	0.1154	-0.063
MgO	<b>-0.8259</b>	0.1459	-0.2254	-0.0202	-0.3581	-0.2666	-0.2132	0.026
K <sub>2</sub> O	<b>-0.6455</b>	-0.2252	-0.0245	0.6547	-0.1974	0.2431	0.047	0.0559
TiO <sub>2</sub>	-0.3790	<b>-0.7668</b>	0.3307	-0.2933	0.2036	-0.0411	0.0191	0.1718

Source: Elaborated by the author.

The factorial plane (Figure 49) exhibits the multivariate relations of major oxides grades of the BIF deposits. From the qualitative geochemical correlations, it is clear:

- ✘ Factorial loads on PC1 exhibit negative correlations between Fe<sub>2</sub>O<sub>3</sub> and CaO, MgO and K<sub>2</sub>O;
- ✘ Factorial loads on PC2 show negative correlations between SiO<sub>2</sub> and Al<sub>2</sub>O<sub>3</sub> and TiO<sub>2</sub>;
- ✘ Al<sub>2</sub>O<sub>3</sub> and TiO<sub>2</sub> are closely associated; the same situation occurs to CaO and K<sub>2</sub>O;
- ✘ Mn grades are virtually uncorrelated to other geochemical variables. The highest factorial load is due to PC5 that explains 10.6% of the total inertia (interpreted as a low value for additional analysis).

PCA results were taken into account to construct the geochemical diagrams used to plot and compare the chemical data of the BIF deposits. The positive and negative correlations were placed in the corners of a ternary diagram. Fe<sub>2</sub>O<sub>3</sub> and SiO<sub>2</sub> were not included due to their high grades that sometimes respond to almost 70% of the bulk composition.

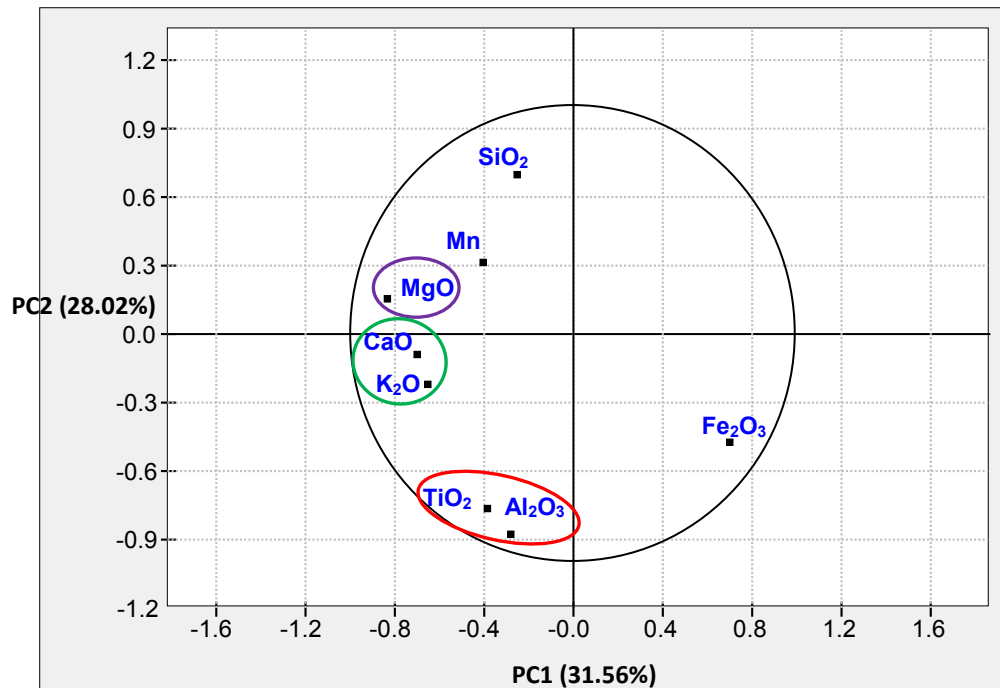
Research conducted by Murray (1994) regarding marine cherts concluded that silica content can act as a diluent to other chemical components. Although BIFs do not have high silica content as that, the summation of Fe<sub>2</sub>O<sub>3</sub> and SiO<sub>2</sub> grades can act in the same way.

In this matter, Murray's study provided some guidelines and insights that contributed to the present investigation.

Based on the relations provided by PCA, a chemical ternary diagram is proposed to aid the classification scheme of BIF deposits (See Table 18 for reference). The ternary diagram was built using the combination  $\text{Al}_2\text{O}_3+\text{TiO}_2$  -  $\text{CaO}+\text{K}_2\text{O}$  -  $\text{MgO}$  obtained from the factorial relations exhibited in Figure 49.

No prior data transformation or normalization was imposed on the primary major oxides database except where indicated (Figure 50). A geochemical interpretation in terms of metallogenic settings is possible due to chemical data plotting in this diagram.

Figure 49 – PC1 x PC2 factorial plane of the geochemical variables.



Source: Elaborated by the author.

Figure 50 shows three distinct metallogenic domains that encompass BIF chemical data. The geometry of the domain boundaries did not result from interpolated curves and/or lines. They separate similar deposits regarding their geological origin. The delimited zones did not consider age differences, post-deformational processes, and geographical locations. BIF deposits spread in several domains of the ternary diagram.

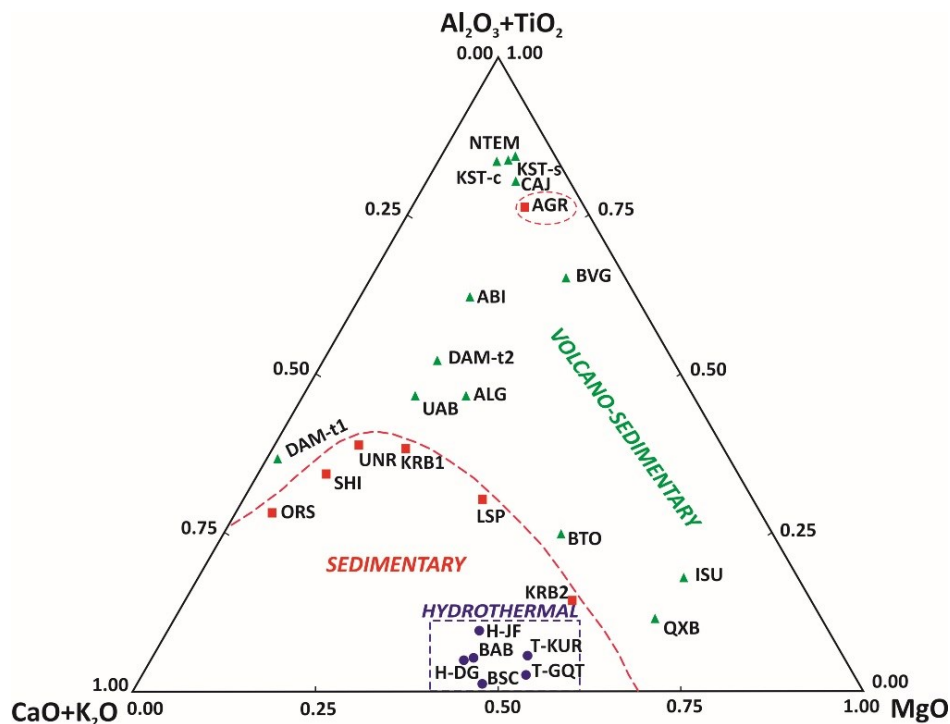
Particularly, hydrothermal-influenced deposits plot locally closer to the CaO+K<sub>2</sub>O - MgO axis. Most part of the samples is clearly related to hydrothermal input as a crucial contribution to the iron enrichment in the deposit.

The smaller number of BIF deposits samples fell into the sedimentary-type domain and, the rest represents the greater number of the samples plotted inside the volcano-sedimentary type domain. Extending the previous study of the classification deposits, geochemical data of the Bonito Mine BIF typology model (FONTELES *et al.* 2018), the samples were plotted into the volcano-sedimentary type domain (Figure 51).

The proposed ternary diagram (Figure 50) was unable to discriminate the glaciogenic deposits, in terms of major oxides content. Therefore, a broader classification was presented encompassing major oxides ratio and NASC-normalized REE ratio (GROMET *et al.* 1984). The bivariate plot exhibited in Figure 52 was developed as an adaptation of a previous classification diagram by Murray (1994).

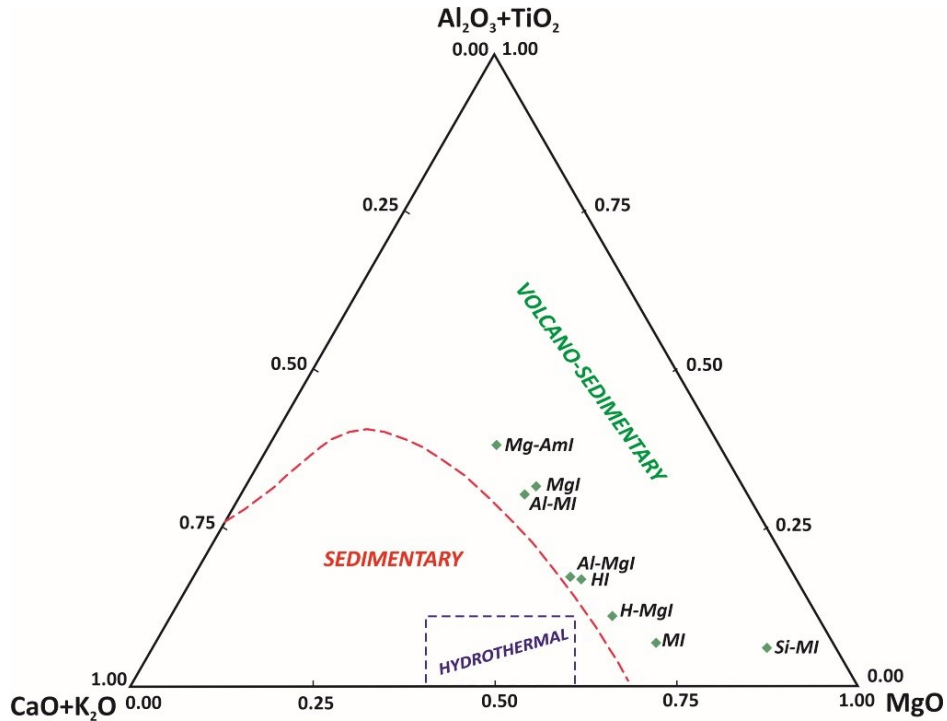
The Y-axis is represented by the La<sub>n</sub>/Ce<sub>n</sub> ratio related to sedimentary fractioning during the deposition stage. The X-axis shows MgO/(CaO+MgO) ratio related to the increase of volcanic input. Owing to the available data for most of the deposits, the glaciogenic domain was sketched. No REE data related to BIF rocks of the Damara Belt was available.

Figure 50 – Al<sub>2</sub>O<sub>3</sub>+TiO<sub>2</sub> - CaO+K<sub>2</sub>O - MgO ternary classification diagram for BIF-related iron deposits including chemical data from the Bonito Mine. See Table 2 for acronyms references.



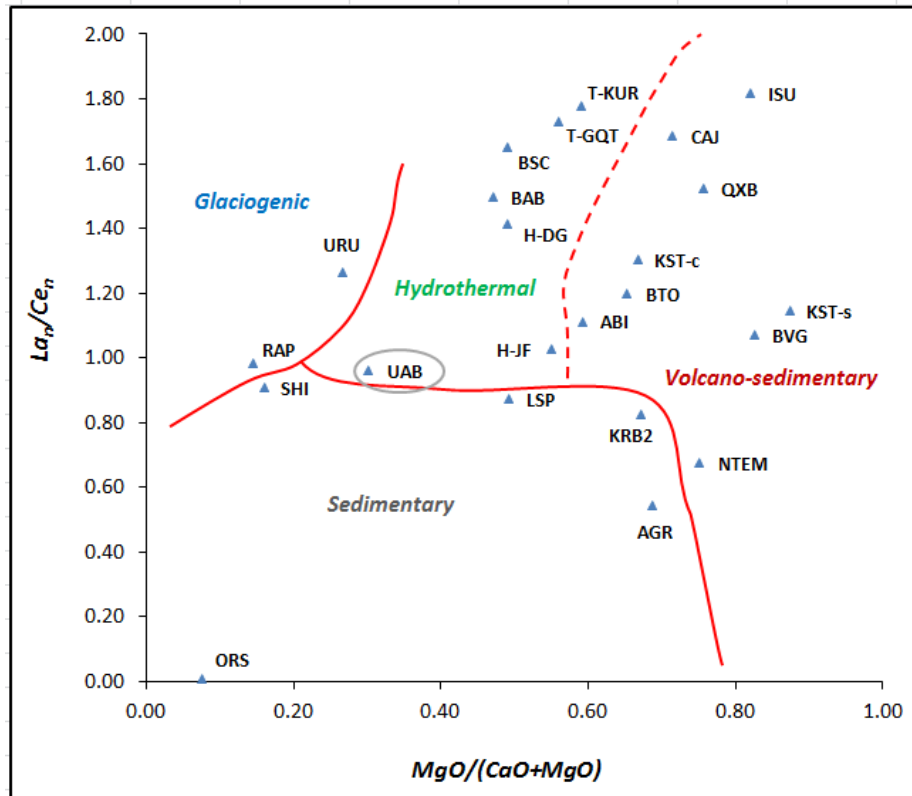
Source: Elaborated by the author.

Figure 51 –  $Al_2O_3+TiO_2$  -  $CaO+K_2O$  -  $MgO$  classification diagram for itabirites from the Bonito Mine. Acronyms: Al-MI – aluminous martitic itabirite; Al-MgI – aluminous magnetitic itabirite; HI – hematitic itabirite; H-MgI – hematic-magnetitic itabirite; MI – martitic itabirite; MgI – magnetitic itabirite; Am- MgI – amphibolitic-magnetitic itabirite; Si-MI – silicate martitic itabirite.



Source: Elaborated by the author.

Figure 52 – Bivariate diagram for BIF deposits based on REE and  $MgO$ - $CaO$  ratios. The  $La_n/Ce_n$  ratio values were normalized to the NASC geochemical standard.



Source: Elaborated by the author.

### 6.3 Discussion

Significant qualitative correlations from PCA results revealed the major oxides' associations that were interpreted to build the ternary diagrams. The data point's arrangement was used to draw the limits between the domains. Figure 50 exhibits how BIF-hosted deposits are grouped throughout three geochemical domains: sedimentary, volcano-sedimentary and hydrothermal. Most part of the deposits is gathered as glaciogenic, hydrothermal and volcano-sedimentary.

Not all BIF-related iron deposits are supposedly plotted into the correspondent metallogenic domain (Figure 50). For instance, Eastern Alegria deposit (VERÍSSIMO, 1999) is a sedimentary-type (or Lake Superior-type) deposit, however, according to the proposed chemical classification, it could be interpreted as a volcano-sedimentary deposit. Meanwhile, Figure 52 reveals controversial information regarding the  $MgO/(CaO+MgO)$  ratio which marks Eastern Alegria as a sedimentary-type deposit.

Veríssimo (1999) integrated mineralogical, structural and geochemical data reaching conclusions that sustained a Lake Superior-type genetic model with absent or low volcanic contribution suited to Alegria BIFs. One of the sound conclusions is based on the negative Eu anomaly which is a very distinctive geochemical REE signature for that type of BIF deposit (GRAF Jr., 1987).

The sedimentary domain occupies a region delimited by the superior  $La_n/Ce_n$  ratio  $\approx 0.90$ . The studied BIF deposits are likely to have similar geochemical sedimentation patterns as the 'North American Shale Composite' – NASC (GROMET *et al.* 1984). Furthermore, there is a  $Ce_n$  relative enrichment trend in this domain, as shown Eastern Alegria and Krivoy Rog 2 BIF deposits.

Bom Sucesso BIF belongs to the homonymous metasedimentary sequence of the Minas Supergroup (NERI *et al.* 2013). The BIF rocks and carbonatic rocks (mainly discontinuous ferruginous dolomite) are considered syn-sedimentary. Owing to the whole-rock geochemical data, a sedimentary-type domain would be expected to classify the Bom Sucesso BIF rocks. However, one of the hypotheses discussed by Neri *et al.* (2013) is that the Bom Sucesso metasedimentary sequence could be associated with the Rio das Mortes greenstone belt, which may have contributed as a possible source of hydrothermal exhalations.

Um Anab BIF was reported as a Neoproterozoic volcano-sedimentary sequence without association with the glaciogenic origin. Rather, Basta *et al.* (2011) are emphatic

explaining their origin linked to the breakup of Rodinia paleocontinent and related volcanism. In Figure 50, Um Anab BIFs are plotted into the volcano-sedimentary domain, meanwhile, in Figure 52, the geochemical data suggest a hydrothermal source.

According to Basta *et al.* (2011), Um Anab PAAS-normalized REE+Y data are indicative of the absence of expressive La, Ce, Eu and Y anomalies contradicting a pure hydrothermal origin. For classification purposes, we should consider such a case as a “border-line” case. Nevertheless, no graphical proximity to the volcano-sedimentary in Figure 52 is noticeable.

Beukes and Klein (1990) analyzed the transition of Kuruman-Griquatown Formations/Transvaal Supergroup on deepwater facies and interpreted this stratigraphic feature as a record of an extensive marine platform. Although a depositional system based on deep water deposit reworked by storm action is advocated, REE patterns are strongly suggestive that the hydrothermal component would be crucial on the genesis of the BIFs of the sequence (HORSTMANN; HÄLBICH, 1995).

Hamersley Group data was analyzed referring to three different scientific studies in order to extend the assorted available geochemical data (See Table 17 for reference). According to HAUGAARD *et al.* (2016), Joffre and Dales Gorge Members belong do Brockman Iron Formation.

Although the Hamersley Basin has a long stratigraphical history, the geological evolution model has conciliated the hydrothermal and volcanic inputs showing that hydrothermal fluids have contributed incisively to the iron enrichment within the BIFs (WEBB, 2003; PECOITS, 2009).

Glaciogenic BIF deposits' data presented here are very few. Thus, some caution is necessary for avoiding the general extension of the concept. The link between them is the Neoproterozoic age of deposition clearly correlated to the great glaciations (BREITKOPF, 1987; KLEIN; BEUKES, 1993; YOUNG, 2002; KLEIN; LADEIRA, 2004; COX *et al.* 2013). Nonetheless, this metallogenic domain can be interpreted as a suggestive field related to the genesis of BIFs constrained by anoxic Neoproterozoic marine basins (KLEIN; BEUKES, 1993; YOUNG, 2002; STERN *et al.* 2013; HALVERSON *et al.* 2010).

Volcano-sedimentary-type deposits such as Abitibi (Algoma-type), Isua, Elom BIF (Ntem greenstone belt), Damara Belt, Kushtagi Schist Belt (Dharwar Craton), Boa Viagem/Quixeramobim BIFs, and Carajás IOCG BIF complex have typical volcanic input signatures (Figures 50 and 52). The common features are the positive Eu anomaly, the presence of interbedded volcanic rocks and, stratigraphic relations pointing the existence of

proximal volcanic sources (GROSS; MCLEOD, 1980; APPEL, 1980; BREITKOPF, 1987; DYMEK; KLEIN, 1988; KHAN; NAQVI, 1996; MACAMBIRA; SCHRANK, 2002; VERÍSSIMO *et al.* 2009; TANER;CHEMAM, 2015) .

REE data provided by Barbosa (2013) and Sial *et al.* (2015) revealed the basic Algoma-type Eu positive anomaly. This geochemical pattern is compatible with volcano-sedimentary BIFs studied over the years.

The itabirites from the Bonito Mine were classified as volcanic-sedimentary-type deposits. According to Angelim *et al.* (2006), the BIF rocks in the mining site are associated to the Serra dos Quintos Formation/Seridó Group, a metasedimentary sequence which was metamorphosed reaching the amphibolite facies, encompasses several lithologies such as schist, paragneiss, marble, metavolcanics (amphibolite) and phyllite. The geological drill-hole database provided by MHAG Company clear indicates volcanic input, both mafic and felsic in the area.

The extended interpretation of the  $Al_2O_3+TiO_2$  -  $CaO+K_2O$  -  $MgO$  diagram to the typological model presented by Fonteles *et al.* (2018) supports the aforementioned lithostratigraphic concept. In Figure 52 the REE data for the BIF types were extracted from a study by BARBOSA (2013).



## 7 MINERALIZED THICKNESS MODELING BASED ON GEOSTATISTICAL ANALYSIS<sup>4</sup>

The primary focus of this study is to enhance the geometric feature of the mineralized thickness and to discuss its geological significance in terms of structural control as a starting point to a metallogenic model. Hence, this study shall not be as conclusive as a three-dimensional (3-D) geological model. Meanwhile, mapping the mineralized thickness may yield quicker information concerning the most interesting mining spots with known Fe<sub>2</sub>O<sub>3</sub> grade range in a mining site.

To achieve the goals proposed in this study, geostatistical estimation and simulation methods were employed. Although the “best” method to achieve the expected results is not the primary aim of this study, few experiments must be performed to improve the analytical tasks involved (BOUFASSA; ARMSTRONG, 1989; DEUTSCH, 1992; JOURNAL, 1994; GOOVAERTS, 1998; SOARES, 2001; PARAVARZAR *et al.* 2015).

In this study, a geostatistical map of mineralized thickness is presented. When using the *mineralized thickness* as a regionalized variable, linking it to a topographic reference is dismissible. This allows for ore resources evaluation to be performed without the ambiguity of elevation data absence.

### 7.1 Geological database and analytical tools

The database used in this study is from a survey on a previous BIF typological model based on geochemical composition and petrographic content (FONTELES *et al.* 2018). Among the proposed typological schemes, four BIF types were pre-selected owing to their Fe<sub>2</sub>O<sub>3</sub> grades; subsequently, a survey was performed throughout the entire ore typological model to extract the available thickness data values measured in meters from the core logs (Figure 53).

The geochemical data were exploited from a major geological databank that has been structured to gather data and information depicted from an exhaustive exploratory drilling program supporting mining studies in the research site.

It is noteworthy that not all drilling boreholes have reached the mineralized strata owing to the geological setting of the mine site. Therefore, from 126 drilling cores, we could analyze 78 that constitute the BIF types of interest.

---

<sup>4</sup> This chapter takes part of an original manuscript submitted (*under review* status) to the *Journal of South American Earth Sciences* in July/2019.

From a geochemical perspective, hematitic itabirites, magnetitic itabirites, and martitic itabirite represent ore types with 44.61% Fe<sub>2</sub>O<sub>3</sub> mean grade and were used to provide the geostatistical input data.

No prior mathematical transformation was applied to the original data in order to produce the results shown in the following sections. The necessary data transformations were executed during the simulation procedures.

Regarding the study area, four types were described and identified. In this study, three of them were considered, as their Fe<sub>2</sub>O<sub>3</sub> content exhibit petrographic and geochemical relevance (as already defined in section 3 of this study). Table 22 summarizes the Fe<sub>2</sub>O<sub>3</sub> mean grades of each type.

Table 22 – Itabirites Fe<sub>2</sub>O<sub>3</sub> mean grades.

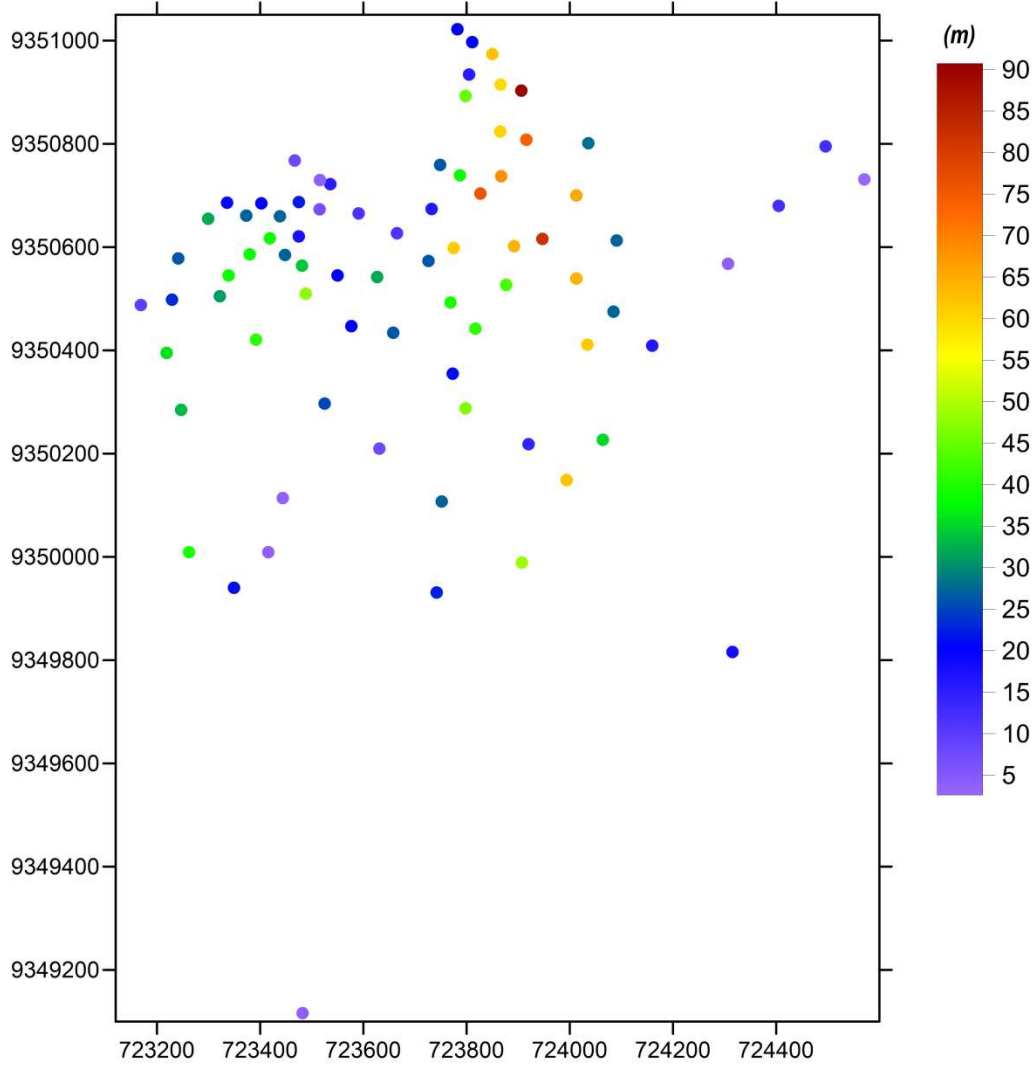
<b>BIF type</b>	<b>Fe<sub>2</sub>O<sub>3</sub> mean grade (%)</b>
Hematitic Itabirite	46.32
Magnetitic Itabirite	37.45
Martitic Itabirite	40.68

Source: Elaborated by the author.

## 7.2 Exploratory analysis

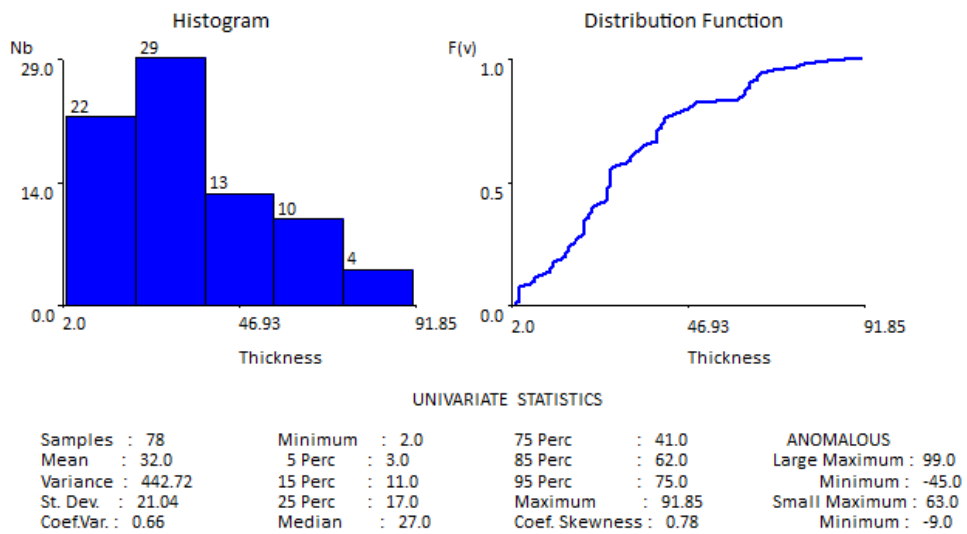
Exploratory data analysis revealed a positively skewed pattern histogram that does not fit a Gaussian probability function model (Figure 54). Although no further statistical tests were considered, the data distribution function clearly indicates that more than one geostatistical estimation method can be applied.

Figure 53 – Location map for data points (Color scale expressed in meters).



Source: Elaborated by the author.

Figure 54 – Mineralized thickness basic descriptive statistics and related graphs.



Source: Elaborated by the author.

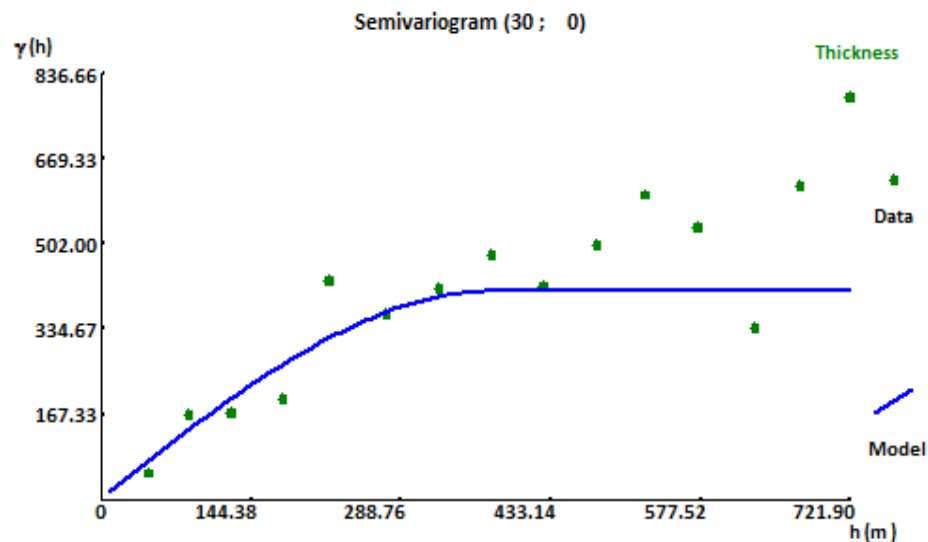
Spatial variance patterns were explored through variographic analysis to model the sample spatial dependency. After several attempts, two experimental directional semivariograms were constructed capturing spatial variance structures related to 30° Az and 300° Az (or -60, by software default). The 30° Az structure shows a longer data spatial continuity through that direction compared with its orthogonal component (300° Az). This pattern is crucial in the definition of the ellipsoid search parameters in kriging and simulation procedures (Figures 55 and 56).

The experimental semivariograms were both fitted to spherical models represented by the following models:

$$\left\{ \begin{array}{l} \gamma(h)_{30\text{ Az}} = 3.35 + 404.94 \left[ 1.5 \left( \frac{h}{374.94} \right) - 0.5 \left( \frac{h}{374.94} \right)^3 \right], \text{ if } h < 374.94\text{m} \\ \gamma(h)_{30\text{ Az}} = 408.29, \text{ if } h \geq 374.94\text{m} \end{array} \right.$$

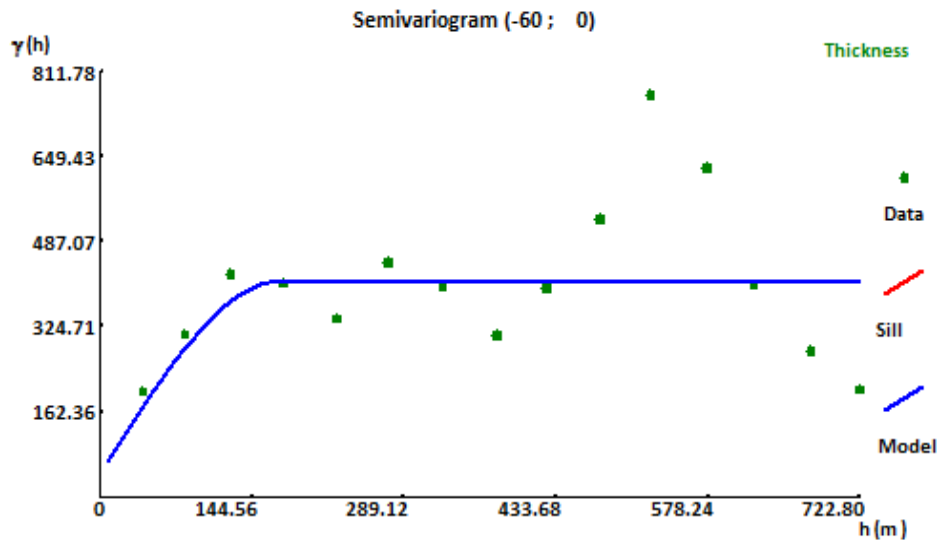
$$\left\{ \begin{array}{l} \gamma(h)_{300\text{ Az}} = 41.88 + 365.55 \left[ 1.5 \left( \frac{h}{171.21} \right) - 0.5 \left( \frac{h}{171.21} \right)^3 \right], \text{ if } h < 171.21\text{m} \\ \gamma(h)_{300\text{ Az}} = 410.43, \text{ if } h \geq 171.21\text{m} \end{array} \right.$$

Figure 55 – Adjusted experimental semivariogram modeled along the direction 30°Az.



Source: Elaborated by the author.

Figure 56 – Adjusted experimental semivariogram modeled along the direction 300 °Az (-60, by software default).



Source: Elaborated by the author.

### 7.3 Estimating the mineralized BIF rocks thickness

The irregular sample spacing shows that some sectors were more densely drilled than others (Figure 53). An average sample distance of 49 m was measured to aid the estimation/simulation gridding design. Thus, the size of the square grid-spacing was set to

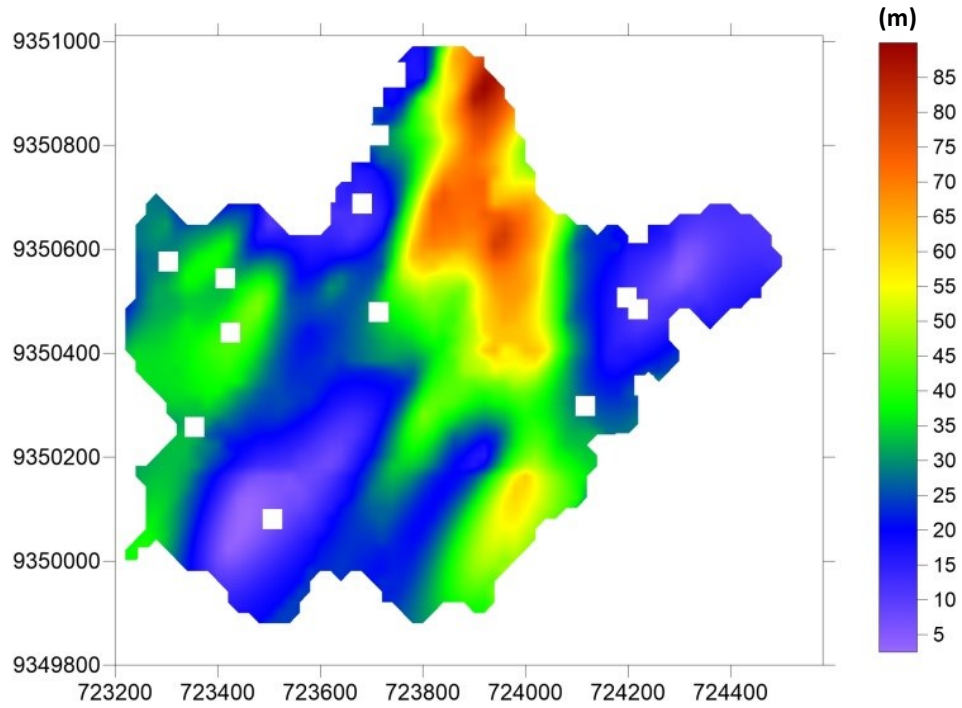
20 m  $\times$  20 m. The moving search ellipsoid was configured to consider the variographic anisotropic range. As mentioned previously, the dataset comprises absent thickness values that are positioned as blanked squares indicating that no estimation or simulation was performed. A total of 4,406 blocks were estimated.

To minimize edge effects, a minimum of four points and a maximum of eight were selected within the search radii. This avoids the unnecessary extrapolation far beyond the geological boundaries of the BIF of the Serra dos Quintos Formation. Furthermore, the geological contact between the BIF and other lithologies was used to mask out the estimation/simulation border (See Figure 15 for reference).

The first round of geostatistical modeling was initiated with ordinary kriging (OK) and simple kriging (SK) estimations (Figures 57 to 60). For both estimation methods, kriging variances were computed and displayed. OK estimates were processed based on unknown global mean and second-order stationarity. Meanwhile, SK estimates were obtained by considering the arithmetic mean (see Figure 54 for reference) as the global mean and

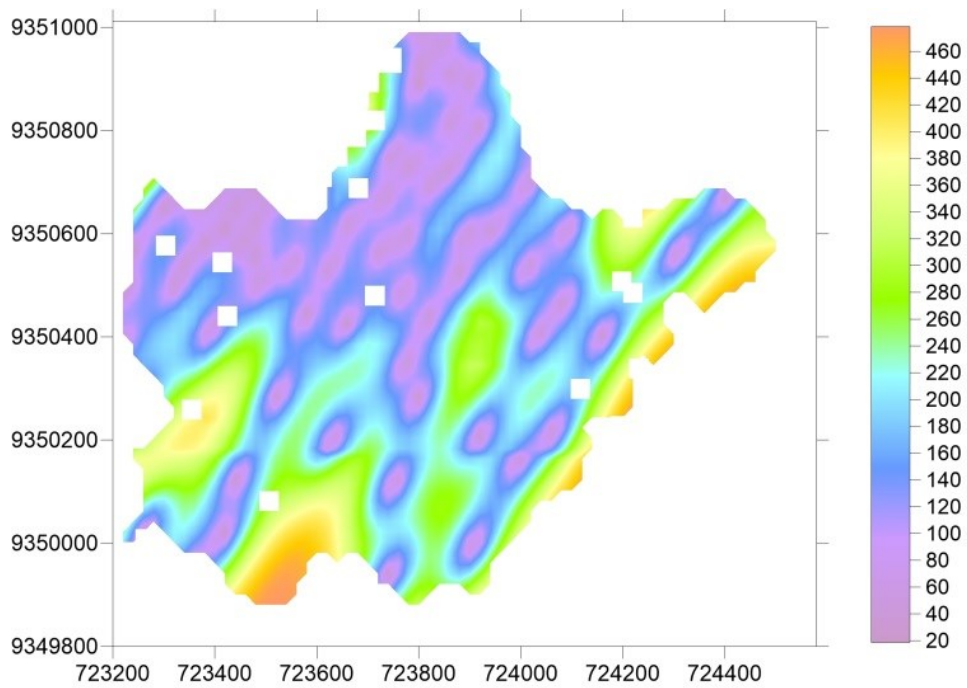
assuming a non-second order stationarity condition. The results are displayed in Figures 57 and 58.

Figure 57 – Ordinary kriging estimates map. Blanked-off squares are related to absent data points.



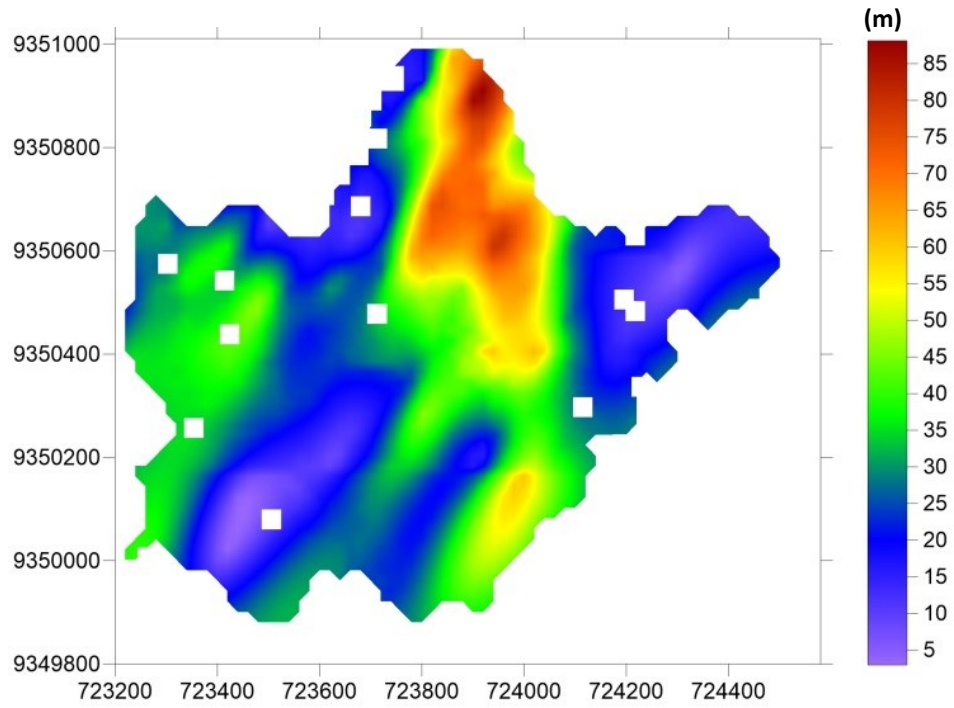
Source: Elaborated by the author.

Figure 58 - Ordinary kriging variance map. Blanked-off squares are related to absent data points.



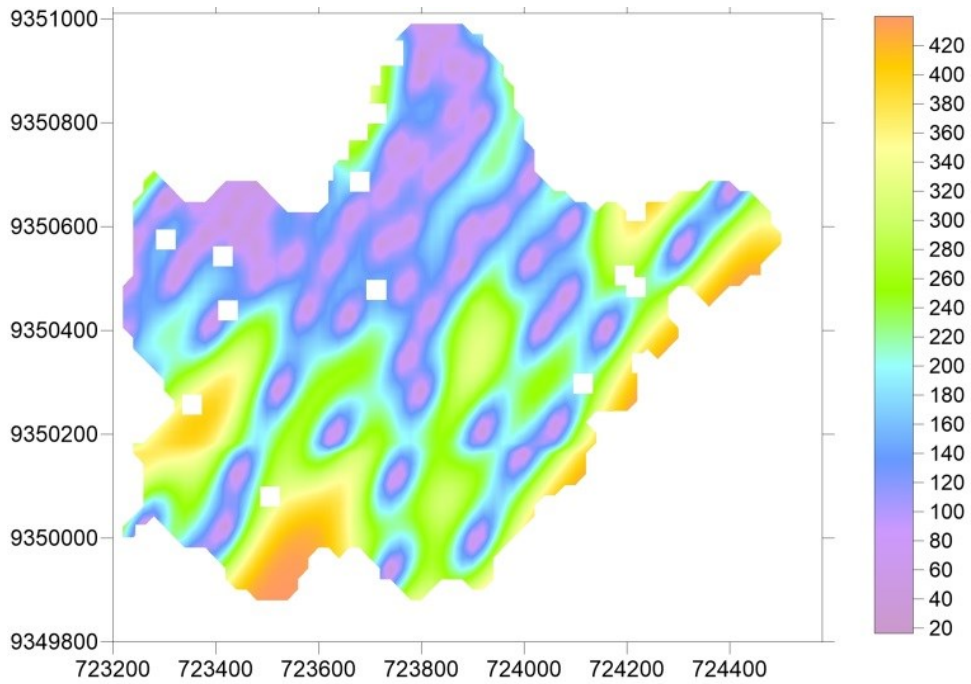
Source: Elaborated by the author.

Figure 59 – Simple kriging estimates map. Blanked-off squares are related to absent data points



Source: Elaborated by the author.

Figure 60 – Simple kriging variance map. Blanked-off squares are related to absent data points.



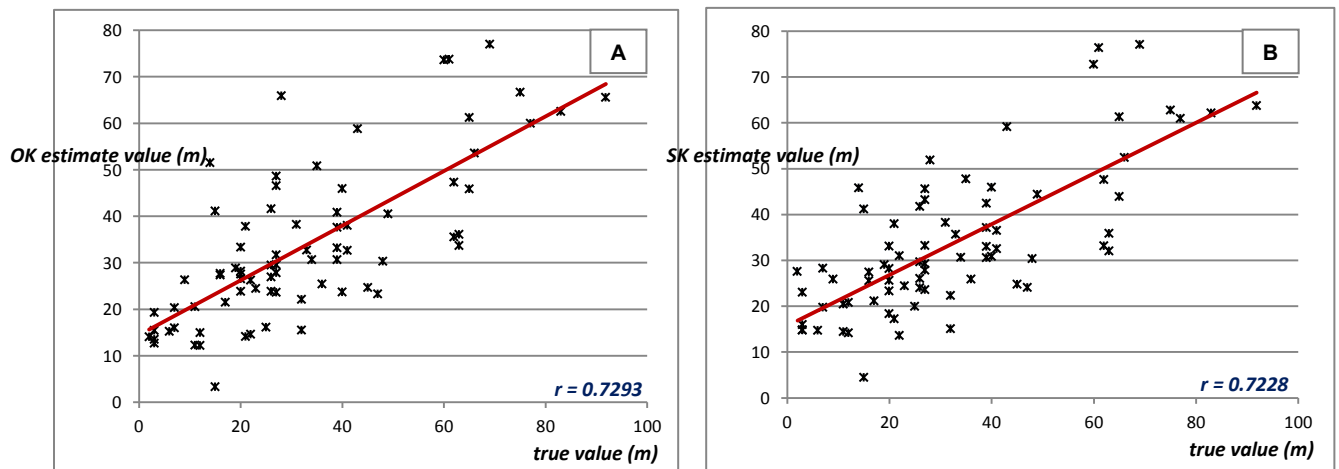
Source: Elaborated by the author.

According to Deutsch and Journel (1992) and Goovaerts (1997), in the SK estimation technique, the global mean is embedded within its formulation, thus allowing the mathematical expectation to be incorporated. The SK approach was selected as an alternative linear solution to the traditional OK estimation method (Figure 59 and 60).

The outcomes from the SK estimation are highly similar to OK estimates. Despite introducing the global mean, it is noteworthy that no relevant differences were found in the results of both geostatistical interpolation methods.

Cross-validation tests unveiled that the correlations between thickness true values and their estimates (for both methods) are statistically identical (Figure 58). Pearson's correlation coefficients for cross-validated OK and SK estimates are equal. Furthermore, the SK estimates are smoothed and the SK variances are slightly minor on the top values (Figure 61).

Figure 61 – Cross-validation scattergrams for OK estimates (A) and SK estimates (B). One can note that the difference between  $r$  values from kriging procedures is almost irrelevant.



Source: Elaborated by the author.

Kriging variances maps in accordance with the classical Regionalized Variables Theory formally presented by Matheron (1963, 1965) well represent minimized squared differences that tend to increase in sectors with low sampling, as already discussed by Journel (1974) and Yamamoto (2000). Lower kriging variance values are closely associated to sample spots; conversely, the higher ones are related to the unsampled sites.



#### 7.4 Geostatistical conditional simulations

To improve the thickness spatial model, some stochastic simulation methods were selected and examined. In this study, 100 realizations were generated. The exception was the SA that was handled as a post-processor DSS simulated images. All simulations were performed under the conditioning of the original thickness data.

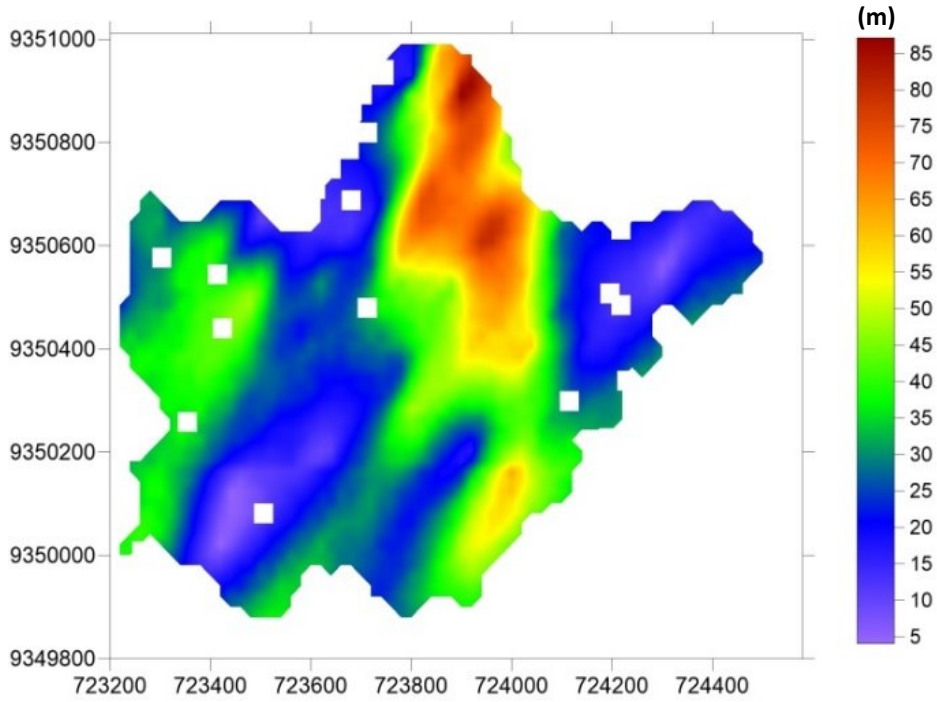
The same 20-m grid scheme applied to kriging estimation was used to simulate the stochastic images. Although this study is not necessarily devoted to comparing geostatistical estimation and simulation methods, an exploratory approach was used to expand the possibilities of modeling the BIF mineralized thickness of the Bonito Mine. For the SGS and DSS, we obtained E-type and M-type composite mineralized thickness images based on simple kriging algorithms (DEUTSCH; JOURNAL, 1992; GOOVAERTS, 1997).

Among hundreds of realizations, five stochastic images (for each method) were randomly selected and analyzed in terms of their basic statistics. Some of these results indicate a complete reproduction of the original histogram and descriptive statistics as demonstrated by realizations SGS #11 and DSS #79 (CAERS, 2000; SOARES, 2001; LEUANGTHONG *et al.* 2004). Nevertheless, a stochastic simulation image describes one conditional probabilistic scenario among many others.

If multi-Gaussianity cannot be assured, DSS was chosen to address a skewed data histogram, with the advantage of no data anamorphosis in advance (Figure 54). Theoretical proofs and practical examples have provided by Caers (2000) and Soares (2001) regarding spatial data simulations indicating that variables with non-Gaussian distributions can be modeled. Although a single realization can be used to reproduce the basic statistics of the original database, average images tend to present smoothed data amplitudes (Table 23).

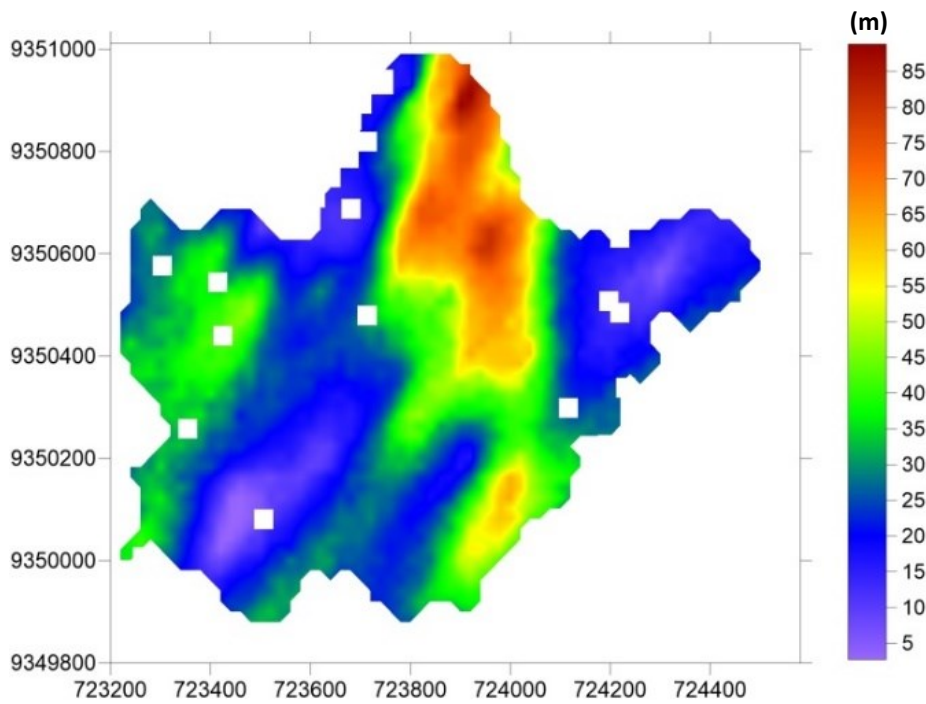
As exhibited in figures 62 and 63, the E-type and M-type estimated images were obtained from the 100 DSS realizations. Both of them present overestimated low values and underestimated high values. Figure 62 presents the overestimated statistical parameters listed in table 23 in comparison to those related to the original thickness data.

Figure 62 – E-type mineralized thickness map after 100 DSS realizations. Blanked-off squares are related to absent data points.



Source: Elaborated by the author.

Figure 63 – M-type mineralized thickness map after 100 DSS realizations. Blanked-off squares are related to absent data points.



Source: Elaborated by the author.

To adjust the global data accuracy to the local exactitude, the optimization algorithm embedded in SA was used to post-process the DSS M-type output data. Following a basic idea of the method, an initial image (the training image) was perturbed by swapping one data pair at a constant temperature with a reducing factor of 0.01 from the initial temperature ( $T = 1$ ) during 25.000 iterations.

This method allows for the simulation of a quenching process where one pair of data points at one time is swapped until the number of iterations is reached. The entire process is mathematically forced by the algorithm constraining the local data (original data values) to match the local simulated values on their grid positions.

To validate the SA simulated image, we constructed new semivariograms modeling the spatial variance of this stochastic realization. The research window was the same as that used in the prior variographic exploratory analysis (see section 7.3). As suggested by Leuangthong et al. (2004), the SA data histogram was obtained and indicated that not all descriptive statistics were reproduced; however this is considered acceptable because it represents the summarization of all 100 stochastic realizations accumulated previously by DSS (Table 23; Figures 64, 65 and 66) The mineralized thickness map generated by SA is illustrated in Figure 67.

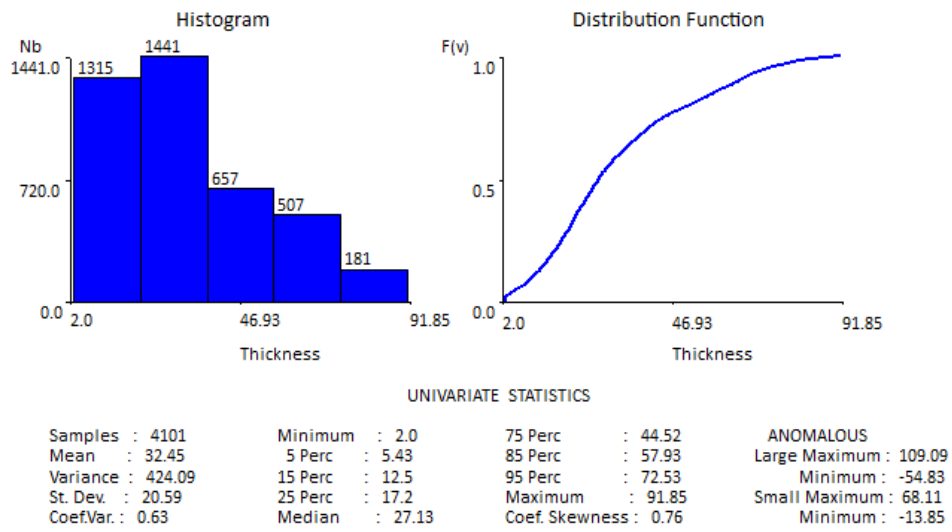
Table 23 – Comparative statistical summary of the estimation and simulation output data.

<b>Data source</b>	<b>Mean</b>	<b>Median</b>	<b>Min.</b>	<b>P<sub>25</sub>*</b>	<b>P<sub>75</sub>*</b>	<b>Max.</b>	<b>Variance</b>	<b>C.V.*</b>
Thickness	32.00	27.00	2.00	17.00	41.00	91.85	442.72	0.66
OK	28.32	25.94	2.50	18.83	34.46	89.97	213.99	0.52
SK	30.86	31.32	2.96	24.10	33.01	88.12	161.12	0.41
SGS #11	32.02	27.00	2.00	17.86	41.00	91.85	416.97	0.64
SGS #42	29.69	26.00	2.00	15.00	39.77	91.85	463.76	0.66
SGS #63	32.32	27.00	2.00	17.30	42.17	91.85	427.45	0.64
SGS #82	27.43	23.71	2.00	12.00	39.00	91.85	404.65	0.73
SGS #95	31.88	27.00	2.00	18.05	40.01	91.85	419.95	0.64
SGS E-type	30.18	29.89	2.50	22.18	34.52	86.77	183.61	0.45
SGS M-type	27.67	26.30	2.41	20.00	30.64	89.44	201.40	0.51
DSS #8	31.98	28.04	2.00	18.88	42.35	91.85	339.93	0.58
DSS #33	31.82	27.84	2.00	17.00	43.56	91.85	401.93	0.63
DSS #54	31.82	27.25	2.00	17.45	43.82	91.85	396.43	0.62
DSS #79	32.09	26.99	2.00	17.28	43.82	91.85	421.22	0.64
DSS #91	32.47	27.16	2.00	17.19	44.57	91.85	425.33	0.63
DSS E-type	33.34	30.51	4.03	22.22	42.28	87.15	261.56	0.48
DSS M-type	32.50	27.91	2.71	20.71	40.20	88.83	287.96	0.52
SA	32.45	27.13	2.00	17.20	44.52	91.85	424.09	0.63

\*P<sub>25</sub> - 25%; P<sub>75</sub> - 75%; C.V. - coefficient of variation.

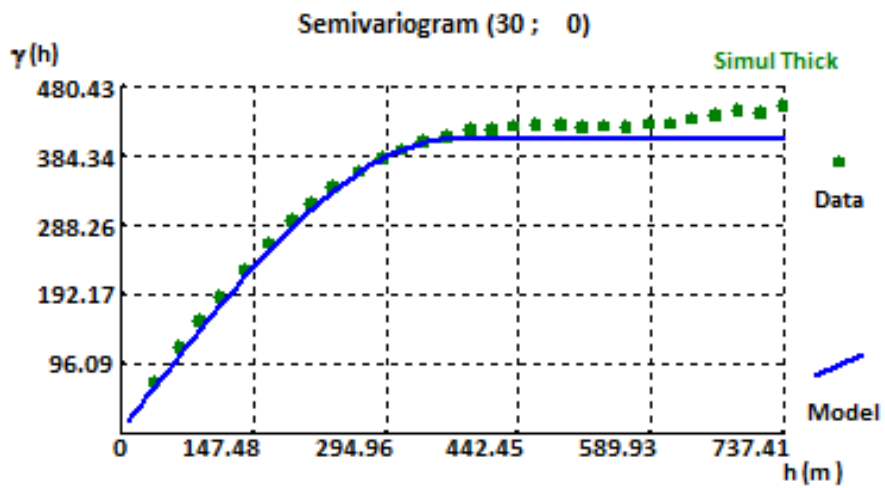
Source: Elaborated by the author.

Figure 64 – Conditional histogram and distribution function of simulated BIF ore mineralized thickness in the study area reproduced by simulated annealing.



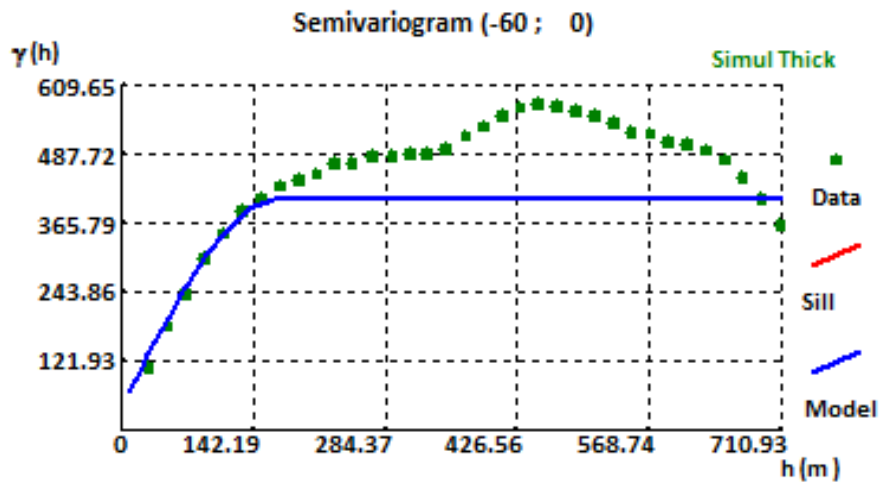
Source: Elaborated by the author.

Figure 65 – Adjusted semivariogram model of simulated BIF ore mineralized thickness values by simulated annealing method (30°Az direction).



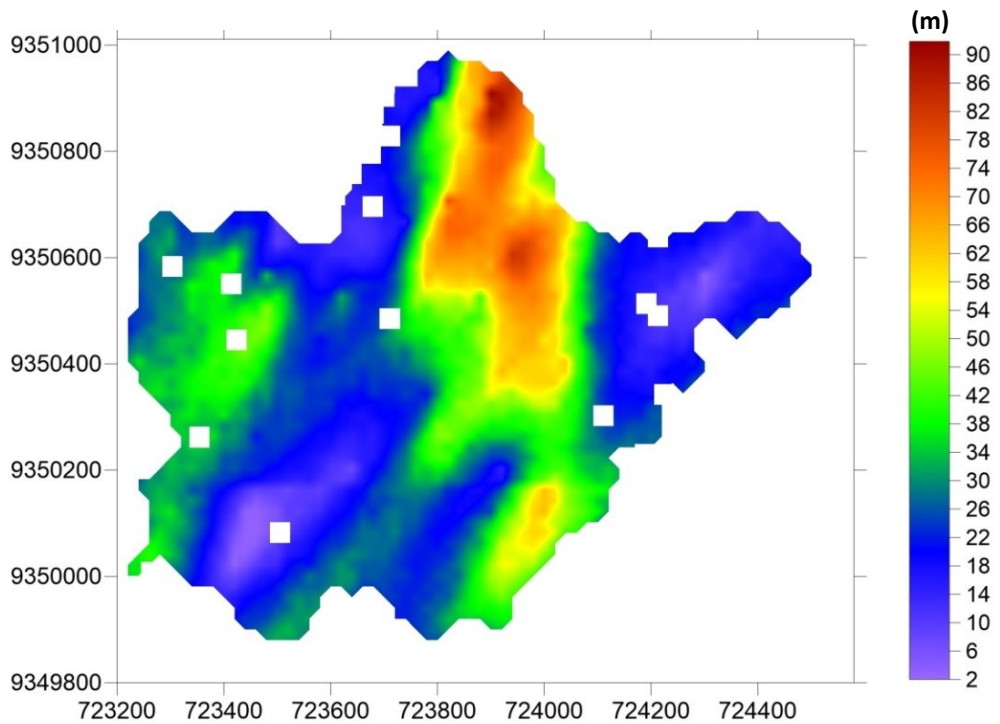
Source: Elaborated by the author.

Figure 66 – Adjusted semivariogram model of simulated BIF ore mineralized thickness values by simulated annealing method (300°Az direction).



Source: Elaborated by the author.

Figure 67 – Mineralized thickness map based on SA simulation. Blanked-off squares are related to absent data points.



Source: Elaborated by the author.

## 7.5 Discussion

The positively skewed histogram has revealed a possible data trend. In the first round of geostatistical analysis of the mineralized thickness, an alternative estimation method to the traditional OK was adopted. Thus, SK was selected to assess the mineralized thickness.

In the second-order stationarity model for natural phenomena, the high nugget effect on semivariograms tends to contribute to smooth kriging estimates. However, this does not apply to the case of the mineralized thickness data. Cross-validation tests have shown acceptable estimation outcomes; nonetheless, the smoothing effect was still noticeable.

OK estimates, as clearly reported by Boufassa and Armstrong (1989) and Yamamoto (2000, 2008), are smoothed (Table 23). In this particular case, theoretical semivariogram models were tested (spherical, exponential and Gaussian) to obtain less smoothing estimation results such that the spherical model yielded the best fit.

Gaussian models were interactively adjusted to the experimental semivariogram. Nevertheless, they produced unrealistic negative kriged thickness values. The exponential model provided slightly smoother estimates than the spherical model.

SGS is widely used on the stochastic modeling of natural resources, as mentioned previously. In this study, owing to this broad appeal, we performed a conditional simulation of 100 realizations. Although some images reproduce almost the same statistical parameters (Table 23), the E-type and M-type estimations disclose far deviated values from those of the target histogram. As shown, those estimated images suffered from the undesirable smoothing effect.

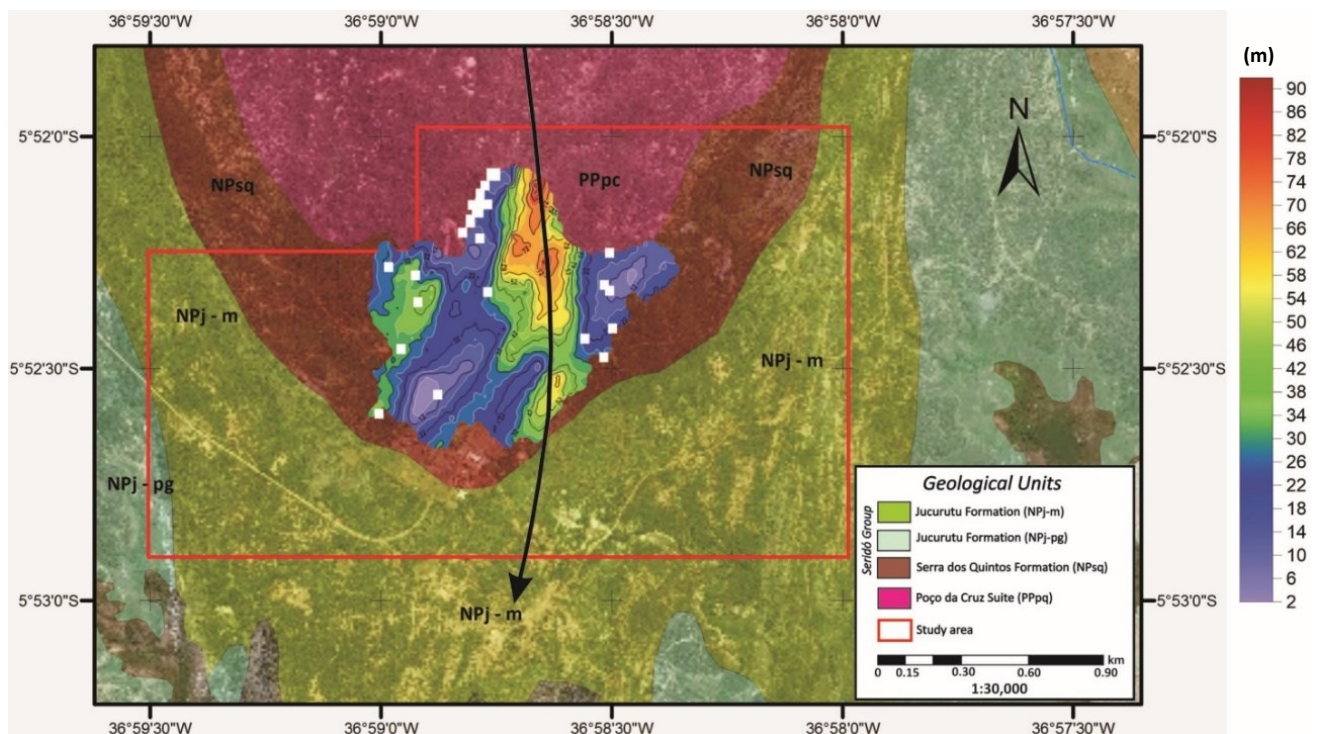
As observed in SGS estimations, DSS E-type and M-type estimated images presented the same feature. However, DSS exhibits an improvement owing to the implementation of local correction for deviations on the global mean and variance (Soares, 2001). As shown, the DSS M-type estimated image provided closer figures to mineralized thickness descriptive statistics.

The DSS M-type image was used as a training image to be perturbed in SA. Once the primary statistical features were acceptably reproduced, using an equal direction component weighting improved the stochastic simulation. Furthermore, the scheme used allowed for the local raw data to be perturbed (Deutsch and Cockerham, 1994).

The upgraded stochastic image of the mineralized thickness exhibited that the thicker mineralized BIF rocks could match to a fold axis of an antiform heading south. The Seridó Group is a prominent geological window to a major tectono-metamorphic event,

namely, the Brasiliano/Pan-African event that has promoted intense granitic uplifting, tangential tectonics and folding in Neoproterozoic Era. Folding during the Brasiliano/Pan-African tectonic event has compressed the BIF ore mass concentrating it in that area (Figure 68).

Figure 68 – Mineralized thickness map constrained to the geological boundaries of the Serra dos Quintos Formation (NPsq). The black arrow heading south shows the antiform's fold axis. Blanked-off squares are related to absent data points. Acronyms list: NPsq - Serra dos Quintos formation/BIFs; NPj-m - Jucurutu Formation/marble; NPj-pg - Jucurutu formation /paragneiss; PPpc - Poço da Cruz suite/gneiss.



Source: Adapted geological map after Angelim et al. (2006).

## 8 TRIDIMENSIONAL GEOLOGICAL MODELING OF THE BONITO MINE

The ‘voxel’ jargon is a contraction of “volumetric pixel” terms denoting the tridimensional unit related to a specific attribute (JESSEL, 2001; CATARINO, 2009; TONINI *et al.* 2009; JØRGENSEN *et al.* 2013; VAN MAANEN *et al.* 2015; RASKA, 2017). In this study, the analyzed attribute is the lithology described in the core logs. The modeled solid integrates all voxels representing all the previously identified lithotypes. The method uses the Nearest Neighbor algorithm through the horizontal lithoblasting to produce a discrete solid model.

Voxel modeling was the applied method for the geomodeling of the Bonito Mine site. The software package RockWorks<sup>®</sup>16 (ROCKWARE, 2017) was applied to borehole data management and lithological modeling. Extensive explanation and documentation can be consulted in the RockWorks<sup>®</sup>16 manual (ROCKWARE, 2017) and in some available scientific references (CATARINO, 2009; ALMEIDA, 2011; JØRGENSEN *et al.* 2013; RASKA, 2017)

Meanwhile, voxel modeling does not produce solid models with high spatial continuity and smoothed surfaces separating the modeled lithotypes. The lithological units are formed of similar geometrical blocks considering the properties of each block (voxel) as a basic construction unit of the modeled lithology.

The geometrical model is geographically constrained by the tridimensional grid with XYZ coordinates and referred to the UTM geodetic data and to the elevation values of each borehole (Table 24). Therefore, 2,731,040 grid-nodes were generated. The horizontal 20m x 20m grid followed the previous geostatistical study focused on mineralized thickness mapping (Chapter 7).

Table 24 – Gridding parameters applied to the geological modeling of the Bonito deposit.

<b>Coordinate</b>	<b>Minimum</b>	<b>Maximum</b>	<b>Spacing (m)</b>	<b>Nodes</b>	<b>Range (m)</b>
UTM North (X)	722,160	725,334	20	160	3,174
UTM East (Y)	9,349,100	9,351,100	20	101	2,000
Elevation (m)	-424.00	415.00	5	169	839

Source: Elaborated by the author.

According to the extracted data from the geological database, 16 rock types were recognized, as shown in Table 25. For each rock type, a code-value known as “g-value” was



assigned to it, identifying the lithotypes. Although the lithological assemble was modeled, some rock types will not be visible owing to their interbedding characteristics. Lithotypes such as quartzite, volcanic basic and acidic rocks and amphibolite have been modeled separately, as shown in section 8.1.2.

### 8.1 3-D geologic model of the bonito mine site

#### 8.1.1 Solid Modeling

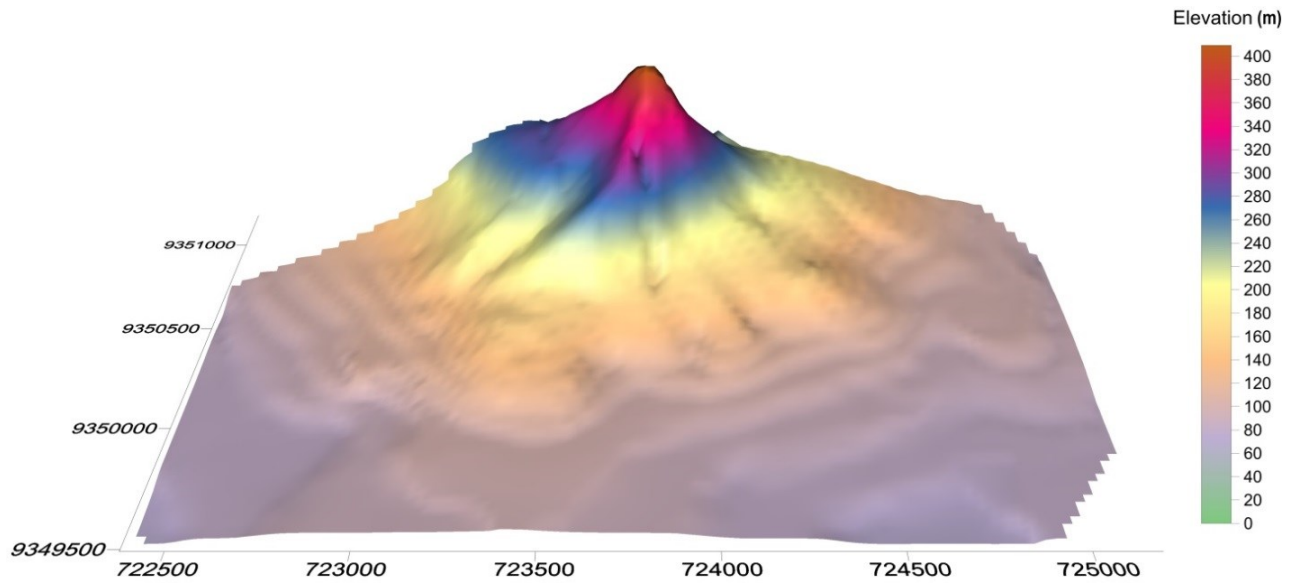
To generate a proper geologic model, a digital elevation model (DEM) was drawn. Not only for terrain visualizations purposes the DEM was created, but also as a fundamental piece for the geologic model constraining. (Figure 69). The geometric dimensions of the DEM match the same parameters used in the geological modeling. This is a *sine qua non* condition to perform the lithology modeling task. Inverse distance squared (IDS) algorithm from the inverse distance weighted (IDW) family as employed to perform the DEM interpolation as an appropriate method (FONTELES, 2003).

Table 25 – Lithological units used to generate the geological model of the research site.

<b>Lithology</b>	<b>Brief description</b>	<b>Symbol</b>
Soil	Unconsolidated sand with silt and clay.	SO
Colluvium	Moderately to well-consolidated silt, sand, and diverse size rock blocks.	CO
Amphibolite	Metamorphosed basic rock; gray to green colored.	AMB
Ferruginous quartzite	Metachert with iron minerals.	FEQ
Marble	Metacarbonatic rock based on dolomitic composition.	MAR
Gneiss	Augen leuco-ortogneiss and paragneiss	GNS
Schist	Actinolite-schist and garnet-tremolite schist	SCT
Phyllite	Metapelitic composed of quartz and sericite.	PHY
Quartzite	Metamorphosed psammitic rock.	QTZ
Quartz vein	Tabular quartz body.	QV
Itabirite	BIF rocks mainly formed of martitic, amphibolitic, hematitic and magnetitic itabirites.	ITB
Mylonite	Highly deformed felsic rock.	MYL
Intrusive acidic	Quartz-monzonitic to granitic rocks.	INA
Intrusive mafic	Interbedded mafic rock	INB
Volcanic acidic	Interbedded felsic rock	VA
Volcanic mafic	Interbedded mafic rock	VB

Source: Elaborated by the author.

Figure 69 – DEM of the research site executed by the IDS interpolation method. (south view).



Source: Elaborated by the author.

During the drilling program executed by MHAG Company, the previous geologic knowledge of the area has shown that some drill holes were located to extract the best data owing to the geological features. The structural delineation of the mining area is consistent with the regional trend exhibited in major folds in the Seridó Belt (SÁ, 1994; HACKSPACHER, *et al.* 1997; ANGELIM *et al.* 2006 – See Annex: Lithologic Map for reference). Figure 70 displays the boreholes' spatial distribution in the Bonito Mine.

For lithology modeling, Rockworks<sup>®</sup>16 software package allows the user to choose two different modeling algorithms: closest point and lithoblending. The closest point method calls for setting a radius distance among the boreholes (lithotypes included) and then interpolate the geometrical structure.

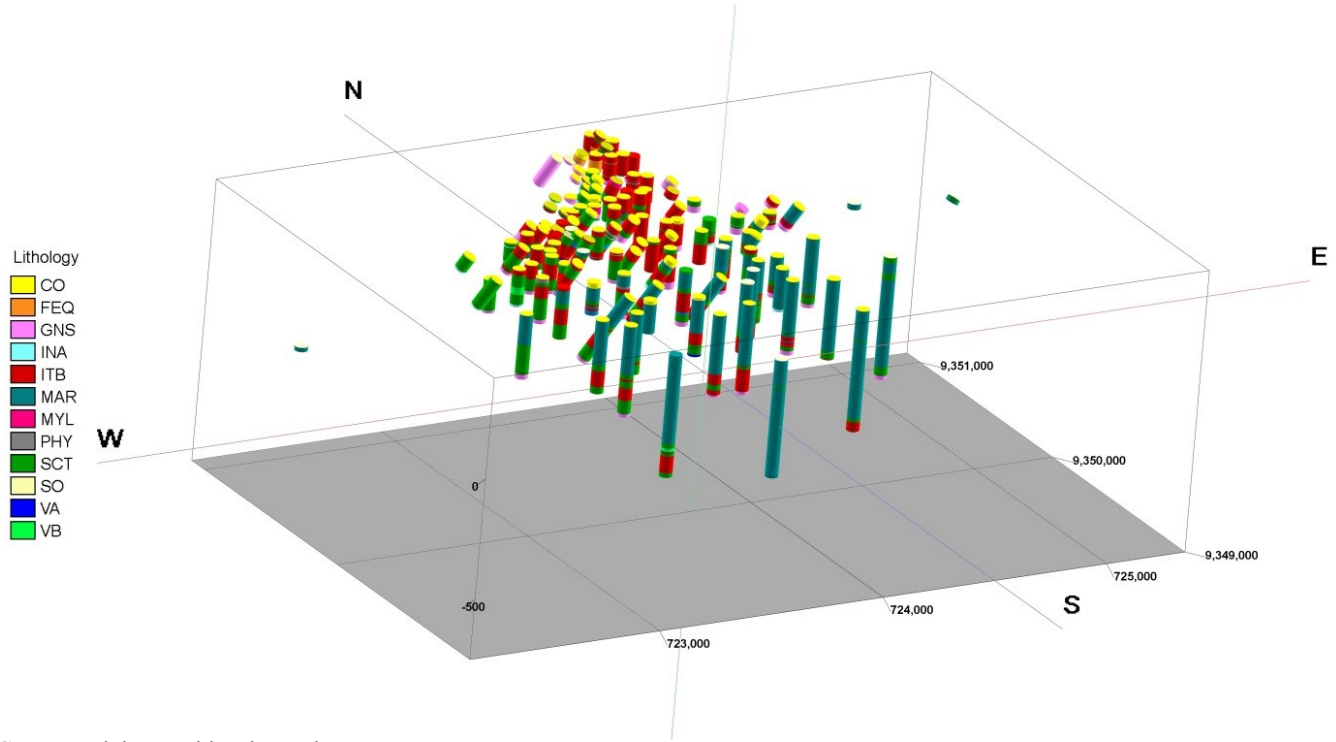
The output model was formed of joint “muffin-like” lithological agglomerates with limited continuity among them. With such an algorithm, a structural constraint cannot be modeled as well. The lithological strata became horizontal despite the drilling orientation.

Lithoblending method is based on the Nearest Neighbor algorithm that interpolates the geometry between similar lithotypes despite the distance. Creating a voxel model for sedimentary deposits, this method is highly recommended. To build a more realistic geological model of the Bonito Mine, additional model constraints were applied.

The first constraint was warping the geological data to the DEM assuring that no interpolated lithology will extrapolate the terrain level. The second constraint relates to the

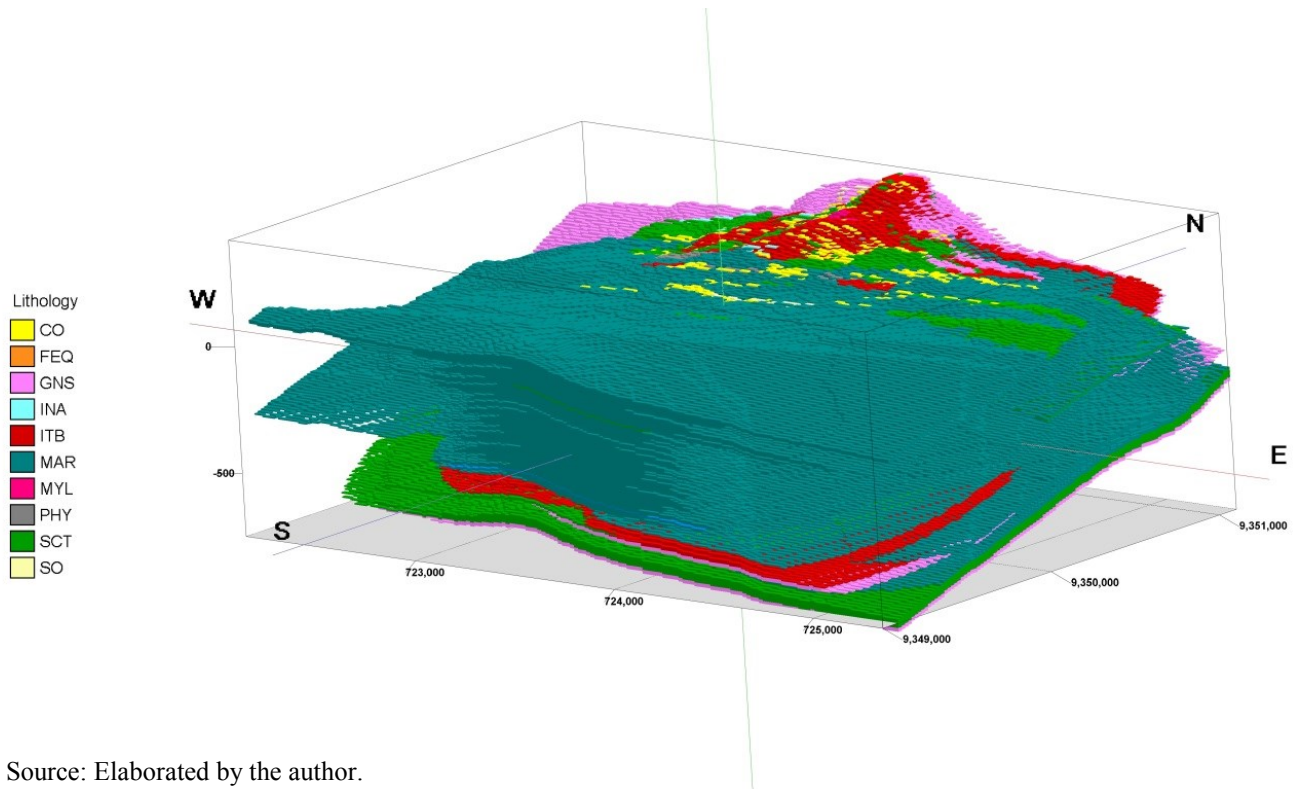
structural control of the lithology model, which is the average dip/strike data of the lithological package (“tilted modeling”) (Figures 71, 72 and 73).

Figure 70 – Spatial display (SW view) of the boreholes in the Bonito Mine site.



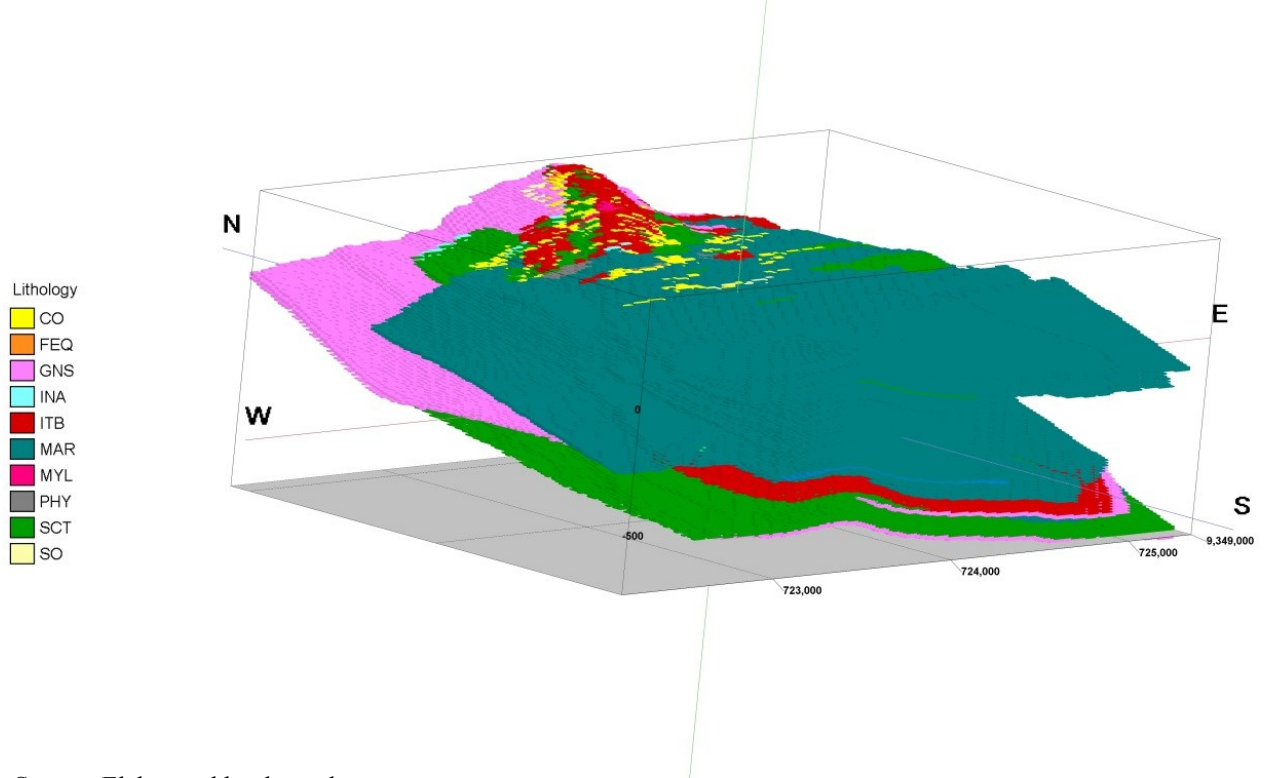
Source: Elaborated by the author.

Figure 71 – Lithologic 3D model of the Bonito Mine site (SE view).



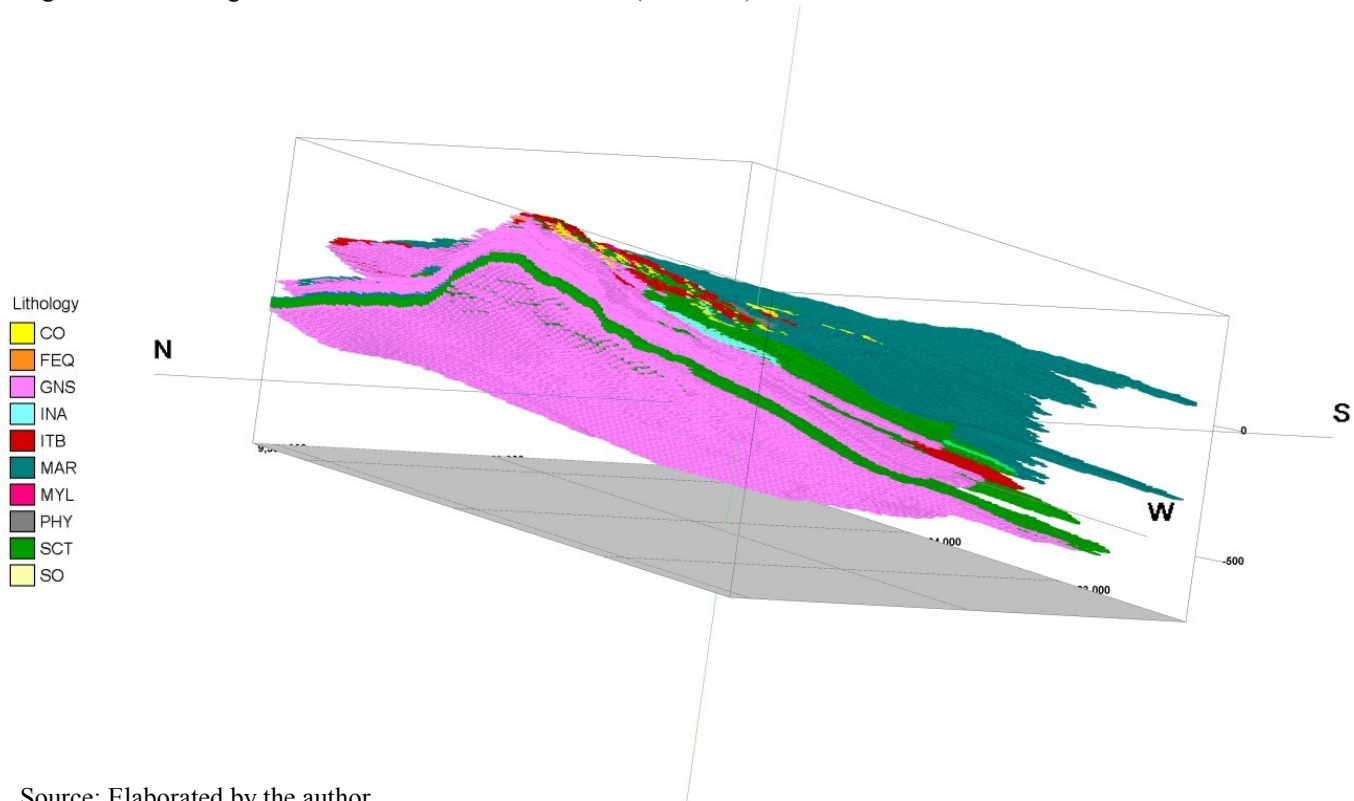
Source: Elaborated by the author.

Figure 72 – Lithologic 3D model of the Bonito Mine site (SW view).



Source: Elaborated by the author.

Figure 73 – Lithologic 3D model of the Bonito Mine site (NW view).



Source: Elaborated by the author.

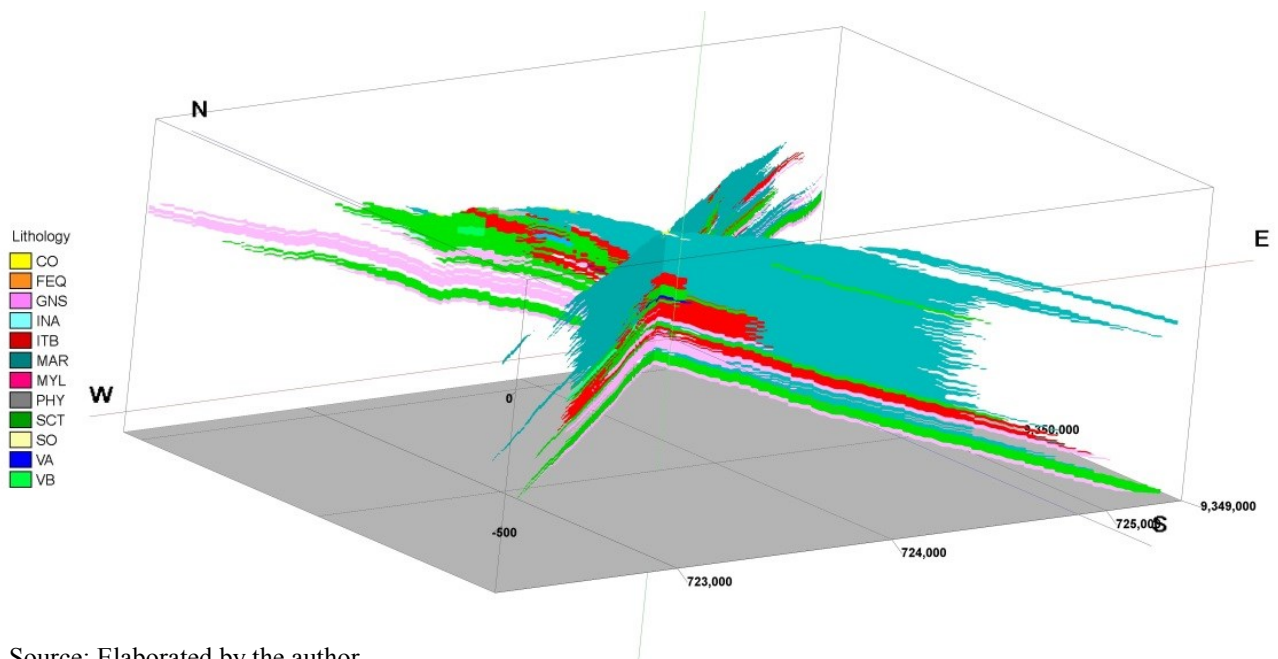
Figures 71, 72 and 73 clearly demonstrate the existence of an antiform fold, named in this study as the Bonito fold. The geostatistical analysis of the mineralized thickness has shown that the thicker zones correspond to the antiform's hinge zone.

Figure 73 shows the delineation of the uppermost part of this hinge zone. The folded strata owing to the visual pattern of the 3D model reveal the prominent folding of itabirites, gneiss, and schist. The fold axis is N-S orientated with a gentle plunge heading south. Geometrically, it appears to be a non-cylindrical fold.

Angelim *et al.* (2006) identified this fold occurring as a deformational feature of Poço da Cruz Suite (orthogneiss) and Serra dos Quintos (itabirites) and Jucurutu (paragneiss, marble, and schist) Formations of the Seridó Group.

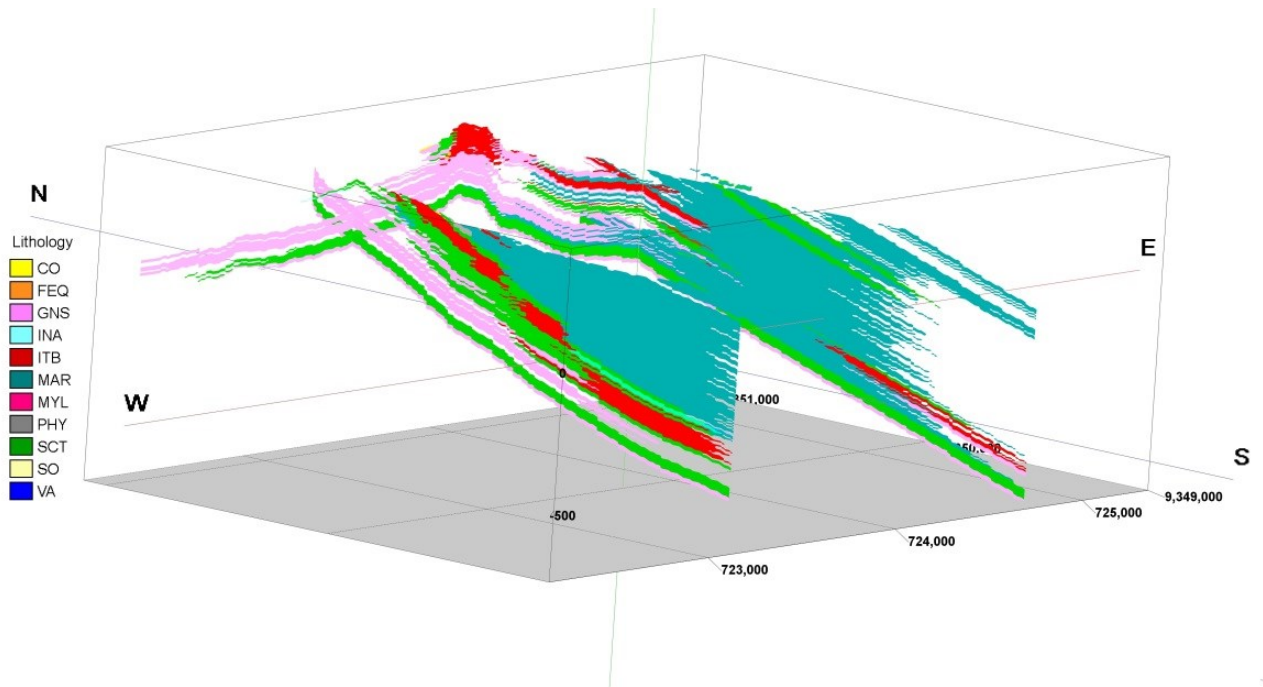
The lower gneiss layer is probably related to the Poço da Cruz Suite that occurs underlying the schist of the Jucurutu Formation (Figures 74 to 77). The geological database provided by MHAG Company does not address the stratigraphic positioning or correlations between lithological units. Therefore, the proposed lithology model, at this moment, cannot deliver complete answers to appropriate questions regarding the stratigraphic evolution of the metavolcano-sedimentary sequence.

Figure 74 – Lithologic fence model (SW view).



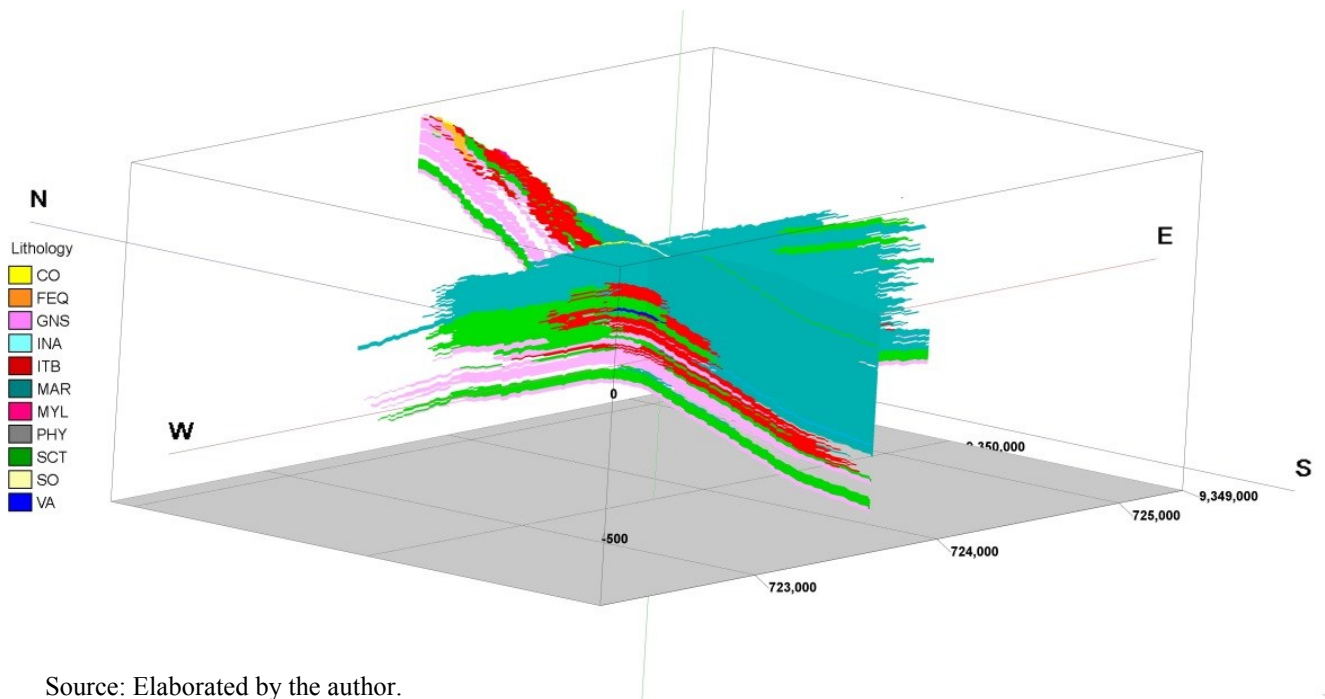
Source: Elaborated by the author.

Figure 75 – Lithologic double-cross-fenced model (SW view).



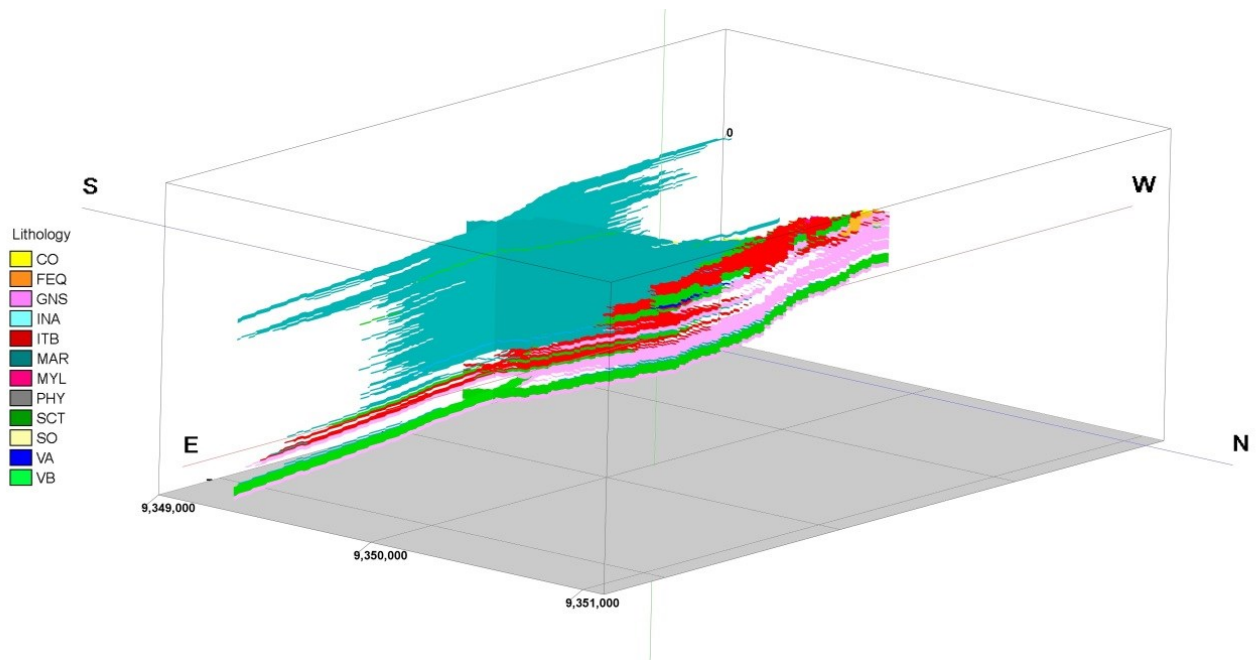
Source: Elaborated by the author.

Figure 76 – Lithologic cross-fenced model (SW view).



Source: Elaborated by the author.

Figure 77 – Lithologic T-fence model (NE view).



Source: Elaborated by the author.

### 8.2.2 3-D Isopach modeling

Owing to the fact that not all lithotypes have expressive volume, neither they have large exposed areas; volumetric models of each rock type were generated. The available approach to address this task was to create 3D isopach models.

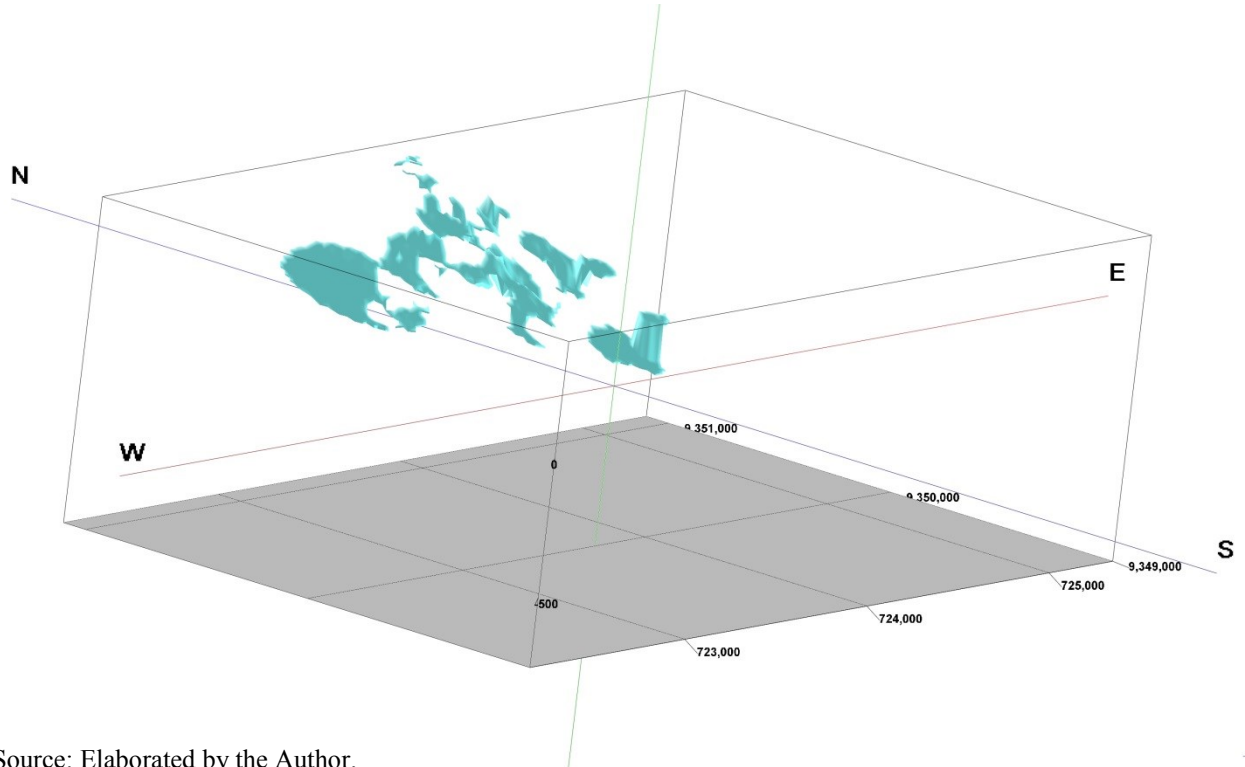
These models are based on the main lithology model (Figure 71) that provided the grid-data used to define the voxels from the uppermost occurrence of chosen lithology to the lowermost occurrence. The geometric solid of the designated lithotype will be displayed between these surfaces (ROCKWARE, 2017).

Although this modeling technique allows the rapid assessment of these small-volume lithotypes, such representation is not suitable to model large-volume lithologies, which may be interbedded with other different lithologies and appear inside the model (Figures 78 to 86).

The lithology model has revealed some relevant genetic aspects of the Bonito Mine. The association of volcanic rocks, both felsic and mafic could be related to the hydrothermal input to the sequence regarding the formation of Fe-skarn rocks and magnetitite (high iron grades) (BARBOSA, 2013). The Bonito fold becomes more apparent with some

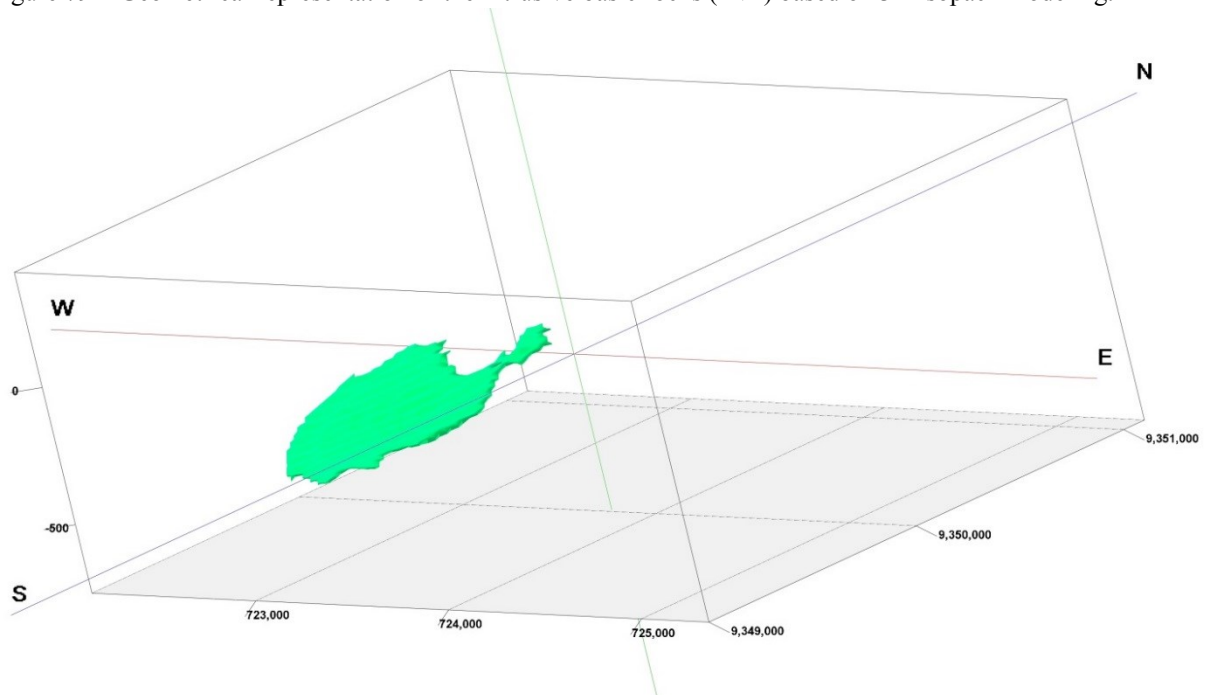
lithology models, such as the one presented in Figure 84 that shows the “bending” in the geometry of the quartzite.

Figure 78 – Geometrical representation of the intrusive acidic rocks (INA) based on 3D isopach modeling.



Source: Elaborated by the Author.

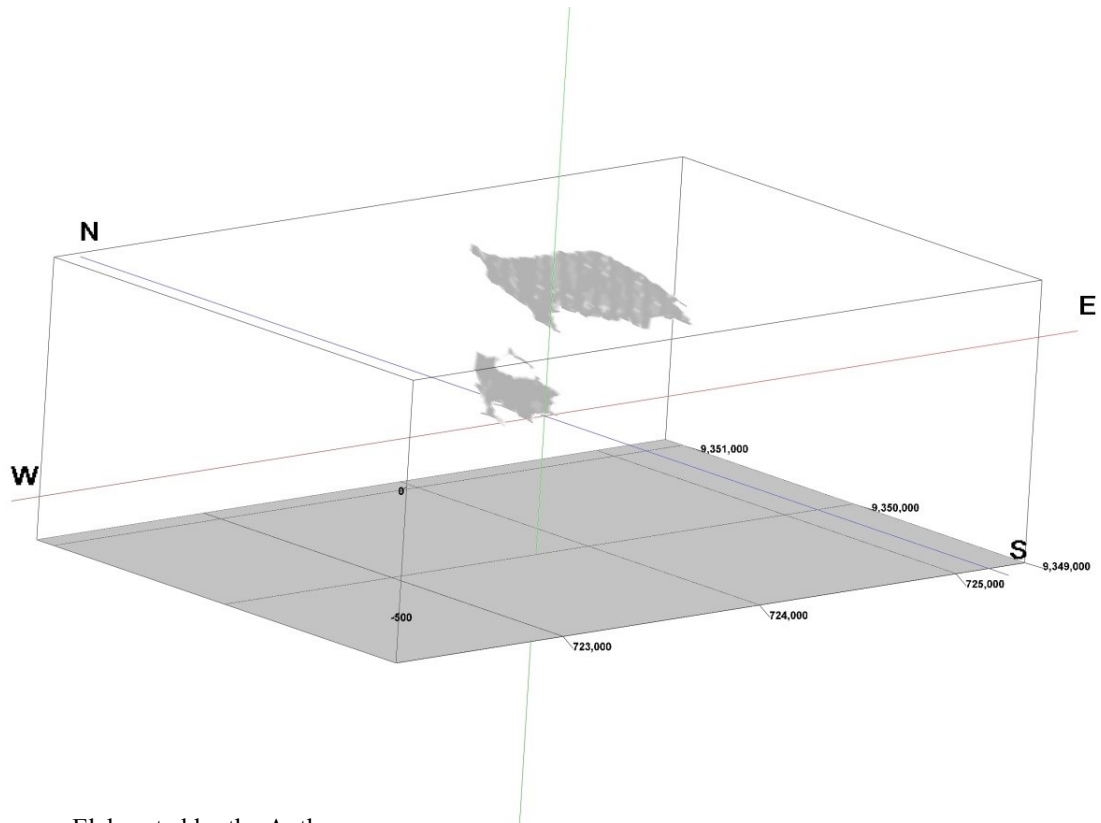
Figure 79 – Geometrical representation of the intrusive basic rocks (INB) based on 3D isopach modeling.



Source: Elaborated by the Author.

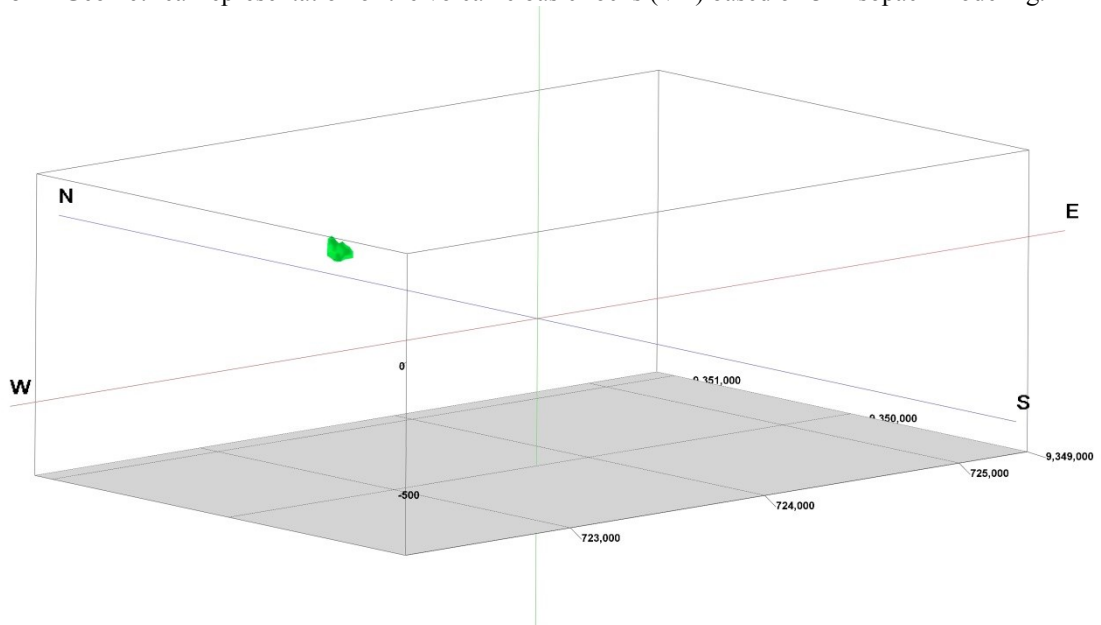


Figure 80 – Geometrical representation of the volcanic acidic rocks (VA) based on 3D isopach modeling.



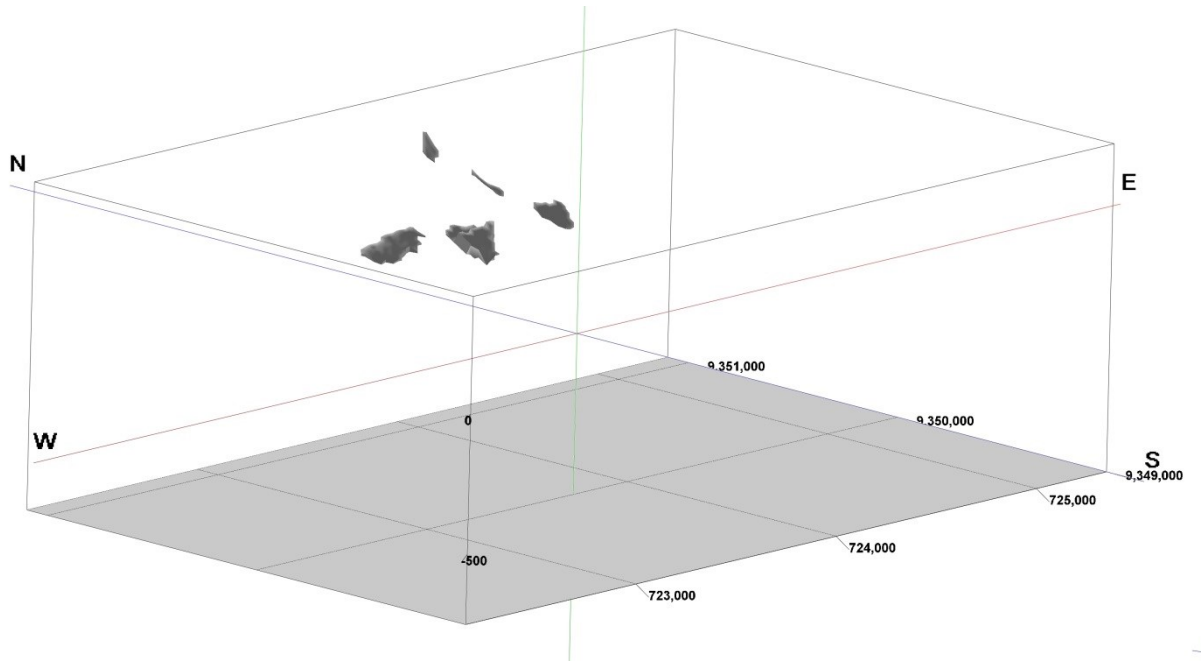
Source: Elaborated by the Author.

Figure 81 – Geometrical representation of the volcanic basic rocks (VB) based on 3D isopach modeling.



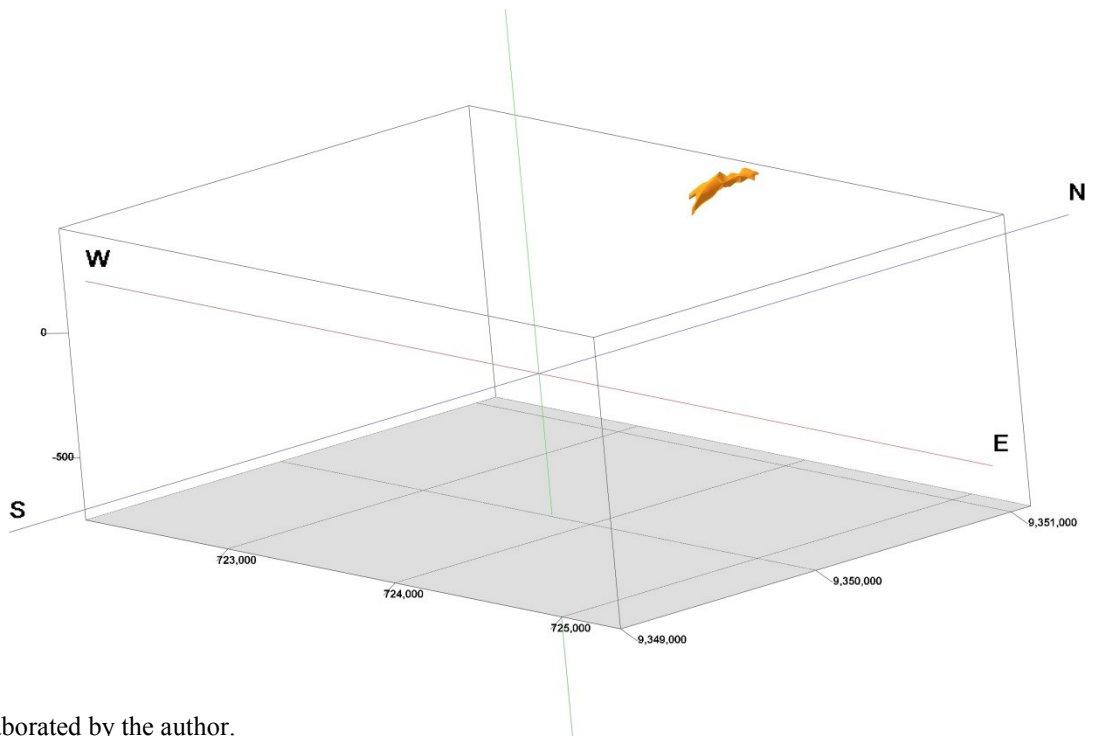
Source: Elaborated by the Author.

Figure 82 – Geometrical representation of the phyllite (PHY) based on 3D isopach modeling.



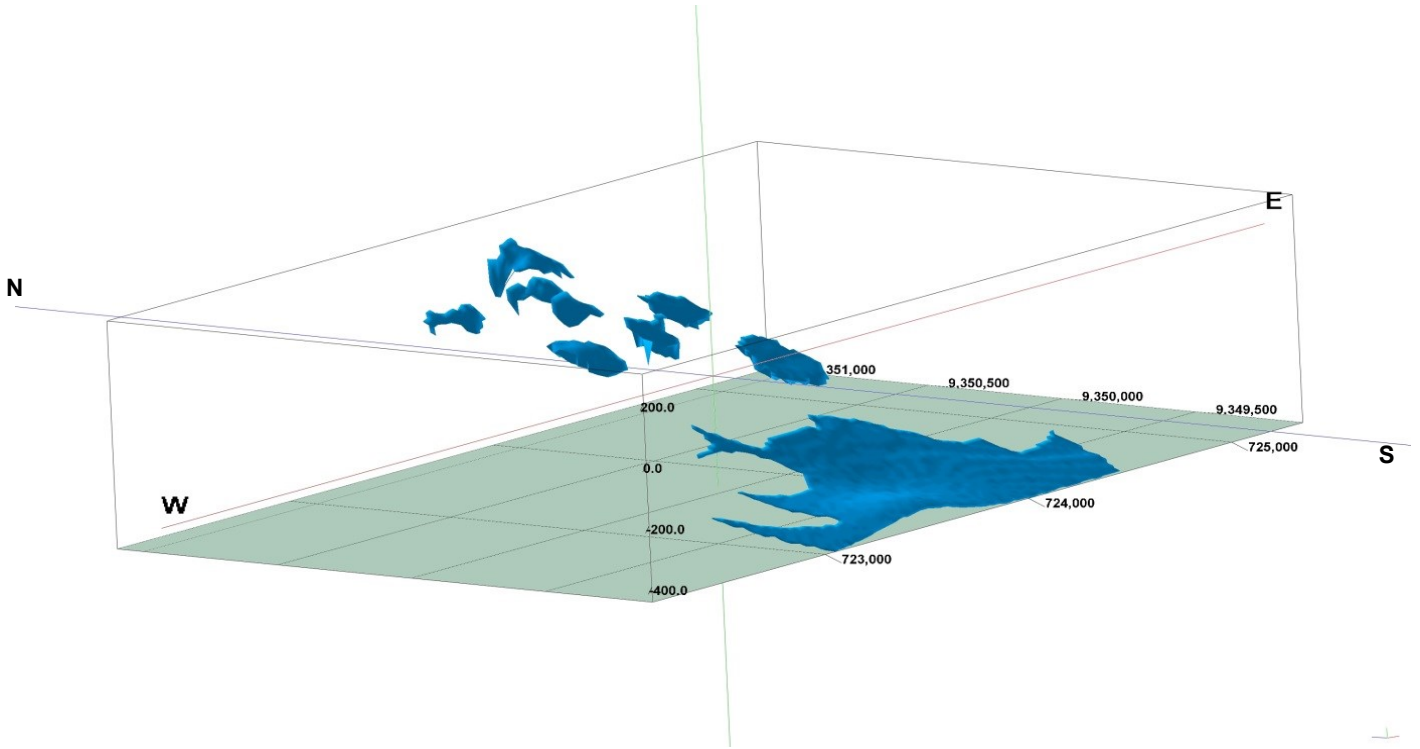
Source: Elaborated by the author.

Figure 83 – Geometrical representation of the ferruginous quartzites (FEQ) based on 3D isopach modeling.



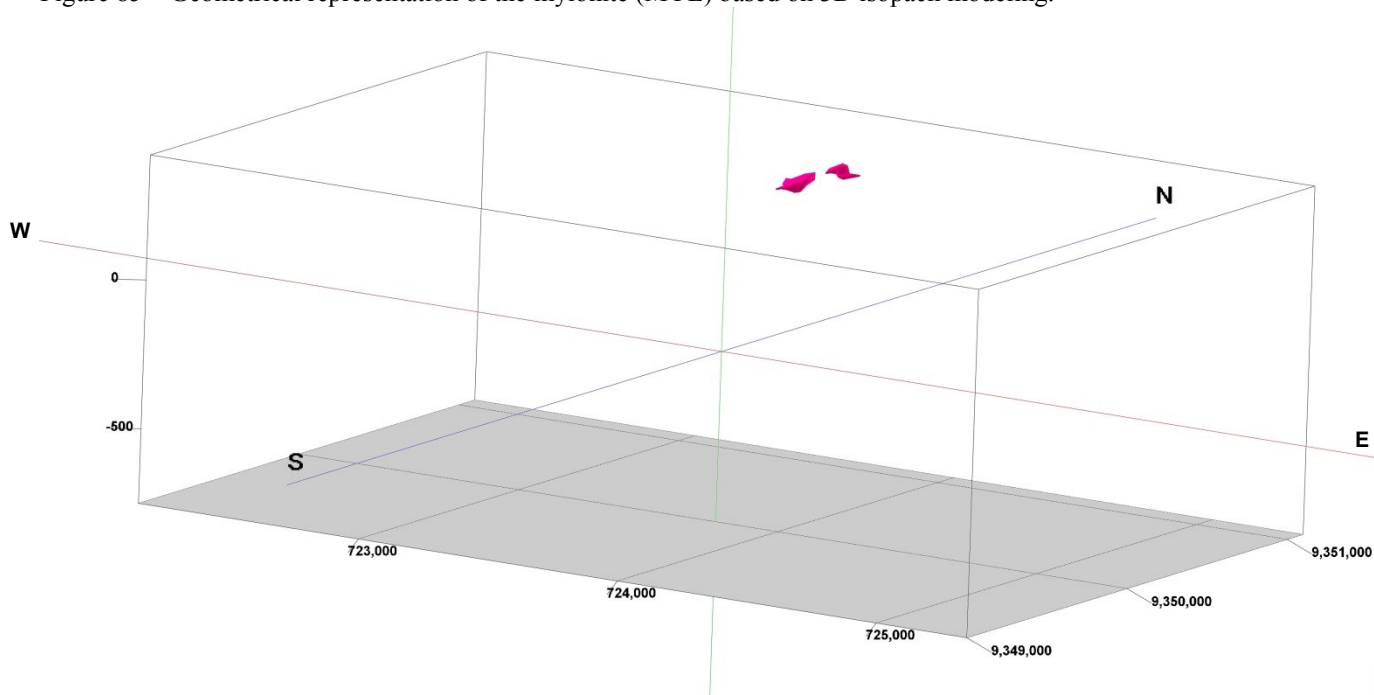
Source: Elaborated by the author.

Figure 84 – Geometrical representation of the quartzite (QTZ) based on 3D isopach modeling.



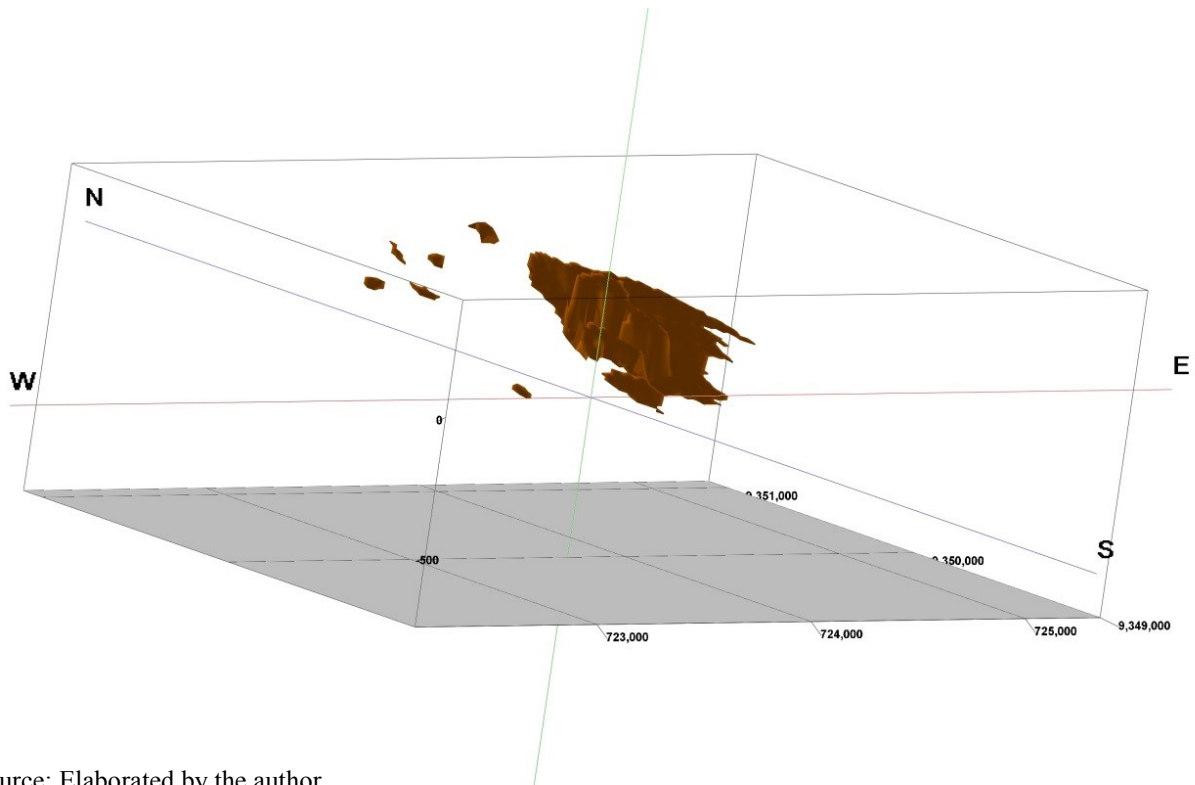
Source: Elaborated by the author.

Figure 85 – Geometrical representation of the mylonite (MYL) based on 3D isopach modeling.



Source: Elaborated by the author.

Figure 86 – Geometrical representation of the amphibolite (AMB) based on 3D isopach modeling.



Source: Elaborated by the author.

The previous chapter of this thesis presented a proposal of a geochemical classification scheme identifying the Bonito Mine BIFs as volcano-sedimentary itabirites. As discussed in-deep by Neves (1975), Sá (1994), Hackspacher *et al.* (1997) and Van Schmus *et al.* (2003), just to name a few, metamorphism and deformation took place at the Seridó fold belt throughout the Paleoproterozoic and Neoproterozoic terrains.

The geological features in the Bonito Mine are also a record from those events. Amphibolite rocks as a metabasic rock are indicative of the general metamorphic conditions that have encompassed the entire lithological package (Figure 86). Nonetheless, as exhibited in Figure 81, volcanic basic rocks occur as the less representative lithotype in the entire sequence.

## 8.2 3-D typology model of the itabirites

### 8.2.1 Solid modeling

The geochemical database is stemmed from MHAG's databank, as previously discussed in the typology section 5.2 of this thesis. Fonteles *et al.* (2018) presented a

typological model proposal to the itabirites of the Bonito Mine based on geochemical and petrographic studies that allowed recognizing eight itabirite-types regarding their multivariate interrelations.

This ground model was used to classify all geochemical samples of the database and its geometrical model is similar to the operations performed to build the lithological model of the study area. Noteworthy mention that the typological model was generated without other lithologies (Table 26). We aimed to process the 3D model based on two separate databases that were managed and submitted to the proper procedures.

The spatial modeling of the BIF typology followed the same steps as the geological modeling task. The 3D typology model depends on a proper DEM for the geometrical definition of the solid model. Thus, the specific DEM was built by using the IDS interpolator to generate a typology surface. The 3D typology model gathers the previous multivariate geochemical data analysis' results (Table 11, Chapter 5). Figures 87 and 88 exhibit complex spatial distributions throughout the itabiritic body. This “patchwork” pattern owes to the geochemical variability that was modeled during the multivariate data evaluation.

Table 26 – BIF encoding of itabirites from the Bonito Mine.

<b>BIF Type</b>	<b>Code</b>
Aluminous magnetitic itabirite	Al-MgI
Aluminous martitic itabirite	Al-MI
Hematitic itabirite	HI
Hematitic-magnetitic itabirite	H-MgI
Magnetitic-amphibolitic itabirite	Mg-AmI
Magnetitic itabirite	MgI
Martitic itabirite	MI
Silicate martitic itabirite	Si-MI

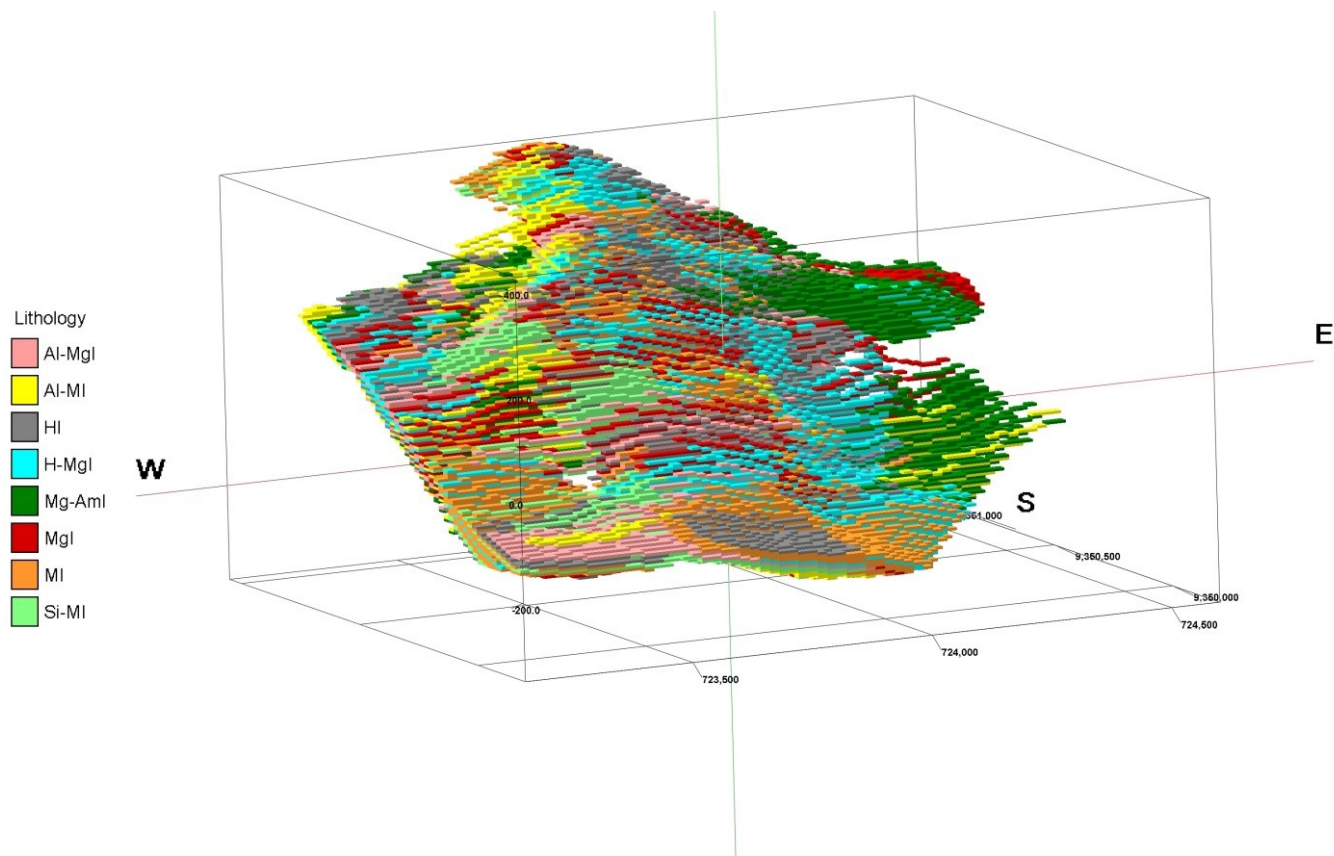
Source: Adapted from Fonteles *et al.* (2018)

Figures 87 and 88 exhibit Mg-AmI type occurring mostly at the eastern limb of the Bonito Fold associated with MgI. HI and H-MgI can be seen occupying several sectors of the BIF body, but they are frequently distributed at the hinge zone, from top to bottom levels of the model. MI and Al-MgI are easily identified at the bottom sectors of the BIF body. Al-MI and Si-MI are quite dispersed throughout the modeled itabiritic solid.

Fonteles *et al.* (2019b) reported the weathering of the BIF rocks from the Bonito Mine are due to physical/mechanical processes rather than chemical changes in mineralogy. Therefore, the transformation of magnetite into martite, by pseudomorphism of the primer, can be assigned to metamorphic processes.

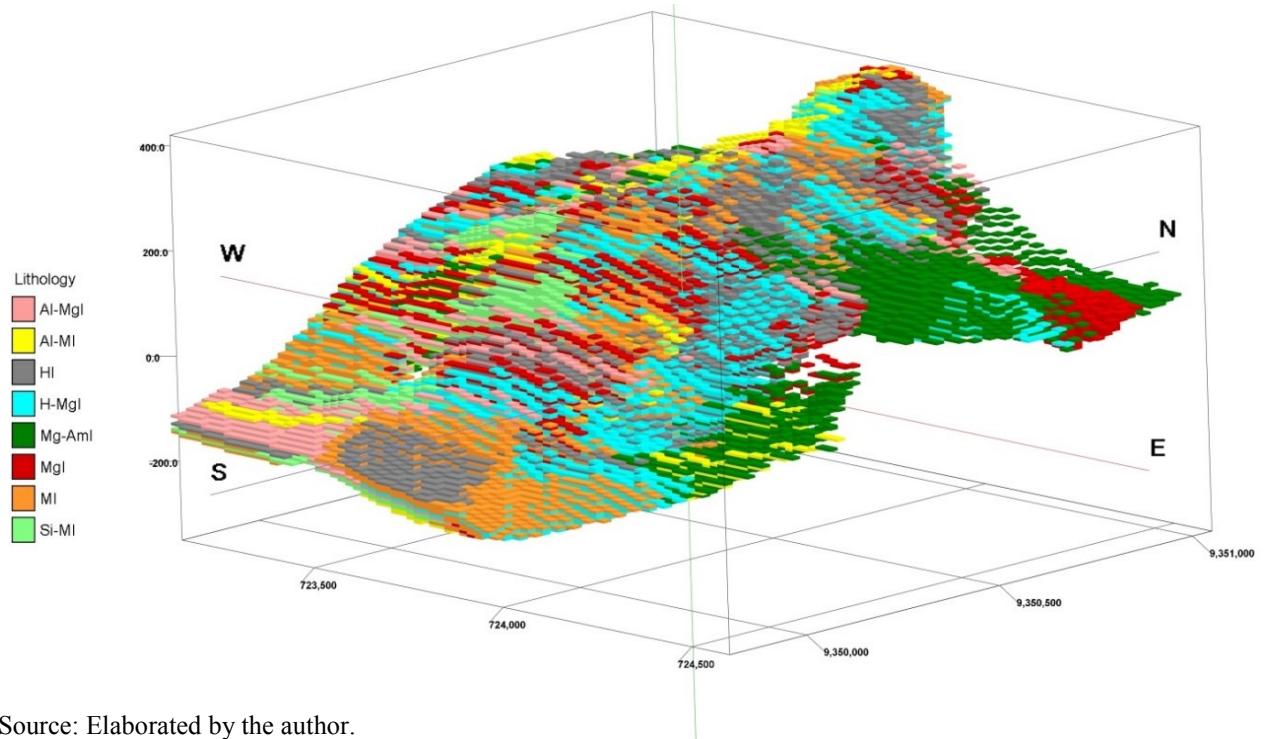
The presence of Al-MI, along an N-S cross-section (Figures 89 and 90), shows that martitization was a pervasive mineralogical transformation within the itabiritic body. The E-W cross-sections (Figures 91 to 94) reveal the same spatial fact, regarding martitic itabirites. The BIF types HI and H-Mgl occupy the uppermost part of the itabiritic body (Figure 89). The geometric features of the BIF types are due to voxel modeling with no drawing enhancement.

Figure 87 – Typological 3D model of the itabirites (SW view).



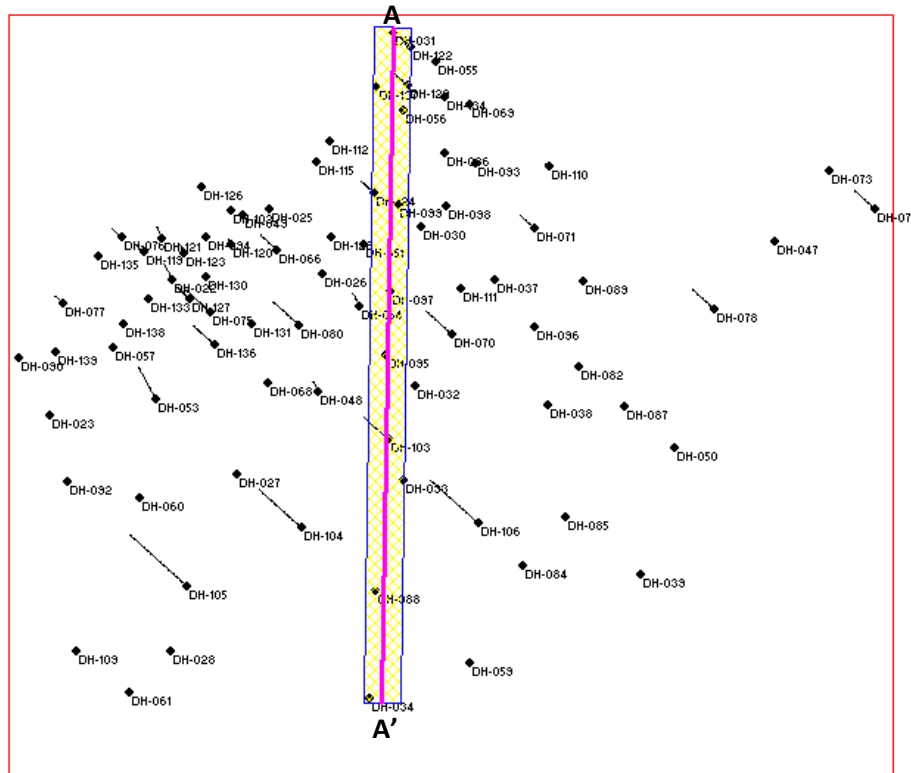
Source: Elaborated by the Author.

Figure 88 – Typological 3D model of the itabirites (SE view).



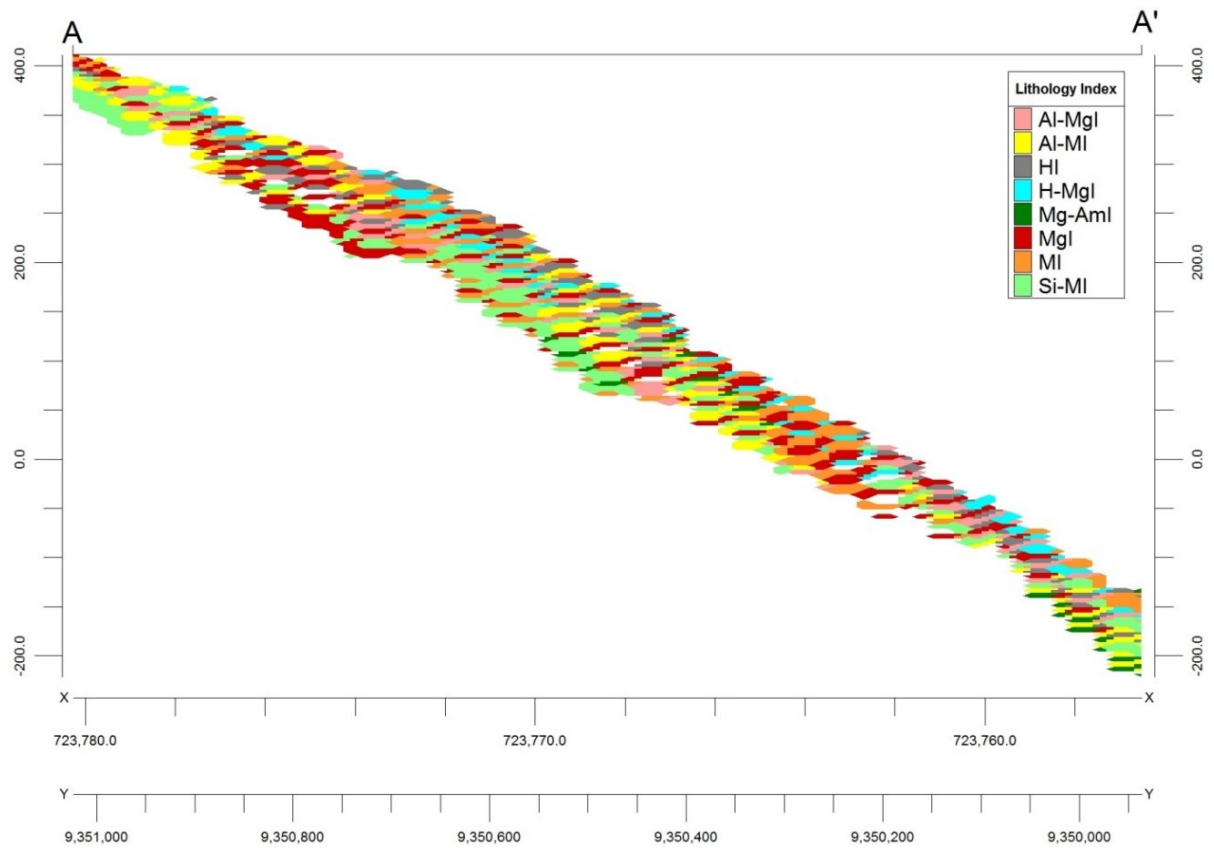
Source: Elaborated by the author.

Figure 89 – Schematic location map of the cross-section A (723,780E/9,351,030N) - A' (723,762E/9,349,923N).



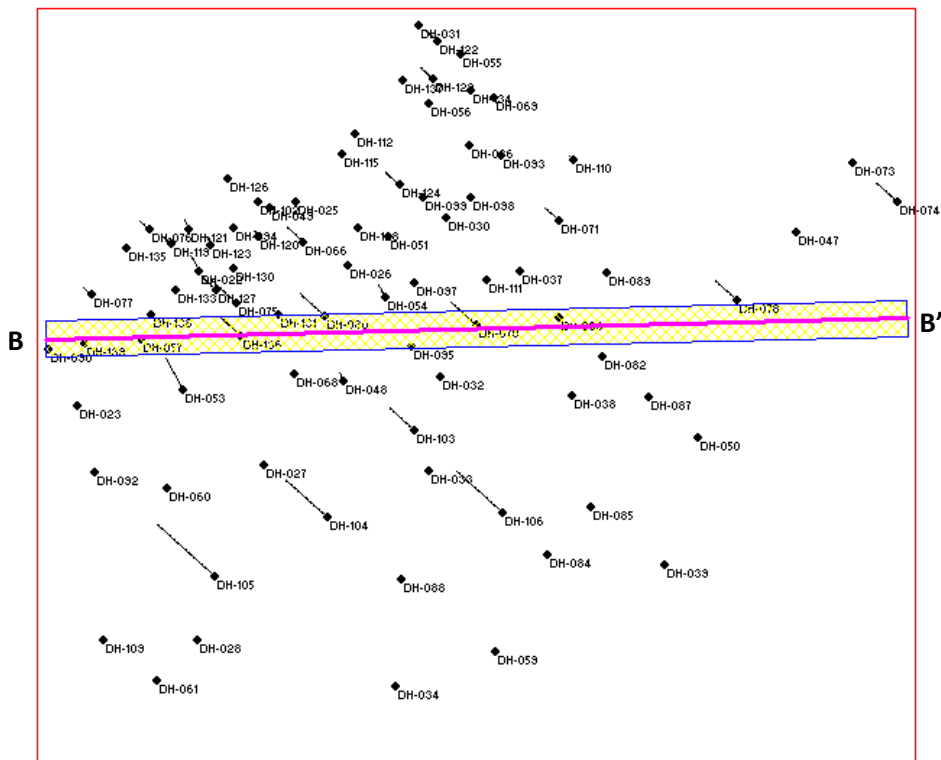
Source: Elaborated by the author.

Figure 90 – Cross-section A-A' drawn along the N-S direction.



Source: Elaborated by the author.

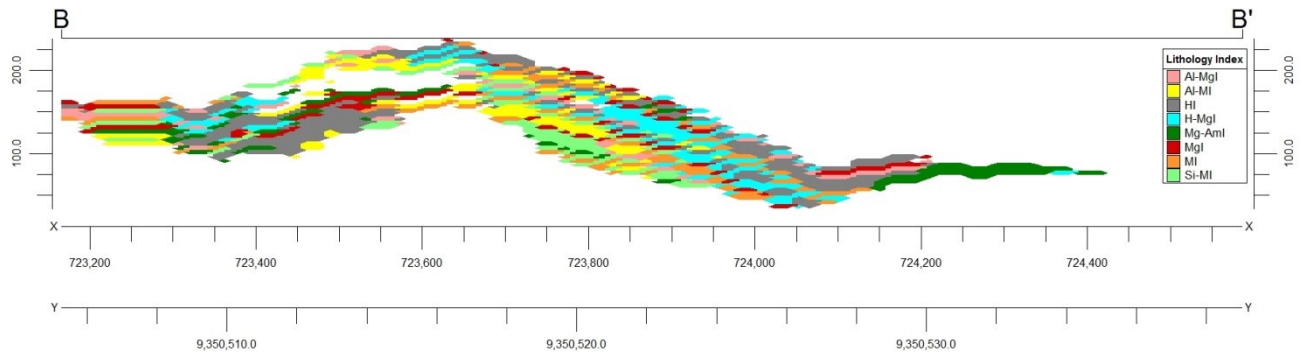
Figure 91 – Schematic location map of the cross-section B (723,166E/9,350,505N) - B' (724,587E/9,350,539N).



Source: Elaborated by the author.

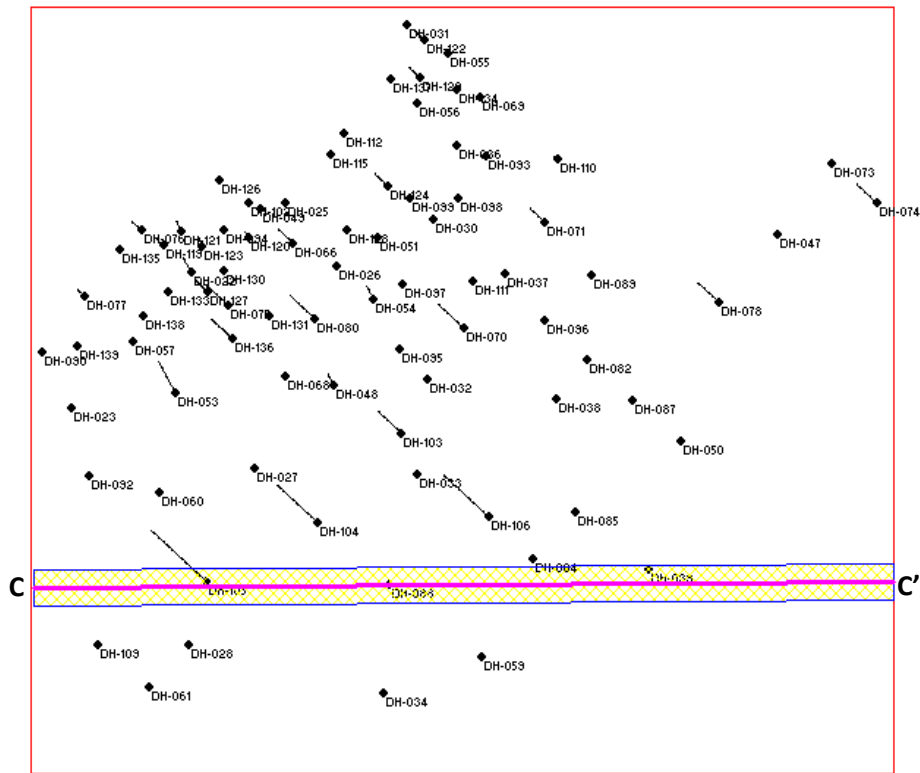


Figure 92 – Cross-section B-B' drawn along the E-W direction (middle zone of the itabiritic body).



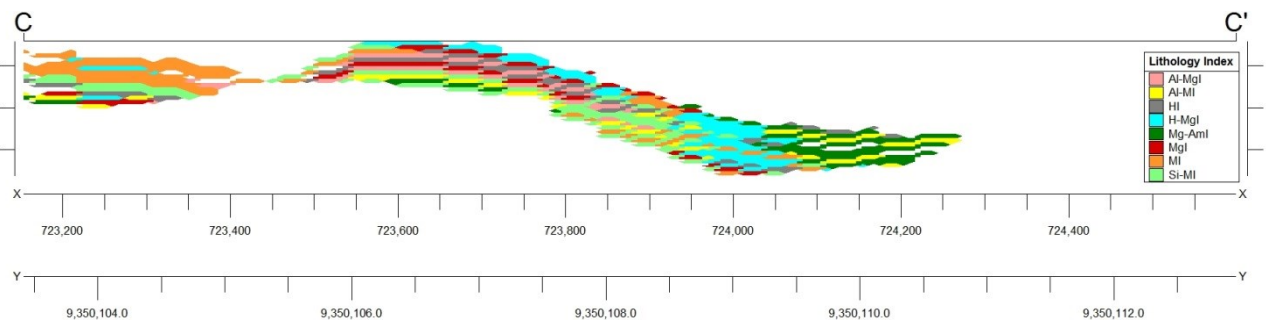
Source: Elaborated by the author.

Figure 93 – Schematic location map of the cross-section C (723,153E/9,350,103N) - C' (724,600E/9,350,113N).



Source: Elaborated by the author.

Figure 94 – Cross-section C-C' drawn along the E-W direction (bottom-end zone of the itabiritic body).

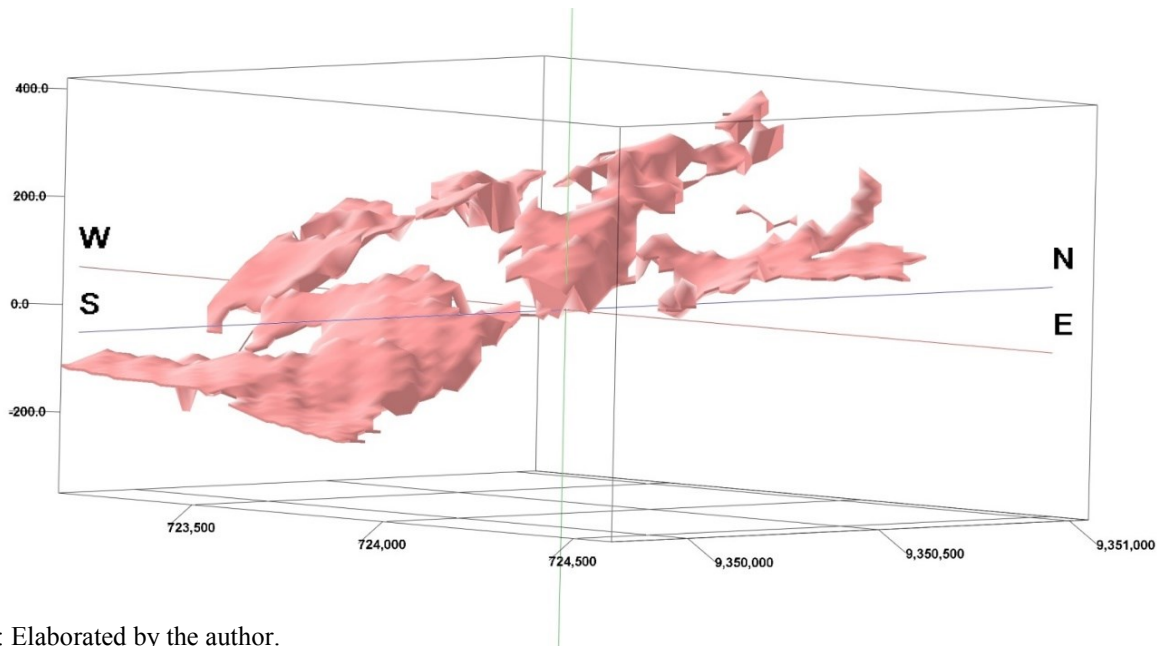


Source: Elaborated by the author.

**8.2.2 3-D Isopach modeling**

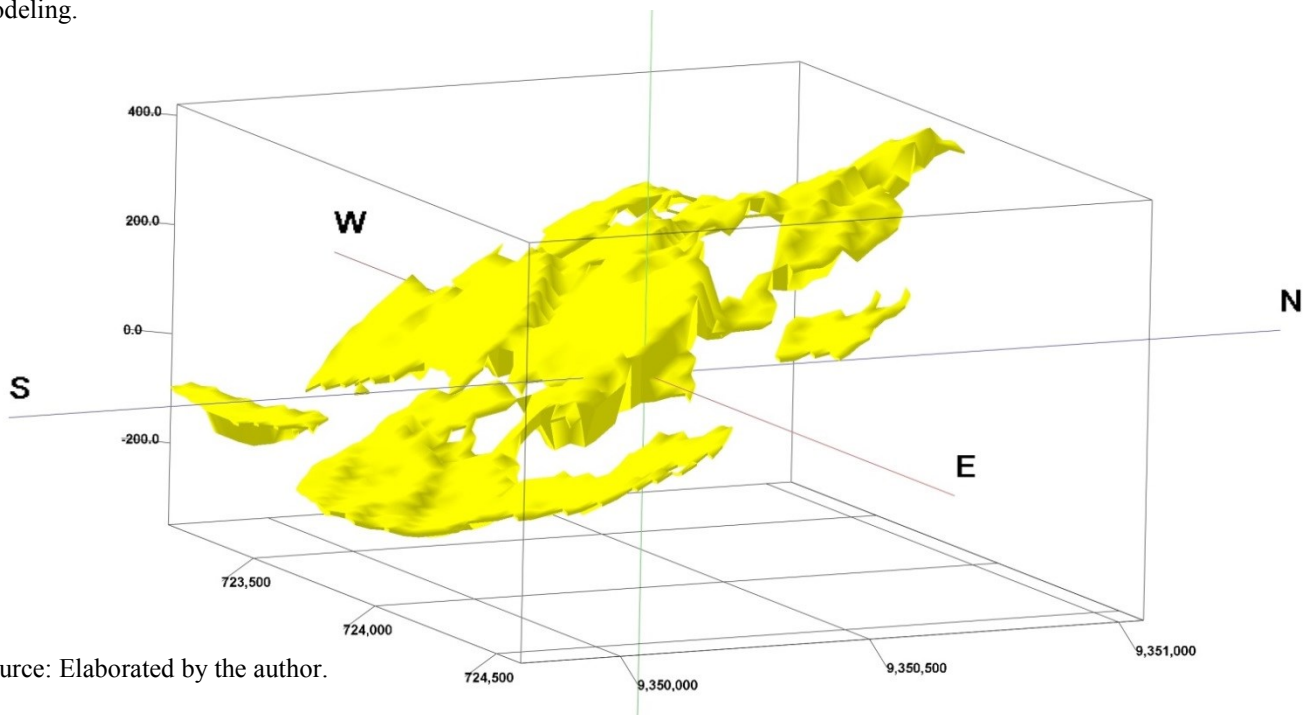
Isopach modeling was performed on a 3D typology model in order to cope with the individual geometry of each itabirite type. These models will make easier to see the BIF types on 3D space. The geometric principles are similar to those employed to create the lithological models (Figures 95 to 102).

Figure 95 – Geometrical representation of the aluminous magnetitic itabirite (Al-MgI) based on 3D isopach modeling.



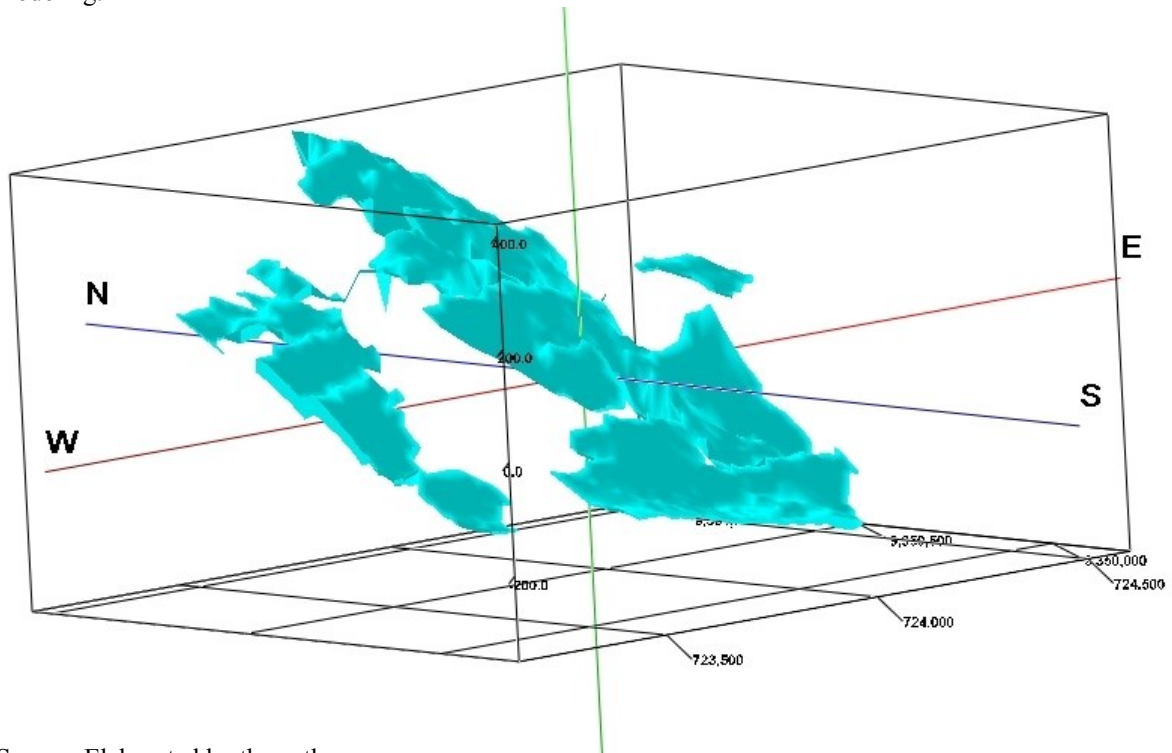
Source: Elaborated by the author.

Figure 96 – Geometrical representation of the aluminous martitic itabirite (Al-MI) based on 3D isopach modeling.



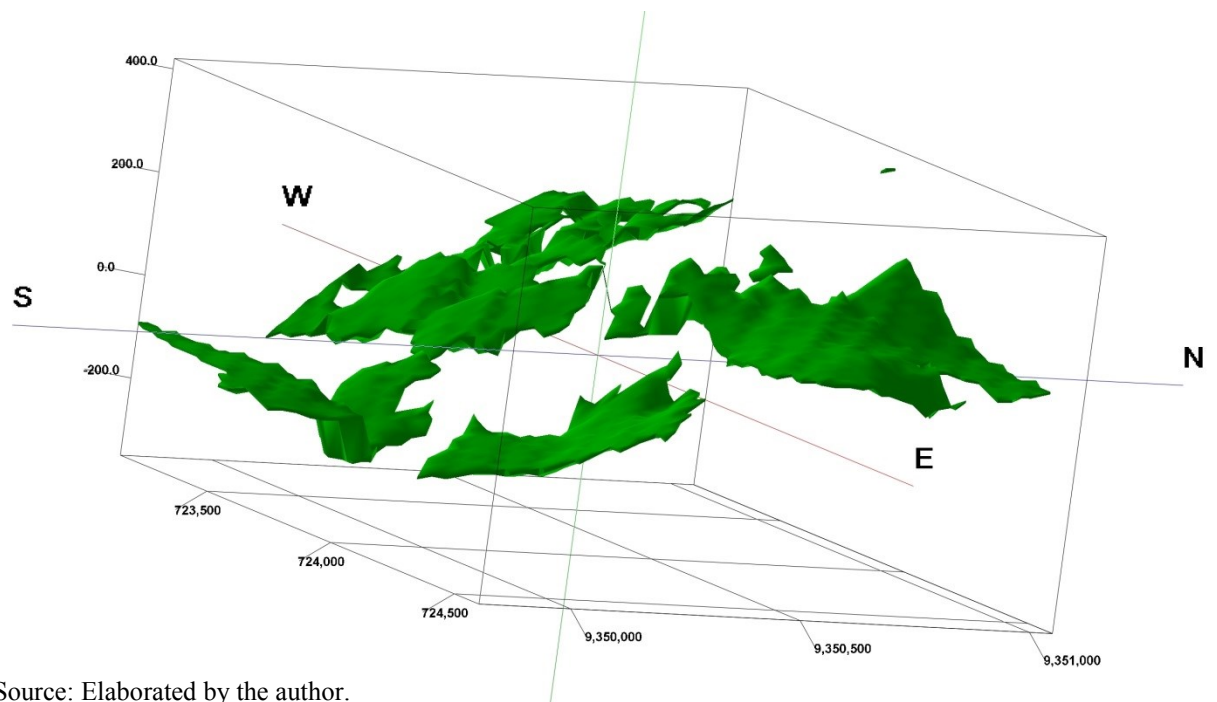
Source: Elaborated by the author.

Figure 97 – Geometrical representation of the hematitic-magnetitic itabirite (H-MgI) based on 3D isopach modeling.



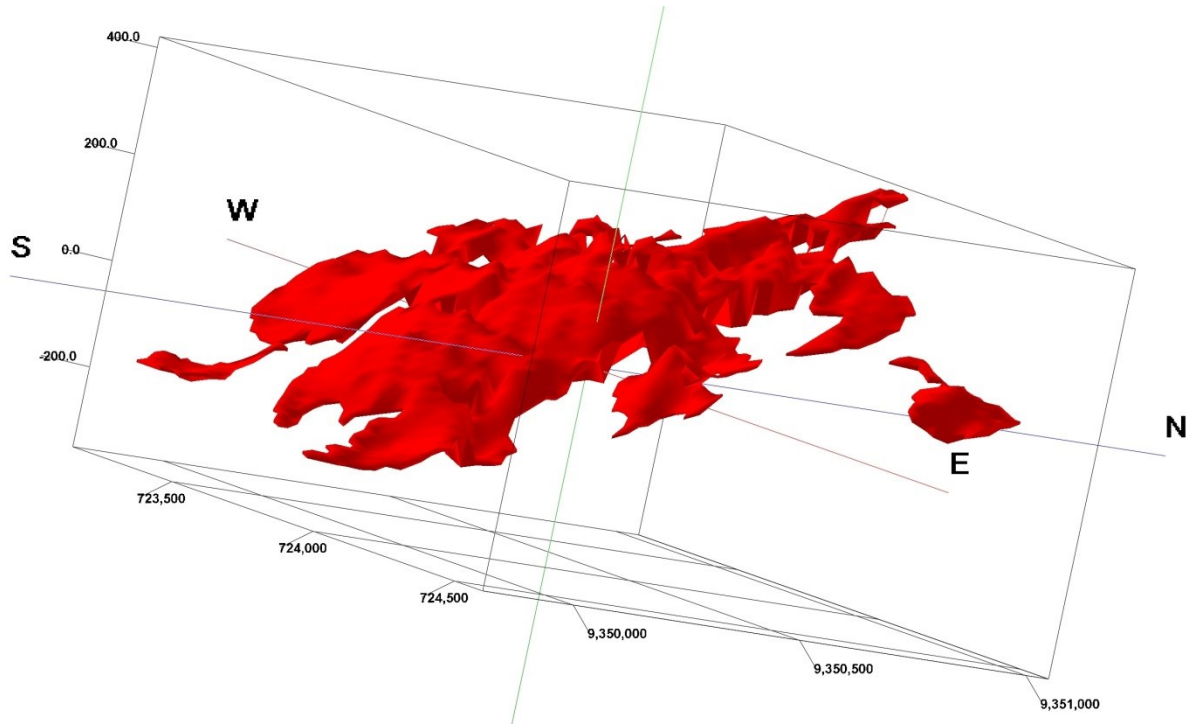
Source: Elaborated by the author.

Figure 98 – Geometrical representation of the magnetitic-amphibolitic itabirite (Mg-AmI) based on 3D isopach modeling.



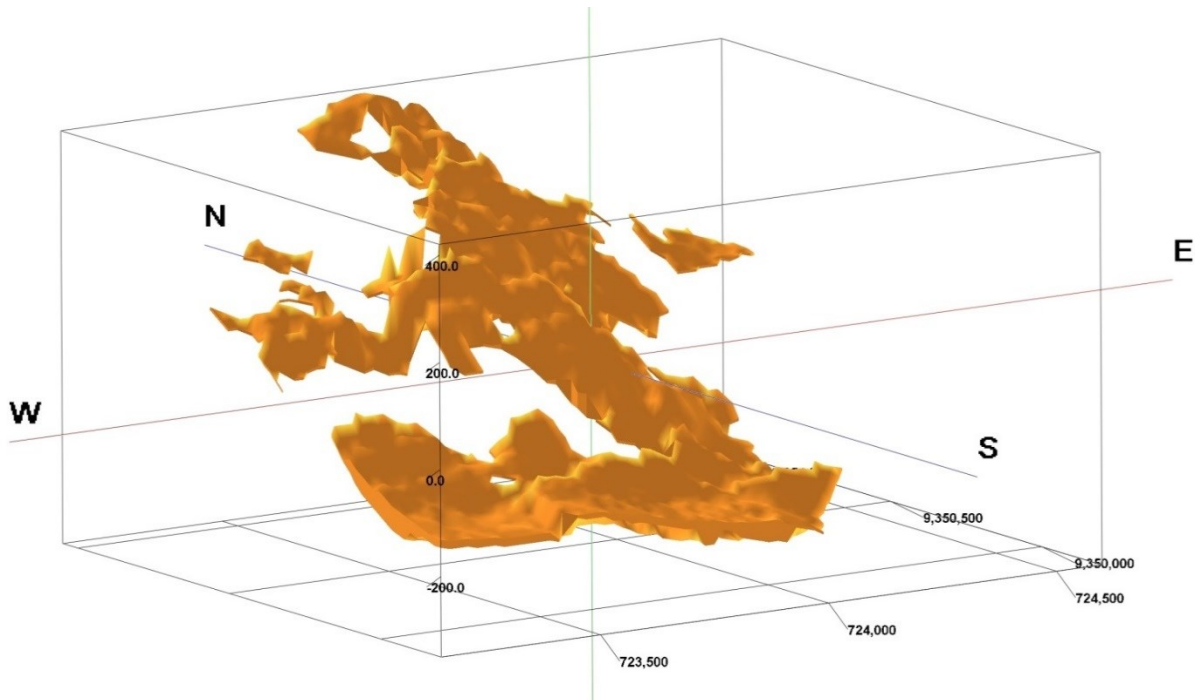
Source: Elaborated by the author.

Figure 99 – Geometrical representation of the magnetitic itabirite (MgI) based on 3D isopach modeling.



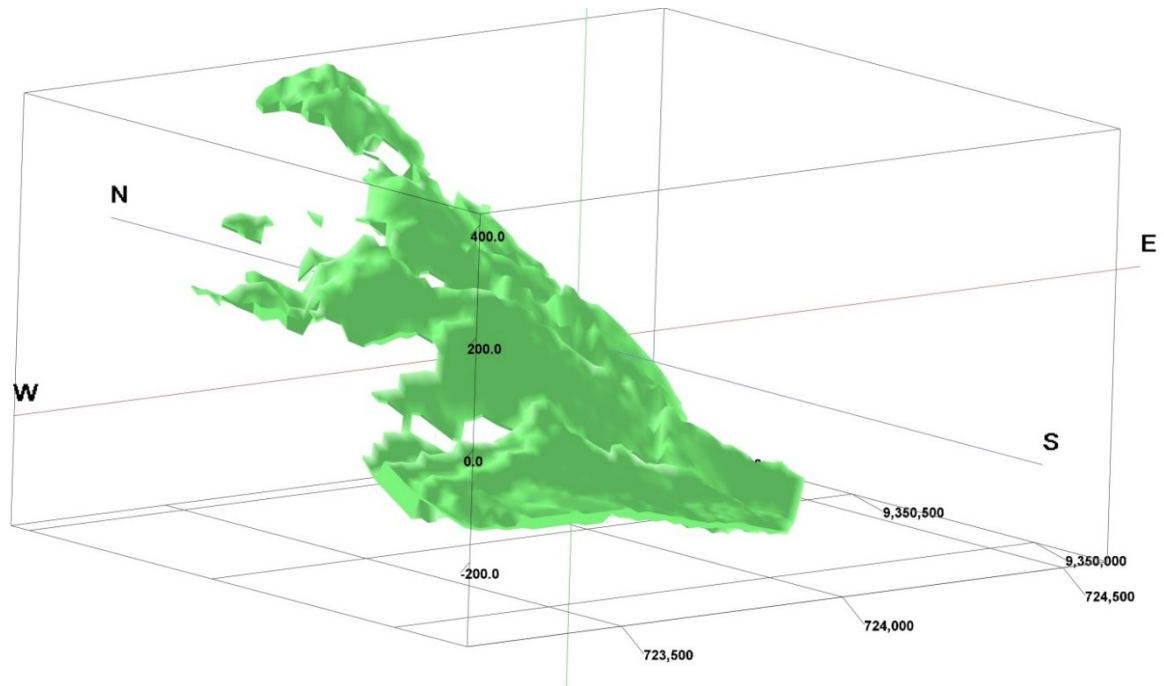
Source: Elaborated by the author.

Figure 100 – Geometrical representation of the martitic itabirite (MI) based on 3D isopach modeling.



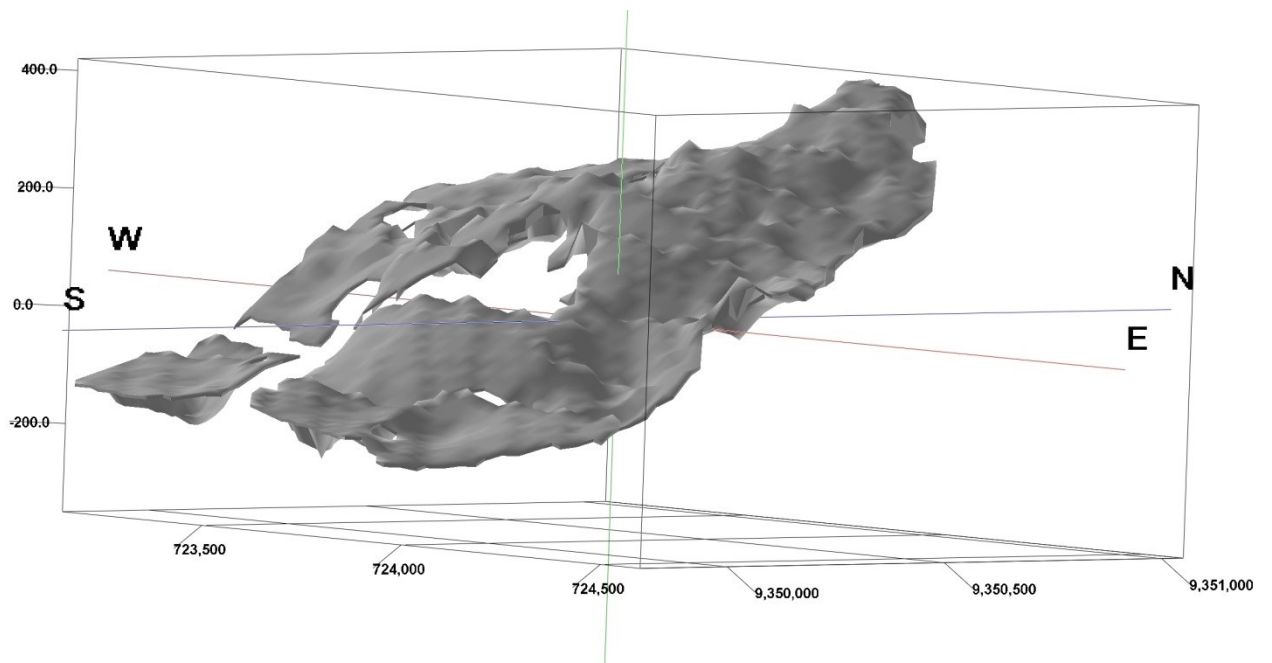
Source: Elaborated by the author.

Figure 101 – Geometrical representation of the silicate martitic itabirite (Si-MI) based on 3D isopach modeling.



Source: Elaborated by the author.

Figure 102 – Geometrical representation of the hematitic itabirite (HI) based on 3D isopach modeling.



Source: Elaborated by the author.

## 9 GEOLOGICAL EVOLUTION MODEL OF THE STUDY AREA

The Borborema Province – Northeastern Brazil, encompasses the Seridó fold belt whose development is associated to the Brasiliano/Pan-African cycle (ALMEIDA *et al.* 1981; ARCHANJO; BOUCHEZ, 1991; SÁ, 1994; SÁ *et al.* 1995; VAN SCHMUS *et al.* 2003). The entire province experienced intense tectonic compression due to the convergence of West African-São Luís and São Francisco/Congo cratons that culminated in the assembly of Western Gondwana (FETTER, 1994).

Although most recognized events are related to compressional deformation events, extensional episodes also occurred throughout the Borborema Province. Regarding the Seridó region, the deposition sequences were interpreted by Van Schmus *et al.* (2003) as a back-arc sedimentation system installed upon the Rio Piranhas basement (Paleoproterozoic). The detritus are supposedly Neorchean age until ca. 650 Ma, registering the extension/contraction event between 700 and 600 Ma (ANGELIM *et al.* 2006). The extensive analyses made by Van Schmus *et al.* (2003) led these authors to conclude the basin has received detritus from several different sources.

The QPC (quartzite-pelite-carbonates) sequence related to the Serra dos Quintos/Jucurutu Formations was interpreted by Sá (1994), Nascimento (2002) and Angelim *et al.* (2006), as shallow marine deposits.

Van Schmus *et al.* (2003) argued Seridó Group's maximum deposition age was about 650 Ma ( $634 \pm 13$  Ma as minimum age) based on U-Pb isotopic data obtained from sampled detrital zircons of the Jucurutu Formation.

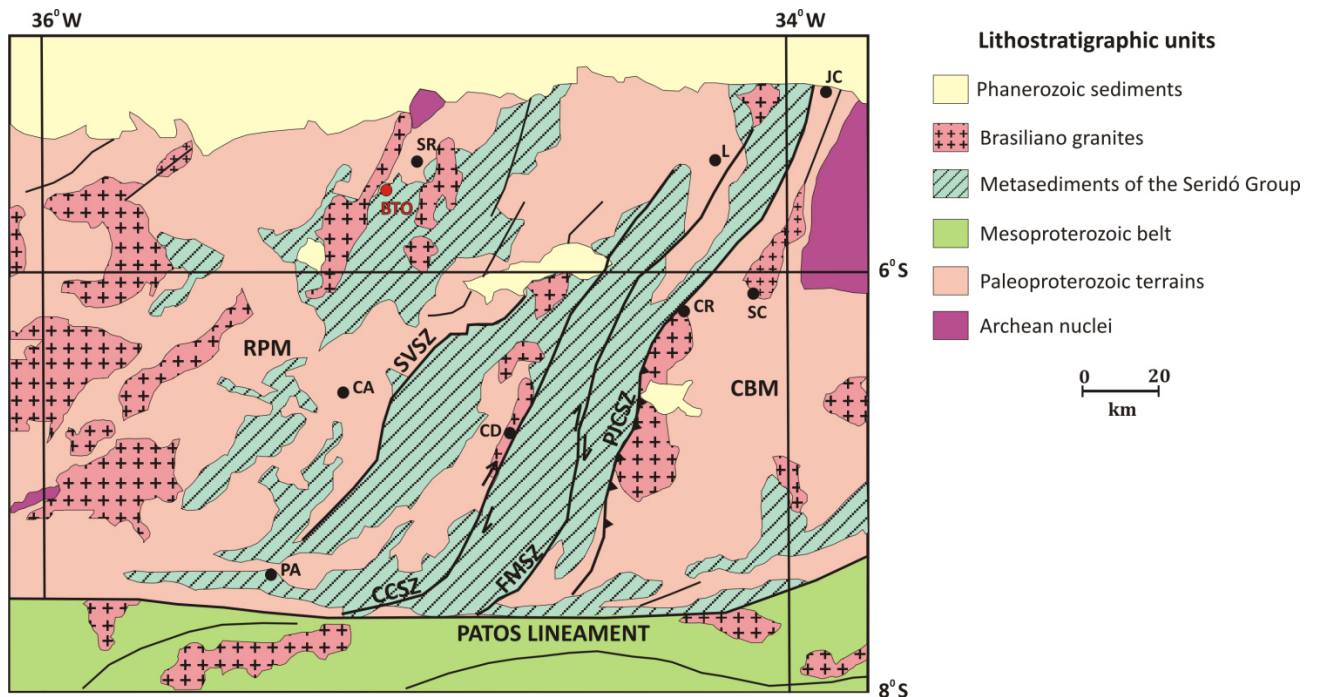
According to Hackspacher *et al.* (1997), the tectono-metamorphic history can be summarized by a transitional and progressive deformation from a primary thrust in a syn-collisional regime to a secondary and local strike-slip regime, both in similar metamorphic conditions (Figure 103).

Another remarkable feature related to the Brasiliano orogeny is the abundant granite-genesis producing large plutons all over the Borborema Province, especially in the Seridó belt (ALMEIDA *et al.* 1981; SÁ, 1994; CABY *et al.* 1995; HACKSPACHER *et al.* 1997; VAN SCHMUS *et al.* 2003; NEVES; FUCK, 2013).

On the northern region of Patos shear zone (lineament) (Figure 104), i.e. the Northern Borborema Province, the first noticeable deformation event ( $D_1/D_2$ ) is referred to as the Brasiliano orogeny with WNW thrusts associated with isoclinal folding and penetrative subhorizontal or mylonitic foliation ( $S_2$ ) (Figure 104). This event is succeeded by transcurrent

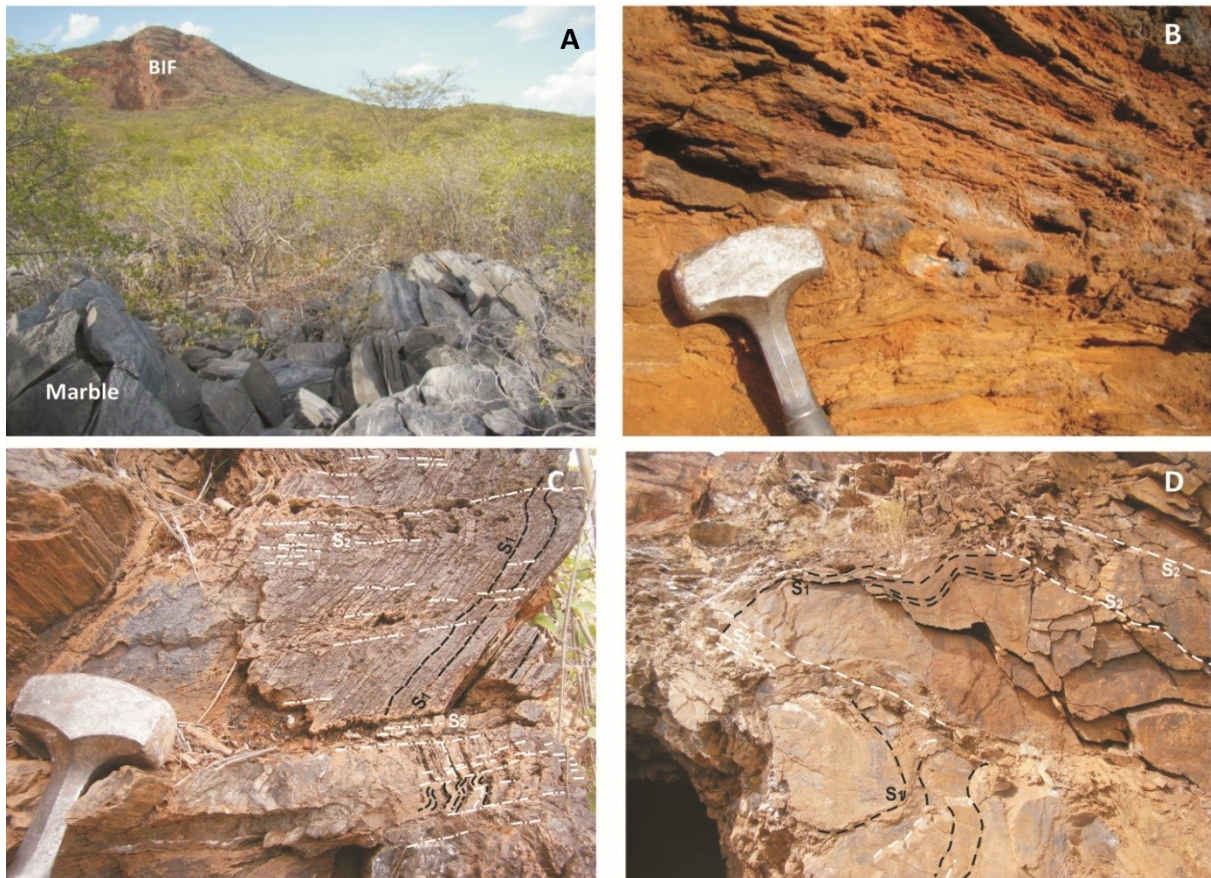
tectonics regime ( $D_3$ ) that created a vertical or mylonitic foliation ( $S_3$ ) related to expressive dominant dextral transpressional shear zones in the NE-SW direction generating positive flower structures. Hackspacher *et al.* (1997) suggested the thrust regime occurred between 650 and 580 Ma, whereas the strike-slip regime was developed from 580 to 500 Ma.

Figure 103 – Simplified geological map of part of the Seridó belt and main lithological units. Abbreviations and symbols: Rio Piranhas Massif (RPM) Caldas Brandão Massif (CBM); São Vicente shear zone (SVSZ); Picuí/João Câmara shear zone (PJCSZ); Frei Martinho shear zone (FMSZ); Cerro Corá shear zone (CCSZ). Map localities: Angicos (A); Caicó (CA); Caiçara dos Rios dos Ventos (CV); Carnaúba dos Dantas (CD); Currais Novos (CN); Campo Redondo (CR); João Câmara (JC), Lages (L); Pedra Preta (PP); Picuí (P); Santa Cruz (SC); São Rafael (SR); São Vicente (SV); Bonito Mine (BTO, red circle).



Source: Adapted from Hackspacher *et al.* (1997).

Figure 104 - (A) BIFs are seen in the most elevated terrains at the mining site whereas marble is displayed in the first plan as grey massive folded rocks. (B) Hematitic itabirite outcropped at the higher grounds corresponding to the hinge of the Bonito antiform. (C,D) Folded BIF rocks exhibit the field relations of  $S_1/S_2$  foliations.



Source: Photo A was taken from Barbosa (2013). The remaining photos were taken from the collection of C.U.V. Veríssimo.

### 9.1 Preliminary geological evolution staged-model

A preliminary geological evolution model is here presented in order to explore the available geological, geochemical and geochronological (from quoted literature) information. The basic goal is to discuss this model as a concept developed according to a number of stages until reaching the final conformation, matching the 3D geological model, as presented in Chapter 8.

Discussions about stratigraphical schemes or models, putting them on conflict with each other, were not considered. The description of each evolving stage as a result of combined sedimentary and volcanic processes is presented in the following section.



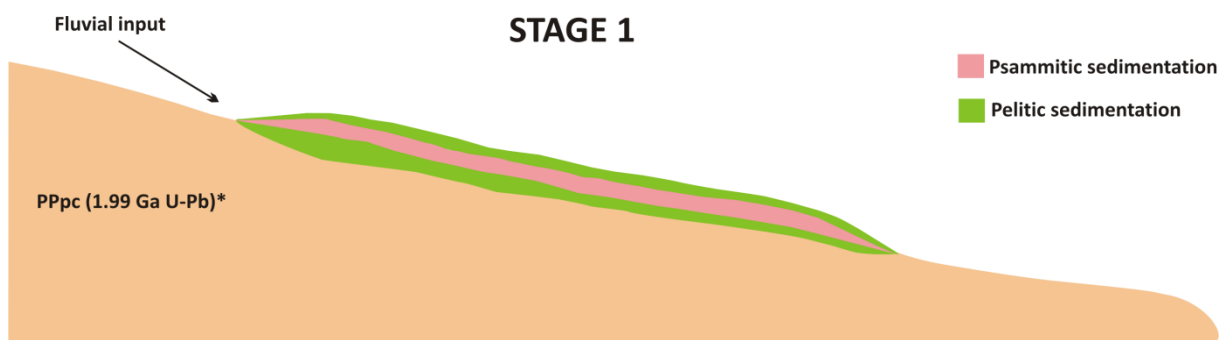
The stage-based geological evolution model is intended to be a contribution to the state-of-art about the possible depositional systems and tectonic processes regarding the study area. Not all lithologies were able to be illustrated owing to graphic representation issues.

The geological premises and hypotheses, considered for the proposal of the evolution model are:

1. Early stages of sedimentation were due to fluvial and transitional systems;
2. Volcanic activity which led the input of dissolved iron oxides to the basin (Short scale restricted basin?).
3. Iron oxides precipitation due to changes on Eh/pH conditions;
4. Implantation of a shallow marine environment. Deposition of carbonate rocks.
5. The Brasiliano/Pan-African orogeny as the main cause of deformation and metamorphism of the lithologies of Jucurutu and Serra dos Quintos Formations.

The suggested model is comprised of a 6-staged evolution concept attempting to recreate the main depositional environments. The schematic sections representing the stages are N-S oriented. The stage #1 was conceived to explain the development of the depositional systems grounded by a Paleoproterozoic platform, in this case, represented by the granitic ortogneisses of the Poço da Cruz suite (VAN SCHMUS *et al.* 2003; ANGELIM *et al.* 2006). At this stage, pelitic lenses were transported into the proto-basin and then succeeded by coarse sediments interpreted as arkosic (immature) sands. Pelitic sediment would eventually seal the sandy sediments which were deposited due to a fluvial system (Figure 105).

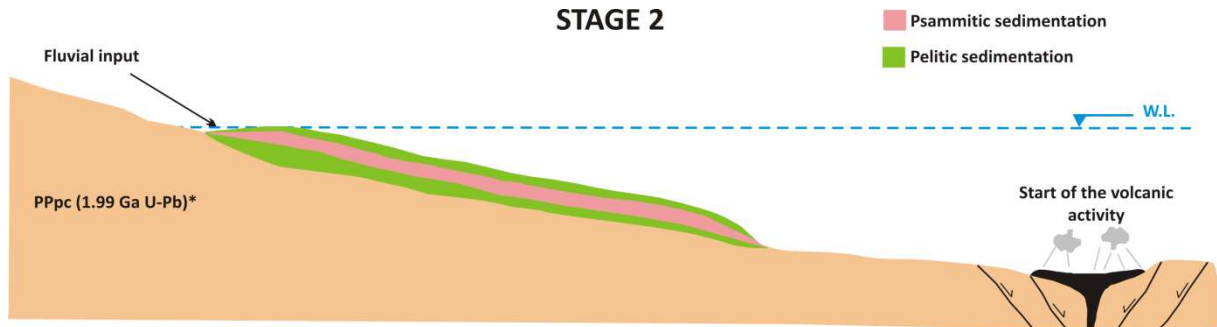
Figure 105 – The first stage describing the implantation of the primordial sedimentary environment.



Source: Elaborated by the author. \*Angelim *et al.* (2006).

Stage #2 describes the continuing process of sedimentation of the pelitic and psammitic sequences. Additionally, it is proposed the start of volcanic activity due to the implantation of a local extensional (transtensional?) regime (Figure 106).

Figure 106 – The second stage exhibiting the initial phases of the volcanic activity.

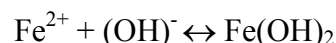


Source: Elaborated by the author. \*Angelim *et al.* (2006).

Stage #3 was modeled to describe the ongoing volcanic activity input of dissolved iron oxides (Figure 107). Atmospheric exchanges would gradually affect oxidation and pH conditions of the basin; even though local low Eh environment at the proximal sites can be perceived, the incoming seawater would be also responsible for the elevation of oxygenation level propitiated by new water circulation. James (1954) emphasized the relationships, regarding Eh-pH conditions, between sulfide, carbonate, and oxides – in his classical genetic model for BIFs, are practically non-dependent.

Dissolved iron oxides as  $\text{Fe}(\text{OH})_2$  have come from the volcanic input as flowing spots (hydrothermal vents?) which were distributed as the water currents moved within the basin. Following one of the premises postulated by Van Schmus *et al.* (2003) and Sial *et al.* (2015), the Bonito basin would fit with a small narrow basin model, owing to its small outcropped area.

According to Mel'nik (1982) and Krauskopf and Birk (1995), under reducing and alkaline conditions,  $\text{Fe}(\text{OH})_2$  compound is soluble in the deeper waters of the narrow basin and, thus, at the proximal volcanic sites. The soluble compound is described as



The following chemical reaction possible to describes how iron oxide plumes may have come from the volcanic exhalations

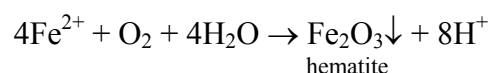
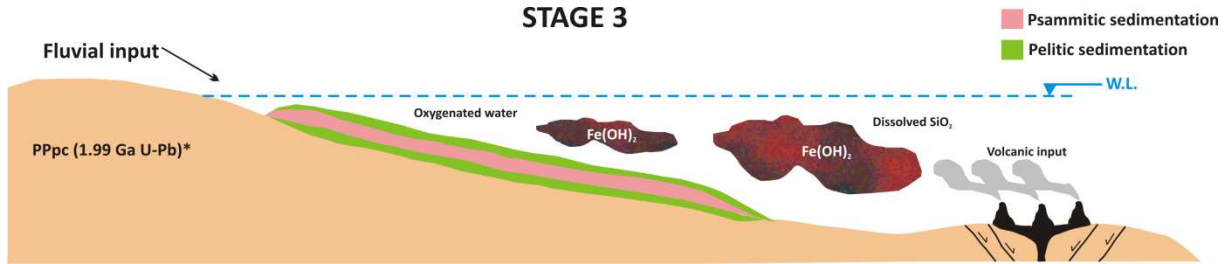


Figure 107 – The third stage exhibiting the volcanic input activity. Dissolved iron oxides flow due to the inner basin water circulation mechanisms.

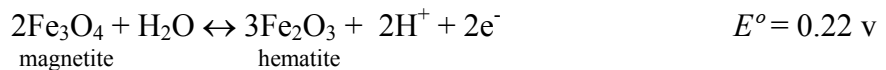


Source: Elaborated by the author. \*Angelim *et al.* (2006).

The progressive volcanic input and variations of overall physicochemical conditions of the basin may have induced the precipitation of the forming-minerals of the BIFs of the Bonito Mine. Stage #4 foresees iron oxides precipitation as hematite and/or magnetite. Drever (1974) has postulated that magnetite would be crystallized as a diagenetic product, as observed in Umm Nar BIF deposit, Eastern Egypt (AREF *et al.* 1993).

The pH conditions are constrained by a narrow window indicated by the classical Eh-pH diagram by Krumbein and Garrels (1952) wherein the pH field on oxidating conditions ( $Eh > 0.1$ ) is limited by values of 7.0 and 8.0. Notwithstanding, Klein and Bricker (1977) have shown that magnetite is stable over a large range of pH, but constrained under well defined Eh conditions in the presence of sulfides and carbonates.

The accurate governing Eh-pH constraints of the Bonito basin cannot be achieved, but the approximation to normal conditions ( $T = 25^\circ$ ,  $P_{total} = 1$  bar) can be used as a ground reference to exam those conditions. According to Krauskopf and Bird (1995), setup of the electrochemical equation for hematite and magnetite can yield an idea of what has occurred at stage #3 of our model:



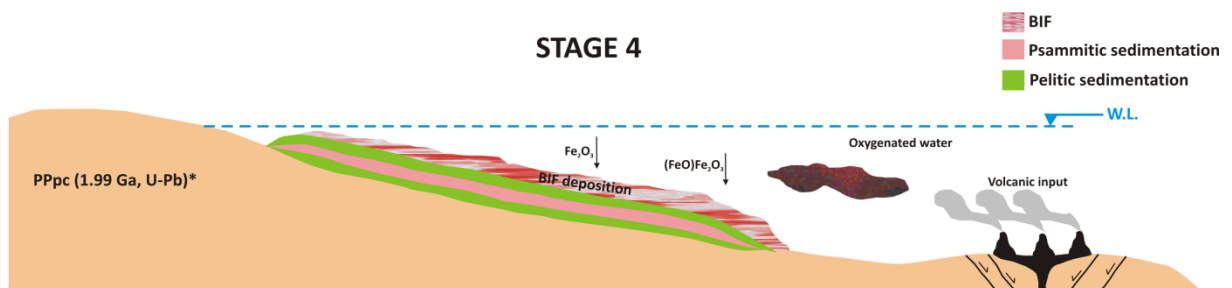
The fact is, hematite and magnetite can be in equilibrium in a large range of Eh-pH conditions (KRAUSKOPF; BIRD, 1995). The inexistence of large sulfide layers in the study area led us to conclude that extreme reducing and alkalinity conditions have not been attained the deposition of the BIF of the Bonito Mine.

In Chapter 4, the mineralogic study based on XRD data indicated the existence of greenalite as a matched-mineral-substance to be interpreted along other minerals. Although this ‘survivor mineral’ was reluctantly identified, it matches our understanding of more

oxidizing environment at stage #4 (Figure 108). Following the discussion of Krauskopf and Bird (1995), and tracing a subtle parallel to Lake Superior deposition paradigm, the Bonito BIF would be deposited not so far from the shore due to alternate volcanic emanations, so would be the silicate and silica gels dissolved in the ancient water (MEL'NIK, 1982).

The silica source (in the colloidal form) would be provided by the Neoproterozoic sea and the terrigenous input, as well. However, instead of what happens regarding the proposed facies model by James (1954), dissolution of colloidal silica is very sensitive to pH variations and to different concentration proportions (OKAMOTO *et al.* 1957).

Figure 108 – The fourth stage exhibiting the volcanic input activity and the deposition of the BIFs of Serra dos Quintos formation.



Source: Elaborated by the author.

Stage #5 represents the final stage of the volcano-sedimentary history of the Bonito basin (Figure 109). This stage can be divided into two phases: 5.1) implantation of a shallow marine environment, as a coast shoreline; 5.2) solute oversaturation provoking the precipitation of  $\text{CO}_3^{2-}$  forming a marine carbonatic platform.

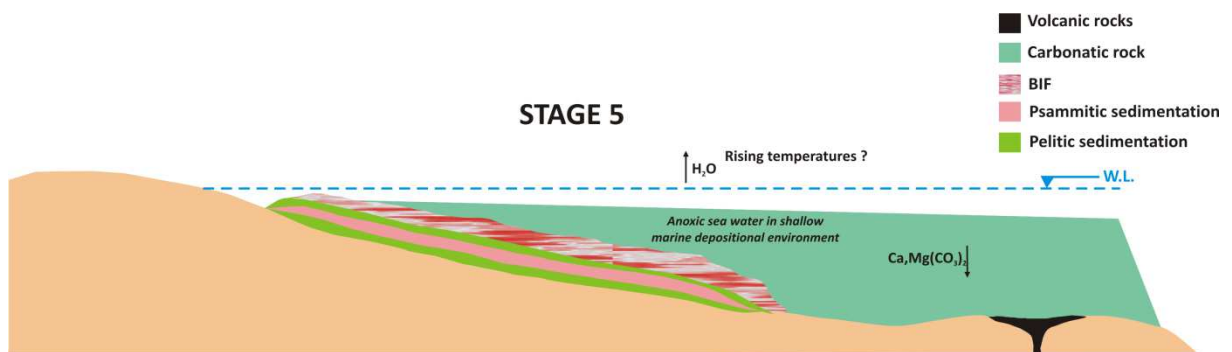
The source of  $\text{CO}_2$  of carbonate rocks would be provided by expressive volcanism which occurred in the last hundred million years of Neoproterozoic Era. Well documented magmatic syn and post-collisional events are widespread on the geological record at different sites in the world - related to the Pan-African orogenic event, such as Southern Brazil (SOMMER *et al.* 2013), Southeastern Turkey (GÜRSU *et al.* 2015), Central Iranian terrain (HONARMAND *et al.* 2016), to name a few.

The extreme volcanism event was responsible for the enormous input of hundreds of millions tons of  $\text{CO}_2$  in the atmosphere of that time. The Neoproterozoic oceans and narrow seas acted as super large carbon traps and they have transformed themselves into very expressive carbonate reservoirs. This particular event was taken into account for the formulation of the Snow Ball Earth hypothesis (SBE) by Kirschvink (1992).

The hypothesis for this stage can be explained by an extreme reversal of the oxygenation conditions, possibly, owing to an evaporation event that propitiated anoxic conditions and reducing the solubility of the carbonates. As an analog to well known evaporitic basins, extreme climate conditions have induced crucial changes to the hydrogeochemical balance within the basin (Figure 109). One possible scenario would be linked to high temperatures and dry air weather that forced the elevation of the basinal evaporation rates. Another scenario can be drawn from the SBE hypothesis that explains successfully the metallogenesis and the geological evolution of Rapitan Group (KLEIN; BEUKES, 1993), Urucum/Jacadigo Group (KLEIN; LADEIRA, 2004), Damara belt (BREITKOPF, 1987) and other correlative glaciogenic BIF deposits.

Krauskopf and Bird (1995), however, argued about some laboratory experiments results on dolomite formation and precipitation on natural conditions, as well. Under low temperatures, the massive dolomite production seems unlikely, in consequence of very low rates of formation. These authors concluded the low rates of formation is due to the lack of proper conditions to reach highly ordered crystallographic structures under low temperatures condition.

Figure 109 – The fifth stage depicts a shallow marine depositional environment developed owing to a narrow sea.



Source: Elaborated by the author.

## 9.2 Stage 6: Metamorphism and deformation

Although there is no schematic illustration for stage #6 of our model, it would be related to the tectonic events of the Brasiliano/Pan-African orogeny. Intense folding, transcurrent shear zones and lateral escapes(?) are the major features already reported by many authors. Putting Bonito basin in a wider geotectonic context is not an easy task, due to

its small area of occurrence, however, the available data allows us to explore some peculiarities of the evolution of this particular geological window of the Serido belt.

The geological model (solid modeling) exhibits both volcanic and intrusive bimodal (acidic and basic) activity, modeled as interbedded rocks within the metasedimentary sequence. In this study, however, determining accurately whether these rocks are syn-depositional, or post-depositional was not possible. However, some scenarios can be drawn.

Once magmatic events do not take expressive areas within the research site, one can consider these events been related to the Neoproterozoic granites emplacement, remarking a late-magmatic pulse – represented by granitoids of Itaporanga and Dona Inês intrusive suites (collectively named by ANGELIM *et al.* 2006 as the ‘São Rafael Brasileiro Magmatism’, 580 - 555 Ma SHRIMP U-Pb). Furthermore, the hydrothermal activity would explain the metamorphic reactions on the sedimentary protoliths (See section 4.4 for reference).

Although there is no clear evidence of syn-tectonic emplacement of the plutons surrounding the study area, on a regional scale, Angelim *et al.* (2006) reported the batholiths as syn- to late-tectonic.

Other regions of the Borborema Province, equally affected by the Brasileiro orogeny, such as the Northwest and Central domains of Ceará State, transcurrent tectonics regime and emplacement of intrusive bodies went through transtensional zones, between 614 and 591 Ma (FETTER, 1994). Regarding the study area, with proper structural mapping and field relations control, probably, such a geotectonic frame would fit the Neoproterozoic granites and the Seridó metasedimentary sequences.

The BIF typology is a response to the post-tectonic-metamorphic event. Martitization process has modified the mineralogical structure of magnetitic itabirites, as already discussed in section 4.2 of this thesis. Such a process would be related to the metasomatic episodes that have acted in some expressive parts of the itabiritic body.

In the study area, the subhorizontal foliations associated with the D<sub>2</sub> phase are present in the Bonito Mine establishes an expressive antiformal fold with an N-S axial plane and dip-direction heading south. The Fe-richer itabirites are positioned at the central sector corresponding to a thicker lithology whereas the marbles of the Jucurutu Formation surround the external border of the major fold (See Figure 104D for reference).

### 9.3 Discussion

Many authors have proposed geodynamic models for the Seridó mobile belt. Sá (1994) and Sá *et al.* (1995) gathered massive structural, lithostratigraphic and geochronological data concluded that Seridó belt evolved from an intracontinental rift until a passive continental margin, insomuch Seridó metasedimentary sequence was deposited under an extensional tectonic regime. The main point of Sá's geodynamic model is that the entire sequence would evolve based on the polycyclic geodynamics paradigm. The transcurrent regime would be related to the collisional phase (ocean closure) during the Brasiliano orogeny.

Caby *et al.* (1995) discussed the Brasiliano evolution model in terms of monocyclic deformation phases. Hackspacher *et al.* (1997) followed the general concept of Caby *et al.* (1995) to discuss the overthrusting structures interpreted as lateral escapes during the Brasiliano orogeny.

Nascimento (2002) presented two possible deposition ages of Seridó Group (640 – 590 Ma and 573 Ma, as minimum age). According to this author, the complex lithological association and the difficulties of identification of the main geotectonic features of the rift system (SÁ, 1994), the oceanic magmatism, basin inversion, and the collisional suture were considered as remaining issues.

Van Schmus *et al.* (2003) expressively contributed with Sm-Nd and U-Pb (on detrital zircons) data collected from several localities throughout the Seridó coverage. Their evolving model does not encompass the stages of Wilson's Cycle. They concluded the deposition occurred ca. 610 - 650 Ma and, the deformation and metamorphism of the units of the Seridó Group was interpreted as a syn-Brasiliano orogeny event (ca. 600 Ma).

Van Schmus *et al.* (2003) discussed an evolving model based on small marine intracontinental basins developed upon a Paleoproterozoic embasement (in our study represented by Poço da Cruz suite).

Sial *et al.* (2015) argued in favor of a deposition model in accordance with the highly glaciogenic influenced environment. The Seridó's geological setting and their consistent isotopic data conducted these authors to sound conclusions. Not only the carbonate cap would be explained by the extreme carbonatic dissolution, but the entire metasedimentary sequence would fit the large scale glaciation during the end of Cryogenian glacial event (known as Varenger or Marinoan, YOUNG, 2002). In a broader context, these glaciations play their roles in the SBE hypothesis postulated by Kirschvink (1992).

Other evidence presented by Campos (2011) and Sial *et al.* (2015) was the reporting of tilitas at Ouro Branco (Rio Grande do Norte State) and Serra dos Quintos (Paraíba and Rio Grande do Norte States) – firstly identified by Legrand *et al.* (2008), as an unusual interpreted glaciogenic rock placed between the gneisses and marbles of Jucurutu Formation and mica schists of Seridó Formation. These authors, however, described the glacial deposit as highly deformed rocks with unpreserved primary features.

Barbosa (2013) described the marbles of Jucurutu Formation as derived from a magnesian limestone protolith. Campos (2011) presented chemical data related to a calcitic marble as a lithologic unit of Jucurutu Formation. The hydrothermally formed iron ore studied by Barbosa (2013) and broadly exploited by MHAG Co. as a magnesian skarn (high-grade iron ore) is strongly indicative that this iron ore became as an Mg-enriched lithology related to the marbles of Jucurutu Formation.

The above reportings are subjects for further investigations, whereas the proper characterization has its own implications regarding the evidence; whether the glaciation phenomena can be confirmed, or reviewed under new data perspective, or refuted under the state-of-art knowledge.

The six-staged model presented in this study is supported by the basic concept that Bonito basin has evolved from a very small basin, initially receiving fluvial sedimentary input (chiefly corresponding to the clastic sequences of the Serra dos Quintos Formation) and, inasmuch the stress field related to the assembly of the Western Gondwana was progressively increasing, a basin floored by the Paleoproterozoic basement was forming.



## **10 CONCLUSIONS, FINAL REMARKS AND SUGGESTIONS FOR FUTURE WORKS**

This closing chapter reunites the conclusions reached for research field developed throughout this thesis. Each section is related to one specific topic forming the previous chapters. Moreover, suggestions for future works are presented as final thoughts concerning the continuation or extension of some specific branch of the research field.

### **10.1 Petrographic and mineralogical characterization of the BIF**

The petrographic studies were conducted in order to recognize the compounding BIF rocks in the Bonito Mine. Although this study was not specialized in ore petrology, the information stemmed from the petrographic data was crucial to the multivariate analyses. The petrographic information was combined and conciliated with the large geochemical database offering a supervised CA modeling methodology.

XRD on powdered samples of BIF were analyzed providing additional information of the present mineral assemblages. Although XRD analyses provide qualitative mineralogical data, much of that confirmed was observed and identified under optical microscopy.

Hence, the petrographic studies were, indeed, the starting point to the analytical work on this thesis.

### **10.2 Identification geochemical outliers with PCA**

Considering the PCA results, it can be concluded, despite the multiGaussian distribution model does not necessarily fit the research data presented in this study, PCA has proven to be a quick start to evaluate the exhaustive dataset, and to map the geochemical anomalies within it. Once the main correlation ( $\text{Fe}_2\text{O}_3 \times \text{SiO}_2$ ) was determined on the factorial plane, the other variables were interpreted as an auxiliary source of relevant information.

The joint  $\text{Al}_2\text{O}_3$ -Mn plot analysis exhibits an important terrigenous input to the basin. Phosphorus content has a strict relation to the origin of the Fe-rich BIF. Notwithstanding, the lack of additional mineralogical data does not allow us to identify what is the precise source of phosphorus contents. However, the mapped anomalies can be considered as a starting point to investigate more accurately what sources could be.

### 10.3 The Bonito Mine BIF multivariate typology model

As the main result obtained from the ore typological model proposed in this work, it can be stated that not all ore petrographic types were separated into distinct groups over the factorial plane. A clear-cut conclusion is that CA applied to the geochemical data has shown that some *a priori* ore types are closely associated with each other.

Hence, in this case, CA modeling itself can be interpreted as a factorial cluster technique, where each point on the factorial plane can encompass more than one sample (Figure 39). The K-means non-hierarchical cluster method has proven to be the appropriate tool to obtain the *nuclei* of each group (ore type), allowing to recognize other similar geochemical BIF samples and to establish the most reliable ore typology that can be established on the basis of the available data.

Even though, it was not possible to verify whether the martitization was due to medium-high temperatures on amphibolite facies metamorphism or related to a strong weathering process, as it was reported on other iron ore deposits (AIRES-BARROS, 1963; RAMDOHR, 1969; VERÍSSIMO, 1999; KLEIN, 2004). The trend to a certain dominance of martitic itabirites at the negative sector of Axis 1 indicates an increase in silicates in that area.

As an outcome of the proposed methodology, the BIF lithology in Serra dos Quintos Formation is now advantageously understood in terms of geological processes. The information derived from typology modeling can disclose elements useful for enhancing important undertakings like geological modeling, mining planning, and ore processing.

### 10.4 Weathering conditions evaluation through multivariate analysis

This study stemmed from the combination of geochemical quantitative data and qualitative geotechnical data. Multivariate modeling disclosed important information regarding the differentiation of BIF rocks due to their geological characteristics.

In order to manage such a large database, multivariate modeling tools were applied as the obvious solution to summarize the whole bunch of diversified data. CA procedures integrated quantitative hard data (geochemical) and qualitative soft data (geotechnical).

The methodological strategy linking CA to clustering techniques was accomplished. Although the main structure was graphically and clearly understood some issues remained hazy, such as a border-like division for an intended classification of samples-

variables interaction. In this particular case, petrographic samples were used as a proxy for supervised classification.

Similar to a try-and-error procedure, several clustering techniques were applied and the results have shown that the Complete Linkage algorithm has delivered the most adequate model. Minkowski's Power metric was able to improve the interpretation of CA results taking into account that factorial scores are outcomes from an orthogonal transformation (Figure 46).

From the ore geology point of view, mining efforts can be orientated to BIF types within Cluster 2 that gathers the Fe-richer itabirites classified as moderately to highly weathered friable porous materials. Conversely, BIF rocks assembled by Cluster 1 are less weathered and more compact non-porous materials, mostly positioned at deeper levels that may implicate higher exploitation costs.

According to the proposed methodological strategy, an overload of information on the dendrogram's compressed structure was avoided. The limits built on Figure 47 rely on a broad principle to interpret the factorial plane where closer samples and variables are positively associated, and otherwise, they are not or they are negatively associated.

The supervised classification provided by the joint interpretation is the base of the model. Therefore, we think this approach is suitable for any situation and despite the geological setting; it can deal with a wide range of miscellaneous geological issues.

It remained unclear how intense chemical weathering has contributed to the balance between land forming and soil covering. Fieldwork, however, has shown an absence of extensive and well-developed soil profiles topping at the studied BIFs.

Finally, some mining and mineral processing issues of Bonito mine were not properly addressed. Since some groups of Fe- richer itabirites were gathered in a major multivariate structure, namely Cluster 2, a detailed emphasis can be drawn on these types. Cluster 2 is electable to be treated as a subset in terms of more specific mining operational constraints such as depth intervals, BIF typology, geochemical grades, and geomechanical characterization.

### **10.5 Simple chemical criteria for geochemical classification of the analyzed BIF**

This chapter resulted from a study that was based on geochemical data treatment to elaborate chemical diagrams for BIF deposits classification. The chemical database is

provided by published scientific studies that presented raw data such as major oxides and REE data.

Preliminary analysis based on PCA has shown that the two first principal components describe the general factorial display of the correlated geochemical variables. The multi-dimensional reduction allowed choosing the most significant geochemical variables. Figures 50 and 51 exhibit the BIF deposits display into the ternary diagram field. Most of the BIF deposits, according to their genetic model, were plotted into domains; each of them referring to a metallogenic setting.

The use of  $Al_2O_3+TiO_2 - CaO+K_2O - MgO$  formula discarding  $Fe_2O_3$  and  $SiO_2$ , avoided the dilution effect that these chemical components would promote. Furthermore,  $Fe_2O_3$  and  $SiO_2$  contents are highly variable and would introduce some kind of bias to the analysis.

The bivariate plot  $La_n/Ce_n$  vs.  $MgO/(CaO+MgO)$  was constructed to investigate possible new metallogenic grouping. In this plot, all the metallogenic models were analyzed and the genetic domains were delimited. The use of NASC-normalizes REE ratio improved the interpretation of the glaciogenic deposits. Although few data have been analyzed, the geochemical trend is indicative of its own signature. Consultations to available scientific studies have demonstrated the lack of analyzed data concerning glaciogenic BIF deposits.

In each of the projected diagrams, not all BIF deposits were plotted in their correct domains. In such cases, additional work is necessary to increase the knowledge about these particular situations.

The presented diagrams are not intended to be a definitive analytical tool, but a preliminary contribution to the geochemical study of BIF deposits. The simple chemical criteria developed in this study can be used to evaluate additional data.

## **10.6 Geostatistical modeling of the mineralized thickness**

Mineralized thickness can be considered as a simplified approximation to 3-D geostatistical block modeling (JOURNEL; HUIJBREGTS, 1978; DEUTSCH; JOURNEL, 1992). Mass estimation with kriged grade modeling was not the goal of this research.

Owing to the typological complexity of the Bonito Mine (FONTELES *et al.* 2018), it was not possible to discriminate which itabirite type was thicker in terms of spatial distribution. In the same core log, an alternating itabirite type pattern was often noticeable.

The variable “thickness” was based on the geological continuity through the Serra dos Quintos Formation, whereas not all drill holes contain sampled itabiritic rocks. Therefore, blanked-off squared areas were delimited indicating the absence of kriged and simulated thickness data.

Spatial mineralized thickness assessment indicated that estimation methods such as OK and SK could be applied as a first step in the modeling process. Both OK and SK variance maps revealed a measure of uncertainty in some areas, primarily those with low sampling spots. The smoothing effect related to these estimation methods cannot be avoided without any post-processing technique (YAMAMOTO, 2008; ZHAO *et al.* 2014). The use of SK was justified using the arithmetic mean as a known global mean. As shown in Table 23, the SK estimates did not present any advantage.

Regarding SGS simulated realizations, basic descriptive statistics and target histogram reproduction were performed using stochastic images. However, the E-type and M-type estimated images did not reproduce the statistical features. It was expected that a positively skewed data distribution (Figure 54) would be difficult to replicate.

DSS operates based on the Gaussianity-free hypothesis. In our study, 100 simulations were generated with deviation corrections of the global mean and variance. DSS stochastic images presented more consistent target statistics than SGS. Nevertheless, SA was necessary as a post-processor method to yield the best statistical results and reproduce the target semivariograms.

Instead of selecting the best stochastic realization (among 100) to SA post-processing and match the target statistics precisely, a broader approach, i.e., through E-type and M-type estimate images, was presented. The SA method was not performed unconditionally, inasmuch as the goal of this study was to map the mineralized thickness surface as accurately as possible. Hence, the stochastic simulation would have to represent both the global statistics of the target histogram and local data honoring.

The mineralized thickness map assembled by stochastic simulation provided a clear delimitation of the thicker areas that may correspond to the most deformed strata of the BIF within the Serra dos Quintos Formation in the Bonito Mine (Figure 68) in the hinge of the Bonito Fold. Jiafu *et al.* (1987) when studying some Precambrian BIFs in South China, also observed such a situation. Despite the small area of the mining site, the folded BIF rocks may match a major transpressional area formed during the most intense overthrusting phase of the Seridó Group.

### 10.7 Tridimensional geological modeling of the Bonito Mine

The geological modeling exhibited the most relevant geological features of the Bonito Mine, enhancing the lithological relations of the study area. Voxel modeling as the working method has provided substantial geological information, mainly, about the less voluminous rocks, such as the volcanic rocks, phyllite, ferruginous quartzite, etc.

The volcanic rocks appear concordant to the main lithostratigraphic setting. These lithotypes are a relevant record and must be subjected to additional investigation in order to accurate their stratigraphical and geochronological relations with the metamorphic sequence.

The solid models have revealed that the stratigraphical setting matches with the main general stratigraphic schemes, which have been proposed previously (SÁ, 1994; CABY *et al.* 1995; FERREIRA; SANTOS, 2000; ANGELIM *et al.* 2006). Although in this thesis, the stratigraphic proposal by ANGELIM *et al.* (2006) was adopted, the small area displaying the modeled lithological assemblage has shown that some stratigraphic issues are also subjects for additional study.

According to Angelim *et al.* (2006) BIFs are described in both Serra dos Quintos Formation and Jucurutu Formation. In our study, we have modeled the itabirite body interbedded within the gneisses (paragneisses) and schists of the Serra dos Quintos and the marbles of Jucurutu Formation. The deeper gneisses of the geological model were considered as the representatives of the ortogneisses of the Poço da Cruz suite.

### 10.8 Evolution model of the Bonito Mine study area

Proposing an evolution model to such a small area can be, at the same time, a simple task, or a very tricky one. As discussed in Chapter 9, the Bonito Mine area has a very particular lithological setting and it is clearly related to a former volcano-sedimentary basin. As proposed on the grounds of the geological modeling, the early stages of the opening basin have occurred on a Paleoproterozoic basement (Poço da Cruz suite). The basic model would be a rift-type, which allowed the development of a narrow sea during the evolving stages of the local extensional regime.

Due to unknown onsite geochemical constraints of the BIF deposition, a question regarding what primary iron ore mineral was the first to precipitate remains unclear.

The identification of volcanic rocks (bimodal volcanism) may assign a specific magmatic record regarding a post-Brasiliano/Pan-African orogeny event. Further studies are

necessary to test this hypothesis. In addition, this magmatic event could be the source of the hydrothermal action on the BIF rocks.

Strong evidence of a possible glaciogenic has solid support on isotopic data analyzed by Campos (2011) and Sial *et al.* (2015). However, marbles comprised of Jucurutu Formation in the study area are derived from magnesian limestones protoliths. As pointed out by Krauskopf and Bird (1995), this chemical character may be interpreted as evidence against a glaciogenic environment for the deposition of BIFs. Nonetheless, further scientific investigation needs to be carried on to reinforce the available gathered data and information.

### **10.9 Suggestions for future work**

This thesis is not a final statement regarding the study area. Many issues arose from the diverse investigation areas developed during the research work. Hence, we shall indicate some research subjects that can be eligible for future studies:

- ✘ Extend the BIF typological model with the aid of machine learning algorithms. The study performed coupling factorial and cluster methods could be evaluated under the modern classification algorithms;
- ✘ Geomagnetic properties of magnetitic and martitic itabirites should be explored establishing geological and/or tectonic relations with similar BIF rocks throughout the Seridó mobile belt. Special sampling methods are required;
- ✘ Volcanic rocks identified and spatialized, within the solid geological model, could be sampled from the boreholes for chemical and isotopic analyses purposes. A geochronological study would bring sound information regarding the particular timing of the Neoproterozoic volcanism in that area. This would elucidate whether these rocks are syn-orogenic or, post-orogenic.

## REFERENCES

- AIRES-BARROS, Luís. **Mineralogia dos jazigos de ferro e manganês de Goa**. 1963. 223 f. Tese (Cátedra de Mineralogia e Petrologia), Instituto Superior Técnico, Universidade de Lisboa, Lisboa, 1963.
- AKELLA, Jagannadham; WINKLER, Helmut G. F. Orthorhombic amphibole in some metamorphic reactions. **Contributions to Mineralogy and Petrology**, [s.l.], v. 12, n. 1, p.1-12, mar. 1966. Springer Science and Business Media LLC. Disponível em: <http://dx.doi.org/10.1007/bf02651124>. Acesso em: 15 jul. 2019.
- ALBERÈDE, François. **Geochemistry: An Introduction**. 2.ed. Cambridge: Cambridge University Press, 2009. 356 p.
- ALMEIDA, F.F.M. *et al.* Brazilian structural provinces: An introduction. **Earth-Science Reviews**, [s.l.], v. 17, n. 1-2, p.1-29, abr. 1981. Elsevier BV. Disponível em: [http://dx.doi.org/10.1016/0012-8252\(81\)90003-9](http://dx.doi.org/10.1016/0012-8252(81)90003-9). Acesso em: 09 ago. 2016.
- ALMEIDA, Ricardo Froitzheim Rinelli de. **Modelagem Geológica do Entorno da Lagoa de Jacarepaguá**. 2011. 175 f. Dissertação (Mestrado) – Pós-Graduação em Engenharia Civil, PUC-RIO, Rio de Janeiro, 2011.
- AMORIM, Renato Cordeiro de. A survey on feature weighting based k-means algorithms. **Journal of Classification**, [s.l.], v. 33, n. 2, p.210-242, jul. 2016. Springer Nature. Disponível em: <http://dx.doi.org/10.1007/s00357-016-9208-4>. Acesso em: 25 out. 2017.
- ANGELIM, Luís Alberto de Aquino; MEDEIROS, Vladimir Cruz de; NESI, Júlio de Rezende. **Mapa geológico do Estado do Rio Grande do Norte**. Programa Geologia do Brasil–PGB. CPRM/FAPERN. Projeto Geologia e Recursos Minerais do Estado do Rio Grande do Norte. Recife, 2006. Color. Escala. 1:500.000.
- APPEL, Peter W Uitterdijk. On the early Archaean Isua iron-formation, West Greenland. **Precambrian Research**, [s.l.], v. 11, n. 1, p.73-87, fev. 1980. Elsevier BV. Disponível em: [http://dx.doi.org/10.1016/0301-9268\(80\)90081-9](http://dx.doi.org/10.1016/0301-9268(80)90081-9). Acesso em: 15 mai. 2019.
- ARCHANJO, Carlos José; BOUCHEZ, Jean Luc. Le Seridó, une chaîne transpressive dextre au Proterozoïque supérieur du Nord-est du Brésil. **Bulletin de La Société Géologique de France**, [s.l.], v. 162, n. 4, p.637-647, 1 jul. 1991. EDP Sciences. Disponível em: <http://dx.doi.org/10.2113/gssgfbull.162.4.637>. Acesso em: 01 set. 2016.
- ARCHANJO, Carlos José.; VIEGAS, Luis G. F.; HOLLANDA, Maria Helena B. M.; SOUZA, Laécio C., LIU, Dunyi. Timing of the HT/LP transpression in the Neoproterozoic Seridó Belt (Borborema Province, Brazil): Constraints from U-Pb (SHRIMP) geochronology and implications for the connections between NE Brazil and West Africa. **Gondwana Research**, [s.l.], v. 23, n. 2, p.701-714, mar. 2013. Elsevier BV. Disponível em: <http://dx.doi.org/10.1016/j.gr.2012.05.005>. Acesso em: 01 set. 2016
- AREF, M. M. El *et al.* Diagenetic and metamorphic history of the Umm Nar BIF, Eastern Desert, Egypt. **Mineralium Deposita**, [s.l.], v. 28, n. 4, p.264-278, set. 1993. Springer



Science and Business Media LLC. Disponível em: <http://dx.doi.org/10.1007/bf02421576>. Acesso em: 20 jul. 2018.

ARORA, M. *et al.* Geochemistry and origin of Archean banded iron-formation from the Bababudan schist belt, India. **Economic Geology**, [s.l.], v. 90, n. 7, p.2040-2057, 1 nov. 1995. Society of Economic Geologists. Disponível em: <http://dx.doi.org/10.2113/gsecongeo.90.7.2040>. Acesso em: 11 jun. 2018.

BALLADUR, Jean-Pierre. Analyse factorielle des correspondances. **Annales de L'insée**, Paris, v. 4, n. 1, p.47-79, set. 1970.

BARBOSA, Irla Gonçalves. **Mina do Bonito – Tipologia e geoquímica dos minérios de ferro, Jucurutu/RN – Brasil**. 2013. 186 f. Dissertação (Mestrado) – Pós-graduação em Geologia, Departamento de Geologia, Universidade Federal do Ceará, Fortaleza, 2013. Disponível em: <http://www.repositorio.ufc.br/handle/riufc/21818>. Acesso em: 10 out. 2016.

BASTA, Fawzy F. *et al.* Petrology and geochemistry of the banded iron formation (BIF) of Wadi Karim and Um Anab, Eastern Desert, Egypt: Implications for the origin of Neoproterozoic BIF. **Precambrian Research**, [s.l.], v. 187, n. 3-4, p.277-292, jun. 2011. Elsevier BV. Disponível em: <http://dx.doi.org/10.1016/j.precamres.2011.03.011>. Acesso em: 10 out. 2016.

BASU, A.; CELESTINO, Tarcísio Barreto; BORTOLUCCI, Airton A. Evaluation of rock mechanical behaviors under uniaxial compression with reference to assessed weathering grades. **Rock Mechanics and Rock Engineering**, [s.l.], v. 42, n. 1, p.73-93, 5 maio 2009. Springer Science and Business Media LLC. Disponível em: <http://dx.doi.org/10.1007/s00603-008-0170-2>. Acesso em: 12 nov. 2018.

BELEVTSSEV, Ya N; BELEVTSSEV, R Ya; SIROSHTAN, R I. The Krivoy Rog Basin. In: TRENDALL, A F; MORRIS, R C (Ed.). **Iron-Formation: Facts and Problems**. Amsterdam: Elsevier Science, 1983. p. 211-252

BENZÉCRI, Jean-Paul. **L'Analyse des Données, Vol. 2: L'Analyse des Correspondances**. Paris: Dunod, 1973. 632 p.

BENZÉCRI, J. P. Histoire et préhistoire de L'Analyse des Données - Partie V: L'analyse des correspondances. **Cahiers de L'analyse des Données**, Paris, v. 1, n. 2, p.9-40, 1977. Disponível em: [http://www.numdam.org/item/1977\\_2\\_1\\_9\\_0/](http://www.numdam.org/item/1977_2_1_9_0/). Acesso em: 19 set. 2015.

BEUKES, Nicolas J.; KLEIN, Cornelis. Geochemistry and sedimentology of a facies transition from microbanded to granular iron-formation — in the early Proterozoic Transvaal Supergroup, South Africa. **Precambrian Research**, [s.l.], v. 47, n. 1-2, p.99-139, abr. 1990. Elsevier BV. Disponível em: [http://dx.doi.org/10.1016/0301-9268\(90\)90033-m](http://dx.doi.org/10.1016/0301-9268(90)90033-m). Acesso em: 19 jul. 2016.

BIRKS, Hillary John B. Multivariate analysis in geology and geochemistry: An introduction. **Chemometrics and Intelligent Laboratory Systems**, [s.l.], v. 2, n. 1-3, p.15-28, ago. 1987. Elsevier BV. Disponível em: [http://dx.doi.org/10.1016/0169-7439\(87\)80082-5](http://dx.doi.org/10.1016/0169-7439(87)80082-5). Acesso em: 25 jun. 2016.

BOSTRÖM, Kurt. Submarine volcanism as a source for iron. **Earth and Planetary Science Letters**, [s.l.], v. 9, n. 4, p.348-354, nov. 1970. Elsevier BV. Disponível em: [http://dx.doi.org/10.1016/0012-821x\(70\)90134-2](http://dx.doi.org/10.1016/0012-821x(70)90134-2). Acesso em: 25 jul. 2019.

BOUFASSA, Azeddine; ARMSTRONG, Margaret. Comparison between different kriging estimators. **Mathematical Geology**, [s.l.], v. 21, n. 3, p.331-345, abr. 1989. Springer Science and Business Media LLC. Disponível em: <http://dx.doi.org/10.1007/bf00893694>. Acesso em: 20 mar. 2019.

BRAGA, Flávia Cristina Silveira; ROSIERE, Carlos Alberto; SANTOS, João Orestes Schneider; HAGEMANN, Steffen G.; SALLES, Pedro Valle. Depicting the 3D geometry of ore bodies using implicit lithological modeling: An example from the Horto-Baratinha iron deposit, Guanhões block, MG. **REM - International Engineering Journal**, [s.l.], v. 72, n. 3, p.435-443, set. 2019. FapUNIFESP (SciELO). Disponível em: <http://dx.doi.org/10.1590/0370-44672018720167>. Acesso em: 02 set. 2019.

BREITKOPF, Jörg H. Iron formations related to mafic volcanism and ensialic rifting in the southern margin zone of the Damara Orogen, Namibia. **Precambrian Research**, [s.l.], v. 38, n. 2, p.111-130, fev. 1988. Elsevier BV. Disponível em: [http://dx.doi.org/10.1016/0301-9268\(88\)90087-3](http://dx.doi.org/10.1016/0301-9268(88)90087-3). Acesso em: 07 jul. 2019.

BRONNER, G.; CHAUVEL, J. J. Precambrian banded iron-formations of the Ijil Group (Kediat Ijil, Reguibat Shield, Mauritania). **Economic Geology**, [s.l.], v. 74, n. 1, p.77-94, 1 fev. 1979. Society of Economic Geologists. Disponível em: <http://dx.doi.org/10.2113/gsecongeo.74.1.77>. Acesso em: 07 jul. 2019.

BROWN, Charles E. **Applied Multivariate Statistics in Geohydrology and Related Sciences**. Berlin: Springer-Verlag, 1998. 248 p.

CABY, Renault.; ARTHAUD, Michel Henri; ARCHANJO, Carlos José. Lithostratigraphy and petrostructural characterization of supracrustal units in the Brasiliano belt of Northeast Brazil: geodynamic implications. **Journal of South American Earth Sciences**, [s.l.], v. 8, n. 3-4, p.235-246, jul. 1995. Elsevier BV. Disponível em: [http://dx.doi.org/10.1016/0895-9811\(95\)00011-4](http://dx.doi.org/10.1016/0895-9811(95)00011-4). Acesso em: 01 set. 2016.

CABY, Renault; ARTHAUD, Michel Henri. Major Precambrian nappes of the Brazilian belt, Ceara, northeast Brazil. **Geology**, [s.l.], v. 14, n. 10, p.871-874, 1986. Geological Society of America. Disponível em: [http://dx.doi.org/10.1130/0091-7613\(1986\)142.0.co;2](http://dx.doi.org/10.1130/0091-7613(1986)142.0.co;2). Acesso em: 01 abr. 2016.

CABY, Renault; SIAL, Alcides da Nóbrega; ARTHAUD, Michel Henri. Crustal evolution and the Brasiliano orogeny in Northeastern Brazil. In: **THE WEST AFRICAN OROGENS AND CIRCUM-ATLANTIC CORRELATIONS, 1, 1991**, Berlin. The West African orogens and circum-Atlantic correlations. Berlin: Springer Verlag, 1991. p. 373 - 397.

CAERS, Jeff. Adding local accuracy to direct sequential simulation. **Mathematical Geology**, [s.l.], v. 32, n. 7, p.815-850, 2000. Springer Nature. Disponível em: <http://dx.doi.org/10.1023/a:1007596423578>. Acesso em: 19 fev. 2019.

CAMPOS, Marcel Sena. **Quimioestratigrafia isotópica de carbono e estrôncio e geoquímica de elementos terras raras em formações carbonáticas e ferríferas do Cinturão Seridó, Nordeste do Brasil**. 2009. 99 f. Dissertação (Mestrado) – Pós-graduação em Geociências, Departamento de Geologia, Universidade Federal do Pernambuco, Recife, 2011.

CARVALHO, Helena. **Análise Multivariada de Dados Qualitativos: Utilização da Análise de Correspondências Múltiplas com SPSS**. 2. ed. Lisboa: Edições Sílabo, 2017. 261 p.

CARVALHO, Ilson Guimarães. **Fundamentos da Geoquímica dos Processos Exógenos**. Salvador: Bureau Gráfica e Editora Ltda, 1995. 213 p.

CASTRO, Luís Oscar. Genesis of banded iron-formations. **Economic Geology**, [s.l.], v. 89, n. 6, p.1384-1397, 1 out. 1994. Society of Economic Geologists. Disponível em: <http://dx.doi.org/10.2113/gsecongeo.89.6.1384>. Acesso em: 01 set. 2017.

CATARINO, Bruno Manuel Prates. **Modelação tridimensional de uma jazida mineral prospectada por sondagens e objectivando a sua exploração a céu aberto**. 2009. 101 f. Dissertação (Mestrado) – Pós-graduação em Engenharia Geológica e de Minas, Instituto Superior Técnico, Lisboa, 2009.

CELEBI, M. Emre; KINGRAVI, Hassan A.; VELA, Patricio A. A comparative study of efficient initialization methods for the k-means clustering algorithm. **Expert Systems with Applications**, [s.l.], v. 40, n. 1, p.200-210, jan. 2013. Elsevier BV. Disponível em: <http://dx.doi.org/10.1016/j.eswa.2012.07.021>. Acesso em: 25 nov. 2017.

CMRP-IST. 2000. Geostatistical Modelling Software - GeoMS. Superior Technical Institute, University of Lisbon. Disponível em: <https://sites.google.com/site/cmrpsoftware/geoms>. Acesso em 13 mai. 2019.

COLLYER, P. L.; MERRIAM, D. F. An application of cluster analysis in mineral exploration. **Journal of the International Association for Mathematical Geology**, [s.l.], v. 5, n. 3, p.213-223, set. 1973. Springer Science and Business Media LLC. Disponível em: <http://dx.doi.org/10.1007/bf02111811>. Acesso em 30 nov. 2018.

COX, Grant M. *et al.* Neoproterozoic iron formation: An evaluation of its temporal, environmental and tectonic significance. **Chemical Geology**, [s.l.], v. 362, p.232-249, dez. 2013. Elsevier BV. Disponível em: <http://dx.doi.org/10.1016/j.chemgeo.2013.08.002>. Acesso em 25 jul. 2019.

CRAIG, James R.; VAUGHAN, David J. **Ore Microscopy and Ore Petrography**. 2. ed. New York: John Wiley and Sons, Inc., 1994. 434 p.

CVRM. 2002. **ANDAD 7.20** Software. Geosystems Centre. IST. Lisbon. Disponível em: <http://biomonitor.ist.utl.pt/~ajsousa/Andad.html>. Acesso em 12 fev. 2019.

DANTAS, Alexandre Ranier; NASCIMENTO, Marcos Antônio Leite do; COSTA, Alan Pereira; CAVALCANTE, Rogério. Petrografia e litoquímica de rochas ferríferas na região central do estado do Rio Grande do Norte (Domínio Rio Piranhas – Seridó, NE da Província Borborema). **Geologia USP. Série Científica**, [s.l.], v. 17, n. 3, p.163-187, 1 set. 2017.

Universidade de São Paulo Sistema Integrado de Bibliotecas - SIBiUSP. Disponível em: <http://dx.doi.org/10.11606/issn.2316-9095.v17-125622>. Acesso em 12 jun. 2018.

DAVIS, John C. **Statistics and Data Analysis in Geology**. 3. ed. New York: John Wiley and Sons Inc., 2002. 620 p.

DEARMAN, W. R. Weathering classification in the characterisation of rock for engineering purposes in British practice. **Bulletin of the International Association of Engineering Geology**, [s.l.], v. 9, n. 1, p.33-42, jun. 1974. Springer Science and Business Media LLC. Disponível em: <http://dx.doi.org/10.1007/bf02635301>. Acesso em 19 jun. 2018.

DEUTSCH, Clayton V.; COCKERHAM, Perry W. Practical considerations in the application of simulated annealing to stochastic simulation. **Mathematical Geology**, [s.l.], v. 26, n. 1, p.67-82, jan. 1994. Springer Science and Business Media LLC. Disponível em: <http://dx.doi.org/10.1007/bf02065876>. Acesso em 07 mar. 2019.

DEUTSCH, Clayton Vernon. **Annealing techniques applied to reservoir modeling and the integration of geological and engineering (well test) data**. 1992. 306 f. Tese (Doutorado) - Department of Applied Earth Sciences, Stanford University, Stanford, 1992.

DEUTSCH, Clayton V.; JOURNEL, André G. **GSLIB: Geostatistical Software Library and User's Guide**. New York: Oxford Press University, 1992. 352 p.

DORR II, J. V. N.; BARBOSA, A. L. M. 1963. Geology and ore deposits of the Itabira District, Minas Gerais, Brazil. **United States Geological Survey Professional Paper 341-C**, Washington, 110p.

DREVER, James I. Geochemical Model for the origin of Precambrian banded iron formations. **Geological Society of America Bulletin**, [s.l.], v. 85, n. 7, p.1099-1106, 1974. Geological Society of America. Disponível em: [http://dx.doi.org/10.1130/0016-7606\(1974\)852.0.co;2](http://dx.doi.org/10.1130/0016-7606(1974)852.0.co;2) Acesso em 09 jun. 2019.

DYMEK, Robert F.; KLEIN, Cornelis. Chemistry, petrology and origin of banded iron-formation lithologies from the 3800 MA Isua supracrustal belt, West Greenland. **Precambrian Research**, [s.l.], v. 39, n. 4, p.247-302, ago. 1988. Elsevier BV. Disponível em: [http://dx.doi.org/10.1016/0301-9268\(88\)90022-8](http://dx.doi.org/10.1016/0301-9268(88)90022-8). Acesso em 09 jul. 2019.

EMERY, Xavier; PELÁEZ, María. Assessing the accuracy of sequential Gaussian simulation and cosimulation. **Computational Geosciences**, [s.l.], v. 15, n. 4, p.673-689, 28 abr. 2011. Springer Science and Business Media LLC. Disponível em: <http://dx.doi.org/10.1007/s10596-011-9235-5>. Acesso em 15 mai. 2019.

ESSELL, Mark. Three-dimensional geological modelling of potential-field data. **Computers & Geosciences**, [s.l.], v. 27, n. 4, p.455-465, maio 2001. Elsevier BV. Disponível em: [http://dx.doi.org/10.1016/s0098-3004\(00\)00142-4](http://dx.doi.org/10.1016/s0098-3004(00)00142-4). Acesso em 16 jun. 2019.

FERREIRA, Cícero Alves, SANTOS, Edilton José dos. **Folha SB. 24-Z. Estados do Ceará, Rio Grande do Norte e Pernambuco. Jaguaribe SE**. Programa Levantamentos Geológicos Básicos do Brasil. CPRM. Recife, 2000. Color, Escala 1: 500.000.

FETTER, Allen H. **U-Pb and Sm-Nd geochronological constraints on the crustal framework and geologic history of Ceará State NW Borborema Province, NE Brazil: Implications for the assembly of Gondwana.** 1999. 164 f. Tese (Doutorado) – Pós-graduação em Geologia, University of Kansas, Kansas City, 1999.

FONTELES, Helano Régis da Nobrega. **Caracterização geotécnica do subsolo da porção nordeste do município de Fortaleza (CE) com base em Geoestatística.** 2003. 135 f. Dissertação (Mestrado) – Pós-graduação em Geotecnia, Universidade de São Paulo, São Carlos, 2003.

FONTELES, Helano Regis da Nóbrega; VERÍSSIMO, César Ulisses Vieira; PEREIRA, Henrique Garcia. Um modelo tipológico de minérios de ferro do tipo BIF por análise multivariada de dados geoquímicos: Uma aplicação à Mina do Bonito, Jucurutu (RN). In: CONGRESSO BRASILEIRO DE GEOLOGIA, 49., 2018, Rio de Janeiro. **Anais...** Rio de Janeiro: SBG, 2018. v.1, p. 1434.

FONTELES, H., PEREIRA, H., ROCHA, C., VERISSÍMO, C. 2019a. Mapping geochemical anomalies through principal components analysis in BIF Mines: An approach referring to the Bonito Mine, Northeastern Brazil. In: Doronzo, D., Schigaro, E., Armstrong-Altril, J., Zoheir, B. (eds). *Petrogenesis and Exploration of the Earth's Interior. **Advances in Science, Technology & Innovation.*** Springer Nature. Berlin, 245-247. Disponível em: [https://doi.org/10.1007/978-3-030-01575-6\\_59](https://doi.org/10.1007/978-3-030-01575-6_59). Acesso em 02 fev. 2019.

FONTELES, H. R. N.; PEREIRA, H. G.; VERÍSSIMO, C. U. V. Weathering Conditions Evaluation of Banded Iron Formations of Bonito Mine (Northeastern Brazil) Based on Coupled Cluster-Correspondence Analysis. **Anuário do Instituto de Geociências - UFRJ**, [s.l.], v. 42, n. 2, p.86-99, 9 ago. 2019b. Instituto de Geociências - UFRJ. Disponível em: [http://dx.doi.org/10.11137/2019\\_2\\_86\\_99](http://dx.doi.org/10.11137/2019_2_86_99). Acesso em 07 jul. 2019.

FOOKES, Peter G. **Tropical Residual Soils: A Geological Society Engineering Group Working Party Revised Report.** London: Geological Society, 1997. 184 p.

GEMAN, Stuart; GEMAN, Donald. Stochastic relaxation, Gibbs distributions, and the bayesian restoration of images. **IEEE Transactions On Pattern Analysis and Machine Intelligence**, [s.l.], v. -6, n. 6, p.721-741, nov. 1984. Institute of Electrical and Electronics Engineers (IEEE). Disponível em: <http://dx.doi.org/10.1109/tpami.1984.4767596>. Acesso em 07 mai. 2019.

GOOVAERTS, Pierre. **Geostatistics for Natural Resources.** New York: Oxford Press University, 1997. 496 p.

GOOVAERTS, Pierre. Accounting for estimation optimality criteria in simulated annealing. **Mathematical Geology**, [s.l.], v. 30, n. 5, p.511-534, 1998. Springer Nature. Disponível em: <http://dx.doi.org/10.1023/a:1021738027334>. Acesso em 07 mai. 2019.

GRAF, Joseph L. Rare earth elements, iron formations and sea water. **Geochimica et Cosmochimica Acta**, [s.l.], v. 42, n. 12, p.1845-1850, dez. 1978. Elsevier BV. Disponível em: [http://dx.doi.org/10.1016/0016-7037\(78\)90239-9](http://dx.doi.org/10.1016/0016-7037(78)90239-9). Acesso em 07 jul. 2019.

GRENACRE, Michel; BLASIUS, Jörg. **Multiple Correspondence Analysis and Related Methods: Methods. Statistics in the Social and Behavioral Sciences Series.** Boca Raton: Chapman & Hall/CRC, 2006. 607 p.

GROMET, Peter L. *et al.* The “North American shale composite”: Its compilation, major and trace element characteristics. **Geochimica et Cosmochimica Acta**, [s.l.], v. 48, n. 12, p.2469-2482, dez. 1984. Elsevier BV. Disponível em: [http://dx.doi.org/10.1016/0016-7037\(84\)90298-9](http://dx.doi.org/10.1016/0016-7037(84)90298-9). Acesso em 10 jul. 2019.

GROSS, Gilad A.; MCLEOD, Christopher R. A preliminary assessment of the chemical composition of iron formations in Canada. **Canadian Mineralogist**, Vancouver, v. 18, n. 2, p.223-229, 1 maio 1980.

GÜRSU, Semih *et al.* Neoproterozoic continental arc volcanism at the northern edge of the Arabian Plate, SE Turkey. **Precambrian Research**, [s.l.], v. 258, p.208-233, mar. 2015. Elsevier BV. Disponível em: <http://dx.doi.org/10.1016/j.precamres.2014.12.017>. Acesso em 01 ago. 2019.

GUTERRES, Ana Cristina Marques Coelho de Brito. **Análise de dados e geoestatística na tipologia de recursos petrolíferos.** 1993. 90 f. Dissertação (Mestrado) – Engenharia dos Petróleos, Instituto Superior Técnico, Lisboa, 1993.

HACKSPACHER, Peter Christian.; DANTAS, E. L.; Neves, Benjamin Bley Brito; LEGRAND, Jean Michel. Northwestern Overthrusting and Related Lateral Escape During the Brasiliano Orogeny North of the Patos Lineament, Borborema Province, Northeast Brazil. **International Geology Review**, [s.l.], v. 39, n. 7, p.609-620, jul. 1997. Informa UK Limited. Disponível em: <http://dx.doi.org/10.1080/00206819709465291>. Acesso em 05 jun. 2019.

HAIR Jr, Joseph F; ANDERSON, Rolph e; TATHAM, Ronald L. BLACK, William C. **Análise Multivariada de Dados.** 5. ed. São Paulo: Bookman Editora, 2005. 593 p. Trad.

HALVERSON, Galen P. *et al.* Neoproterozoic chemostratigraphy. **Precambrian Research**, [s.l.], v. 182, n. 4, p.337-350, out. 2010. Elsevier BV. Disponível em: <http://dx.doi.org/10.1016/j.precamres.2010.04.007>. Acesso em 25 jul. 2019.

HARDER, E. C. The “Itabirites” iron ores of Brazil. **Economic Geology**, [s.l.], v. 9, n. 2, p.101-111, 1 mar. 1914. Society of Economic Geologists. Disponível em: <http://dx.doi.org/10.2113/gsecongeo.9.2.101>. Acesso em 25 jul. 2016.

HARTIGAN, J. A.; WONG, M. A. Algorithm AS 136: A K-Means Clustering Algorithm. **Applied Statistics**, [s.l.], v. 28, n. 1, p.100-108, 1979. JSTOR. Disponível em: <http://dx.doi.org/10.2307/2346830>. Acesso em 25 nov. 2016.

HAUGAARD, Rasmus *et al.* The Joffre banded iron formation, Hamersley Group, Western Australia: Assessing the palaeoenvironment through detailed petrology and chemostratigraphy. **Precambrian Research**, [s.l.], v. 273, p.12-37, fev. 2016. Elsevier BV. Disponível em: <http://dx.doi.org/10.1016/j.precamres.2015.10.024>. Acesso em 21 jul. 2019.

HOHN, Michael E.; MCDOWELL, Ronald R. Uncertainty in coal property evaluation in West Virginia: A case of study. **Mathematical Geology**, [s.l.], v. 33, n. 2, p.191-216, 2001.

Springer Nature. Disponível em: <http://dx.doi.org/10.1023/a:1007535301969>. Acesso em 17 mar. 2019.

HOLLANDA, M. H. B. M.; ARCHANJO, C. J.; BAUTISTA, J. R.; SOUZA, L. C. Detrital zircon ages and Nd isotope compositions of the Seridó and Lavras da Mangabeira basins (Borborema Province, NE Brazil): Evidence for exhumation and recycling associated with a major shift in sedimentary provenance. **Precambrian Research**, [s.l.], v. 258, p.186-207, mar. 2015. Elsevier BV. Disponível em: <http://dx.doi.org/10.1016/j.precamres.2014.12.009>. Acesso em 26 abr. 2017.

HONARMAND, Maryam *et al.* Neoproterozoic–Early Cambrian tectono-magmatic evolution of the Central Iranian terrane, northern margin of Gondwana: Constraints from detrital zircon U–Pb and Hf–O isotope studies. **Gondwana Research**, [s.l.], v. 37, p.285-300, set. 2016. Elsevier BV. Disponível em: <http://dx.doi.org/10.1016/j.gr.2016.05.007>. Acesso em 26 ago. 2019.

HORSTMANN, Uwe E.; HÄLBICH, Ingo W. Chemical composition of banded iron-formations of the Griqualand West Sequence, Northern Cape Province, South Africa, in comparison with other Precambrian iron formations. **Precambrian Research**, [s.l.], v. 72, n. 1-2, p.109-145, mar. 1995. Elsevier BV. Disponível em: [http://dx.doi.org/10.1016/0301-9268\(94\)00086-7](http://dx.doi.org/10.1016/0301-9268(94)00086-7). Acesso em 26 jun. 2019.

HOTELLING, Harold. Analysis of a complex of statistical variables into principal components. **Journal of Educational Psychology**, [s.l.], v. 24, n. 6, p.417-441, 1933a. American Psychological Association (APA). Disponível em: <http://dx.doi.org/10.1037/h0071325>. Acesso em 16 jun. 2017.

HOTELLING, Harold. Analysis of a complex of statistical variables into principal components. **Journal of Educational Psychology**, [s.l.], v. 24, n. 7, p.498-520, 1933b. American Psychological Association (APA). Disponível em: <http://dx.doi.org/10.1037/h0071324>. Acesso em 16 jun. 2017.

JAIN, Anil K. Data clustering: 50 years beyond K-means. **Pattern Recognition Letters**, [s.l.], v. 31, n. 8, p.651-666, jun. 2010. Elsevier BV. Disponível em: <http://dx.doi.org/10.1016/j.patrec.2009.09.011>. Acesso em 05 dez. 2017.

JAMES, Harold Lloyd. Sedimentary facies of iron-formation. **Economic Geology**, [s.l.], v. 49, n.3, p.235-293, 1 maio 1954. Society of Economic Geologists. Disponível em: <http://dx.doi.org/10.2113/gsecongeo.49.3.235>. Acesso em 21 fev. 2017.

JESSELL, Mark. Three-dimensional geological modelling of potential-field data. **Computers & Geosciences**, [s.l.], v. 27, n. 4, p.455-465, maio 2001. Elsevier BV. Disponível em: [http://dx.doi.org/10.1016/s0098-3004\(00\)00142-4](http://dx.doi.org/10.1016/s0098-3004(00)00142-4) Acesso em 21 ago. 2019.

JI, H.; ZHU, Y.; WU, X. Correspondence cluster analysis and its application in exploration geochemistry. **Journal of Geochemical Exploration**, [s.l.], v. 55, n. 1-3, p.137-144, dez. 1995. Elsevier BV. Disponível em: [http://dx.doi.org/10.1016/0375-6742\(95\)00025-9](http://dx.doi.org/10.1016/0375-6742(95)00025-9) Acesso em 02 ago. 2018.

JØRGENSEN, Flemming; MOLLER, Rasmus Ronde; NEBEL, Lars; JENSEM, Niels-Peter; CHRISTIANSEN, Anders Vest; SANDERSEN, Peter B. E. A method for cognitive 3D geological voxel modelling of AEM data. **Bulletin of Engineering Geology and the Environment**, [s.l.], v. 72, n. 3-4, p.421-432, 12 nov. 2013. Springer Science and Business Media LLC. Disponível em: <http://dx.doi.org/10.1007/s10064-013-0487-2>. Acesso em 11 ago. 2019.

JOURNAL, Andrés G. Geostatistics for Conditional Simulation of Ore Bodies. **Economic Geology**, [s.l.], v. 69, n. 5, p.673-687, 1 ago. 1974. Society of Economic Geologists. Disponível em: <http://dx.doi.org/10.2113/gsecongeo.69.5.673>. Acesso em 09 dez. 2018.

JOURNAL, André G; HUIJBREGTS, Charles J. **Mining Geostatistics**. London: Academic Press, 1978. 600 p.

JOURNAL, André G. Modeling Uncertainty: Some Conceptual Thoughts. **Geostatistics for The Next Century**, [s.l.], p.30-43, 1994. Springer Netherlands. Disponível em: [http://dx.doi.org/10.1007/978-94-011-0824-9\\_5](http://dx.doi.org/10.1007/978-94-011-0824-9_5). Acesso em 09 dez. 2018.

KAKELA, Peter. Iron Ore: From Depletion to Abundance. **Science**, [s.l.], v. 212, n. 4491, p.132-136, 10 abr. 1981. American Association for the Advancement of Science (AAAS). Disponível em: <http://dx.doi.org/10.1126/science.212.4491.132>. Acesso em 15 dez. 2017.

KAUFMANN, Olivier; MARTIN, Thierry. 3D geological modelling from boreholes, cross-sections and geological maps, application over former natural gas storages in coal mines. **Computers & Geosciences**, [s.l.], v. 34, n. 3, p.278-290, mar. 2008. Elsevier BV. Disponível em: <http://dx.doi.org/10.1016/j.cageo.2007.09.005>. Acesso em 15 ago. 2019.

KHAN, R.M.K.; NAQVI, S.M. Geology, geochemistry and genesis of BIF of Kushtagi schist belt, Archaean Dharwar Craton, India. **Mineralium Deposita**, [s.l.], v. 31, n. 1-2, p.123-133, jan. 1996. Springer Nature. Disponível em: <http://dx.doi.org/10.1007/bf00225403>. Acesso em 15 ago. 2019.

KIRKPATRICK, S.; GELATT, C. D.; VECCHI, M. P. Optimization by Simulated Annealing. **Science**, [s.l.], v. 220, n. 4598, p.671-680, 13 maio 1983. American Association for the Advancement of Science (AAAS). Disponível em: <http://dx.doi.org/10.1126/science.220.4598.671>. Acesso em 15 mar. 2019.

KIRSCHVINK, Joseph L. Late Proterozoic Low-Latitude Global Glaciation: The Snowball Earth. *In: IN THE PROTEROZOIC BIOSPHERE: A MULTIDISCIPLINARY STUDY*, 1, 1992, Cambridge. **Proceedings...** Cambridge: Cambridge University Press, 1992. p. 51 - 52.

KLEIN Jr, Cornelis. Greenalite, stilpnomelane, minnesotaite, crocidolite and carbonates in a very low-grade metamorphic Precambrian iron-formation. **Canadian Mineralogist**, Vancouver, v. 12, n. 7, p.475-498, 1 nov. 1974.

KLEIN, C.; BRICKER, O. P. Some aspects of the sedimentary and diagenetic environment of Proterozoic banded iron-formation. **Economic Geology**, [s.l.], v. 72, n. 8, p.1457-1470, 1 dez. 1977. Society of Economic Geologists. Disponível em: <http://dx.doi.org/10.2113/gsecongeo.72.8.1457>. Acesso em 30 jul. 2019.



KLEIN, Cornelis; BEUKES, Nicolas J. Sedimentology and geochemistry of the glaciogenic late Proterozoic Rapitan Iron-Formation in Canada. **Economic Geology**, [s.l.], v. 88, n. 3, p.542-565, 1 maio 1993. Society of Economic Geologists. Disponível em: <http://dx.doi.org/10.2113/gsecongeo.88.3.542>. Acesso em 28 jul. 2019.

KLEIN, Cornelis; LADEIRA, Eduardo A. Geochemistry and mineralogy of Neoproterozoic Banded iron-formations and some selected, siliceous manganese formations from the Urucum District, Mato Grosso do Sul, Brazil. **Economic Geology**, [s.l.], v. 99, n. 6, p.1233-1244, 1 set. 2004. Society of Economic Geologists. Disponível em: <http://dx.doi.org/10.2113/gsecongeo.99.6.1233>. Acesso em 28 jul. 2019.

KLEIN, Cornelis. Some Precambrian banded iron-formations (BIFs) from around the world: Their age, geologic setting, mineralogy, metamorphism, geochemistry, and origins. **American Mineralogist**, [s.l.], v. 90, n. 10, p.1473-1499, 1 out. 2005. Mineralogical Society of America. Disponível em: <http://dx.doi.org/10.2138/am.2005.1871>. Acesso em 03 jul. 2017.

KLEN, André Monteiro. **Algoritmo para agrupamento de descontinuidades em famílias baseado no método fuzzy K-means**. 2015. 141 f. Tese (Doutorado) - Pós-graduação em Geotecnia, Escola de Minas/UFOP, Universidade Federal de Ouro Preto, Ouro Preto, 2015.

KONHAUSER, Kurt O. *et al.* Iron formations: A global record of Neoarchean to Palaeoproterozoic environmental history. **Earth-science Reviews**, [s.l.], v. 172, p.140-177, set. 2017. Elsevier BV. Disponível em: <http://dx.doi.org/10.1016/j.earscirev.2017.06.012>. Acesso em 13 jul. 2019.

KRAUSKOPF, Konrad B. Separation of manganese from iron in sedimentary processes. **Geochimica et Cosmochimica Acta**, [s.l.], v. 12, n. 1-2, p.61-84, jan. 1957. Elsevier BV. Disponível em: [http://dx.doi.org/10.1016/0016-7037\(57\)90018-2](http://dx.doi.org/10.1016/0016-7037(57)90018-2). Acesso em 23 abr. 2018.

KRAUSKOPF, Konrad B.; BIRD, Dennis K. **Introduction to Geochemistry**. Singapore: McGraw-hill Book Co, 1995. 646 p.

KRETZ, Ralph. Symbols for rock-forming minerals. **American Mineralogist**, Mclean, v. 68, n.1-2, p.277-279. Disponível em: <https://pubs-geoscienceworld-org.ez11.periodicos.capes.gov.br/msa/ammin/article-standard/68/1-2/277/41456/Symbols-for-rock-forming-minerals>. Acesso em: 30 set. 2019.

KRIGE, Danie G. A statistical approach to some basic mine valuation problems on the Witwatersrand. **Journal of Chemical Metallurgy and Mineralogical Society of South Africa**, Johannesburg, v. 52, n. 6, p.119-139, 6 dez. 1951.

KRUMBEIN, W. C.; GARRELS, R. M. Origin and Classification of Chemical Sediments in Terms of pH and Oxidation-Reduction Potentials. **The Journal of Geology**, [s.l.], v. 60, n. 1, p.1-33, jan. 1952. University of Chicago Press. Disponível em: <http://dx.doi.org/10.1086/625929> Acesso em: 23 set. 2018

KULIK, Dmitri A.; KORZHNEV, Michael N. Lithological and geochemical evidence of Fe and Mn pathways during deposition of Lower Proterozoic banded iron formation in the Krivoy Rog Basin (Ukraine). **Geological Society, London, Special Publications**, [s.l.], v.

119, n. 1, p.43-80, 1997. Geological Society of London. Disponível em: <http://dx.doi.org/10.1144/gsl.sp.1997.119.01.04>. Acesso em: 23 set. 2018.

LEBART, Ludovic; MORINEAU, Alain; WARWICK, Kenneth M. **Multivariate Descriptive Statistical Analysis: Multivariate Descriptive Statistical Analysis: Correspondence Analysis and Related Methods for Large Matrices**. New York: John Wiley and Sons, 1984. 231 p.

LEITH, Charles Kenneth; HARDER, E. C. Hematite ores of Brazil and a comparison with hematite ores of Lake Superior. **Economic Geology**, [s.l.], v. 6, n. 7, p.670-686, 1 out. 1911. Society of Economic Geologists. Disponível em: <http://dx.doi.org/10.2113/gsecongeo.6.7.670>. Acesso em: 23 jul. 2016.

LEUANGTHONG, Oy; MCLENNAN, Jason A.; DEUTSCH, Clayton V. Minimum Acceptance criteria for geostatistical realizations. **Natural Resources Research**, [s.l.], v. 13, n. 3, p.131-141, set. 2004. Springer Nature. Disponível em: <http://dx.doi.org/10.1023/b:narr.0000046916.91703.bb>. Acesso em: 02 mai. 2019.

LIN, Yu-pin; CHANG, Tsun-kuo; TENG, Tung-po. Characterization of soil lead by comparing sequential Gaussian simulation, simulated annealing simulation and kriging methods. **Environmental Geology**, [s.l.], v. 41, n. 1-2, p.189-199, 14 jul. 2001. Springer Science and Business Media LLC. Disponível em: <http://dx.doi.org/10.1007/s002540100382>. Acesso em: 02 mar. 2019.

LIN, Yu-pin; TAN, Yih-chi; ROUHANI, Shahrokh. Identifying spatial characteristics of transmissivity using simulated annealing and kriging methods. **Environmental Geology**, [s.l.], v. 41, n. 1-2, p.200-208, 14 jul. 2001. Springer Science and Business Media LLC. Disponível em: <http://dx.doi.org/10.1007/s002540100383>. Acesso em: 02 mar. 2019.

MACAMBIRA, Joel Buenano; SCHRANK, Alfonso. Químio-estratigrafia e evolução dos jaspilitos da Formação Carajás (PA). **Revista Brasileira de Geociências**, São Paulo, v. 32, n. 4, p.567-578, dez. 2002.

MAERZ, Norbert H; ZHOU, Wei. Multivariate analysis of bore hole discontinuity data. *In: US ROCK MECHANICS SYMPOSIUM*, 37., 1999, Vail. **Proceedings...** Vail: Rock Mech, 1999. p. 431 - 438.

MAJUMDER, Tapan; CHAKRABORTY, K.L.; BHATTACHARYYA, Auditeya. Geochemistry of banded iron formation of Orissa, India. **Mineralium Deposita**, [s.l.], v. 17, n. 1, p.107-118, mar. 1982. Springer Nature. Disponível em: <http://dx.doi.org/10.1007/bf00206379>. Acesso em: 02 mar. 2016.

MALLET, Jean-laurent. **Geomodelling**. New York: Oxford Press University, 2002. 624 p.

MANLY, Brian F J. **Multivariate Statistical Methods: A Primer**. 2. ed. London: Chapman & Hall, 1994. 215 p.

MATA, Maria das Vitorias Medeiros da. **Análise de agrupamentos dos dados de DFA oriundos de perfis elétricos de indução de poços de petróleo**. 2009. 69 f. Dissertação (Mestrado) – Pós-graduação em Ciência e Tecnologia do Petróleo/Física Aplicada à

Exploração e à Produção de Petróleo e Gás Natural, Universidade Federal do Rio Grande do Norte, Natal, 2009.

MATHERON, Georges. **Traité de Géostatistique Appliquée. Tome II: Le Krigeage.** Paris: Editions Technip, 1963. 380 p.

MATHERON, Georges. **Les Variables Régionalisées et leur Estimation.** Paris: Masson Et Cie, Éditeurs, 1965. 306 p.

MAXWELL, Charles H. **Geology and ore deposits of the Alegria District, Minas Gerais, Brazil.** Washington: United States Government Printing Office 341-J, 1972. 72 p.

MBOUDOU, Germain M. M.; SUH, Cheo E.; MAFANY, George T. Geochemical Characterization of Novokrivoyrog metavolcanics: Tectonic Implications and Relationship with the Early Proterozoic Banded Iron Formation (BIF) of Krivoy Rog in Ukraine. **Open Journal of Geology**, [s.l.], v. 02, n. 03, p.121-135, 2012. Scientific Research Publishing, Inc. Disponível em: <http://dx.doi.org/10.4236/ojg.2012.23013>. Acesso em: 16 nov. 2016.

MELLINGER, Michel. Correspondence analysis in the study of litho-geochemical data: General strategy and the usefulness of various data-coding schemes. **Journal of Geochemical Exploration**, [s.l.], v. 21, n. 1-3, p.455-469, jul. 1984. Elsevier BV. Disponível em: [http://dx.doi.org/10.1016/0375-6742\(84\)90067-0](http://dx.doi.org/10.1016/0375-6742(84)90067-0). Acesso em: 05 mai. 2016.

MELLINGER, Michel. Multivariate data analysis: Its methods. **Chemometrics and Intelligent Laboratory Systems**, [s.l.], v. 2, n. 1-3, p.29-36, ago. 1987a. Elsevier BV. Disponível em: [http://dx.doi.org/10.1016/0169-7439\(87\)80083-7](http://dx.doi.org/10.1016/0169-7439(87)80083-7). Acesso em: 05 mai. 2016.

MELLINGER, Michel. Correspondence Analysis: The Method and Its Application. **Chemometrics and Intelligent Laboratory Systems**, [s.l.], v. 2, n. 1-3, p.61-77, ago. 1987b. Elsevier BV. Disponível em: [http://dx.doi.org/10.1016/0169-7439\(87\)80086-2](http://dx.doi.org/10.1016/0169-7439(87)80086-2). Acesso em: 05 mai. 2016.

MEL'NIK, Y. P. **Precambrian Banded Iron-Formations: Physicochemical Conditions of Formation.** Amsterdam: Elsevier Science, 1982. 310 p.

METROPOLIS, Nicholas; Rosenbluth, Ariana W.; Rosenbluth, Marshall N.; Teller, Augusta H. Equation of State Calculations by Fast Computing Machines. **The Journal of Chemical Physics**, [s.l.], v. 21, n. 6, p.1087-1092, jun. 1953. AIP Publishing. Disponível em: <http://dx.doi.org/10.1063/1.1699114>. Acesso em: 15 mai. 2019.

MHAG Serviços e Mineração S.A. Projeto produção *de pellet feed* 2.0 MPTA: Mapa geológico de detalhe. Unpublished Internal Report, 3<sup>rd</sup> Revision. Jucurutu, Brazil. 2013. 29pp.

MOHR, Steve *et al.* Projection of iron ore production. **Natural Resources Research**, [s.l.], v. 24, n. 3, p.317-327, 27 nov. 2014. Springer Science and Business Media LLC. Disponível em: <http://dx.doi.org/10.1007/s11053-014-9256-6>. Acesso em: 15 mai. 2019.

MORRIS, R. C.; KNEESHAW, M. Genesis modelling for the Hamersley BIF-hosted iron ores of Western Australia: a critical review. **Australian Journal of Earth Sciences**, [s.l.], v.

58, n. 5, p.417-451, jul. 2011. Informa UK Limited. Disponível em: <http://dx.doi.org/10.1080/08120099.2011.566937> Acesso em: 15 mai. 2016.

MURRAY, Richard W. Chemical criteria to identify the depositional environment of chert: general principles and applications. **Sedimentary Geology**, [s.l.], v. 90, n. 3-4, p.213-232, maio 1994. Elsevier BV. Disponível em: [http://dx.doi.org/10.1016/0037-0738\(94\)90039-6](http://dx.doi.org/10.1016/0037-0738(94)90039-6). Acesso em: 15 jul. 2019.

NASCIMENTO, Rielva Solimairy Campelo do. **Quimioestratigrafia de  $\delta^{13}\text{C}$ ,  $\delta^{18}\text{O}$  E  $^{87}\text{Sr}/^{86}\text{Sr}$  aplicada a mármores da Faixa Seridó (NE do Brasil): Implicações geotectônicas e paleoambientais**. 2002. 122 f. Tese (Doutorado) – Pós-graduação em Geociências, Universidade Federal de Pernambuco, Recife, 2002.

NASCIMENTO, Rielva Solimairy Campelo do; SIAL, Alcides da Nóbrega.; PIMENTEL, Márcio M. Chemostratigraphy of Medium-grade Marbles of the Late Neoproterozoic Seridó Group, Seridó Fold Belt, Northeastern Brazil. **Gondwana Research**, [s.l.], v. 7, n. 3, p.731-744, jul. 2004. Elsevier BV. Disponível em: [http://dx.doi.org/10.1016/s1342-937x\(05\)71059-5](http://dx.doi.org/10.1016/s1342-937x(05)71059-5). Acesso em: 11 mai. 2016.

NERI, Marcos Eduardo Nilton Vieira; ROSIÈRE, Carlos Alberto; LANA, Cristiano de Carvalho. Supergrupo Minas na Serra de Bom Sucesso, extremo sudoeste do Quadrilátero Ferrífero - MG: petrografia, geoquímica e isótopos de U-Pb. **Geologia USP. Série Científica**, [s.l.], v. 13, n. 2, p.175-202, 1 jun. 2013. Universidade de São Paulo Sistema Integrado de Bibliotecas - SIBiUSP. Disponível em: <http://dx.doi.org/10.5327/z1519-874x2013000200010>. Acesso em: 15 mai. 2016.

NEVES, Benjamim Bley de Brito. **Regionalização geotectônica do precambriano nordestino**. 1975. 198 f. Tese (Doutorado) - Curso de Pós-graduação em Geologia Regional, Instituto de Geociências, Universidade de São Paulo, São Paulo, 1975.

NEVES, Benjamim Bley de Brito; FUCK, Reinhardt Adolfo. Neoproterozoic evolution of the basement of the South-American platform. **Journal of South American Earth Sciences**, [s.l.], v. 47, p.72-89, nov. 2013. Elsevier BV. Disponível em: <http://dx.doi.org/10.1016/j.jsames.2013.04.005>. Acesso em: 25 jul. 2016.

NISHISATO, Shizuhiko. Measurement and Multivariate Analysis. In: MEASUREMENT AND MULTIVARIATE ANALYSIS, 1, 2002, Tokyo. **Measurement and Multivariate Analysis**. Tokyo: Springer, 2002. p. 25 - 36.

OKAMOTO, Go; OKURA, Takeshi; GOTO, Katsumi. Properties of silica in water. **Geochimica et Cosmochimica Acta**, [s.l.], v. 12, n. 1-2, p.123-132, jan. 1957. Elsevier BV. Disponível em: [http://dx.doi.org/10.1016/0016-7037\(57\)90023-6](http://dx.doi.org/10.1016/0016-7037(57)90023-6). Acesso em: 23 jul. 2016.

PARAVARZAR, Shahrokh; EMERY, Xavier; MADANI, Nasser. Comparing sequential Gaussian and turning bands algorithms for cosimulating grades in multi-element deposits. **Comptes Rendus Geoscience**, [s.l.], v. 347, n. 2, p.84-93, mar. 2015. Elsevier BV. Disponível em: <http://dx.doi.org/10.1016/j.crte.2015.05.008>. Acesso em: 17 jun. 2017.

PARKS, James M. Cluster analysis applied to multivariate geologic problems. **The Journal of Geology**, [s.l.], v. 74, n. 52, p.703-715, set. 1966. University of Chicago Press. Disponível em: <http://dx.doi.org/10.1086/627205> Acesso em: 11 jun. 2017.

PATINHA, C. *et al.* Definition of geochemical patterns on the soil of Paul de Arzila using correspondence analysis. **Journal of Geochemical Exploration**, [s.l.], v. 98, n. 1-2, p.34-42, jul. 2008. Elsevier BV. Disponível em: <http://dx.doi.org/10.1016/j.gexplo.2007.10.001>. Acesso em: 11 jun. 2017.

PEARSON, Karl. L. On lines and planes of closest fit to systems of points in space. **The London, Edinburgh, and Dublin Philosophical Magazine and Journal of Science**, [s.l.], v. 2, n. 11, p.559-572, nov. 1901. Informa UK Limited. Disponível em: <http://dx.doi.org/10.1080/14786440109462720>. Acesso em: 11 jun. 2017.

PECOITS, E. *et al.* Petrography and geochemistry of the Dales Gorge banded iron formation: Paragenetic sequence, source and implications for paleo-ocean chemistry. **Precambrian Research**, [s.l.], v. 172, n. 1-2, p.163-187, jul. 2009. Elsevier BV. Disponível em: <http://dx.doi.org/10.1016/j.precamres.2009.03.014>. Acesso em: 11 jul. 2018.

PEREIRA, Henrique José Figueiredo Garcia. **Análise estrutural e seus reflexos na avaliação económica de recursos minerais**. 1981. 460 f. Tese (Doutorado) - Doutoramento em Ciências da Engenharia, Universidade de Lisboa, Lisboa, 1981.

PEREIRA, Henrique Garcia; SOUSA, António Jorge de; SALGUEIRO, Rita; DOWD, Peter. **Correspondence Analysis as a Modeling Tool**. Lisbon: IST Press, 2015. 236 p.

PODANI, Jannüs. **Introduction to the Exploration of Multivariate Biological Data**. Leiden: Backhuys Publishers, 2006. 407 p.

RAMDOHR, Paul. **The Ore Minerals and Their Intergrowths**. 2. ed. Oxford: Pergamon Press, 1969. 1269 p.

RANKAMA, Kalervo; SAHAMA, Th. G. **Geochemistry**. Chicago: The University of Chicago Press, 1960. 911 p.

RASKA, Nadine. **3D geologic subsurface modeling within the Mackenzie Plain, Northwest Territories, Canada**. 2017. 87 f. Dissertação (Mestrado) - Geographic Information Sciences, Department of Physical Geography and Ecosystem Science, Lund University, Lund, 2017.

REIS, A.; SOUSA, A.J.; SILVA, E. Ferreira da; PATINHA, C.; FONSECA, E.C. Combining multiple correspondence analysis with factorial kriging analysis for geochemical mapping of the gold-silver deposit at Marrancos (Portugal). **Applied Geochemistry**, [s.l.], v. 19, n. 4, p.623-631, abr. 2004. Elsevier BV. Disponível em: <http://dx.doi.org/10.1016/j.apgeochem.2003.09.003>. Acesso em: 14 jul. 2017.

RENGER, Friedrich E. O “quadro geognóstico do Brasil” de Wilhelm Ludwig von Eschwege: Breves comentários à sua visão da geologia no Brasil. **Geonomos**, [s.l.], p.91-95, 17 fev. 2013. GEONOMOS. Disponível em: <http://dx.doi.org/10.18285/geonomos.v13i1e2.139>. Acesso em: 05 fev. 2019.

RHODES, J. M. The application of cluster and discriminatory analysis in mapping granite intrusions. **Lithos**, [s.l.], v. 2, n. 3, p.223-237, jan. 1969. Elsevier BV. Disponível em: [http://dx.doi.org/10.1016/s0024-4937\(69\)80017-4](http://dx.doi.org/10.1016/s0024-4937(69)80017-4). Acesso em: 05 jun. 2016.

RODRIGUES, Rafael de S.; BRANDÃO, Paulo R. G. Influência da liberação mineral nas etapas de moagem e flotação do minério de ferro. **Tecnologia em Metalurgia Materiais e Mineração**, [s.l.], v. 14, n. 3, p.279-287, 2017. Editora Cubo Multimídia. Disponível em: <http://dx.doi.org/10.4322/2176-1523.1153>. Acesso em: 05 mar. 2019.

ROSSI, Daniel Quinaud; ENDO, Issamu; GABRIEL, Eduardo Guimarães. Structural framework of the iron district of Itabira, Iron Quadrangle, Minas Gerais. **REM - International Engineering Journal**, [s.l.], v. 72, n. 1, p.39-45, mar. 2019. UNIFESP (SciELO). Disponível em: <http://dx.doi.org/10.1590/0370-44672017720108>. Acesso em: 12 abr. 2019.

ROY, A. Application of cluster analysis in the interpretation of geochemical data from the Sargipalli lead-zinc mine area, Sundergarh district, Orissa (India). **Journal of Geochemical Exploration**, [s.l.], v. 14, p.245-264, jan. 1981. Elsevier BV. Disponível em: [http://dx.doi.org/10.1016/0375-6742\(81\)90115-1](http://dx.doi.org/10.1016/0375-6742(81)90115-1). Acesso em: 12 abr. 2019.

SÁ, Emanuel Ferraz Jardim de; SALIM, José. Reavaliação dos conceitos estratigráficos na região do Seridó (RN-PB). **Mineração Metal**, São Paulo, v. 1, n. 80, p.16-28, 1980.

SÁ, Emanuel Ferraz Jardim de. Geologia da região do Seridó: Reavaliação dos dados. In: SIMPÓSIO DE GEOLOGIA DO NORDESTE, 11, 1984, Natal. **Anais...** Natal: SBG, 1984. p. 278 - 296.

SÁ, Emanuel Ferraz Jardim de. **Faixa Seridó (Província Borborema, NE do Brasil) e o seu significado geodinâmico na Cadeia Brasileira/Pan-Africana**. 1994. 804 f. Tese (Doutorado) Pós-graduação em Geologia, Instituto de Geociências, Universidade de Brasília, Brasília, 1994.

SÁ, Emanuel Ferraz Jardim, Fuck R.A., Macedo, M.H.F., Peucat, J.J., Kawashita, K., Souza, Z.S., Bertrand, J.M. Pre-Brasiliano orogenic evolution in the Seridó belt, NE Brazil: Conflicting geochronological and structural data. **Revista Brasileira de Geociências**, [s.l.], v. 25, n. 4, p.307-314, 1 dez. 1995. Sociedade Brasileira de Geologia. Disponível em: <http://dx.doi.org/10.25249/0375-7536.1995307314>. Acesso em: 12 jun. 2016.

SAHA, A.K.; SARKAR, S.N.; BASU, S.; GANGULY, D. A multivariate statistical study of copper mineralization in the central section of Mosaboni Mine, Eastern Singhbhum, India. **Mathematical Geology**, [s.l.], v. 18, n. 2, p.215-235, fev. 1986. Springer Science and Business Media LLC. Disponível em: <http://dx.doi.org/10.1007/bf00898284>. Acesso em: 12 out. 2018.

SHIMISU, Viviane Kotani. **Classificação e caracterização de tipos de minério de cobre da mina de Sossego - Região de Carajás**. 2012. 121 f. Dissertação (Mestrado) – Pós-graduação em Engenharia Mineral, Escola Politécnica da Universidade de São Paulo, São Paulo, 2012.

SIAL, Alcides da Nóbrega *et al.* Algoma-type Neoproterozoic BIFs and related marbles in the Seridó Belt (NE Brazil): REE, C, O, Cr and Sr isotope evidence. **Journal of South American Earth Sciences**, [s.l.], v. 61, p.33-52, ago. 2015. Elsevier BV. Disponível em: <http://dx.doi.org/10.1016/j.jsames.2015.04.001>. Acesso em: 12 out. 2018.

SMITH, P. P. K. The observation of enantiomorphous domains in a natural maghemite. **Contributions to Mineralogy and Petrology**, [s.l.], v. 69, n. 3, p.249-254, 1979. Springer Nature. Disponível em: <http://dx.doi.org/10.1007/bf00372327>. Acesso em: 12 ago. 2019.

SOARES, Amilcar. Direct sequential simulation and cosimulation. **Mathematical Geology**, [s.l.], v. 33, n. 8, p.911-926, 2001. Springer Nature. Disponível em: <http://dx.doi.org/10.1023/a:1012246006212>. Acesso em: 12 fev. 2019.

SOMMER, Carlos Augusto *et al.* Recognition and characterization of high-grade ignimbrites from the Neoproterozoic rhyolitic volcanism in southernmost Brazil. **Journal of South American Earth Sciences**, [s.l.], v. 47, p.152-165, nov. 2013. Elsevier BV. Disponível em: <http://dx.doi.org/10.1016/j.jsames.2013.07.010>. Acesso em: 12 ago. 2019.

SOUSA, António Jorge Gonçalves de. **Análise de dados e geoestatística multivariada**: Aplicação à tipologia de minérios. 1988. 152 f. Tese (Doutorado) - Doutoramento em Ciências da Engenharia, Universidade de Lisboa, Lisboa, 1988.

STATSOFT Inc. **Statistica 10** Enterprise User's Manual. Tulsa. 2010.

STERN, Robert J. *et al.* Evidence for the Snowball Earth hypothesis in the Arabian-Nubian Shield and the East African Orogen. **Journal of African Earth Sciences**, [s.l.], v. 44, n. 1, p.1-20, jan. 2006. Elsevier BV. Disponível em: <http://dx.doi.org/10.1016/j.jafrearsci.2005.10.003>. Acesso em: 12 ago. 2019.

STERN, Robert J. *et al.* ~750Ma banded iron formation from the Arabian-Nubian Shield—Implications for understanding Neoproterozoic tectonics, volcanism, and climate change. **Precambrian Research**, [s.l.], v. 239, p.79-94, dez. 2013. Elsevier BV. Disponível em: <http://dx.doi.org/10.1016/j.precamres.2013.07.015>. Acesso em: 12 ago. 2019.

SYLVESTRE, Ganno *et al.* Petrology and geochemistry of the banded iron-formations from Ntem complex greenstones belt, Elom area, Southern Cameroon: Implications for the origin and depositional environment. **Geochemistry**, [s.l.], v. 75, n. 3, p.375-387, out. 2015. Elsevier BV. Disponível em: <http://dx.doi.org/10.1016/j.chemer.2015.08.001>. Acesso em: 01 jul. 2017.

TANER, Mehmet F.; CHEMAM, Madjid. Algoma-type banded iron formation (BIF), Abitibi Greenstone belt, Quebec, Canada. **Ore Geology Reviews**, [s.l.], v. 70, p.31-46, out. 2015. Elsevier BV. Disponível em: <http://dx.doi.org/10.1016/j.oregeorev.2015.03.016>. Acesso em: 07 jul. 2017.

TANG, Jiafu; FU, Heqin; YU, Zhiqing. Stratigraphy, type and formation conditions of the late Precambrian banded iron ores in south China. **Chinese Journal of Geochemistry**, [s.l.], v. 6, n. 4, p.331-341, out. 1987. Springer Science and Business Media LLC. Disponível em: <http://dx.doi.org/10.1007/bf02872262>. Acesso em: 18 jun. 2016.

TEIL, H. Correspondence factor analysis: An outline of its method. **Journal of The International Association for Mathematical Geology**, [s.l.], v. 7, n. 1, p.3-12, fev. 1975. Springer Science and Business Media LLC. Disponível em: <http://dx.doi.org/10.1007/bf02080630>. Acesso em: 02 jul. 2016.

TEIL, H.; CHEMINEE, J. L. Application of correspondence factor analysis to the study of major and trace elements in the Erta Ale Chain (Afar, Ethiopia). **Journal of The International Association for Mathematical Geology**, [s.l.], v. 7, n. 1, p.13-30, fev. 1975. Springer Science and Business Media LLC. Disponível em: <http://dx.doi.org/10.1007/bf02080631>. Acesso em: 02 jul. 2016.

TEILLARD, Pierre; VOLLE, Michel. Détection des points aberrants en analyse factorielle des correspondances. **Annales de l'Inséé**. n.22/23,p.237-254, set,1976.

TONINI, Andrea; GUASTALDI, Enrico; MECCHERI, Marco. Three-dimensional reconstruction of the Carrara Syncline (Apuane Alps, Italy): An approach to reconstruct and control a geological model using only field survey data. **Computers & Geosciences**, [s.l.], v. 35, n. 1, p.33-48, jan. 2009. Elsevier BV. Disponível em: <http://dx.doi.org/10.1016/j.cageo.2007.09.010>. Acesso em: 15 set. 2017.

VALENCHON, F. The use of correspondence analysis in geochemistry. **Journal of The International Association for Mathematical Geology**, [s.l.], v. 14, n. 4, p.331-342, ago. 1982. Springer Science and Business Media LLC. Disponível em: <http://dx.doi.org/10.1007/bf01032594>. Acesso em: 02 jul. 2016.

VAN MAANEN, Peter-Paul *et al.* Quality control of geological voxel models using experts' gaze. **Computers & Geosciences**, [s.l.], v. 76, p.50-58, mar. 2015. Elsevier BV. Disponível em: <http://dx.doi.org/10.1016/j.cageo.2014.11.011>. Acesso em: 30 jul. 2019.

VAN SCHMUS, W. R., BRITO NEVES, B.B., WILLIAMS, I.S., HACKSPACHER, P.C., FETTER, A.H., DANTAS, E.L., BARBINSKI, M. The Seridó Group of NE Brazil, a late Neoproterozoic pre- to syn-collisional basin in West Gondwana: insights from SHRIMP U–Pb detrital zircon ages and Sm–Nd crustal residence ( $T_{DM}$ ) ages. **Precambrian Research**, [s.l.], v. 127, n. 4, p.287-327, dez. 2003. Elsevier BV. Disponível em: [http://dx.doi.org/10.1016/s0301-9268\(03\)00197-9](http://dx.doi.org/10.1016/s0301-9268(03)00197-9). Acesso em: 26 abr. 2016.

VERÍSSIMO, César Ulisses Vieira. **Jazida de Alegria: Gênese e Tipologia dos Minérios de Ferro (Minas 3,4 e 5 - Porção Ocidental)**. 1999. 2V. 234 f. Tese (Doutorado) – Pós-graduação em Geociências, Universidade Estadual Paulista Júlio de Mesquita, Rio Claro, 1999.

VERÍSSIMO, César U. V. *et al.* Petrografia e litoquímica das formações ferríferas bandadas da região de Quixeramobim - Boa Viagem, Ceará, Brasil. **Geociências**, Rio Claro, v.28, n.1, p.43-52, Abr./2009.

VOLLGGER, Stefan A.; CRUDEN, Alexander R.; AILLERES Laurent; COWAN, E. Jun. Regional dome evolution and its control on ore-grade distribution: Insights from 3D implicit modelling of the Navachab gold deposit, Namibia. **Ore Geology Reviews**, [s.l.], v. 69, p.268-284, set. 2015. Elsevier BV. Disponível em: <http://dx.doi.org/10.1016/j.oregeorev.2015.02.020>. Acesso em: 26 abr. 2016.



WARD, Joe H. Hierarchical grouping to optimize an objective function. **Journal of the American Statistical Association**, [s.l.], v. 58, n. 301, p.236-244, mar. 1963. Informa UK Limited. Disponível em: <http://dx.doi.org/10.1080/01621459.1963.10500845>. Acesso em: 18 jul. 2016.

WEBB, Adam D. **From banded iron-formation to iron ore: Geochemical and mineralogical constraints from across the Hamersley Province, Western Australia**. 2004. 269 f. Tese (Doutorado) - Geosciences, School of Earth Sciences, James Cook University, Queensland, 2003.

WOLD, Svante; ESBENSEN, Kim; GELADI, Paul. Principal Component Analysis. **Chemometrics and Intelligent Laboratory Systems**, [s.l.], v. 2, n. 1-3, p.37-52, ago. 1987. Elsevier BV. Disponível em: [http://dx.doi.org/10.1016/0169-7439\(87\)80084-9](http://dx.doi.org/10.1016/0169-7439(87)80084-9). Acesso em: 16 jun. 2016.

XU, Deru R. *et al.* Petrography and geochemistry of the Shilu Fe–Co–Cu ore district, South China: Implications for the origin of a Neoproterozoic BIF system. **Ore Geology Reviews**, [s.l.], v. 57, p.322-350, mar. 2014. Elsevier BV. Disponível em: <http://dx.doi.org/10.1016/j.oregeorev.2013.08.011>. Acesso em: 18 jul. 2018.

YAMAMOTO, Jorge Kazuo. An alternative measure of the reliability of ordinary kriging estimates. **Mathematical Geology**, [s.l.], v. 32, n. 4, p.489-509, 2000. Springer Nature. Disponível em: <http://dx.doi.org/10.1023/a:1007577916868>. Acesso em: 02 fev. 2016.

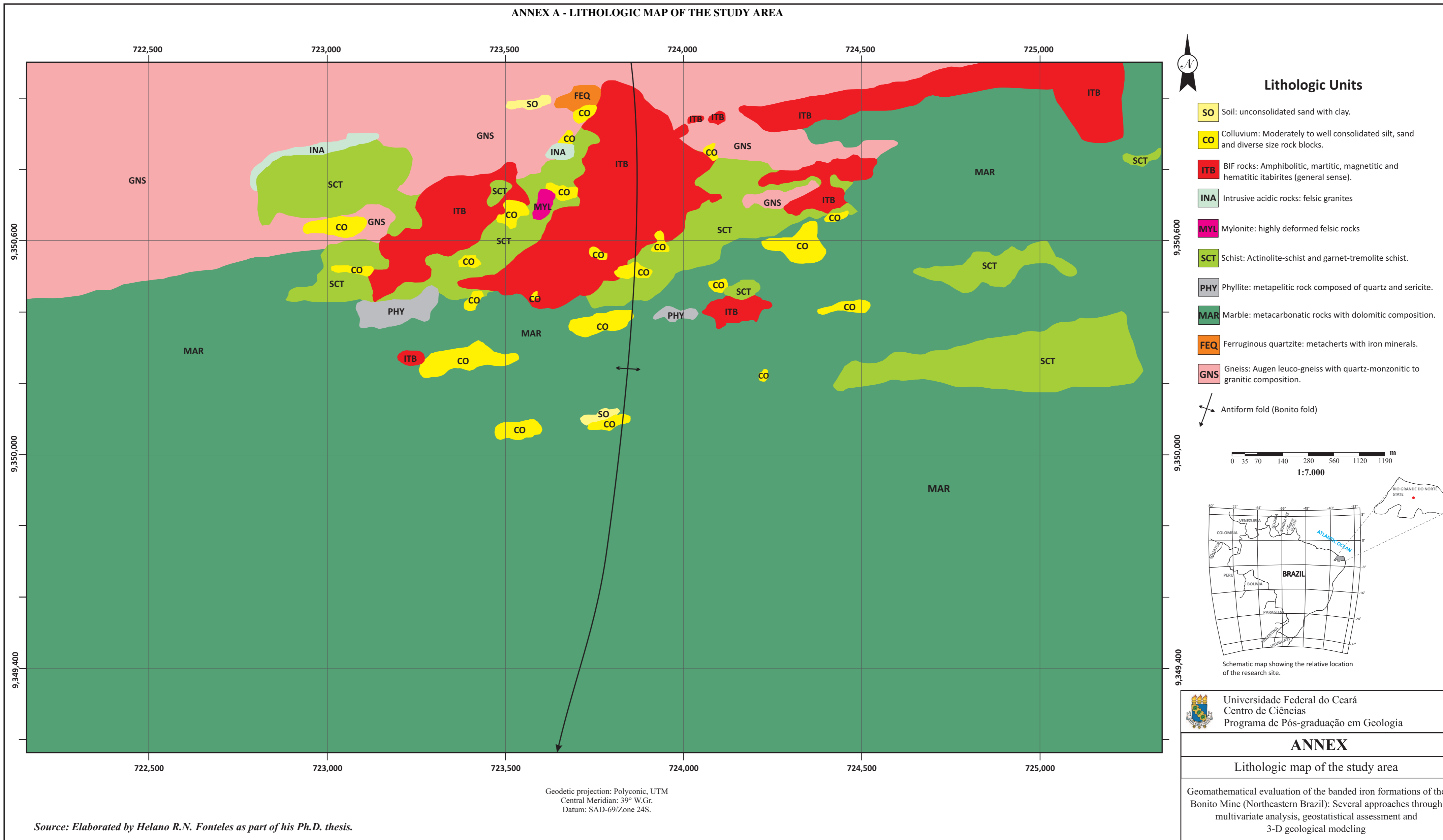
YAMAMOTO, Jorge Kazuo. Estimation or simulation? That is the question. **Computational Geosciences**, [s.l.], v. 12, n. 4, p.573-591, 17 ago. 2008. Springer Science and Business Media LLC. Disponível em: <http://dx.doi.org/10.1007/s10596-008-9096-8>. Acesso em: 02 fev. 2016.

YOUNG, Grant M. Stratigraphic and tectonic settings of Proterozoic glaciogenic rocks and banded iron-formations: relevance to the snowball Earth debate. **Journal of African Earth Sciences**, [s.l.], v. 35, n. 4, p.451-466, nov. 2002. Elsevier BV. Disponível em: [http://dx.doi.org/10.1016/s0899-5362\(02\)00158-6](http://dx.doi.org/10.1016/s0899-5362(02)00158-6). Acesso em: 16 mar. 2016.

ZHAO, Shan; Zhou, Y.; Wang, M.; Xin, X.; Chen, C. Thickness, porosity, and permeability prediction: comparative studies and application of the geostatistical modeling in an Oil field. **Environmental Systems Research**, [s.l.], v. 3, n. 1, p.7-24, 2014. Springer Nature. Disponível em: <http://dx.doi.org/10.1186/2193-2697-3-7>. Acesso em: 22 mar. 2018.

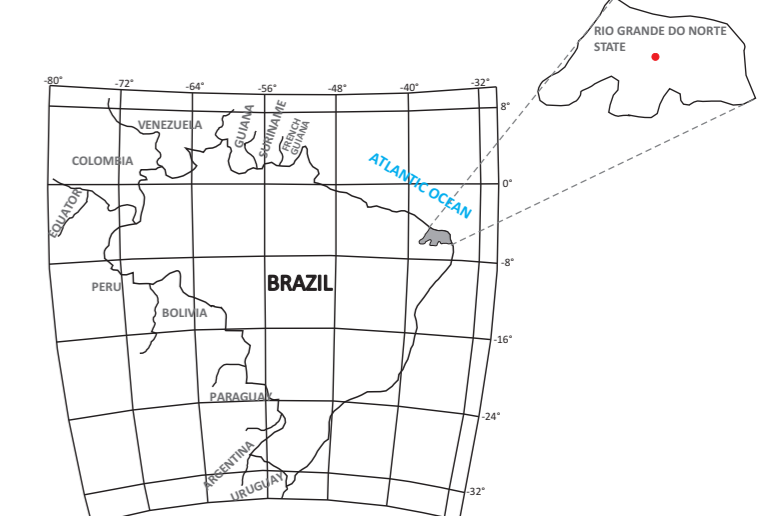
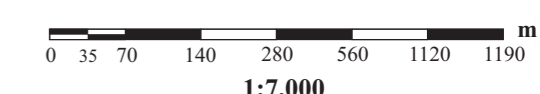
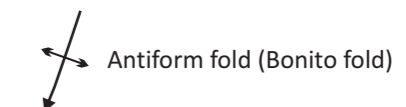
ZHOU, Di; CHANG, Theodore; DAVIS, John C. Dual extraction of R-mode and Q-mode factor solutions. **Journal of The International Association for Mathematical Geology**, [s.l.], v. 15, n. 5, p.581-606, out. 1983. Springer Science and Business Media LLC. Disponível em: <http://dx.doi.org/10.1007/bf01093413>. Acesso em: 08 mar. 2016.

ANNEX A - LITHOLOGIC MAP OF THE STUDY AREA




Lithologic Units

- SO Soil: unconsolidated sand with clay.
- CO Colluvium: Moderately to well consolidated silt, sand and diverse size rock blocks.
- ITB BIF rocks: Amphibolitic, martitic, magnetitic and hematitic itabirites (general sense).
- INA Intrusive acidic rocks: felsic granites
- MYL Mylonite: highly deformed felsic rocks
- SCT Schist: Actinolite-schist and garnet-tremolite schist.
- PHY Phyllite: metapelitic rock composed of quartz and sericite.
- MAR Marble: metacarbonatic rocks with dolomitic composition.
- FEQ Ferruginous quartzite: metacherts with iron minerals.
- GNS Gneiss: Augen leuco-gneiss with quartz-monzonitic to granitic composition.



Geodetic projection: Polyconic, UTM  
Central Meridian: 39° W.Gr.  
Datum: SAD-69/Zone 24S.

Source: Elaborated by Helano R.N. Fonteles as part of his Ph.D. thesis.


 Universidade Federal do Ceará  
 Centro de Ciências  
 Programa de Pós-graduação em Geologia

---

**ANNEX**

Lithologic map of the study area

---

Geomathematical evaluation of the banded iron formations of the Bonito Mine (Northeastern Brazil): Several approaches through multivariate analysis, geostatistical assessment and 3-D geological modeling